The Dissertation Committee for Rodrigo Ruizpalacios Certifies that this is the approved version of the following dissertation:

Laser Direct-Write of Optical Components Prepared Using the Sol-Gel Process

Committee:

Kristin L. Wood, Supervisor

Joseph J. Beaman, Supervisor

Richard H. Crawford

David L. Bourell

Matthew I. Campbell

Colin F. Norman

Laser Direct-Write of Optical Components Prepared Using the Sol-Gel Process

by

Rodrigo Ruizpalacios, B.S., M.S.

Dissertation

Presented to the Faculty of the Graduate School of

The University of Texas at Austin

in Partial Fulfillment

of the Requirements

for the Degree of

Doctor of Philosophy

The University of Texas at Austin

December, 2004

Dedication

To my parents Guillermo and Beatriz for their endless support, and for their encouragement in my academic career. To my sister Betty and brother Alonso who have been close to me from the start of this journey.

To my wife Laura, who joined me on the last leg of this very long trip, for her encouragement, patience and love, and for being an endless source of inspiration during the last part of my doctorate.

To the memory of my grandmother Maria Luisa. To my grandparents Jose and Estela for all their wisdom and love.

Acknowledgements

my great friend David Thompson, whom I admire deeply for his knowledge and humbleness.

To my friends at the LFF lab, Seoyuk Ahn, Jeremy Murphy, Vinay Sriram, Scott Evans, and Jorge Ramos, who was a great mentor. A special thank you to Carey King for his friendship and encouragement; I always suffered watching the USA-Mexico soccer games.

To Mike Mignatti, who became a good friend, I wish to thank him for the work we did together for this project. He always showed great enthusiasm, professionalism, and kept the spirits high with good humor.

Many of the things that I was able to achieve could not have been possible without the support and patience from Cindy Pflughoft, the administrative associate for the LFF lab, and an angel behind every challenge. Brisa Ponce, as an undergraduate student, also provided me with the best support, friendship, and enthusiasm. To Dr. Hideki Kyogoku, for those long hours in the cold lab.

On a similar note, I wish to thank Danny Jares and the rest of the people at the Machine Shop, for being extremely patient with me. Thank you for your hard work; it was crucial to mine.

And last but not least, I want to thank my families, Ruizpalacios, Remus, and my new family, Cruz-Moya, for always being supportive. You always kept my spirit high.

Thank you,

RODRIGO RUIZPALACIOS

The University of Texas at Austin, Austin Texas

December 2004

Laser Direct-Write of Optical Components Prepared Using the Sol-Gel Process

Publication No._____

Rodrigo Ruizpalacios, Ph.D.

The University of Texas at Austin, 2004

Supervisor: Kristin L. Wood

Co-Supervisor: Joseph J. Beaman

Research in manufacturing techniques for novel and cost effective optical components has focused on versatile new materials and low temperature processing. The laser direct-write of sol-gel optical films has the potential for addressing these two needs for the fabrication of photonic components for rapid prototyping purposes. The combination of Solid Freeform Fabrication (SFF) and Direct-Write (DW) approaches to manufacturing, along with the use of high optical quality materials prepared by the sol-gel process, can result in optical components produced with maskless techniques and with the potential of being used as real products.

The fundamental approach in this research consisted in four steps. Initially the sol was synthesized under controlled atmospheric conditions. This was followed by the deposition of the sol-gel thin films by spin coating. After deposition the film was thermally and in some cases chemically treated. The

final step involved the use of a laser source for photothermal or photochemical processing of the film, translating the sample through an XY stage. This research provides a detailed study of the preparation procedures of various sol-gel materials (inorganic and hybrid organic/inorganic), with the goal of developing a repeatable and reliable process of high optical quality films. The main experimental aspects explored were the synthesis, deposition, thermal and laser processing of the sol-gel materials. It also presents experimental results that demonstrate light propagation through a simple waveguide made by the proposed process.

In addition, this research provides an example of the importance of using design methodology and systems design techniques, as effective strategies for the development of innovative manufacturing processes that involve a great number of parameters. The results of this research set the groundwork for the development of a fully automated direct-write SFF machine that is capable of depositing high optical quality sol-gel films, thermally treating the films, and using a laser to direct-write the structures on inorganic or hybrid organic/inorganic glassy matrices.

Table of Contents

List of Tables

List of Figures

Chapter 1. Introduction

1.1. Direct-Write Technologies

Direct-write technologies are manufacturing processes characterized by the use of computer-generated patterns and shapes for direct fabrication without part-specific tooling. Conflicting definitions can be found in the literature on what constitutes a direct-write technique, and no definitive definition has been established. For example, Pique and Chrisey have defined direct-write as: "…any technique or process capable of depositing, dispensing, or processing different types of materials over various surfaces following a preset pattern or layout" (Piqué and Chrisey, 2002). They view them as a subset of rapid prototyping techniques applied mainly for two-dimensional manufacturing in the micro- and meso-scales. On the other hand, Church *et al.*, though not providing a concrete definition, see direct-write processes as the universe of techniques that emerged from the concept of Rapid Prototyping (RP), in particular Stereolithography (SLA), by uniquely integrating Computer Aided Design and Computer Aided Manufacturing (CAD/CAM), lasers, and materials (Church, Fore *et al.*, 2000). Figure 1.1 illustrates some examples of applications of direct-write processes.

Regardless of the exact meaning of the term, direct-write processes represent a set of emerging technologies that compete with more conventional fabrication techniques and lie at the forefront in research and development in manufacturing (Church, Fore *et al.*, 2000; Piqué and Chrisey, 2002). Direct-write

techniques are aimed at fabricating net-shape two- and three-dimensional structures. The application areas are broad, beginning in the RP industry with techniques such as SLA, Selective Laser Sintering (SLS), Fused Deposition Modeling (FDM), and Laser-Engineered Net Shaping (LENS) for producing net-shape three-dimensional prototypes (Jacobs, 1992; Beaman, Barlow *et al.*, 1997).

A common trend observed in recent years is a push for the miniaturization of these techniques for applications in the meso- and micro-scales in the fields of microelectronics, microelectromechanics (MEMS) and
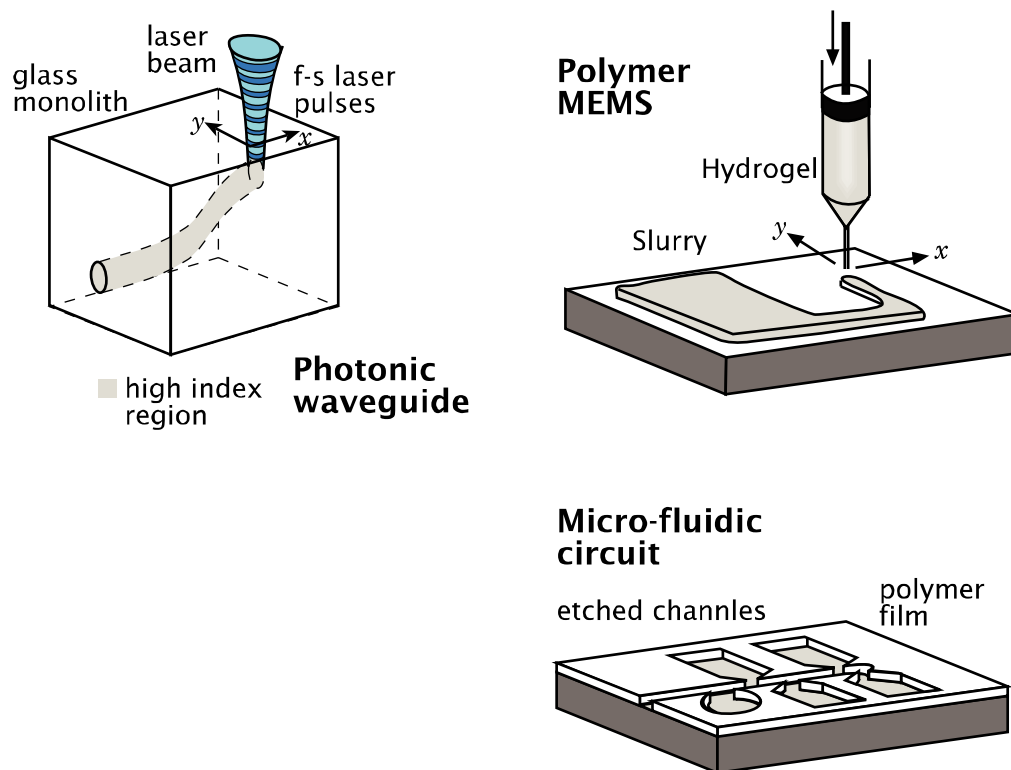
Figure 1.1. Examples of direct-write processes and applications

photonics. Some approaches have focused on diverse material delivery, while others on bringing the advantages of truly three-dimensional manufacturing for meso-, micro-, and nano-scale applications. Examples of some techniques are: matrix assisted pulsed laser evaporation (MAPLE) for electronic components (McGill, Chrisey *et al.*, 1998), micro-stereolithography (μSL) for MEMS devices (Maruo and Ikuta, 1998; Maruo and Ikuta, 1999; Zhang, Jiang *et al.*, 1999), femtosecond laser direct-write for optical waveguides (Miura, Qiu *et al.*, 1997; Zhang, Jiang *et al.*, 1999; Piqué and Chrisey, 2002), and colloidal ink direct-write for photonic band gap structures (Lewis, 2000).

Despite the application, scale of manufacturing, or approach, direct-write methods have three common aspects: (1) use of engineered materials, (2) a delivery process, and (3) a conversion process (Church, Fore *et al.*, 2000). An additional common aspect is the CAD/CAM approach to manufacturing, which represents one of the major strengths of these techniques for a rapid transfer from idea to product while minimizing the total fabrication cost. Direct-write and solid freeform fabrication techniques can be further classified according to three main approaches (Beaman, Barlow et al., 1997): subtractive, net-shape, and additive. For applications in the electronics and photonics industries they could represent a substantial reduction of process steps, with the possibility of eliminating complex masking and etching steps.

A number of key factors have enabled the rapid development and continuous improvement of these technologies. Price, availability, and higher performance (speed and resolution) of computer controlled motion devices (e.g., XYZ stages, galvanometer mirrors, among others) have played an important role in commercialization. Lower cost and enhanced performance of lasers have

contributed to improve the feature resolution, while allowing a broader range of materials to be processed by these techniques. High precision and high speed liquid delivery systems have achieved important results in ink-jet slurry and colloidal suspension systems. There has been a better understanding of the physics of material processing at both the meso- and micro-scales, aided by computational modeling of complex phenomena. The emergence of highly engineered materials (e.g., composites, polymers, hybrid organic/inorganic colloidal materials, self-assembled nano-materials, etc.) has played a fundamental role in the development of new techniques.

Many challenges remain ahead for these technologies to be fully embraced by the industry and not exist as mere research curiosities or prototyping tools, but as actual tools for end-products. These challenges include achieving repeatability at the manufacturing level and a high throughput for mass-production implementation (Church, Fore *et al.*, 2000). In many cases, direct-write technologies can find successful application as an intermediate step of a manufacturing process, where geometrical challenges exist in conventional methods. For example, the use of a directed CO_2 laser beam to enhance the performance of an optical resonator by four orders of magnitude (Armani, Kippenberg *et al.*, 2003).

Direct-write techniques have only been in the market for roughly eighteen years. These emerging set of technologies to date have not reached their full potential and remain a work in progress.

1.2. Optical Networking

The recent increase in demand for information bandwidth has created the need for improving current technologies for data, voice and video transmission. New technologies have emerged addressing different aspects of networking, such as transmission protocols, communication devices, and manufacturing methods of networking devices. Telecommunication networks today expand through optical, electrical and wireless electromagnetic domains for signal transmission, optical being the fastest method. Two main trends can be observed: all-optical networks, and more recently a hybrid electrical-optical-wireless networks. Semi- or all-optical networks find applications in city-to-city or long-haul networks, as well as in intranets within schools or corporations. On the other hand, hybrid and wireless networks can be found in lower speed applications, especially linking the end-user in mobile environments (Hunsperger, 2002). This means that no single technology (optical, electronic, or wireless) can solve these challenges alone.

For optical data transmission, the current bottleneck does not lie in long-haul connections, where the majority of the networks are already fully optical and installed capacity has not been reached to date, but in the last portion of the optical link, where switching of signals between fiberoptic lines is crucial. Larger deployment of these networks requires in part cost-effective products and processes, with the ability of being scalable and reconfigurable. Therefore, the design of such optical components requires both novel fabrication technologies and systematic processes to design them.

Manufacturing processes in the field of photonics maintain a high degree of resemblance with those in microelectronics, for example vapor deposition and lithographic techniques. Semiconductor and dielectric materials are common to both fields, as are the manufacturing tolerances and material purity levels. In fact, the idea of optical fibers was conceived in the late 19th century, but it was not until the 1960's, when chemical vapor deposition was incorporated in the fabrication process, that optical signal transmission became a reality (Agrawal, 1997). The key contribution of these techniques was the ability to produce high-purity materials with ultra-low optical losses, for example attenuation levels below 40 dB/km (Agrawal, 1997; Hecht, 1999).

Since then, the field has witnessed a rapid growth due to key technological advancements. Some of these include wavelength division multiplexing (WDM), which takes advantage of the current installed optical fiber capacity to multiplex signals at different wavelengths and send them through a single fiber, allowing multiple information streams to be transmitted simultaneously at typical rates up to 40 Gb/s or higher (Hecht, 1999). Two additional developments closely related to WDM systems are Erbium-doped amplifiers (EDAs), and Multiplexers/Demultiplexers through fiber gratings, mainly through the Bragg grating effect. Advancements in progress include the realization of Integrated Optics (IO) devices in the short-term, and as future long-term developments the areas of photonic crystals and quantum optics, which have the promise of revolutionizing the field by reducing the device size and conducting computations with light.

Components critical to optical signal processing and transmission can be classified as passive and active. Passive components require no external energy

input and include fibers, connectors, splicers, splitters, couplers, filters, gratings, and attenuators, among others. Alternatively, active components require input power to operate, and are generally associated with switching or modulating operations (Agrawal, 1997). Applications of these two types of components differ for the long-haul, metropolitan, or local area networks. Long-haul connections are mainly concerned with minimizing the number of amplifiers and laid fibers in, for example, city-to-city connections. Solutions to these needs are ultra low loss fibers and WDM systems. On the other hand, metropolitan connections are more concerned with what is known as the *last mile*, in a cost-effective way. Although fully optical switching seems like the solution to this problem, it is still under development, and it will require several years to be a reality. Some of the interests of local area networks include low-cost components, with scalability and reconfigurable capabilities. An important area of opportunity lies in this sector, which leads to the need for developing low cost passive components, and therefore of competitive manufacturing processes. Direct-write technologies have the opportunity to impact this sector, mainly in the manufacture of complex shape and multiple material passive or semi-active components.

1.3. Manufacturing Processes for Optical Components

The fabrication of photonic and microelectronic components involves a complex series of steps, including lithographic masking and chemical etching (see Figure 1.2). One of the trends in production methods for both microelectronics and photonics industries is towards lower processing temperatures, which now range
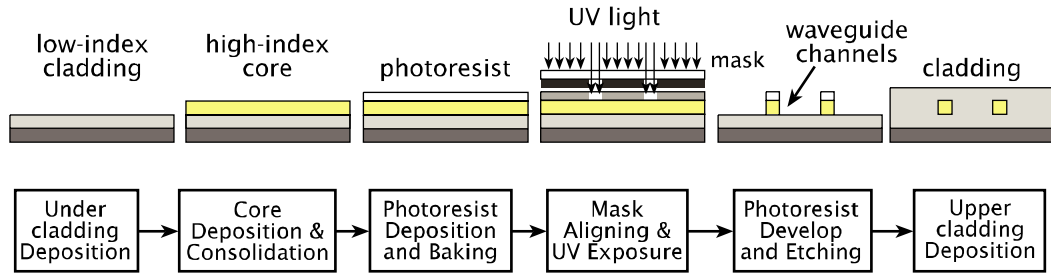
Figure 1.2. Example of a lithographic process

in the order of ~500°C, considering that softening points of common semiconductors are well above this temperature (e.g., for silicon ~1800°C). Developments in the field of chemistry have played a crucial role not only in the production of high-purity grade materials, but also in the processing of these materials.

Typical processes for waveguide manufacturing include thermal oxidation and nitridation, sputtering, chemical vapor deposition, plasma enhanced chemical vapor deposition, molecular beam epitaxy, flame hydrolysis deposition, and sol-gel deposition (Syms, 1994).

These methods successfully produce components with the level of purity and geometrical tolerances demanded by microelectronics and telecommunications applications. Yet their standard processing approach is limited to the creation of 2½-D (planar feature) structures, precluding the production of 3D light pathways for optical applications.

Elements that will play a fundamental role in future optical networks include photonic band-gap structures (Vlasov, Bo *et al.*, 2001). These elements have the potential to reduce the aspect ratios of current waveguide circuits, as well as being applied to systems with computing capabilities by exploiting the

use of the third dimension. The technology to manufacture such devices is still in its infancy, one of the most promising being self-assembly of colloidal particles (Vlasov, Bo *et al.*, 2001). A competing technology for the manufacture of photonic crystals that exploits the flexibility of CAD/CAM systems is two-photon polymerization by ultra-fast pulsed infrared lasers (Miura, Qiu *et al.*, 1997; Cumpston, Ananthavel *et al.*, 1999; Kuebler, Ananthavel *et al.*, 1999). Soft lithography is also an emerging strategy for low-cost micro- and nano-processing by combining stamping and molding techniques with polymeric materials (Xia and Whitesides, 1998). The manufacture of these complex shape devices remains a challenge.

The manufacture of components for future generation networks must address issues of integration of functions such as guiding, filtering, and compensation of environmental effects (e.g., thermal and swelling caused by moisture absorption), including polarization and dispersion compensation. The packaging of such devices for passive alignment in 3D-space remains a challenge. The same applies for connections of fiber-waveguide/device-fiber, in order to compensate for mode mismatch and reduce the overall number of physical connections, which increase losses. Manufacturing of true 3D devices therefore requires a flexible manufacturing process that can manipulate diverse materials.

In general, the key characteristics of emerging manufacturing processes for devices for next generation optical networks are: (1) handling of diverse materials, and (2) processing materials at nano- and micro-scale levels, while maintaining compatibility with transmission windows at high signal-to-noise ratios. These characteristics have to be realized in an economic manner such that it enables proliferation of the technology.

Of the manufacturing and material deposition techniques mentioned above, the sol-gel process holds great promise for being incorporated into a direct-write approach. Sol-gel processing allows the creation of high optical-quality coatings and monoliths through the strict control of processing parameters (pH, temperature, humidity, pressure) in combination with high-purity sol-gel precursors (Brinker and Scherer, 1990). The advantages of sol-gel materials include the ability to synthesize at the molecular level extremely pure materials with unique properties, with the use of low processing temperatures and standard atmospheric conditions, together with the possibility to control the layer thickness through chemistry and processing. The sol-gel process is an economic alternative for processing of highly engineered materials (Gvishi, Narang *et al.*, 1997). High optical-quality materials have been demonstrated with sol-gels, following single or multiple layer deposition approaches (Brinker, Hurd *et al.*, 1990; Syms and Holmes, 1994; Righini and Pelli, 1997). The patterning of sol-gel films has been approached in various ways, for example by standard lithographic techniques with masking and etching, or by direct laser photothermal processing (Taylor, Fabes *et al.*, 1990; Chia, 1992; Taylor and Fabes, 1992; Pelli, Righini *et al.*, 1996), or by ultraviolet light photopolymerization (Najafi, Li *et al.*, 1995; Coudray, Chisham *et al.*, 1997; Fardad, Andrews *et al.*, 1998; Bae and Park, 2001; Park, Jung *et al.*, 2001).

Purely inorganic sol-gel materials have properties similar to those of materials currently used and compatible to the communications windows. They can be synthesized and processed to have low optical losses for these windows, while having low thermal expansion coefficients. On the other hand, an important limitation of these materials is the maximum layer thickness

10

achievable before cracking occurs (Brinker, Hurd *et al.*, 1992). Recently, so-called hybrid sol-gel materials have gained much attention by combining the benefits of inorganic sol-gels covalently bonded to organic materials, which increase the compliance of the network.

Thus, sol-gel materials represent an important technology to be combined with direct-write manufacturing approaches for cost effective and low temperature processing of novel optical components.

1.4. Motivation

The manufacture of optical components is a challenging problem. The same holds true for both standard processing techniques and direct-write processing. From preliminary work, a series of research issues have been identified. These research issues can be approached by the following areas: Materials Science and Chemistry, System Design, and Information Processing. Table 1.1 summarizes the major research issues for the manufacture of optical components and potential solutions. Some of the key initial challenges from Table 1.1 include the synthesis of a high-purity homogeneous material, the manufacturing of devices that are dimensionally compatible with current single- or multi-mode fiber optic products, and the achievement of uniform refractive index.

Table 1.1 Research challenges and strategies

Research Issue	Strategies for Solution		
	Materials Science: Chemistry & Processing	Laser Processing	Information Processing: Modeling & Computer Eng.
Residual stress minimization	Addition of surfactants Rapid thermal processing	Photophysical processing of sol-gel; photopolymerization of high index area	Characterization of time constants for photochemical and photothermal processes
Control and location of laser effects	Photo-initiating agents Organically modified sol-gels	Photopolymerization processing; two-photon polymerization	Numerical laser-matter interaction model
Compatible with component dimensions	Control of layer thickness Use of organically modified sol-gels	Optimization of heat effected zone	
Compatible materials with optical comm. transmission windows	Inorganic backbone (low loss), same refractive index. Index control by dopants (Ge, Ti, Al, Zr)		
Feature size and resolution	Concentration of photoinitiator Layer thickness	Laser parameters (fluence, wavelength, CW or pulsed). Multi-photon polymerization	Modeling of thermal diffusion
Device integration	Selective deposition of sol-gel material	Laser control to minimize disruption of other features within the substrate	Predict from modeling allowable index diff. Design and model integral sol-gel devices
Novel components	Synthesis of high-index materials by control of dopant concentration	Induce localized high-index contrast by control of laser parameters (power and pulse rate)	Design high-index devices: junctions
Economic process	Minimizing process temperature Using low-cost sol-gels Batch processing		
Function integration	Control of rheology for selective deposition	Selective laser processing Minimize disruption with other features within the substrate	Accurately model heat diffusion effects into material Predict absorption length

Many of the research issues depend on multiple aspects of the manufacturing process. The machine and process design are crucial for the production and marketing of novel optical waveguides. Materials must be found that operate efficiently in the wavelengths used by the optical networking

industry. Modeling and control of the laser-matter interaction are recommended in order to achieve continuous properties in the x, y, and z directions. Repeatable results can be obtained by modeling of the energy interactions during the process, and by using feedback control and system monitoring to maintain constant environmental parameters. Note that the materials used and the chemistry required to prepare them must not be limited by the final machine design so that flexibility remains in both manufacturing and product function. The desire to create multiple functions in a single package, such as filtering with Bragg gratings, optical coupling, and multiplexing WDM signals, puts demands on control and laser parameters that must be compatible with the tolerances allowed by the machine and the tolerances desired in the final product.

1.5. Problem Definition

The current research considers advancing the field of optical component manufacturing with innovative direct-write capabilities by evolving the basic premise of solid freeform fabrication (SFF) processing. Based on preliminary research (Ruizpalacios, Beaman *et al.*, 2001), it was determined that the sol-gel process holds much promise for the creation of novel products in the optical networking field. Sol-gels are organometallic molecules that are polymerized in an alcohol/water solution with acids to form a ceramic or glass material with unique chemical and microstructural features (McCormick, 1994).

The main research goal entails the development of a novel manufacturing process for the direct-write of optical components, combining the advantages of

controlled laser photophysical processing with sol-gel thin film deposition to potentially create novel optical components.

One of the premises of this work lies in the combination of direct-write and freeform fabrication techniques, aimed at producing complex shapes and reducing the number of steps required for manufacturing. This involves adopting a fundamentally different approach, departing from traditional vapor deposition and lithographic techniques (deposition–masking–etching).

The fundamental requirements of any component in a communication link are to maximize transmission rates and minimize losses and signal distortion, or in communications jargon, maximize bandwidth and channel capacity. These 'high-level' requirements can be restated as achieving high optical quality, low attenuation loss, uniform properties, and high geometrical resolution. For optical communications, high optical quality is defined as transition metals not to be present at levels exceeding 1ppb. Low attenuation loss in optical waveguides refers to achieving attenuation losses <1 dB/cm (Righini and Pelli, 1997; Hibino, 2003). This initial effort will focus on the first two, optical quality and property uniformity.

SFF and direct-write techniques have been successfully applied in diverse fields, such as product development (near net shape prototypes), biomedical sciences (prosthetics and biotechnology), manufacturing (batch production molds), and aerospace engineering (turbine blade tips and missile heads) (Beaman, Barlow et al., 1997). Because of its history of success, Selective Laser Sintering will constitute the foundation of the laser-processing component of this research.

The two fundamental areas of research that constitute the proposed evolution of SLS for the direct-write of optical components include: (1) the unique processing of commercially available sol-gel materials, and (2) laser technology for layer-based fabrication of components. Figure 1.3 illustrates the proposed direct-write manufacturing process with sol-gels and laser processing. The process can be summarized in a series of six basic steps, beginning with the deposition of the sol-gel thin film, followed by thermal treatment, then continuing with the laser direct-write of the feature, and finishing with post-processing operations. A detailed description of the process is provided in Chapter 2.
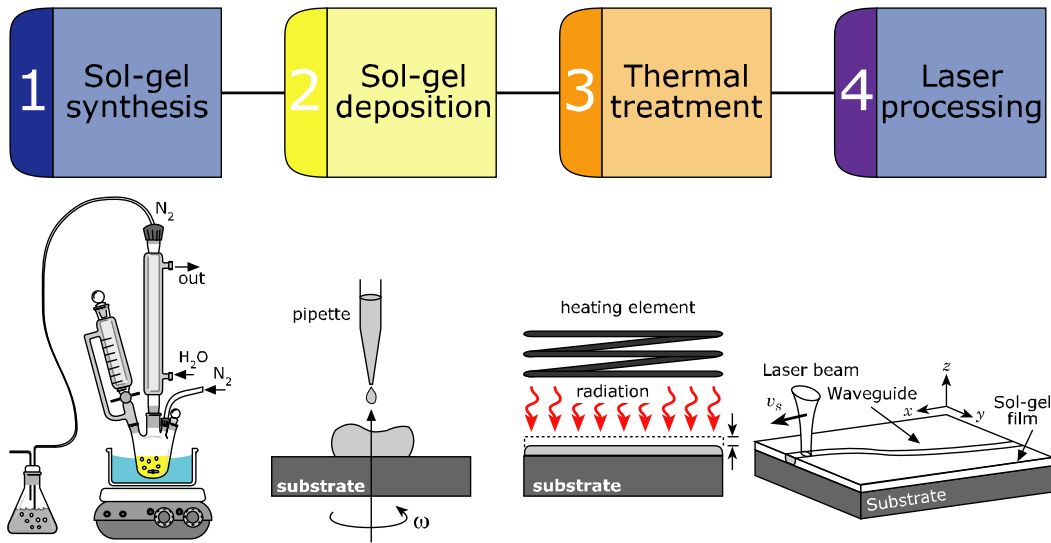
Figure 1.3. Proposed manufacturing process

1.5.1. Hypothesis

The combination of multi-layer deposition of nano-porous thin films obtained through the sol-gel process together with selective laser densification using CAD based models, and multi-step heat treatment with atmospheric control, can produce three dimensional optical networking components with optical-grade quality.

1.5.2. Objectives

The main objective of this research is to develop a novel manufacturing process for optical networking components. Additional specific objectives of this research are stated as follows:

- Expand the knowledge base and technology of freeform fabrication techniques with the incursion into the meso- and micro-scales.

- Provide a cost-effective novel process to manufacture optical components in less time than traditional vapor deposition and lithographic techniques.

- Broaden the knowledge in laser-matter interaction, in particular with nano-porous silica based materials.

- Provide the groundwork through the proposed direct-write process, for the potential achievement of fully three-dimensional optical components.

- Incorporate product development methodologies for the design of complex processes, and demonstrate the importance of a systematical approach to design and how it leads to innovation.

Besides these specific objectives, the proposed work is expected to contribute with basic knowledge for the repeatable synthesis and processing of sol-gel materials, and provide a set of design parameters that can be directly employed for statistical optimization, which is a crucial step to transfer this type of technology from the research laboratory to the industry. Additionally, the research approach followed during this work will attempt to exemplify the importance of a systems design approach by following well established product development methodologies and adapting them to the design of a process.

1.6. Dissertation Outline

This dissertation is divided in seven chapters. This first chapter has introduced the fields of optical communications and direct-write technologies, identifying the area of opportunity for the development of a novel process. Chapter 2 presents the procedure that was pursued for the design of a new process, following a product design methodology approach. This chapter begins with an introduction to product design methodology, illustrating how it can be applied for the design of a process. Also, an introduction to optical communications is provided, followed by a description of some of the most popular manufacturing processes in this field, in order to identify areas for innovation. This chapter ends with a detailed description of the proposed manufacturing process. Chapter 3 describes in detail, the procedures for synthesis of the different sol-gel systems that were used throughout this research. It intends to highlight some of the details of the

synthesis of sol-gels so a repeatable process can be achieved, which is critical for these technologies to be useful in industrial applications. Following the description of the synthesis of the sol mixture, Chapter 4 presents the steps for deposition and post processing of the sol-gel thin film. Detailed experimentation results are provided in this chapter, as well as design solutions implemented to achieve high quality films. The following step in the process is the laser direct-write of the optical path, which is presented in Chapter 5. This chapter discusses the design and evolution of the testbed for laser processing, followed by experimental results and mathematical modeling results of the laser-matter interaction. The design of the optical characterization testbed and experimental results are presented in Chapter 6, which intends to demonstrate the feasibility of the waveguides produced by the proposed process. Chapter 7 discusses the final conclusions of this research.

Chapter 2. Process Design

2.1. Introduction

Innovative product and process development in highly competitive and rapid changing markets requires the aid of systematic approaches (Clark and Wheelright, 1994; Christensen, 1997; Ulrich and Eppinger, 2000; Otto and Wood, 2001). This is the case for optical communications products, and their manufacturing processes. This chapter presents the design of a direct-write manufacturing process, as the result of applying a reverse engineering and redesign methodology based on the selective laser sintering (SLS) technique and the analysis of current optical networking components and their manufacturing methods.

The chapter is organized as follows. The first section establishes the design and research methodology by providing a general description of the design process, which includes the identification of the end product, and the outline of some of the main differences between product and process design. Next, the reverse engineering and redesign methodology is applied to the SLS process, as a learning ground for the development of a novel process. This is followed by an analysis of the field of optical networks, including optical components and the different manufacturing processes involved. The analysis results in the identification of key characteristics and a set of design criteria. Finally, a description of the novel direct-write process is presented.

2.2. Design Methodology for a New Process

A product development process, regardless of the application area, consists of a series of steps to identify an idea and transform it into a commercial product (Pugh, 1991; Ulrich and Eppinger, 2000; Otto and Wood, 2001). A research process may also be conceptualized as a series of sequential steps, and begins with a well-defined objective. For this research, the clarification of the research task was based on a technical questionnaire and the Harvard Business Method (Otto and Wood, 2001).

As a result of the questionnaires and this systematic approach to process design and development, a set of initial questions was proposed to clarify the research and design task. The set of questions, besides addressing the problem in a systematical way is meant to limit the project within a realizable frame or scope. The following research questions for the design process were established:

1. Can a process similar to SLS be implemented to produce structures with optical quality and low losses?

2. Can this process achieve features with micron (μm) or submicron (nm) size?

3. Can the process produce precise structures with sub-micron tolerances?

These questions help establish a connection between high- and low-level research objectives and design requirements.

The following sections present a review of the product design and development methodology, and the selection of a strategy suitable for the current process design.

2.2.1. Process for Product Design and Development

The product design process has been intensively studied over the past two decades, with objectives such as reduction of time-to-market of products, or the demystification of the design process from one purely artistic to an accurate, repeatable, and teachable scientific process. One only needs to turn to the works of Pahl and Beitz, Pugh, Ullman, Suh, Otto and Wood, to mention a few, to appreciate the developments towards the dissection and accurate representation of product design processes, which are general enough to be applied to a broad range of products (Pugh, 1991; Pahl and Beitz, 1996; Otto and Wood, 2001; Ullman, 2002). A typical product design process is illustrated in Figure 2.1a.

The evolution of most products, and even the introduction of many new ones, involves small changes to the architecture or subsystems of the product. Addressing this issue, and exploiting the ability to teach and learn from past designs, Otto and Wood developed a methodology based on the *reverse engineering* and *redesign* of products (Otto and Wood, 1998). This methodology begins with an existing product, which is studied through a series of systematic steps and techniques. The final implementation can be identified with any of the three redesign categories: parametric, adaptive, or original, as shown in Figure 2.1b.

(a) Product design process (Ulrich and Eppinger, 2000)

(b) Reverse engineering and redesign process (Otto and Wood, 1998)
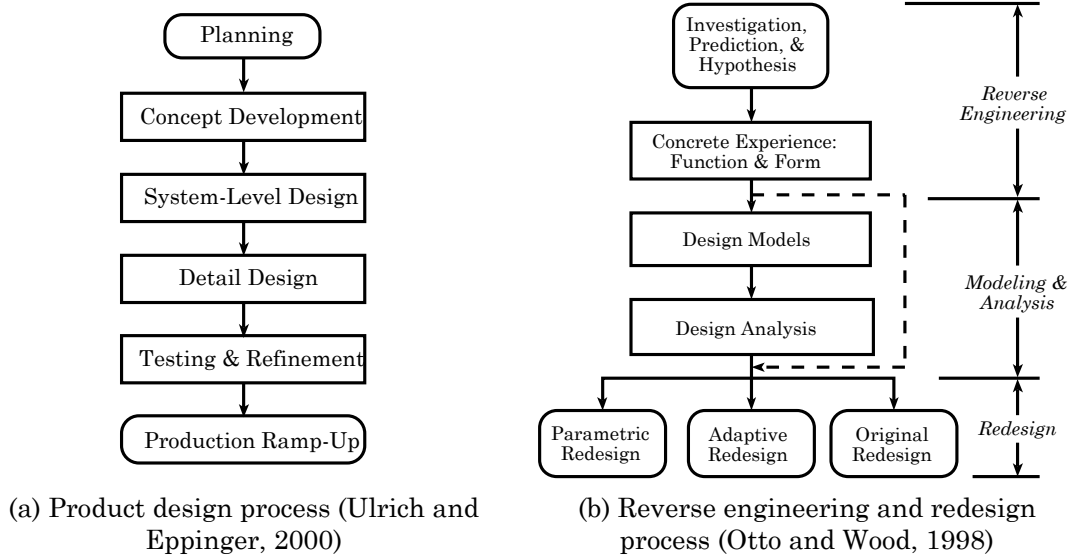
Figure 2.1. Examples of product design processes

These design methodologies have been widely studied and successfully applied to product development of consumer products; yet there has been little or no discussion on their applications such as in process design. It is proposed that the design of research-intensive processes and products can greatly benefit from the adoption of systematic methodologies, reducing the time-to-market and identifying alternate avenues for innovation.

2.2.2. Proposed Process Design Methodology

The current project is immersed in highly competitive and rapidly changing markets, such as telecommunications and networking. This requires the research team to respond in an equally rapid manner, so a suitable strategy is to adopt what is known as a *Spiral and Stage-Gate Model*. This is particularly helpful for projects with high-risk characteristics, and large number of

parameters involved, such as in military or commercial aircraft design where thousands of parts are involved (Fielding, 1999). The *Spiral and Stage-Gate Model* implies the delivery and analysis of progressive results. This approach allows avoiding major pitfalls, by providing the required flexibility to both refine and redefine the research tasks and execution of these tasks as the project progresses in time. Figure 2.2 presents a schematic representation of the spiral research model, where each loop corresponds to a more refined version of the project converging progressively to a solution.

As a starting point to this research, and in addition to the Spiral and Stage-Gate design model, the *Reverse Engineering and Redesign* methodology proposed by (Otto and Wood, 1998) was employed. This design methodology provided one of the building blocks for this research based on the analysis of the Selective Laser Sintering process, which was developed in the Laboratory of Freeform Fabrication from the University of Texas at Austin (Deckard, 1988).
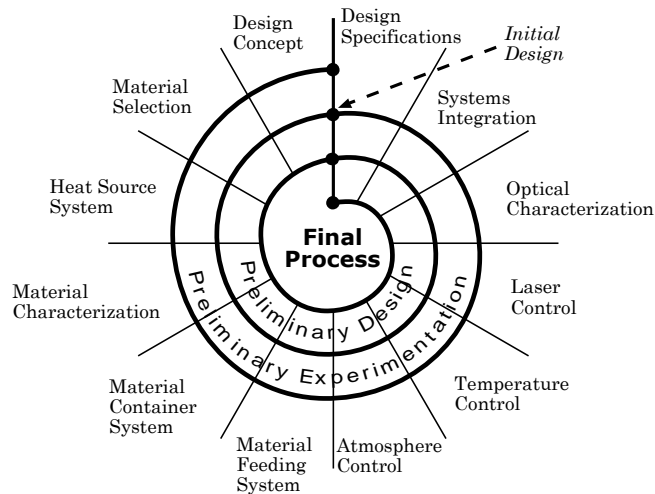
Figure 2.2. Spiral and Stage-Gate Design process

2.3. Reverse Engineering of SLS Process

Selective Laser Sintering (SLS) is a freeform fabrication and direct-write technique developed at the University of Texas at Austin (Deckard, 1988). In this technique, a three dimensional computer model of the part to be manufactured is "sliced" in layers, which are then raster or contour scanned one at a time on a powder bed by a laser source. The laser fuses the pre-heated powder, providing just enough energy to go above a threshold limit. Next, the part cylinder is lowered by one layer, and a counter-rotating roller dispenses a fresh layer of powder from a contiguous dispensing powder bed. The process is repeated layer after layer, until the three-dimensional object is formed. Figure 2.3 illustrates the SLS process.

SLS has been successfully applied to the manufacture of polymer (Deckard, 1988; Beaman, Barlow et al., 1997), metal (Das, 1998), and dielectric (Wang, 1999) three-dimensional parts. Because of this diverse range of
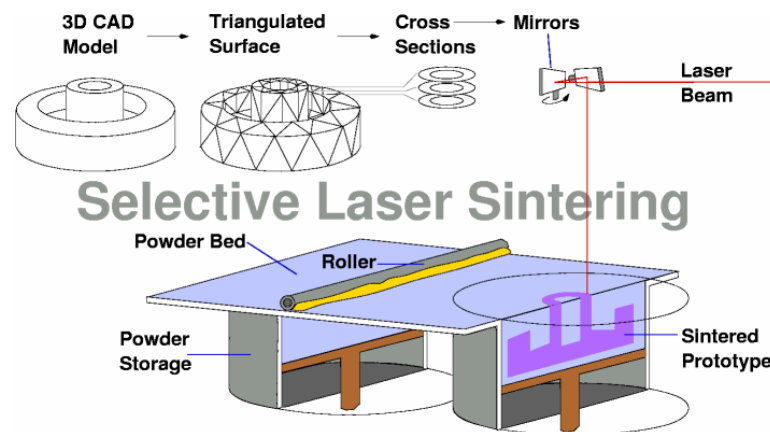
Figure 2.3. Selective Laser Sintering process (Nelson, 1993)

24

applications, SLS will constitute the groundwork of this research.

The first task of the reverse engineering and redesign process is to develop a "black box" model of the system, identifying the inputs and outputs according to *material*, *energy*, and *information* flows through the system. Figure 2.4 shows the black box models for the current SLS process. Following the material, energy and information flows identified in the black box model, a function structure is developed (Figure 2.5). This diagram shows a more complex and detailed interaction of the flows as they occur during the machine's operation. This representation allows us to perform a form-independent analysis of the system's operation, from which we can propose alternative embodiment solutions of the various functions or redesign the architecture of the process.

Powder (solid), Air, Humidity
Gas (for atmospheric ctl)

EE, Gravity, TE (IC's)

Pneumatic (pressure), EM (laser)

Start, IC's (temp, humidity)

STL file, Process Settings

Laser Fabrication of CAD part (from powder)

Sintered solid part, Gas (atm ctl)
Unsintered powder, Gas (reactive)

Debris,

TE (heat waist), Weight

EM (optical losses), Reaction Forces

Part ready!, Process History

Processing conditions

Figure 2.4. Black box model of SLS process
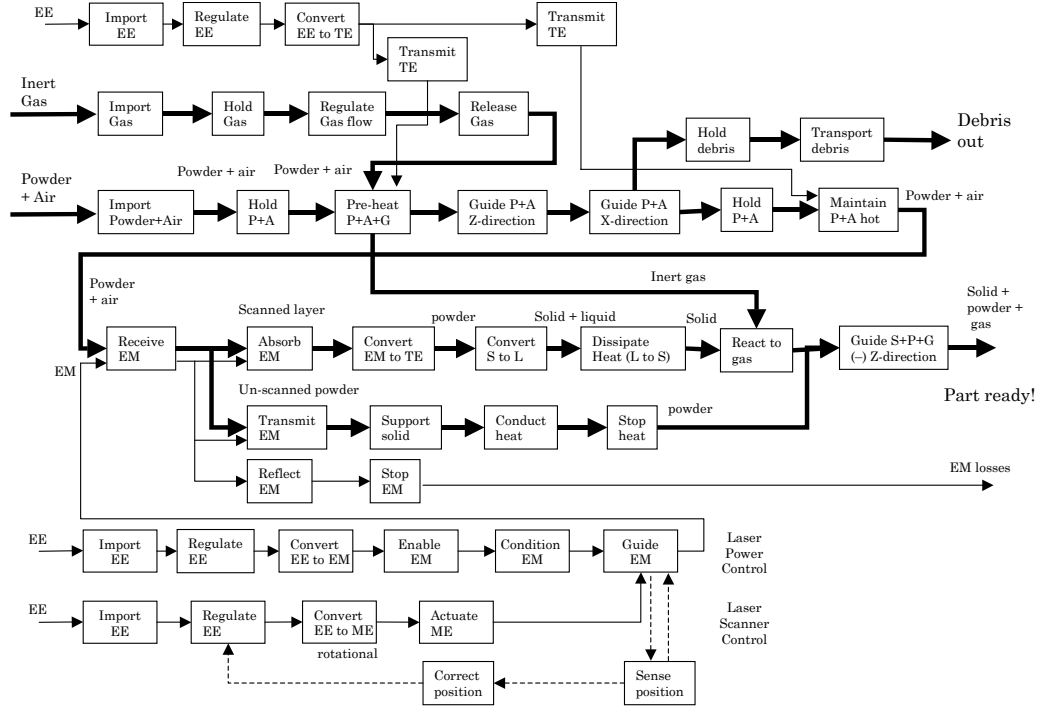
Figure 2.5. Function structure of the SLS process

As a result of applying the reverse engineering and redesign methodology to the SLS process, one can identify the main systems and subsystems of a more general direct-write process. These general systems of the current SLS are shown in Table 2.1. Five main systems can be identified, plus the material to be processed. The systems that form the foundation of the SLS technology are the laser heating source, plus the synchronized way of dispensing a layer of material (powder) and lowering the part bed, all of these controlled by a computer.

We have identified the general architecture and subsystems to begin the design of a novel direct-write process. The next section provides an analysis of the field of optical networks and describes the various potential products or devices that could be manufactured by this technique.

26

Table 2.1. Systems and subsystems of an SLS machine

No	System	Subsystem
1	**Heat source**	Laser cavity Power source and shutter Scanning mirrors Computer controller Temperature sensors
2	**Material containers**	Part cylinder Material containers Heating elements
3	**Material feeder**	Feeder sensors Feeder mechanism and controller
4	**Main computer and controller**	Slicing Vector or contour scanning Scanning velocity
5	**Main structure**	Atmosphere control: - Temperature - Pressure - Concentration of gas
6	**Material**	

2.4. Optical Networks and Components

Continuing with the first phase of the reverse engineering and redesign methodology, this section presents an analysis of the state-of-the-art in optical networks and their components. This analysis is intended to identify specific areas of opportunity for direct-write processes.

2.4.1. Optical Networks: principles and current trends

The elements of a basic optical transmission system are depicted in Figure 2.6, and consist of an emitting module, a transmission medium, and a receiving module (Agrawal, 1997; Hecht, 1999). The emitting module converts an electrical signal into an optical signal, which for digital networks is constituted
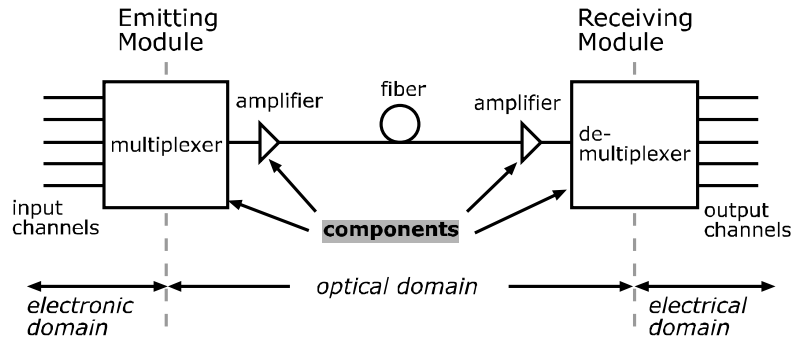
Figure 2.6. Basic optical transmission system

by streams of pulses representing bits, and is typically done with a laser or photodiode. The transmission medium is an optical waveguide, which in a general sense is any structure that directs the propagation of energy in the form of an electromagnetic wave along a predetermined path. This optical waveguide could be an optical fiber, a planar waveguide, or the more recently developed photonic band gap structures (Figure 2.7). The receiving module converts the optical signal back into an electric one, by means of a photosensor.

In some cases, the boundary of the optical domain is extended past the multiplexing modules, where these functions are entirely performed with optical signals. This is typically done by planar lightwave circuits (PLCs) (Hibino, 2003).

Optical waveguides are made from dielectric materials, such as silica-based glasses (SiO_2), III-V type semiconductors (GaAs, InP, etc.), or polymers, with the addition of dopants which alter some of their physical properties. In a general sense, the optical waveguides consist of three distinct regions: a core, the cladding, and the sheath for fibers or substrate for planar devices (see Figure 2.7). The size of a waveguide is related to the wavelength of radiation it guides,

28

Embedded wavegiude   Dielectric strip wavegiude

Rib wavegiude   Trapezoidal Rib wavegiude

Core

Cladding

Sheath

(a) Optical fiber   (b) Planar optical waveguides

EM wave

substrate

(c) Photonic band gap waveguide
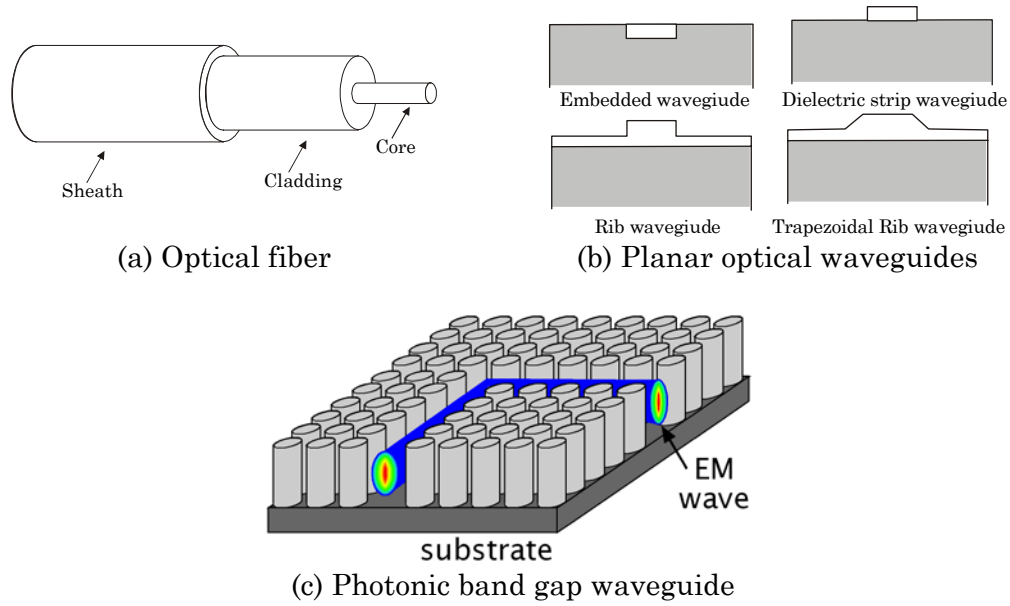
Figure 2.7. Examples of optical waveguides

and thus, the shorter the wavelength, the smaller the guiding structures. As these sizes change, different manufacturing processes and materials are needed.

The most commonly used material for optical waveguides (fibers) is silica (SiO_2) due to its excellent optical, mechanical and thermal characteristics, in particular its low absorption at various wavelength ranges, which in turn have been standardized as the communications wavelengths: 850, 1310, and 1550 nm. Glass can be doped with various materials (Ge, Ti, Zr, Te, P, etc.) to modify the index of refraction, by increasing or decreasing it, while improving other characteristics such as polarization or dispersion.

The basic principle behind transmission of optical signals through optical fibers is based on the phenomenon of *total internal reflection*. The principle of this phenomenon is described by Snell's Law (Figure 2.8a), which relates the ratio between the angle of incidence to angle of transmission (or refraction), to

the ratio of the propagation velocities of the wave in two respective media. This is equivalent to the following expression (Born and Wolf, 1999):

$$\frac{\sin\theta_i}{\sin\theta_t} = \frac{v_1}{v_2} = \frac{n_2}{n_1} \qquad (2.1)$$

For this equation, θ_i and θ_t are the angles of incidence and transmission or refraction, respectively, while v_1 and v_2 are the velocities of propagation of the wave in the two media, and n_1 and n_2 are the indices of refraction of the two media. The propagation of single-mode or multi-mode signals through optical waveguides is based on the same principle of total internal reflection. This is the same case for multiplexed or compound signals that are formed by aggregation of multiple frequency signals. Figure 2.8b illustrates the propagation of an electromagnetic wave, represented as a ray, observing total internal reflection in the guiding media (Kogelnik, 1975).

Typical refractive index distributions on waveguides: optical fiber and planar silica-based waveguide are shown in Figure 2.9. The index difference

(a) Snell's law   (b) Mode propagation
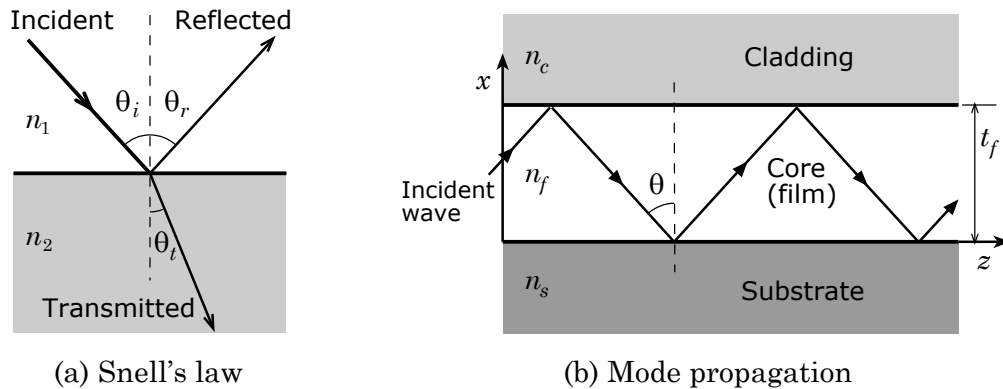
Figure 2.8. Propagation principles of waveguides

(a) Step index optical fiber   (b) Planar optical waveguides
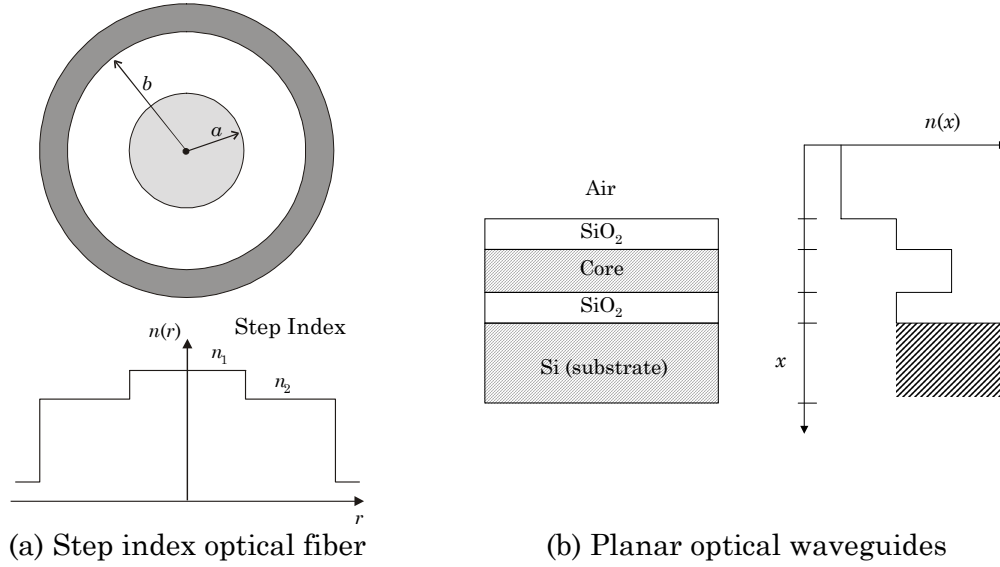
Figure 2.9. Refractive index distribution in waveguides

between core and cladding is generally small ($\Delta n \approx 0.01$-0.05), and it depends directly on the modal nature of the waveguide, the core's characteristic length and refractive index.

Recent technological developments have been to improve and increase the bandwidth for signal transmission. Wavelength Division Multiplexing (WDM), also known as dense wavelength division multiplexing (DWDM), is a solution that has allowed sustained growth of bandwidth (Agrawal, 1997; Hecht, 1999; Hibino, 2003). WDM takes advantage of the current installed optical fiber capacity to multiplex signals at different wavelengths and send them through single fibers (Figure 2.6); this allows multiple information streams to be transmitted simultaneously at typical rates of up to 40 Gb/s or higher (Hecht, 1999).

Two key developments that have permitted the rapid evolution of WDM systems are Erbium-doped amplifiers, and multiplexers and demultiplexers through fiber gratings, mainly through the Bragg grating effect. On the other hand, some deficiencies inherent to WDM include effects such as amplified spontaneous emission and dispersion.

As mentioned earlier, the optical telecommunications and microelectronics fields are strongly related. Most of the operations that require a decision process are still performed in an electric/electronic fashion. However, the two most important trends point towards fully optical networks with switching, routing, and computing capabilities, or a hybrid mixture of optical and wireless networks (Jain, Franz *et al.*, 2001).

In a general sense, large optical networks can be divided in two main categories according to the transmission length: *Long Haul* and *Metropolitan* (or *Metro*). The requirements for each category differ. For *Long Haul* connections the major concern is to minimize the number of amplifiers (originally electronically operated) and laid fibers in, for example, city-to-city connections. Solutions to these needs are ultra low loss fibers, WDM systems, and integrated fiber components.

On the other hand, *Metro* connections require getting past the current bottleneck of what is known as the *last mile* in a cost-effective way (Hecht, 1999). Although fully optical switching seems like the solution to this problem, it is still under development, and it will require several years to become a reality. More recently, a combination of optical and wireless connections have emerged as strong contenders to solve the connectivity and bandwidth problems of this last portion of the link. An important area of opportunity lies in this sector, which

leads to the need for developing low-cost passive components, and therefore of competitive manufacturing processes.

WDM has become an increasingly popular way to pass more information through existing optical fibers. As opposed to long haul networks in which very few components are required, low cost is the key for WDM to be used in metropolitan and access networks, and three-dimensional integrated optical devices have the potential to realize this low cost (Tervonen, 1999). The key for low cost is function integration in both the device and manufacturing process. The result will be an integration of WDM technology (filtering with Bragg gratings, multiplexing, de-multiplexing, and optical coupling) into single packages.

Some of the constraints dictated by the current state-of-the-art are the compatibility with standard transmission wavelengths and protocols and the achievement of low insertion losses in the connections between components. These restrictions are mainly associated with material properties, such as dispersion (which is wavelength dependent), and degradation and shape distortion with time. This implies the use of semiconductor dielectric materials, primarily silicon based glasses. The successful development of these components must consider such factors.

Photonic crystals or photonic band gap structures are at the forefront of technological research, and promise to revolutionize the field by offering unique transmission properties by exploiting the band-gap effect of patterned structures. The applications of photonic crystals range from optical computing circuits to fiber transmission systems at higher speeds through gaseous media. One of the main challenges in this field lies in the manufacturing of these rather complex

geometrical structures in a cost-effective manner. Direct-write and freeform fabrication processes can potentially produce these intricate shapes.

2.4.2. Optical networking components

Of the multiple optical components that comprise photonic circuits today, only a small portion can feasibly be manufactured by means of direct-write processing. This is what our research group concluded in a study of the optical communications field (Beaman, Wood *et al.*, 2001). Therefore only the components that are feasible are discussed in this manuscript.

Table 2.2 shows the various types of components critical to optical signal processing and transmission. These components are classified as passive and active, as described in Section 1.4. Most of these types of components are part of WDM systems, and involve simple forms of manipulation of the optical signal. For instance, a signal power splitter, as the name implies, divides the signal equally in the number of output channels. On the other hand, filters or add/drop connectors separate a specific wavelength while allowing the remaining wavelengths to go through, which is one of the strengths of WDM systems. Signal amplifiers require external power to operate. Erbium-doped optical amplifiers are today some of the most popular and successful in fiber optic communications (Hecht, 1999).

Table 2.2. Types of optical components by general use

Component	General use	Classification
Splitter/combiner	Signal division	Passive
Amplifier	Signal strengthening	Active
Attenuator	Signal reduction	Semi-active
Coupler	Wavelength separation	Passive, semi-active
Filter	Wavelength separation	Passive
Grating	Filter, splitter, DFB laser	Passive
Add/Drop connector	Signal separation	Passive, semi-active
MUX/DEMUX	Wavelength control	Passive, semi-active
Fabry-Perot filter	Wavelength separation	Passive
Lenses	Signal control	Passive
Add Drop Amplifier	Wavelength control	Active, semi-active
Ring resonator	Compensate phase shift	Passive, semi-active

For a mask-less laser direct-write process, components based on localized change of refractive index are a good starting point. Simple straight line waveguides produced by laser processing have been reported in the literature (Fabes, Taylor *et al.*, 1990; Fabes, 1992; Atkins, Charters *et al.*, 2001; Bae and Park, 2001). On the other hand, fiber Bragg gratings are successfully manufactured by means of a laser, with a mask or by interferometry means (Othonos, 1999). Yet, more complex devices, as the ones presented in Table 2.2, remain to be demonstrated. Figure 2.10 shows a few examples of 2D components that can be manufactured by laser direct-write techniques.

The following section presents an overview of various manufacturing techniques for optical waveguides, emphasizing on the sol-gel process.
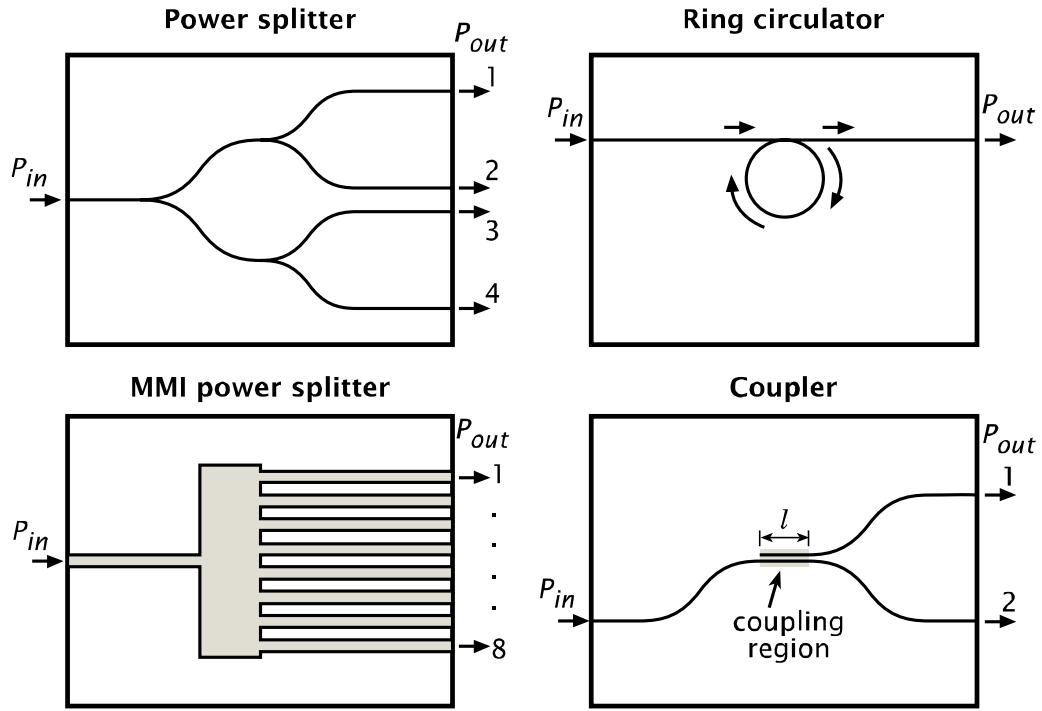
Figure 2.10. Examples of optical components

2.5. Manufacturing Processes

The previous section presented a general overview of the fundamentals behind optical communications and some examples of components. Following the review and analysis of current technologies as part of the design methodology, this section describes some of the most common manufacturing processes for optical waveguides.

2.5.1. Manufacturing Methods for Optical Components

The fields of photonics, optoelectronics, and microelectronics share common production methods. Semiconductor (e.g. Si, Ge, InP) and dielectric materials (metal oxides: SiO_2, GeO_2, $LiNbO_3$, etc.) are common to both fields, as are the manufacturing tolerances. As mentioned in Section 1.3, the most common processes are based on vapor deposition techniques (Hall, 1993). Table 2.3 shows a classification of manufacturing processes for planar waveguides (Patela, 2002).

In Chapter 1 it was mentioned of the emergence of novel techniques that challenge the more traditional CVD processing. Some of the objectives of these techniques are to reduce manufacturing costs, increase the functionality of the devices, and develop true 3D components to address these challenges. Self-assembly of colloidal particles, soft-lithography, and multi-photon polymerization are some of the most promising techniques for the fabrication of complex 3D structures, such as photonic crystals (Figure 2.7c).

Table 2.3. Manufacturing processes for planar waveguides

Type	Fabrication Method
Homogeneous	Vacuum evaporation (resistive or by electron gun)
	Ion sputtering
	Deposition from liquid solutions
	Polymerization in ionic discharge
	Chemical vapor deposition (CVD)
Heterogeneous	Dopant diffusion
	Ion exchange
	Ion implantation
Semiconductor	Waveguiding by lowering concentration of free carriers
	Electro-optical waveguides
	Epitaxial layers

The manufacture of components for future generation networks must address issues of achieving integration of functions such as guiding, filtering, compensation due to environmental effects (e.g., thermal and swelling caused by moisture absorption), polarization, and dispersion compensation. The packaging of such devices for passive alignment in 3D-space remains a challenge. The same applies for connections between fibers and waveguides that compensate for mode mismatch and reduce the overall number of physical connections thereby reducing losses.

In general, the key characteristics of emerging manufacturing techniques for devices used in next generation optical networks are:

1. Processing of diverse materials, and

2. Processing materials at the nano- and micro-scale levels.

These characteristics have to be realized in an economic manner such that it enables proliferation of the technology, while maintaining compatibility with the current transmission wavelengths at high signal-to-noise ratios. In summary, the manufacture of true novel devices (e.g., 3D components) requires a flexible manufacturing process that can manipulate diverse materials.

In order to identify and highlight some of the main manufacturing requirements for optical communications components, the following sections provide a brief review of the most common techniques that are applied today.

Chemical Vapor Deposition

One of the main techniques used in the fabrication of silica-on-silicon waveguides has been chemical vapor deposition (CVD). Fabrication involves

deposition of multiple layers of thin films with different compositions from hot flowing gases through horizontal or vertical furnaces, followed by plasma etching (Syms, 1994). In CVD the temperature and pressure vary according to the material to be deposited and the desired growth rates. It generally employs high temperatures (starting at ~450°C) and the growth rates are rather low. The deposition of thick SiO_2 buffer layers (typically 20 μm) and the plasma etching of thick silica waveguide layers (typically 6 μm) required for low loss, low numerical aperture waveguides with low sidewall roughness, are currently time consuming and cost intensive processes. Plasma modified CVD (PMCVD) has been found to reduce the deposition temperatures, although side walls roughness is compromised, which is not acceptable for low loss waveguides (Hunsperger, 2002). Low losses are only obtained after thermal annealing at high temperatures (above 500°C, and closer to 1000°C).

So called multi-layered 3D vertical couplers have been demonstrated based on metal-organic CVD deposition of InP and InGaAs (Liu, Shakouri *et al.*, 2000). Yet this can still be considered a 2½-D structure.

Flame Hydrolysis Deposition

In flame hydrolysis deposition (FHD) the films are formed from an oxy-hydrogen flame, where the reactants (e.g., $SiCl_4$) are hydrolyzed to form a 'soot' of small particles, which is deposited onto the substrate material (Syms, 1994; Hibino, 2003). This technique is capable of coating large areas in a short time, as well as having the possibility to produce graded refractive index films. Dopants may also be incorporated into the hydrolyzing gas mixture, for example as $TiCl_4$

or GeCl$_4$. However, one of the drawbacks of this technique is that it requires a post-sintering step at elevated temperatures (~1300°C) in order to achieve the desired optical quality, experiencing in the process large shrinkages. Therefore predicting and controlling the final thickness becomes a difficult task (Syms, 1994).

Ion Exchange

Ion exchange is another popular manufacturing process. In this technique, a doped substrate (e.g., with Na) is preheated and exposed to an electric field. The doping ions tend to migrate towards the cathode, where the surface is immersed in a molten salt solution (e.g., thallium nitrate), and the ions from the solution are exchanged with the doping ions from the substrate (Hunsperger, 2002). This process results in an increase of the refractive index. The combination of various types of salts with the appropriate substrate, is able to yield high index contrast waveguides (Δn~0.12). A disadvantage of this process is the low spatial resolution, and concentration gradients may result in variable index profiles.

Molecular Beam Epitaxy

Molecular beam epitaxy (MBE) was developed in the early 1970s as a means of growing high-purity epitaxial layers of compound semiconductors (Hall, 1993). Since then it has evolved into a popular technique for growing III-V compound semiconductors as well as several other materials. MBE can produce high-quality layers with very abrupt interfaces and good control of thickness,

doping, and composition. This high degree of control makes it a valuable tool in the development of sophisticated electronic and optoelectronic devices.

In MBE, the constituent elements of a semiconductor are deposited onto a heated crystalline substrate in the form of 'molecular beams' to form thin epitaxial layers. The 'molecular beams' are typically from thermally evaporated elemental sources, but can include metal-organic, gaseous hydrides or organic precursors, or some combination. The process requires high-purity material sources and it occurs in an ultra-high vacuum environment. In general, the growth rates are on the order of a few Å/s and the beams can be shuttered in a fraction of a second, allowing for nearly atomical abrupt transitions from one material to another.

Pulsed Laser Deposition

Pulsed laser deposition (PLD) is another mature manufacturing method that is largely robust in terms of materials that can be fabricated. This method can make SiO_2, III-V semiconductors, metals and many more materials. In PLD a laser is focused and guided onto a material target (gas, liquid, or solid), causing ablation from the target. The resulting plume hits and deposits onto the substrate. Good tolerances can be achieved making features with 100 nm accuracy possible. The process is rather slow (similar to many SFF processes), but rastering has made it faster. One of the main problems of this technology is controlling the "splashing" as the laser hits the target, causing particles of micron size to eject from the target and contaminate the substrate piece. The process is considered easy to perform experimentally and manufacturing

41

equipment is not difficult to construct. However, the actual physics and modeling of the process are quite complex.

Sol-gel Deposition

Sol-gel processing allows the creation of high optical-quality coatings and monoliths through the strict control of processing parameters (pH, temperature, humidity, pressure) in combination with high-purity sol-gel precursors (Brinker and Scherer, 1990). Advantages of this technique include the use of low processing temperatures and standard atmospheric conditions, together with the ability to control the thickness and refractive index through chemistry and processing, along with the synthesis of low-loss optical materials. Sol-gels have been successfully deposited in a single- and multi-layered fashion (Brinker, Hurd *et al.*, 1990; Taylor and Fabes, 1992; Righini and Pelli, 1997). Thus, it is feasible to create a multi-layered sol-gel film where each layer has been directly written with optical properties that combine to create continuous three-dimensional optical structures. The sol-gel process has been successfully combined with traditional masking and etching lithographic techniques, as well as with laser direct-write techniques (Fardad, Andrews *et al.*, 1997; Atkins, Charters *et al.*, 2001).

Purely inorganic sol-gel materials can be synthesized and processed to have low optical losses for the current communication bands, while having low thermal expansion coefficients. Further, sol-gel materials in general have the advantages of unique properties synthesized at the molecular level (e.g., index of refraction, fluorescence), as well as representing an economic alternative for

preparation of highly engineered materials. On the other hand, purely inorganic sol-gel materials have limitations, including the maximum layer thickness achievable before cracking occurs (Brinker, Hurd *et al.*, 1992). Recently, so-called hybrid sol-gel materials have gained much attention by combining the benefits of inorganic sol-gels covalently bonded to organic materials to increase the integrity and compliance of the matrix.

2.5.2. Direct-Write Technologies

Direct-write technologies are manufacturing processes characterized by the use of computer aided design generated patterns and shapes for direct fabrication without part-specific tooling. They represent a set of emerging technologies, competing with more conventional fabrication techniques primarily in the microelectronics and integrated optics fields and lay at the forefront in research and development for replacement of current photoresist technologies (Church, Fore *et al.*, 2000; Piqué and Chrisey, 2002). Direct-write techniques are aimed at fabricating net-shape planar or three-dimensional structures.

Most of the initial efforts of direct-write technologies are associated with Rapid Prototyping applications. In fact, only recently have these technologies been conglomerated or unified by the term of 'Direct-Write'. Church, *et al.* and Pique, *et al.* provide insightful reviews of different manufacturing processes that fall into the category of Direct-Write processes, and they constitute some of the first attempts to do so (Church, Fore *et al.*, 2000; Piqué and Chrisey, 2002).

Church *et al*. provide a good classification of direct-write technologies (Church, Fore *et al.*, 2000). Some examples according to this classification are the following:

- *Physical Methods*: Stereolithography (SLA), Selective Laser Sintering (SLS), Laser Engineered Net Shaping (LENS), Fused Deposition Modeling (FDM).

- *Electrical Methods*: Laser Particle Guidance (LPG), Matrix Assisted Pulsed Laser Evaporation (MAPLE), Laser-Assisted Chemical Vapor Deposition (LCVD), Focused Ion Beam (FIB), Ion Beam Assisted Deposition (IBAD).

- *Optical Techniques*: femto-second pulsed laser ablation

Of particular interest to this research are SLS (Section 2.3), and laser induced photopolymerization, as in SLA and multi-photon absorption (Jacobs, 1992; Atkins, Charters *et al.*, 2001; Bae and Park, 2001).

The benefits of direct write technologies include having a flexible and highly automated process (CAD/CAM), with a clear reduction in the number of processing steps (Church, Fore *et al.*, 2000), as well as the possibility of creating multiple-material structures. On the other hand, these methods when applied to the meso and microscales, suffer from spatial resolution and poor reproducibility of results.

2.5.3. Observations

The traditional manufacturing processes described above, such as CVD, ion exchange, or FHD, successfully produce components with the level of purity and accuracy demanded by photonic and optoelectronic applications. However, the main drawbacks to these techniques are the large capital investments required for equipment, the large number of steps, and the low flexibility to modify the designs. The majority of these processes are followed by etching techniques to shape the waveguide structures, thus require masks for lithography, the deposition of photoresists, followed by an etching step, and a further cladding deposition step. Therefore, these processes are constrained to the creation of planar and 2½-D structures.

Some differences between the two approaches include:

- *Lithographic processes*: nano and μm scales and features, high resolution, high repeatability, 2½-D processing, thin films, constrained geometry.

- *SFF and DW processes*: μm and meso scales, moderate resolution, moderate repeatability, 2½ and 3D processing, flexible to geometry modifications.

The reverse engineering and redesign methodology suggests a comparison between similar embodied technologies, in order to identify new solutions. Figure 2.11 illustrates the general steps involved in the (a) layered lithographic and (b) layered freeform fabrication approaches, respectively. This figure helps

(a) Layered lithographic process   (b) Layered SFF process
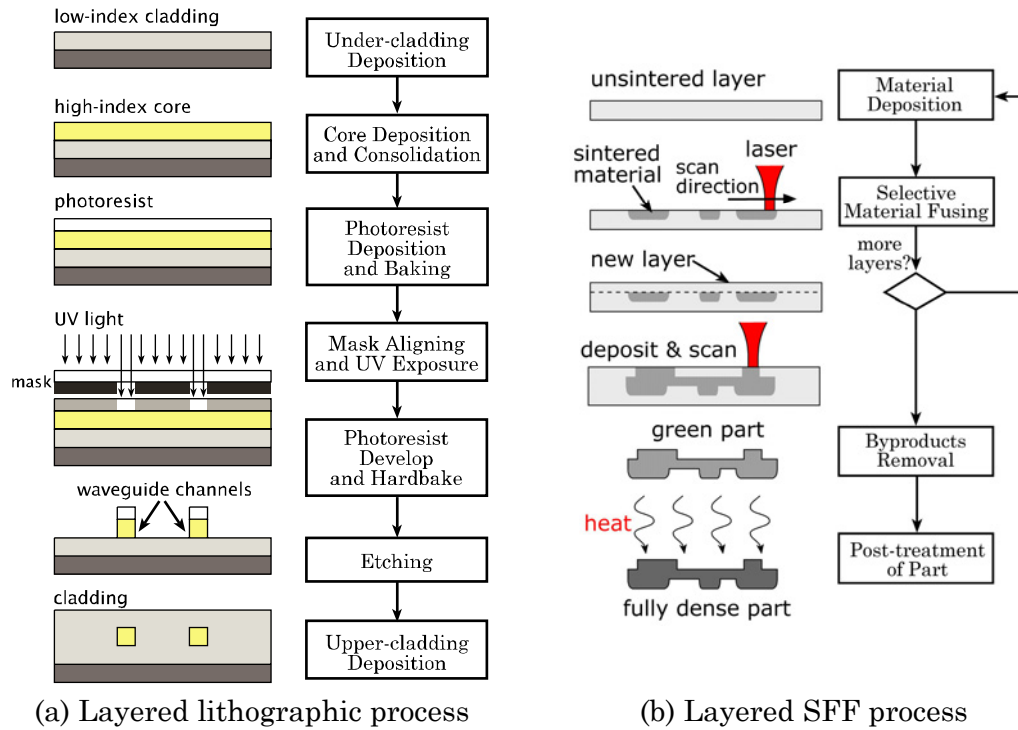
Figure 2.11. Comparison between manufacturing approaches

identify three common high-level processing steps: (1) material deposition, (2) material shaping, and (3) material treatment.

Referring back to the subsystems that were identified for the SLS process (Figure 2.5 and Table 2.1), these three high-level processing steps can also be identified. As mentioned by Otto and Wood, for the design or redesign of products, or in this case of a process, it is good design practice to begin with form-independent functions, such as the three mentioned above (Otto and Wood, 2001). This helps removing bias toward specific solutions, thus allowing the design team to propose innovative solutions. On the other hand, there is also room for what Otto and Wood call *process choices*, which help bound the design task and reduce the number of solutions.

46

For this research two main process choices were made. These were selected after going through the following process: (1) a thorough analysis of the telecommunications field and the manufacturing processes employed (Beaman, Wood *et al.*, 2001), (2) multiple brainstorming sessions with our industrial partner, (3) preliminary experiments with SLS of glass powders (Beaman, Wood *et al.*, 2001; Ruizpalacios, Beaman *et al.*, 2001), and (4) the analysis provided above following the Reverse Engineering and Redesign methodology of (Otto and Wood, 1998). The first process choice that emerged was to use a laser as the heating source, and the second one was to explore the use of sol-gels as the building material. It is worth noting that the idea of using sol-gels did not emerge until the design team did all of the four steps outlined above, which meant following a form-independent methodology in parallel to experimentation with our lab's area of expertise (i.e., SLS). While our approach is not the first, as concluded from the literature search, the concept of an automated rapid prototyping-style of machine did emerge from this research.

The following section discuses the use of direct-write concepts with sol-gel materials.

2.6. Direct-Write of Sol-Gels

Direct-Write methods have recently emerged in the optics field with a similar objective than in the microelectronics field; that is, to offer a cost effective alternative to photolithographic techniques. In particular, the combination of

laser-based direct write techniques with sol-gel materials has drawn some attention (Shaw and King, 1990; Chia, 1992; Taylor, Birnie *et al.*, 1995; Birnie, 1997; Righini and Pelli, 1997; Bae and Park, 2001). The majority of this research has focused on photothermal processing of inorganic sol-gels. The laser is used as a concentrated and controllable heat source to locally modify optical properties, such as index of refraction, to produce components such as graded-index micro-lenses (Chia, 1992) or planar optical waveguides (Righini and Pelli, 1997). More recently, in the works of (Atkins, Charters *et al.*, 2001; Bae and Park, 2001), a UV laser was used to photopolymerize a hybrid organic-inorganic sol-gel film. A similarity between the various applications reviewed was the use of simple laser scanning patterns, mainly spots and lines, where the laser was only used to increase the mass density of the waveguide's core. No further functionalities were incorporated or explored, for example, the use of the un-exposed areas for structural support.

The main advantage of laser scanning of sol-gel matrices is its ability to successfully, selectively, and accurately achieve high-density levels comparable to vapor deposition and melting, see for example (Shaw and King, 1990; Chia, 1992; Hench, 1998). This will be referred to as *Laser Densification*, and what it achieves is the local changing of properties by laser irradiation that results in an increase of mass density, and in turn of index of refraction. The localized change of density is an important characteristic for of the following reasons. A dry sol-gel matrix consists of a highly porous structure. The pores of a dried sol-gel film contain mainly air, although the presence of alcohol and water solutions is also observed, in conjunction with undesirable OH^- bonds and structural water formations (Brinker and Scherer, 1990; Pierre, 1998). In order to attain the

48

same density levels by melting or vapor deposition (~2.2 g/cm^3), high-temperature firing of the sample is required. A direct relation exists between the sample's density and index of refraction (Figure 2.12) (Hench, 1998), hence the ability to control the index of refraction through density changes based on laser power control is an area of keen interest.

The phenomenon of laser-matter interaction in sol-gel matrices is described in (Fabes, Taylor *et al.*, 1990; Shaw and King, 1990; Taylor, Fabes *et al.*, 1990; Chia, 1992; Fabes, 1992; Taylor and Fabes, 1992; Chia, Hench *et al.*, 1994; Pelli, Righini *et al.*, 1996; Ganz, 1997; Ganz, Reich *et al.*, 1997; Ganz, Gasparro *et al.*, 1998; Hench, 1998; Bae and Park, 2001). Yet, it is a subject that requires further investigation and will play a crucial role in the successful implementation of these techniques.
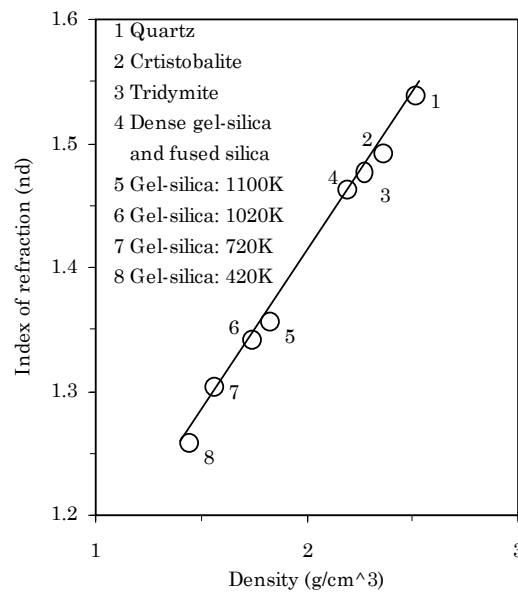
Figure 2.12. Dependence of index of refraction, *n*, on density. Adapted from (Hench, 1998)

49

2.7. Proposed Process

The first phase of the reverse engineering and redesign methodology suggests a thorough investigation of the existing product and an analysis of the state-of-the-art technology. The previous sections covered this first phase, through the review of the optical communications field, the optical components, and the various manufacturing processes involved. Three general processing steps for a direct-write process are identified based on the SLS process and the microelectronics and photonics layered manufacturing techniques. Figure 2.13 illustrates the three general processing steps, which are: (1) material deposition, (2) material shaping, and (3) material treatment. These three steps, as presented on the left part of Figure 2.13, are form independent, as suggested in the design methodology by (Otto and Wood, 1998; Otto and Wood, 2001). Embodied solutions of these three steps are shown on the right side of Figure 2.13, which will be discussed in more detail below.

As mentioned before, care must be taken to translate the functional requirements of current and future optical components according to the set of
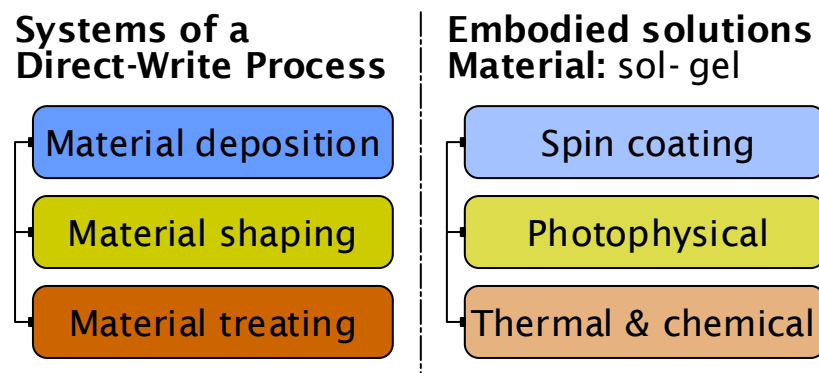
Figure 2.13. Systems for direct-write process

performance metrics demanded by the field of optical communications, into an embodied solution that can realistically be achieved by direct-write processes. This is the intention of this chapter: to provide a solution concept that can successfully be implemented in industry.

The fundamental areas of research that constitute the proposed direct-write process include: (1) the processing of commercially available sol-gel materials, (2) laser technology for layer-based fabrication of components, and (3) the use of CAD based models for product definition. Considering these three *process choices* (as defined by Otto and Wood, 2001), the three general processing steps can be rearranged as depicted by Figure 2.14a. This diagram shows a cyclical process, fully automated and controlled by a computer. This was a requirement established from the early stages of the design, and is characteristic of the processes in the photonics and microelectronics industries. This diagram

(a) Conceptual process flow diagram   (b) brain-map of solutions
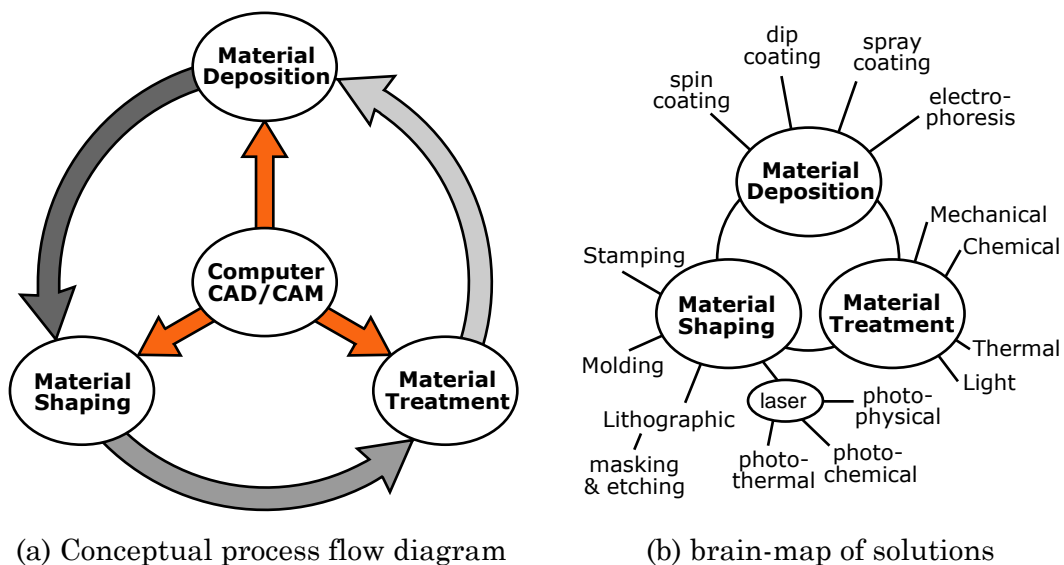
Figure 2.14. Flow diagram of automated process

Table 2.4. Solutions for general process steps

System	Embodiment	
Material Deposition	Spin coating	
	Dip coating	
	Spray coating	
	Electrophoresis	
Material Shaping	Laser	Photothermal
		Photochemical
		Photophysical
	Stamping	
	Molding	
	Lithographic	Masking and etching
Material Treating	Chemical	
	Thermal	
	Mechanical	(polishing)
	Light	Photochemical
		Photophysical

also serves as an initial layout of the process architecture.

In the next step of the design process, the design team must identify potential solutions for each of the sub-systems that were identified (Otto and Wood, 1998). Following this procedure, Figure 2.14b presents an illustration of what is called a "brain map", which presents potential solutions for the three processing steps. The examples of different options for the embodiment of each of the three general steps of the direct-write process are rearranged in Table 2.4.

Narrowing further more the design solution space, a set of solutions to be embodied are selected based mainly on three criteria: (1) robustness and matureness of the technology, as demonstrated in the literature, (2) its ability to be seamlessly integrated into an automated process, and (3) the integrated process can reduce the manufacturing time. The chosen solutions thus are: spin coating for material deposition, laser photophysical processing for material shaping, and thermo-chemical post-processing (see Figure 2.13).

2.7.1. Material Deposition

Spin coating is selected for the *material deposition* step (Figure 2.13) because it is a flexible thin-film deposition method for liquid materials, where one can obtain a specific film thickness by controlling the angular velocity of the spinning substrate over time. This method allows programming complex velocity profiles according to the nature of the solution, and minimizes waste of the dispensed solution. The liquid sol can be successfully deposited by this method to form a porous sol-gel film. In addition to this, considering a fully automated direct-write process, one can envision a robotic manipulator precisely placing the substrate in the spin coater with no human intervention. This process can be repeated for multiple layered structures. Furthermore, spin coating is a standard process in the photonics and microelectronics industries. The spin coating processing is presented in Chapter 4.

2.7.2. Thermal and Chemical Processing

The thermo-chemical post-processing of the sol-gel film corresponds to the next process choice, addressing the *material treatment* step of Figure 2.13. Depending on the nature of the sol-gel (see Chapter 3) and on the type of laser processing (photothermal or photophysical; see Chapter 5) is the application of purely thermal or both thermal and chemical post processing of the film and features. For example, for a purely inorganic doped silicate sol-gel thermal processing at high temperature and high heating rate are required after deposition. On the other hand, for laser induced photopolymerization of a hybrid organic-inorganic

sol-gel thin film, thermal and chemical processing are performed after deposition and laser processing.

Thermal processing is an essential step that follows the deposition of the film, and the objective is to remove the byproducts and unreacted species from the film (e.g., solvent and water), and serves as a pre-densification step before laser processing. It is also employed to reduce the residual stresses induced during multi-layer fabrication and laser processing. This step is performed in a furnace or in a hot-plate under a controlled atmosphere. On the other hand, chemical post-processing is employed to remove the unreacted sol-gel material during laser photophysical polymerization, and "develop" the features by submerging the sample in a bath of a chemical developer. A detailed description of thermo-chemical processing is provided in Chapter 4.

2.7.3. Laser Processing

Laser processing is selected as the next process choice for the *material shaping* step (Figure 2.13) because it provides a highly concentrated energy source that can be easily manipulated in space. The energy being received by the material can be controlled by changing the processing parameters, such as scan speed (for a moving laser beam), maximum laser power (for continuous wave mode), repetition rate and peak power (for pulsed sources), etc. A laser is an efficient energy source for photothermal, photochemical, or photophysical processing of materials (Bäuerle, 2000; Bäuerle, 2002). Disadvantages of this method are mainly related to low spatial resolution, which in the end limits the feature's size

and resolution. For the current research the photothermal and photophysical processing modes were explored. They will be covered in detail in Chapter 5.

A crucial part of the laser processing step for direct-write is to translate either the laser beam or the sample in a trajectory defined by the CAD/CAM system. Two common approaches are by using galvanometer mirrors, which move the beam, or by an XYZ stage, which moves the part in a 3D space. These two configurations were pursued and are discussed in Chapter 5.

2.7.4. Detailed Description of Proposed Direct-Write Process

Following the Reverse Engineering and Redesign strategy, and based on the general three processing steps described above, the following discussion provides a more detailed picture of the proposed process. This process is further modified and updated based on the experimentation that is presented in Chapters 3, 4, and 5. Figure 2.15 shows an illustration of the various steps involved in the proposed process.

The proposed process begins with the preparation of the sol. This is done by mixing the sol-gel precursor (typically silica-based alkoxides) with a solvent, water and a catalyst to initiate the hydrolysis of the precursor. Mixing can take between 2 to 24 hours, depending on the type of sol-gel (i.e. inorganic or hybrid), and might require refluxing at a set temperature until dilution is completed; the pH level is verified and adjusted. After mixing, the liquid mixture is filtered and stored in a sealed container. The filter has a membrane of typically 0.2 μm, and is used to remove any impurities in the sol. Hydrolysis and condensation
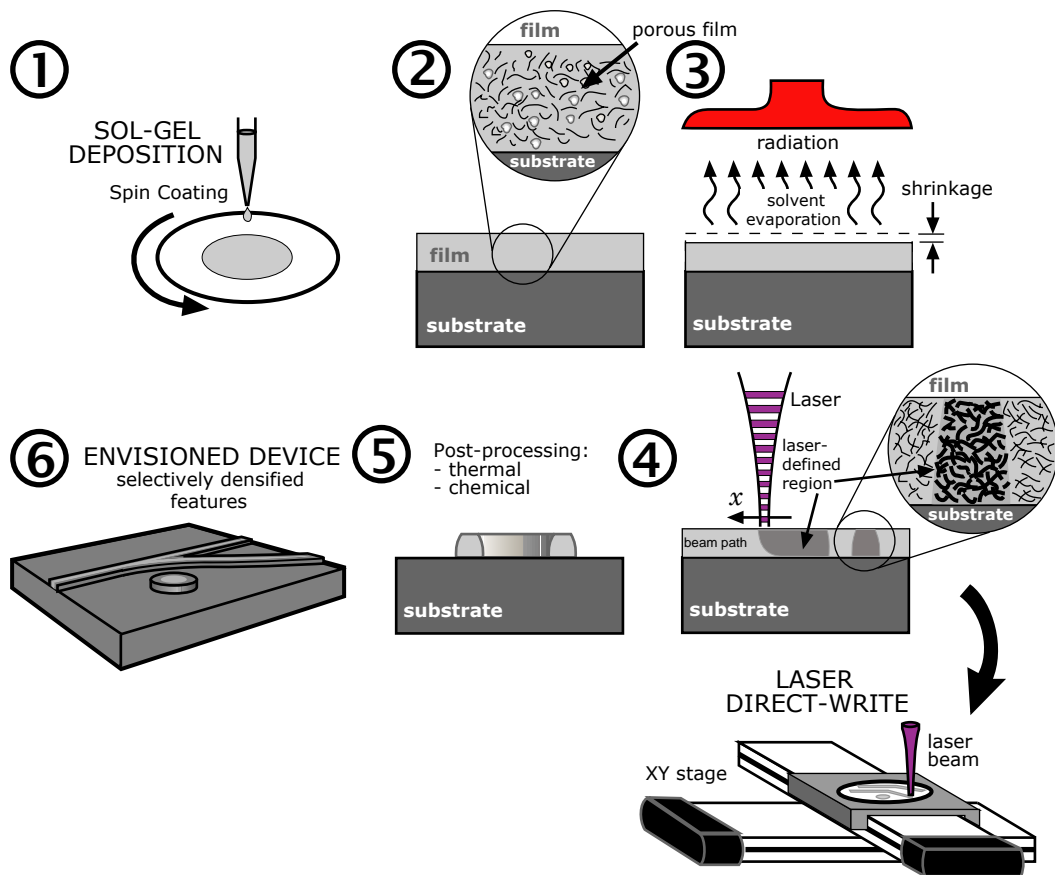
Figure 2.15. Proposed direct-write process

reactions continue during storage. This pre-aging step is crucial to obtain a stable sol with the adequate viscosity.

The sol is deposited over the substrate, by means of spin coating. In this technique, the sample is placed in a vacuum chuck and rotated at a determined angular velocity. The solution is added either before (static deposition) or after (dynamic deposition) the sample is accelerated to the desired velocity.

Condensation reactions, solvent evaporation, and gelling take place almost simultaneously and rapidly during spin coating, producing a solid sol-gel film. Right before deposition, a small volume of the solution is drawn out, diluted with the appropriate solvent, filtered again, and stored in small volumes. After deposition, the sample is placed in a furnace or hot-plate with a controlled atmosphere, and heated to a specified temperature at a certain heating rate. Depending on the nature of the sol, typically a "drying" aging time is devoted to achieve the desired levels of condensation and solvent evaporation once the sol has been deposited. For the proposed process a small amount of time will be devoted during this step, since the thickness of the deposited layer is rather small (~0.1 to 1.0 μm). Once the layer has been deposited the drying stage commences. During drying, the temperature is slowly increased (typically below ~200°C) with the option of a rough vacuum or simply a flow of a gas, such as helium, nitrogen or oxygen. This step can further incorporate the humidity control of the reflowing gas, with the objective of controlling the adsorption and diffusion of water and alcohol mixture contained in the pores of the structure.

After drying the layer has significantly reduced its volume, primarily on the normal direction, and a very porous structure is left. A final "baking" is pursued at a higher temperature in order to drive off any residual water or solvent remaining in the pores. This is done in a furnace with a flowing gas (e.g. dry air, O_2, N_2, He, etc.), and a higher heating rate in the case. Typical temperatures are between 200–1000°C. During this thermal processing, a further reduction in volume is observed and an increase in density. There is also some stress release, which consequently helps to avoid cracking.

The final stage is the laser-writing. This step consists of scanning a tightly focused laser beam over the surface of the sol-gel film, following the desired trajectory. The wavelength of the laser of choice is critical due to the dependence of absorption of the sol-gel film on the wavelength. Silica-based materials have high absorption in the UV or far IR. The lasers available for this research were: CO_2 (IR laser, λ=10.6 μm) and Argon-ion (UV laser, λ=244 nm). The laser will increase the density, and thus the index of refraction, according to Figure 2.12, in the exposed region. The beam is moved either by a set of galvanometer mirrors or by an XY stage, controlled by a computer. The part to be manufactured is designed in a CAD system (e.g. ProEngineer, Solid Works, AutoCAD, etc.), which is then imported into the appropriate software that translates the geometry into trajectories and instructions interpreted by the servosystem. The process proceeds with the addition of a subsequent layer and repetition of the above steps until the part is completed. Further post-processing (e.g. heat or chemical treatment) might be required, including the proper packaging.

2.8. Conclusions

This chapter began with a review product design methodologies and how they can be applied for the design of a process. An emphasis was placed on the use of the Reverse Engineering and Redesign methodology proposed by (Otto and Wood, 1998) to study the SLS process and begin from there the design of a new process. A background review of the optical communications field, including a

series of manufacturing processes, highlighted some of the current trends and helped identify potential areas of opportunity for direct-write processes. When contrasted to the characteristics and specific examples of direct-write processes, helped understand strengths and weaknesses of these techniques, and therefore bound the research problem.

The following conclusions can be drawn from this chapter:

- The importance of following structured design methodologies, and how product design methodologies can be applied to the design of novel processes were illustrated.

- As a consequence of the reverse engineering of the SLS process and after a comparison with layered manufacturing techniques in the microelectronics and photonics fields, three basic processing steps were identified: (1) material deposition, (2) material shaping, and (3) material treatment.

- These three systems became the building blocks of the proposed direct-write process, identifying their interaction as part of a CAD/CAM system.

- The way these three steps interact, also helped define the architecture of an automated machine that can potentially be used in commercial applications.

Chapter 3. Material Preparation

3.1. Introduction

This chapter presents a detailed description of the preparation procedures, from both theoretical and experimental perspectives, of the sol-gels used for this research, as well as the deposition method chosen. The chapter begins by presenting a brief introduction to the sol-gel process, followed by the description of the chemistry of the three main sol-gel systems investigated. This description includes a set of specific goals behind each system. Some theory is provided afterwards on the various techniques used for the analysis of the samples. Next, the experimental procedures for sample preparation are presented, concluding with an analysis of the results.

3.2. The Sol-Gel Process

Sol-gel processing allows the creation of high optical-quality coatings and monoliths through the strict control of processing parameters (pH, temperature, humidity, pressure) in combination with high-purity sol-gel precursors (Brinker and Scherer, 1990). The main strengths of this method include its ability to use low to mid processing temperatures and standard atmospheric conditions. It also offers the possibility to control optical and structural properties from chemical and processing points of view (e.g., refractive index, layer thickness,

etc.). The sol-gel process has the capacity to produce highly pure materials, synthesized at the molecular level.

A sol is a subset of the colloid substances group. A colloid is a suspension of a small-dispersed phase (~1-1000 nm) of particles, where gravitational forces can be neglected, and is dominated by short-range forces such as van der Waals forces and surface charges (Pierre, 1998). Therefore a sol is a colloidal suspension consisting of a solid phase dispersed in a liquid phase.

In general, the sol-gel process can be understood from the evolution of the following steps (Hench, 1998): (1) Mixing, (2) Deposition, (3) Gelation, (4) Aging, (5) Drying, (6) Dehydration and stabilization, and (7) Densification (by furnace or laser heating). Figure 3.1 shows a flow diagram of the process.

In the initial mixing stage of the sol-gel process, the reagents, when combined, form a colloidal dispersion of nano-particles in a liquid, known as sol.
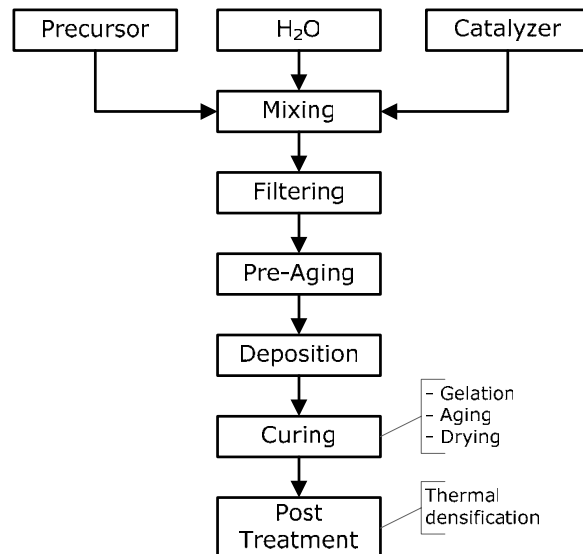
Figure 3.1. The general sol-gel process

The mixing stage is characterized by three main reactions: hydrolysis, water condensation, and alcohol condensation. The general hydrolysis and condensation reactions are the following (Brinker and Scherer, 1990):

Hydrolysis: $$M - OR + H_2O \rightleftharpoons M - OH + ROH \tag{3.1}$$

Alcohol condensation: $$M - OR + HO - M \rightleftharpoons M - O - M + ROH \tag{3.2}$$

Water condensation: $$M - OH + HO - M \rightleftharpoons M - O - M + H_2O \tag{3.3}$$
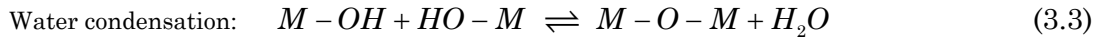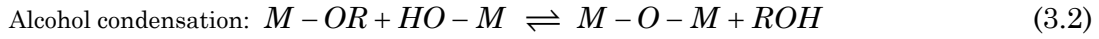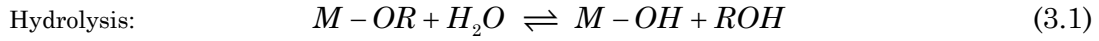
where M represents a metal ion, for example: Si, Ti, Zr, Ge, etc.

The structural evolution that occurs after the initial mixing stage is shown in Figure 3.2, which follows the sequence of Figure 3.1.

The precursors are generally metal alkoxides or other organometallic compounds, for example $Si(OR)_4$, where R is an alcohol, such as: CH_3 (methyl), C_2H_5 (ethyl), or C_3H_7. Metal alkoxides are common sol-gel precursors because
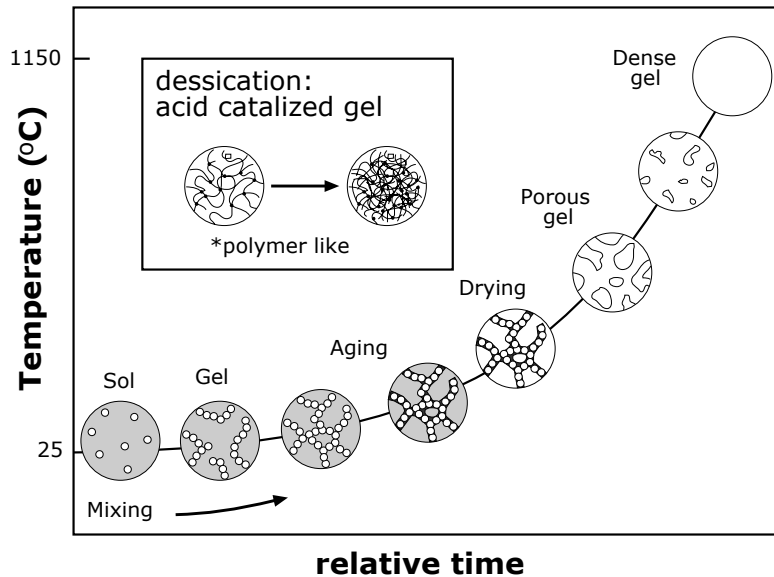
Figure 3.2. Sol-gel structural evolution (based: Hench et al., 1988)

62

they react easily with water, through the hydrolysis reaction described in Equation (3.1) (Brinker and Scherer, 1990). As shown in Figure 3.1, the mixing stage requires a catalyst, water, and the precursor. The catalyst could be for example nitric acid or hydrochloric acid. In the condensation reaction, silica tetrahedra react with each other to form siloxane bonds. Then, a polycondensation reaction occurs between the species, forming a three-dimensional network of metal oxide bonds (e.g., SiO_2) plus water and alcohol. These last two reside in the pores of the network.

The sol is formed when sufficient M–O–M bonds appear, acting as colloidal particles with nanometer size suspended in a liquid. The particle size and particle density of the sol depend mainly on the mixture's pH and the water to alkoxide ratio, R_{wa}, where $R_{wa}=[H_2O]/[M(OR)_4]$, in addition to processing conditions (Brinker and Scherer, 1990; Fardad, Yeatman *et al.*, 1995; Hench, 1998). Acid catalysis forms three-dimensional polymeric chains that are weakly cross-linked, resulting in a clear structure with good flowing conditions suitable for spin coating processes (see inset of Figure 3.2). On the other hand, under basic catalysis conditions, highly branched clusters are formed, resulting in a "foggy" aspect (Klein, 1988).

The deposition of the colloid is done in the liquid sol stage (after aging to allow initial branching) because of the low viscosity. After gelation the ultrastructure is fixed as a consequence of the sharp increase in viscosity, although recent advances have demonstrated the possibility to alter it through the reflow of gas mixtures with etching functionalities (Syms, 1994). Gelation is characterized by polymerization of the sol particles. Gelation times strongly depend on the chemical composition and the processing temperature, and can

vary from a few seconds to several days (Brinker and Scherer, 1985; Brinker, Scherer *et al.*, 1985; Brinker and Scherer, 1990; Hench, 1998). For thin films this process occurs rapidly, and it overlaps the followings steps (Brinker, Hurd *et al.*, 1992).

Crucial steps of the process are aging and drying. Shrinkage and mass loss of gels during drying occur mainly due to departure of water molecules (Pierre, 1998). Dehydration can be characterized by two factors: departure of adsorbed water (in the pores of the gel network), and departure of structural water (molecules within the gel network of O–M–O bonds). The amount of each strongly depends on the method of preparation of the sol-gel. For example, when prepared at room temperature (T~20°C) the gel mostly contains adsorbed water, which in turn is easier to remove and requires lower drying temperatures (~200°C). On the other hand, synthesis at higher temperatures (T~80°C) produces both adsorbed and a high content of structural or chemical water, which requires higher drying temperatures (~300°C) (Pierre, 1998). Dehydration of adsorbed and chemical water is characterized by endothermic reactions, where ΔT is greater for adsorbed water, which occurs between ~80–150°C, while chemical drying occurs between ~160–270°C.

The sol-gel process has been successfully used in a broad range of applications, including thin film coatings (Brinker, Hurd *et al.*, 1990; Brinker, Hurd *et al.*, 1992), monolithic optical components such as micro-lenses (Chia, 1992; Hench, 1998), and more recently in optical fibers preforms (van Blaaderen, Ruel *et al.*, 1997; Roco, Williams *et al.*, 1999) and optical waveguides with gratings for DFB lasers (Coudray, Chisham *et al.*, 1997; Najafi, Touam *et al.*, 1998; Andrews, Zhang *et al.*, 1999; Blanc, Pelissier *et al.*, 1999; Atkins, Charters

et al., 2001; Fardad, Mishechkin *et al.*, 2001). Such diverse range of applications has been achieved by changing the precursor, or by modifying and controlling the processing parameters. This process has recently caught much attention due to the low temperature processing conditions required and the high purity obtained at lower costs. Its application will certainly continue to grow (Wright and Sommerdijk, 2001).

In summary, in order to successfully synthesize mixtures suitable for deposition of thin-films, a proper selection of the precursors and molar concentrations must be done, in conjunction with a strict control of the environmental parameters, in particular humidity and aging time of the solution. The chemistry of the sol-gel has a direct impact in the physical properties of the thin film to be deposited, such as: index of refraction, shrinkage, porosity, etc. In conclusion, the sol-gel process provides a stable structure (chemically pre-sintered) with excellent optical properties.

Mixing	Deposition	Aging	Drying
• Molar concentration - alkoxide - solvent - catalyst • Water/alkoxide ratio, R_{wa} • Solvent/alkoxide ratio, R_{sa} • Catalyst type • Mixing temp., T_{mix} • Reflux temp., T_r • Reflux time, t_r	• Solvent concentration • Volume, V_d • Temperature, T_d • Humidity • Atmosphere • Spin coating: - acceleration - velocity - dwell time	• Temperature, T_a • Dwell time, t_a • Atmosphere • Humidity	• Total time, t_{dt} • Heating rate, $\Delta T/dt_d$ • Max temp, T_{dmax} • Dwell time, t_d • Atmosphere • Flow rate

Figure 3.3. Examples of parameters involved in the sol-gel process

3.3. Selected Sol-Gel Systems

The synthesis of sol-gel materials is a process that involves many parameters, including chemical (e.g., molar concentration, water alkoxide ratio, etc.), thermal (e.g., densification temperature, dwell time, etc.), environmental (relative humidity, atmosphere, etc.) Figure 3.3 presents typical parameters involved in the preparation and deposition by spin coating of a sol-gel thin film.   The successful transformation of a liquid colloid into highly pure, stress free, and optically clear thin film or monolith, requires a great degree of control on the multiple processing parameters.

The synthesis and processing of sol-gel thin films or monolithic structures, doped or undoped systems, varies substantially (Brinker and Scherer, 1990; Wright and Sommerdijk, 2001). For this reason, in this research much time was spent experimenting with various sol-gel systems. Three main groups were investigated:

(1) Purely inorganic silicate system.

(2) Organically-modified Ti-doped silicate system (hybrid).

(3) Organically-modified photosensitive doped silicate systems.

Each system provides a distinct set of physicochemical properties, with different advantages and limitations.   Pure inorganic silicate sol-gels were investigated as a starting point.   Their application for optical waveguides or integrated optics is limited to lower index of refraction cladding layers, or in the scope of this research, the required index difference (Δn) achieved by a small thermally induced change in density. Additional limitations of this system are

the low single-layer maximum thickness achievable before cracking occurs, as well as the maximum number of layers that can be subsequently deposited. High temperature post-processing of inorganic and some hybrid systems solve some but not all of the cracking and residual stress problems. The addition of other metal alkoxides in smaller concentrations acting as dopants was also explored for purely inorganic approach. This proved to be a very challenging task, especially for Ti and Ge alkoxides, where the hydrolysis rates are much faster than for their Si counterpart (Keddie and Giannelis, 1991; Almeida and Christensen, 1997; Grandi, Mustarelli *et al.*, 2002). This led us into exploring the so called *organically modified* or *hybrid* organic/inorganic sol-gel systems.

From the knowledge of the purely inorganic silicate system, combined with recent research in sol-gel science aimed at solving some of the limitations mentioned above, a second system was investigated. This second system incorporates organic ligands, and is part of what has been known as hybrid organic/inorganic or organically modified sol-gels. A comprehensive review of recent advances is provided by (Gvishi, Narang *et al.*, 1997). In particular, for this research the hybrid titanium doped silicate sol-gel system was chosen to form the guiding layer or core. The research was based mainly in the works of (Brusatin, Guglielmi *et al.*, 1997; Guglielmi, Martucci *et al.*, 1998; Seco, Goncalves *et al.*, 2000). In these hybrid systems, the incorporation of nonvolatile organic groups increases the compliance of the network, thus reducing residual stresses, which consequently allows the fabrication of thicker films compatible with single mode fibers. Additionally, the processing temperatures are significantly lowered (T_{max}~500°C). Yet the presence of organic groups increases

67

the attenuation losses due to absorption and a higher presence of unwanted hydroxyls (OH⁻ ions).

Both of the systems described above were initially explored for a laser direct-write process that contemplates only photothermal activation to increase the density, thus raising the index of refraction. This process has some disadvantages because the laser source can easily ablate and damage the surface. Thus, a third system was investigated. This system is a hybrid doped Si-based sol-gel that incorporates methacryl and silicate networks photopolymerizable by photon induced free-radical polymerization. Two doping agents were explored, Zr and Al, based on the works of (Coudray, Chisham *et al.*, 1996; Fardad, Touam *et al.*, 1997; Fardad, Andrews *et al.*, 1998; Fardad and Fallahi, 1998; Saravanamuttu, Du *et al.*, 1998; Fardad, Mishechkin *et al.*, 2001; Fallahi, Bedford *et al.*, 2002). Advantages of these sol-gels are similar to the hybrid system described above (low temperatures, more compliant, etc), in addition to the lithographic-like process of light induced polymerization, making it compatible with current microelectronics manufacturing techniques.

Following is a more detailed description of each individual system and the preparation process.

3.4. System 1: Inorganic Silicate Sol-Gel

Experimentation with sol-gel materials for this research began with the well known purely inorganic silicate system, synthesized from one of the most common alkoxide precursors: tetraethoxysilane (TEOS). This precursor has been

successfully applied for the deposition of thin sol-gel films (Sakka, Kamiya *et al.*, 1984; Brinker, Hurd *et al.*, 1990), which was the initial goal of this research. This sol-gel system has been the subject of detailed studies of both the scientific aspects of physical and chemical properties, as well as the processing parameters that influence the formation of stable films (Bräutigam, Bürger *et al.*, 1989; Klein, 1991; Fardad, Yeatman *et al.*, 1995; Guglielmi, Martucci *et al.*, 1998).

The hydrolysis and condensation reactions that govern the principal chemical processes of this silicon-based system are described by the following equations (Brinker and Scherer, 1990):

Hydrolysis: $\qquad \equiv Si - OR + H_2O \ \rightleftharpoons \ \equiv Si - OH + ROH$ $\qquad$ (3.4)

Alcohol condensation: $\equiv Si - OR + HO - Si \equiv \ \rightleftharpoons \ \equiv Si - O - Si \equiv + ROH$ $\qquad$ (3.5)

Water condensation: $\equiv Si - OH + HO - Si \equiv \ \rightleftharpoons \ \equiv Si - O - Si \equiv + H_2O$ $\qquad$ (3.6)
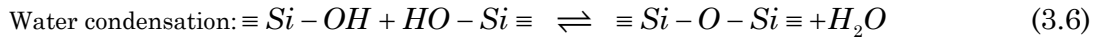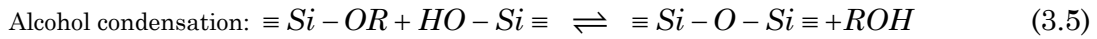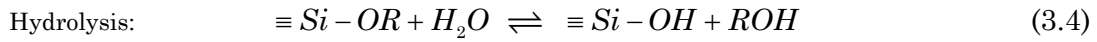
The stoichiometric ratio of water to alkoxide that balances the reaction of Equation (3.4) corresponds to R_{wa}=4 (Wright and Sommerdijk, 2001). Yet less water is required since the condensation reaction of Equation 3.6 results in the production of excess H_2O as byproduct. Back and forth reactions can occur in an undesirable way, depending on the initial concentrations (Brinker and Scherer, 1990). For this reason, the ratio R_{wa} is one of the most important aspects to control.

Due to the ethyl group, TEOS is immiscible in water, so a solvent is generally used prior to the addition of H_2O. Ethyl alcohol (C_2H_5OH or EtOH) is typically used, and was the choice for this research. Figure 3.4 presents a ternary diagram for the system TEOS–H_2O–EtOH. This figure highlights the miscible and immiscible regions (Brinker and Scherer, 1990). It also presents
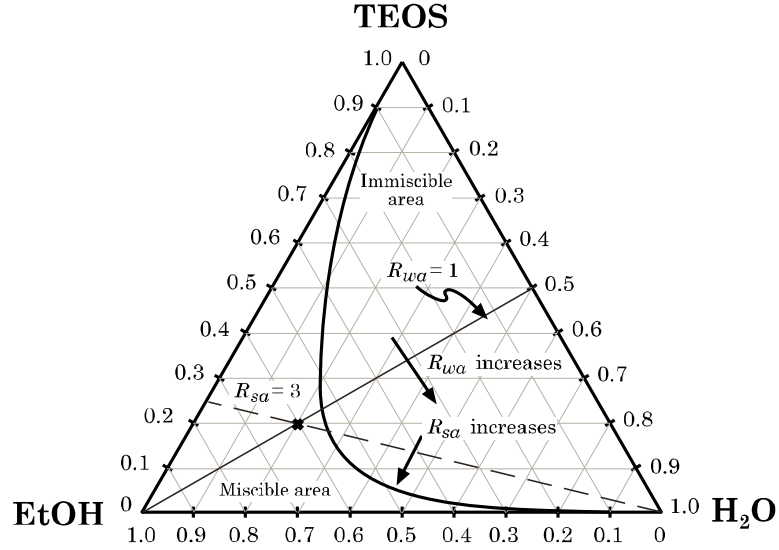
Figure 3.4. Ternary diagram for basic silicate sol-gel from TEOS

the curves for constant water-alkoxide ratio R_{wa} and the curves for constant solvent-alkoxide ratio R_{sa}. These two serve as good design parameters when conducting a design-of-experiments (DOE), since they summarize molar concentrations, and are correlated to reaction rates and material properties.

One of the most influential factors that affect the hydrolysis and condensation reactions is the pH of the initial sol. Solutions hydrolyzed under acidic conditions form long polymeric chains manifested as a three-dimensional network. On the other hand, hydrolysis under basic conditions tends to form nano-size particles grouped in clusters. Acid-catalyzed solutions are preferred for the formation of optically clear films. They are more appropriate for deposition by spin coating (Brinker, Hurd *et al.*, 1990; Brinker and Scherer, 1990; Brinker, Hurd *et al.*, 1992). Additionally, the pH has been found to have direct relation on the gel time (Sakka and Kamiya, 1982; Brinker and Scherer,

70

1985; Scherer, 1988; Wright and Sommerdijk, 2001). For example, the gel time is considerably minimized for 0<pH<1, while it begins rapidly increasing for 1<pH<2, after which it decreases again.

The physicochemical characteristics of the silica sol-gel system are well documented in the literature (Brinker and Scherer, 1990); however, the preparation procedures are rarely described in detail. Also, as reported by (Guglielmi, Martucci *et al.*, 1998), because of the large number of parameters that influence the sol-gel process, additional variability is introduced during the processing by noise variables. For these reasons, a substantial amount of time was spent developing a repeatable process that would provide consistent high-quality films.

In order to do so, the first step was to identify the various parameters involved in sol-gel processing. In *Design Methodology* jargon, as outlined in Chapter 2, the following set of variables and parameters can be identified:

- Design Parameters, **d**: molar concentration of [TEOS], [H_2O], [EtOH], [HCl], R_{wa} and R_{sa}, mixing temperature, refluxing temperature, and aging time of sol.

- Performance Metrics, **p**: pH, viscosity of sol, index of refraction, film thickness, and porosity.

- Noise parameters, **n**: humidity, aging temperature and atmosphere.

In addition to these parameters, some desired outcomes include reducing porosity, achieving a uniform index of refraction throughout the film, finding the optimum viscosity for spin coating deposition, and maximizing the film thickness. The next section describes the preparation procedure.

3.4.1. Preparation Procedure for Pure Inorganic Silica Sol-Gel

Initially a single-step mixing process was pursued. This was based on a literature search, which provided some experimental description and set of suggested molar ratios (Sakka and Kamiya, 1982; Sakka, Kamiya *et al.*, 1984; Brinker and Scherer, 1985; Brinker, Hurd *et al.*, 1990). Table 3.1 shows the different combinations of molar ratios that were gathered from these references. From this table, mixtures 1 through 9 resulted from the literature search, while mixtures 10 through 17 were part of a screening process performed to understand the sensitivity of the sol-gel process and attain repeatable results. A summary of these different mixtures is provided in the ternary diagram TEOS-water-ethanol of Figure 3.5.

Table 3.1. Molar ratios of preliminary experiments: pure silica sols

Mixture	Molar Fraction (%)				R_{wa}	R_{sa}	Observations
	TEOS	H_2O	EtOH	HCl			
1	35.92	45.51	18.56	0.01	1.27	0.52	Poor
2	5.32	58.09	36.23	0.35	10.92	6.81	Poor
3	19.60	21.00	59.40	0.01	1.07	3.03	
4	48.03	3.94	48.03	0.01	0.08	1.00	Poor
5	5.32	58.09	36.23	0.35	10.92	6.81	Poor
6	19.60	21.00	59.40	0.01	1.07	3.03	
7	9.39	9.41	81.20	0.01	1.00	8.65	Poor
8	29.99	29.96	40.05	0.01	0.99	1.34	Too viscous
9	4.48	89.46	6.06	0.01	19.98	1.35	Poor
10	28.00	28.00	44.00	0.01	1.00	1.57	
11	30.00	20.00	50.00	0.01	0.67	1.67	
12	18.00	18.00	64.00	0.01	1.00	3.56	
13	18.00	28.00	54.00	0.01	1.56	3.00	
14	22.00	22.00	56.00	0.01	1.00	2.55	
15	18.00	22.00	60.00	0.01	1.22	3.33	
16	12.00	44.00	44.00	0.01	3.67	3.67	
17	4.34	43.48	52.17	0.01	9.99	11.99	

*Note: From Brinker & Scherer, 1991: 2,3,5,6; Sakka & Kamiya, 1982: 7,8,9
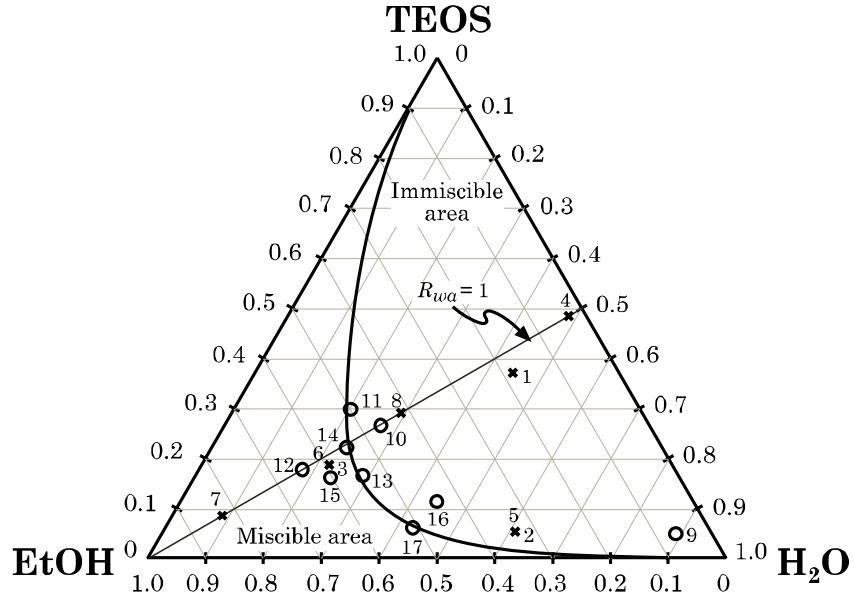
Figure 3.5. Initial experiments in TEOS–H2O–EtOH diagram

The initial goal was to get acquainted with the sol-gel process and to produce high optical quality and crack free films. This proved to be an elusive goal for the single-step process, which provided inconsistent results. This led to explore a different processing approach.

Development of Preparation Procedure

As a result of these initial experiments, a two-step preparation procedure was developed. It is based on a combination of the procedure proposed by Sakka *et al.* (Sakka, Kamiya *et al.*, 1984) and from observations of our own experimentation. The process begins with an initial pre-hydrolysis step, with a water-alkoxide ratio of: R_{wa} =1. Then, this is followed by the addition of reagents to drive the molar concentration, therefore R_{wa} and R_{sa}, to a desired point were

73

the reaction is completed. Figure 3.6 shows a flow diagram of the preparation procedure. The figure is followed by a description of the individual steps and the calculations involved in the proposed process.
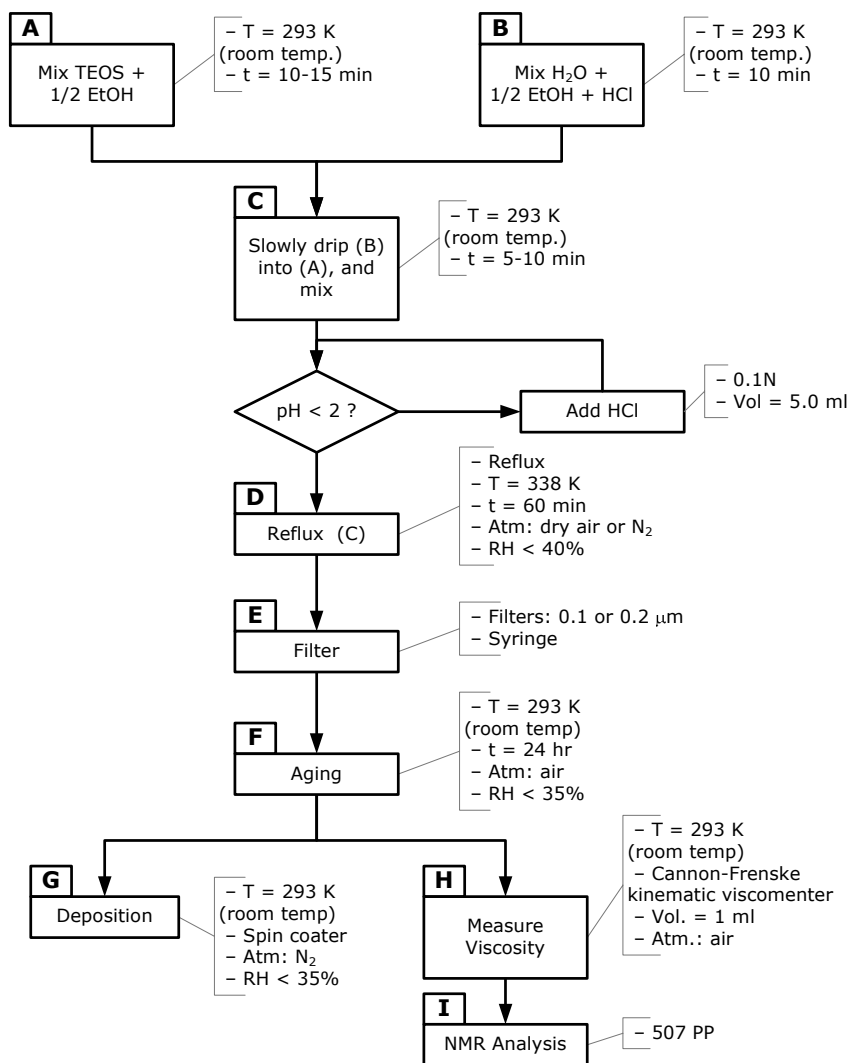
Figure 3.6. Preparation procedure for inorganic silicate sol-gel

Step 1. Partially Hydrolyzed Mixture.

For calculations of weight and volume of individual components given the total weight of the mixture, the following formulas were applied:

$$NM_{T1} = M_{T1} \cdot \left[\frac{1}{X_{A1} \cdot FW_A + X_{B1} \cdot FW_B + X_{C1} \cdot FW_C} \right] \qquad (3.7)$$

$$M_{[\cdot]1} = \left[NM_{T1} \cdot X_{[\cdot]1} \right] \cdot FW_{[\cdot]} \qquad (3.8)$$

$$V_{[\cdot]1} = \frac{M_{[\cdot]1}}{\rho_{[\cdot]}} \qquad (3.9)$$

where the subscripts *A*, *B*, and *C* correspond to TEOS, EtOH and acidified H_2O, respectively. Table 3.2 presents a list of the variables and their units.

Step 2: Final Hydrolyzed Mixture.

For this second step additional reagents are added to bring the final concentration to the desired value. Given a pre-selected combination of R_{wa} and R_{sa}, the individual molar ratios can be calculated as follows:

Table 3.2. Variables for calculations of molar ratios for System #1

Variable	Definition	Units
$NM_{T\#}$	Total number of moles of mixture for step #	mol
M_T	Total mass of solution	g
$M_{T\#}$	Total mass of mixture for step #	g
$X_{[\cdot]\#}$	Mole fraction of component [·] for step #	
$FW_{[\cdot]}$	Formula weight of component [·]	g/mol
$M_{[\cdot]\#}$	Mass of component [·] for step 1	g
$V_{[\cdot]\#}$	Volume of component [·] for step #	ml
$\rho_{[\cdot]}$	Mass density of component [·]	g/cm³

$$X_{A2} + X_{B2} + X_{C2} = 1 \tag{3.10}$$

given,

$$R_{wa2} = \frac{X_{B2}}{X_{A2}} \tag{3.11}$$

$$R_{sa2} = \frac{X_{C2}}{X_{A2}} \tag{3.12}$$

we can solve for X_{A2}, X_{B2} and X_{C2},

$$X_{A2} = \frac{1}{1 + R_{wa2} + R_{sa2}} \tag{3.13}$$

$$X_{B2} = \frac{R_{wa2}}{1 + R_{wa2} + R_{sa2}} \tag{3.14}$$

$$X_{C2} = \frac{R_{sa2}}{1 + R_{wa2} + R_{sa2}} \tag{3.15}$$

M_T represents the total mass of the solution to be prepared; so the total mass for step two is given by:

$$M_T = M_{T1} + M_{T2} \Rightarrow M_{T2} = M_T - M_{T1} \tag{3.16}$$

For calculations of weight and volume of individual components given the total weight of the mixture, the following formulas were applied:

$$NM_{T2} = M_{T2} \cdot \left[\frac{1}{X_{A2} \cdot FW_A + X_{B2} \cdot FW_B + X_{C2} \cdot FW_C} \right] \tag{3.17}$$

$$M_{[\cdot]2} = \left[NM_{T2} \cdot X_{[\cdot]2} \right] \cdot FW_{[\cdot]} \tag{3.18}$$

$$V_{[\cdot]2} = \frac{M_{[\cdot]2}}{\rho_{[\cdot]}} \tag{3.19}$$

The list of variables and units for these equations is provided in Table 3.2. The next section describes the setup used for preparing the solution.

3.4.2. Mixing and Refluxing Apparatus

The mixtures were heated under reflux in a refluxing unit. The purpose of heating under reflux is to accelerate the reaction, since the mixture is driven near to its boiling point (Gilbert and Martin, 2002). The volatile materials continuously evaporate from the flask and condense in the reflux condenser, where cooling water runs from bottom to top (see Figure 3.7a). For example, the boiling point of ethanol, which is the main compound for this system acting as solvent and ligand for the alkoxide, is 78°C. So a common temperature selected for refluxing was 60–70°C, depending on the nature of the system. Figure 3.7 shows both a schematic of a refluxing apparatus and the actual system that was initially used.
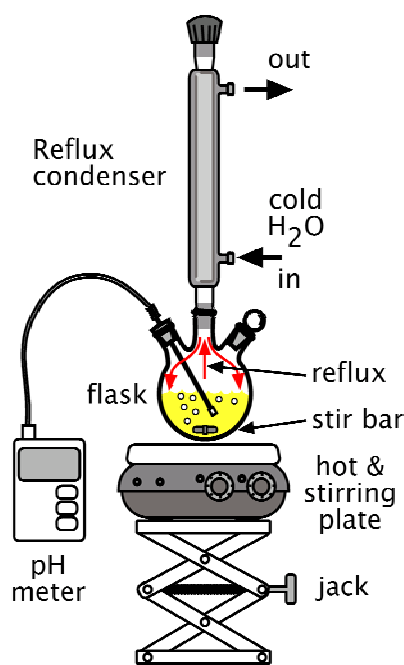
| (a) diagram of initial unit | (b) physical setup |

Figure 3.7. Refluxing apparatus for sol-gel preparation

Since TEOS and the rest of the sol-gel precursors used are highly reactive to water or a moisture-enriched environment, it was necessary to control the processing atmosphere with relative humidity levels between 30–40%. The refluxing unit was therefore modified to cope with this issue by sealing all the entries and exits, and by purging the system with high-purity nitrogen gas (grade 5.0, from Praxair), as described by (Shriver and Drezdzon, 1986). The modified refluxing unit is shown in Figure 3.8. A gas bubbler was coupled to the system exit to maintain a backpressure, while keeping the system sealed.

(a) diagram of refluxing unit   (b) physical setup
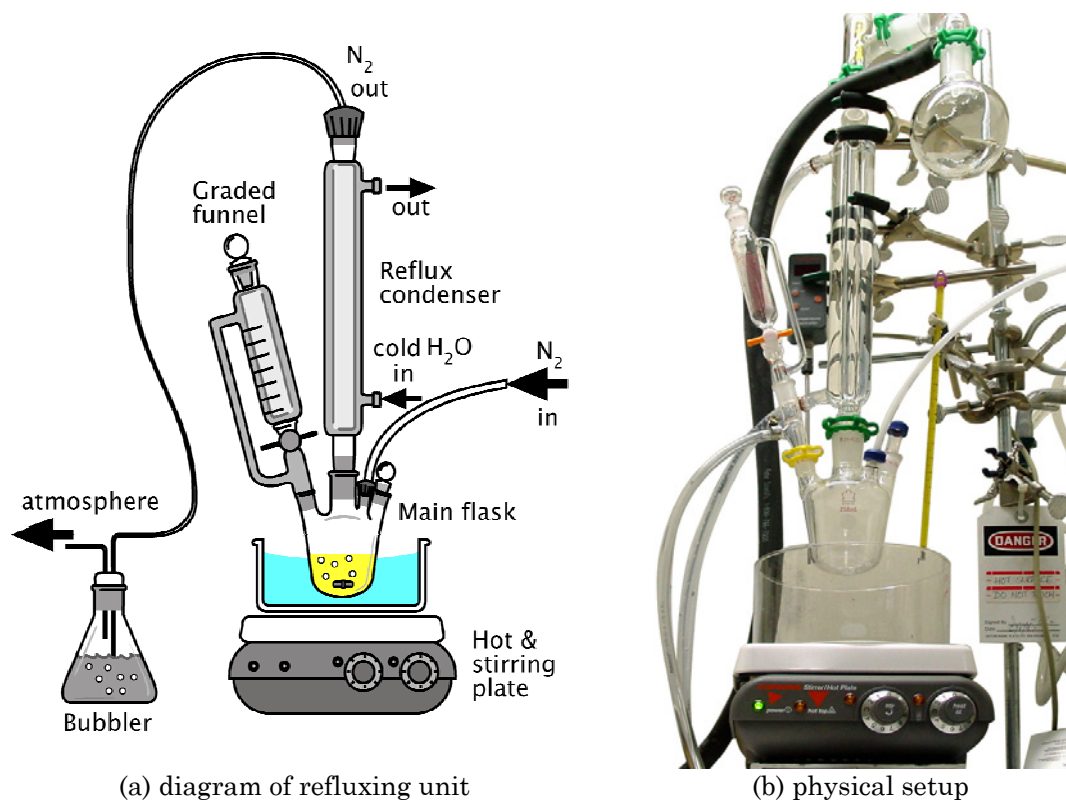
Figure 3.8. Modified refluxing apparatus

3.4.3. Analytical Techniques for Mixture Characterization

A series of techniques were used to characterize different properties of the solutions in the liquid state. The techniques are described below.

Measurement of pH

As mentioned in Section 3.2, the pH of a sol has a direct influence on the structure of the sol-gel. For this reason, a pH probe or electrode was used during mixing of the sol in order to monitor the pH value during the addition of the various chemicals and maintain it between 1 and 2 (see Figure 3.7). The electrode is connected to a digital meter, and is calibrated with buffer solutions prior to each use. The pH electrode was only used during the preliminary experimentation because inorganic residues accumulated on the tip of the probe, degrading the quality of the readouts after a few measurements. The main purpose of the probe was to determine the amount of catalyst (HCl) and the time when to add it to the mixture. Once this was determined, the probe was no longer used and the same molar ratio of catalyst to alkoxide was used for the rest of the experiments.

Viscosity Measurement

The viscosity of the sol-gel solution (sol) was measured using a calibrated Cannon-Frenske kinematic viscometer. This viscometer consists of a glass capillary tube, as seen in Figure 3.9. The measurements were performed according to the standard (ASTM-D445-01, 2001).

Figure 3.9. Cannon-Frenske kinematic viscometer

For each solution to be tested, a volume of 1 ml of sol was used. The measurements were repeated at least two times and the results averaged.

Nuclear Magnetic Resonance Spectroscopy

Nuclear magnetic resonance spectroscopy or NMR was employed to study the change in structure of sol-gel solutions. As recommended in the literature, ^{29}Si NMR spectra was measured with this technique (Brinker and Scherer, 1990). A very basic use of this technique was pursued, and it was only employed during the preliminary experimentation to help elucidate the reasons for a great variability of the solutions. Standard 507 PP tubes were used, filled generally up to 2".

Thermogravimetric Analysis

Thermogravimetric analysis or TGA was done with the use of a TGA7 Perkin Elmer analyzer, in order to measure the change in weight of the sol-gel with temperature. Solid samples were used for these tests, and were prepared by pouring a small volume of sol into a petri dish, then letting the sample dry at room temperature (~20°C) for approximately 10 days. After this period the dried flakes were crushed into a fine powder with a mortar.

The measurements were performed with a heating rate of 3°C/min, beginning at 20°C up to 1000°C with a flowing stream of nitrogen at 50 ml/min. Tests were only performed during preliminary experimentation.

3.4.4. Molar Fractions and Experimentation

Before any experimentation was done, a set of objectives was defined to help guide the process. The main objectives of this initial stage with sol-gel materials were defined as follows:

- Characterize the process, understanding the influence of the various parameters on the preparation and deposition of sol-gel materials.

- Analyze the samples through various experimental techniques, and identify which of these techniques would be more suitable for conducting a thorough process optimization.

- Achieve single-layer deposition of sol-gel films on Si and glass substrates.

Preliminary Experiments

As mentioned in Section 3.4.1, an initial series of mixtures were prepared based on molar fractions found in the literature, based mainly on (Sakka and Kamiya, 1982; Sakka, Kamiya *et al.*, 1984; Brinker and Scherer, 1990). The molar fractions are shown in Table 3.1 and depicted in the ternary diagram of Figure 3.5. The mixture preparation was conducted using the setup shown in Figure 3.7. As the organo-metallic precursor, TEOS was used as obtained from Gelest Inc. This was mixed with ethanol (used as solvent) and hydrolyzed with water. The catalyst for the hydrolysis and condensation reactions was HCl. A list of the chemicals and some properties is provided in Table 3.3. The mixture was prepared at atmospheric conditions and refluxed between 30 and 60 minutes at ~60°C. The mixtures were left generally between 24 h and 3 days to age prior to deposition. All of the final mixtures were filtered using 0.4 μm syringe filters.

Below is a brief discussion of the deposition and thermal processing of the sol-gel films for these preliminary tests. A detailed study on various factors involved in deposition and thermal processing are provided in Chapter 4.

For the deposition of the sol on the substrates a Headway Research

Table 3.3. List of reagents used for pure silica sol-gels

Name	Formula	Source	Purity (%)	FW (g/mol)	Density (g/cm^3)
Tetraethoxysilane (TEOS)	$Si(OC_2H_5)_4$	Aldrich, Gelest	99.999	208.33	0.9330
Ethyl alcohol (EtOH)	C_2H_5OH	Aldrich	9.98	34.0578	0.7893
De-ionized water	H_2O		NA	18.0152	0.9982
Hydrochloric acid, 70%vol	HCl	Aldrich	99.98	36.4606	1.1978

manual spin coater was initially used, and the experiments were conducted under atmospheric conditions. The substrate materials used were microscope slides and silicon wafers (100). The spin coating conditions (e.g., velocity profile and deposition method) were varied until appropriate parameters were found. A typical range is between 2,000 and 4,000 rpm.

After deposition, a set of samples was selected for heat treatment under various temperature conditions. The samples were placed in a tube furnace controlled by a digital controller for the heat treatment. The samples were inserted in a quartz tube. The tube furnace can operate under helium, oxygen or low vacuum atmospheres. The samples were heated for 1–3 h at 150°C, 200°C, and 400°C, with heating rates of ~4 and 6°C/min.

Following spin coating and in some cases heat treatment, the samples were characterized by the following techniques: scanning electron microscope (SEM) Hitachi S4000 to observe the topology of the surface, XPS PHI ESCA for elemental analysis, and atomic force microscopy (AFM) to measure the surface roughness. Samples were taken from the glass-forming liquids (or sol) to be analyzed by NMR (Bruker).

Figure 3.10 presents SEM images of sol-gel films from various mixtures of this preliminary experimentation. These images illustrate a chronological evolution of the results. They also provide evidence of how the combination of good control of the processing parameters and optimal molar ratios improved the uniformity and morphology of the films.

(a) Mixture #2

(b) Mixture #4

(c) Mixture #6

(d) Mixture #7

(e) Mixture #8
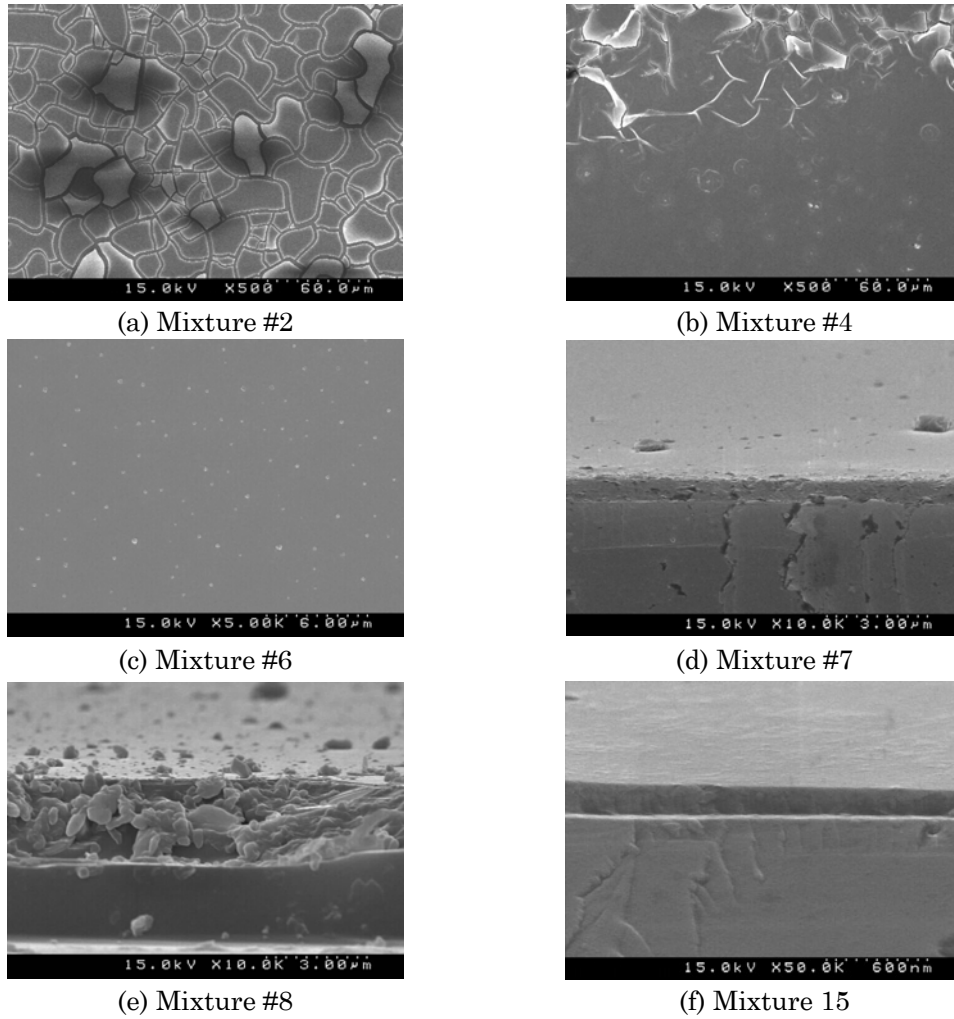
(f) Mixture 15

Figure 3.10. SEM pictures showing evolution of quality of films

Screening Experimental Design

After initial experimentation and as part of this preliminary set of experiments, a series of mixtures were prepared following what is known as *screening experimentation*. Referring to the ternary diagram of Figure 3.5, basically what the screening experimentation means is that a series of data points on this

Table 3.4. Data for screening experimental design

	Molar fractions (%)			Ratios		Kinematic Viscosity (cSt)	Density (g/cm^3)	Dynamic Viscosity (cP)
Mix	X_{TEOS}	X_{H2O}	X_{EtOH}	R_{wa}	R_{sa}			
7	19.60	21.00	59.40	1.07	3.03	2.826	0.928	2.622
15	18.00	18.00	64.00	1.00	3.56	2.082	0.931	1.939
16	18.00	22.00	60.00	1.22	3.33	2.250	0.951	2.140
17	22.00	22.00	54.00	1.00	2.45	2.028	0.937	1.900
18	18.00	28.00	54.00	1.56	3.00	3.107	0.956	2.970
19	10.90	55.70	32.80	5.11	3.01	4.921	0.980	4.821

diagram were chosen based on the results from the initial experiments. The purpose is to get a better feeling of the influence of the various parameters before a more specific design of experiments is pursued, which is described below. This type of experimentation is particularly useful when facing a new problem where there is little information and experience on the process and the outcome. This exercise was also beneficial for the design of the sol-gel preparation procedure depicted in Figure 3.6.

This second iteration involved measuring the density and kinematic viscosity of the solutions, while following a similar preparation procedure as that of the previous section. Table 3.4 presents the molar fractions of the various mixtures. This table also includes data for the density and the kinematic and dynamic viscosities, which were measured with the Cannon-Frenske viscometer of Figure 3.9. These results show the averaged data taken from two to three consecutive measurements. The data is plotted in the 3D graphs of Figure 3.11, which shows density and viscosity versus R_{wa} and R_{sa}.

Density and viscosity play crucial roles in the ability to deposit a sol-gel film by spin coating. This will become clearer in the following experiments. These two intermediate performance metrics, appear to be dependent on both

(a) density   (b) kinematic viscosity
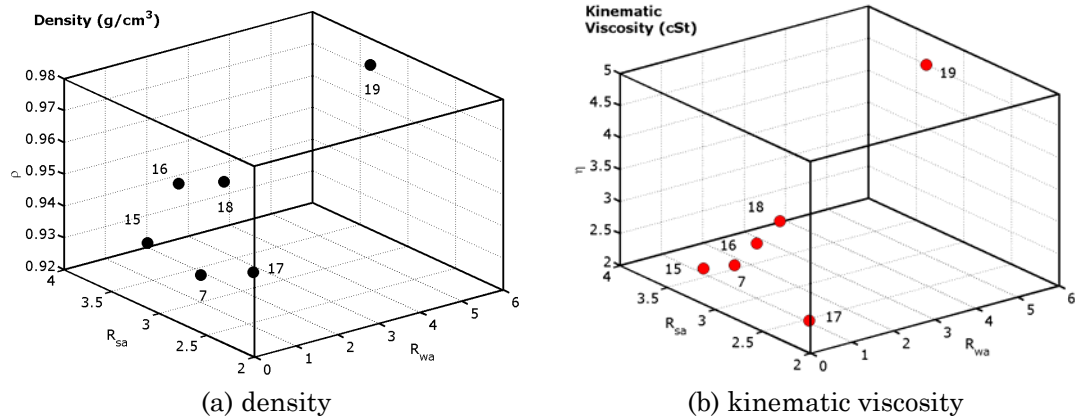
Figure 3.11. Data points for preliminary experiments

water-alkoxide ratio and solvent-alkoxide ratio. The extent of this dependence is explored in the following design of experiments. For this screening design it was enough to see if there was any appreciable dependence at all before pursuing a more thorough study. From the plots of Figure 3.11 it is difficult to distinguish whether the effects of R_{wa} and R_{sa} on density and viscosity are linear on non-linear. Certain dependence can be seen in these plots. The strength of this dependence will be characterized below.

Following are some important observations drawn from these experiments:

- During the mixing process while adding de-ionized water and HCl to the solution, some precipitation occurred, which lead to non-homogeneous solutions. The preparation of these solutions was done with a single-step process, where the alkoxide TEOS was added first, then diluted with EtOH, and finally hydrolyzed with water and HCl.

- The previous observation was particularly true for mixtures with high water content or high R_{wa} values. These solutions had a higher viscosity, as seen in Table 3.4.

- When attempting to replicate some of the mixtures of the previous experiments, in particular #7 from Table 3.4 (equivalent to #3 of Table 3.1), precipitation on the mixture was observed at times, as well as poor results on deposition by spin coating. The films exhibited a high degree of cracking and non homogeneous features.

After conducting these experiments and analyzing the NMR spectra, it was concluded that a full hydrolysis of the mixtures was not taking place. In addition to this, a high solvent content or high R_{sa} value increases the diffusion distance, which can reduce the opportunity of interaction between water and alkoxide molecules (Weisenbach, Zelinski *et al.*, 1991). Thus after some further literature search, it was decided that a single processing step did not produce consistent results for this particular inorganic sol-gel.

Design of Experiments #1

After the screening experiments, a more comprehensive design of experiments or DOE was developed in order to quantify the effects of R_{wa} and R_{sa} on the nature of the solutions. The preparation procedure is now modified into a two-step process. What this means is that an initial solution of TEOS diluted in EtOH is pre-hydrolyzed with certain target values for R_{wa} and R_{sa}, such as $R_{wa}=1$ and $R_{sa}=3$. Then, additional water and solvent are added to "drive" the molar

Table 3.5. Parameters for design of experiments – System#1

Type	Variable Name	Label	Low Level	Cero Level	High Level
Design (independent)	Water-alkoxide ratio, Rwa	x_1	1.5	2.0	5.0
	Solvent to alkoxide ratio, Rsa	x_2	3.0	–	4.0
Design (dependent)	Molar fraction of alkoxide	X_{TEOS}	0.1818	0.1667	0.1250
	Molar fraction of solvent	X_{ETOH}	0.5455	0.5000	0.3750
	Molar fraction of water	X_{H2O}	0.2727	0.3333	0.5000
	Volume of catalyst	V_{HCl}	20 µl	20 µl	20 µl
	Time to add catalyst		10 min	10 min	10 min
Noise	Refluxing temperature		60°C	60°C	60°C
	Mixing temperature		21°C	21°C	21°C
	Aging temperature		21°C	21°C	21°C
	Aging atmosphere		Dry air	Dry air	Dry air
	Aging time		24 hrs	24 hrs	24 hrs
	Drying humidity (RH%)		30%	30%	30%
Performance metrics	Density (g/cm^3)	y_1			
	Kinematic viscosity (cSt)	y_2			

concentration to a desired value or point in the ternary diagram. The resulting preparation procedure is shown in Figure 3.6, while the modified mixing unit is depicted in Figure 3.8.

As observed in Figure 3.3, there are a large number of parameters involved in preparation of sol-gels and their deposition. Therefore this DOE focused mainly on two things: (1) the effects of R_{wa} and R_{sa}, and (2) testing the two-step preparation procedure. Following the methodology proposed by (Box, Hunter *et al.*, 1978; Otto and Wood, 2001), a series of design parameters and performance metrics were selected and are summarized in Table 3.5. From this table two independent design parameters (x_1, x_2) can be observed: R_{wa} and R_{sa}, which affect dependent parameters such as the molar fractions of individual chemicals. A factorial design was selected, where (x_1, x_2) have 3 and 2 levels, respectively, thus lending to a total of $3^1 \times 2^1 = 6$ experiments. The performance

metrics chosen for this DOE were density, with units of g/cm^3, and kinematic viscosity, with units of centi-Stokes or cSt, represented by (y_1, y_2), respectively. The *noise* parameters remained constant.

A total of six mixtures were prepared, which are indicated in Table 3.6 and plotted in the ternary diagram of Figure 3.12. After mixing each solution individually following the two-step hydrolysis process of Figure 3.6, the films were spin coated on two types of substrates: Si wafers (100), and borosilicate glass slides. These were cleaned, prior to deposition by spin coating, following the procedure of Section 4.3.1. The spin coating was carried out at various spinning velocities for various duration times under N$_2$ and standard air using a single-wafer spin processor. The spin-coating profiles consisted in an acceleration step, deposition of 20 μl of filtered solution, acceleration to desired speed, and finally a dwell period for solvent evaporation. Typical deposition velocities ranged from 2000 to 4000 rpm, while the complete process time range was 40–60 sec.

Table 3.6. Data for DOE#1

	Molar fractions			Ratios		Kinematic Viscosity	Density	Easy to spin coat	n_{max}
Exp	X_{TEOS}	X_{H2O}	X_{EtOH}	R_{wa}	R_{sa}	(cSt)	(g/cm^3)	[1-5]	(rpm)
1	0.182	0.273	0.545	1.5	3.0	3.1072	0.956	2	
2	0.154	0.231	0.615	1.5	4.0	2.8943	0.946	4	4000
3	0.167	0.333	0.500	2.0	3.0	4.2101	0.962	3	
4	0.143	0.286	0.571	2.0	4.0	3.0398	0.945	3	4000
5	0.111	0.556	0.333	5.0	3.0	6.8166	0.975	5	2000
6	0.100	0.500	0.400	5.0	4.0	4.1385	0.951	5	4000
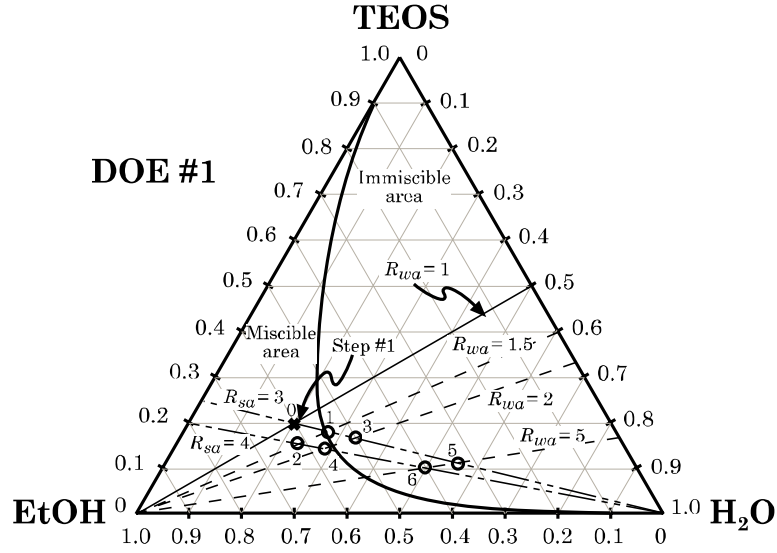
Figure 3.12. Ternary diagram indicating molar ratios for DOE#1

It is recommended that the mixtures are prepared in a random order to avoid any bias. After the experiments are conducted and the data is collected, phenomenological models that relate the performance metrics with the design parameters are assembled. For this particular DOE with $3^1 \times 2^1 = 6$ experiments, the models have the following mathematical expression:

$$\hat{y}_m(\bar{x}) = \beta_0 + \beta_1 x_1 + \beta_2 x_2 + \beta_{12} x_1 x_2 + \beta'_1 x_1^2 + \beta'_{12} x_1^2 x_2 \tag{3.20}$$

In Equation (3.20), $\hat{y}_m(\bar{x})$ corresponds to the performance metric to be approximated by the model, and is a function of the vector $\bar{x} = \{x_1, x_2\}$ of design parameters. The subscript m represents the type of metric y, either: ρ or η. The coefficients β_i are the unknowns.

The coefficients for the model are obtained with the following equation (Box, Hunter *et al.*, 1978):

$$\bar{\beta} = \left[\mathbf{X}^{\mathrm{T}}\mathbf{X}\right]^{-1}\mathbf{X}^{\mathrm{T}}\bar{y} \tag{3.21}$$

where $\bar{y}$ corresponds to the measured data for ρ or η, and $\mathbf{X}$ is an $j \times i$ matrix formed by the substitution of the design parameters x (j is the number of experiments and i the number of coefficients in Equation (3.20)).

After assembling the matrix $\mathbf{X}$, substituting the values for $\bar{y}$ from Table 3.6, and determining the coefficients β_i with Equation (3.21), the following models were obtained for the kinematic viscosity and density, respectively:

$$\hat{y}_{\eta} = -12.957 + 13.524x_1 + 3.870x_2 - 3.327x_1x_2 - 1.592x_1^2 + 0.404x_1^2x_2 \tag{3.22}$$

$$\hat{y}_{\rho} = 0.9084 + 0.062x_1 + 0.011x_2 - 0.017x_1x_2 - 0.00686x_1^2 + 0.002x_1^2x_2 \tag{3.23}$$

Figure 3.13 shows 3-D plots of the models from Equations (3.22) and (3.23), as well as the actual data. As can be seen from this figure, the models accurately fit the experimental data. The error for $\hat{y}_{\rho} : (-0.04, +0.21)\%$, while for $\hat{y}_{\eta} : (-0.17, +1.56)\%$, which indicate a good fit. Also from this figure a non-linear dependence of the kinematic viscosity on R_{wa} (x_1) and R_{sa} (x_2) is appreciable.

(a) Density, $\hat{y}_{\rho}(x_1, x_2)$ (b) Kinematic viscosity, $\hat{y}_{\eta}(x_1, x_2)$
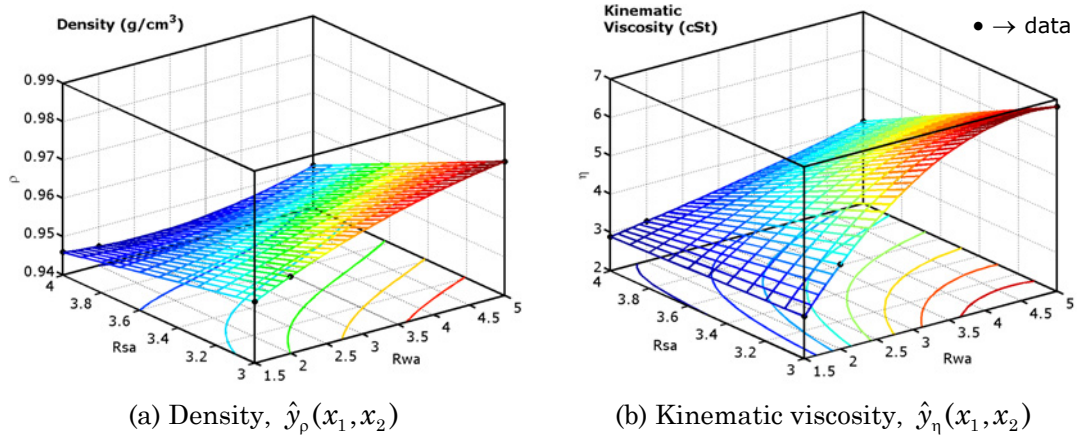
Figure 3.13. Influence of R_{wa} and R_{sa} on density and viscosity

On the other hand, a more linear behavior is observed for the density. This is observed by the curves projected on the R_{wa} and R_{sa} plane.

The following observations can be drawn from this study:

- The water-alkoxide ratio R_{wa} has a greater influence on the viscosity of the sol than R_{sa}.

- A sol with a higher viscosity is easier to deposit by spin coating.

- Sol-gel films from mixtures with high R_{wa} values, typically $R_{wa} \geq 3$, present a high degree of cracking during thermal treatment.

- The morphology of the spin-coated films is influenced by both the molar composition of the solution and the spin coating parameters. Solutions with high branching and mid- to high viscosity (~2.4 cP) produced smooth surfaces (Ra~10nm). On the other hand, less branched solutions produced cloudy and non homogeneous films, with a higher tendency to crack.

- The modified two-step preparation process proposed in Figure 3.6 successfully allowed to produce repeatable results, by pre-hydrolyzing the Si alkoxide (TEOS) with low water content ($R_{wa}=1$) and moderate solvent concentration ($R_{wa}=3$).

Once a repeatable process was developed for the synthesis of inorganic silicate sol-gels, the next step was to explore the addition of dopants to increase the index of refraction, which is required for waveguiding. The next section explores the synthesis of titanium doped sol-gels.

3.5. System 2: Hybrid Ti-Doped Silicate Sol-Gel

Chemical or physical methods can be used to achieve the index change, between the core and cladding, necessary for waveguiding, as explained in Chapter 2. A popular and effective way for the chemical route is to incorporate dopants into the silicate matrix. This was part of the approach followed in this research, and was pursued by exploring a second sol-gel system that incorporates the dopant titanium as TiO_2 (titania). The SiO_2-TiO_2 system was a natural choice to begin with due to the large amount of research published on the subject. Preliminary experiments were performed with a purely inorganic Ti-doped silicate sol-gel. The results and processing difficulties encountered with this approach were similar to what is reported in the literature. From the knowledge and experience gained in System #1, it was thought necessary to look for ways to reduce the cracking phenomenon of the films. Through the literature and discussions with our industrial partner, it was learned that the incorporation of organic moieties into the system helped reduce this problem. So the addition of the index rising dopant Ti, in addition to a hybrid organic-inorganic approach was the next subject of this research in terms of material preparation.

Initial experimentation with the inorganic silica-titania (SiO_2–TiO_2) sol-gel system was done based on the results reported in (Guglielmi, Martucci *et al.*, 1998). The work of Gugliemi *et al.* reports on a round robin study that compares various synthesis strategies and highlights the differences that arise when preparing the sol-gel in various locations. Of particular interest were three different preparation procedures for silica-titania sol-gel films. All three systems were prepared, and the one that gave the best results is dubbed as

INESC90S10T. The synthesis approach for this system is based on a pre-hydrolysis step of the slower reacting alkoxide TEOS, followed by the addition of a highly diluted solution of the titanium alkoxide in solvent (e.g. EtOH), therefore preventing precipitation of species. The system also uses a small amount of the Ti alkoxide, so the theoretical molar concentration is 10% for TiO_2 and 90% for SiO_2. The molar ratios of this system are similar to the ones proposed by (Almeida, Vasconcelos $et\ al.$, 1994), which was also tested, but gave poor reproducibility, attributed to the single hydrolysis step.

Therefore, noting the similarities between the approach proposed by (Guglielmi, Martucci $et\ al.$, 1998) and the resulting two-step hydrolysis process described in the previous section, it was decided to incorporate this strategy in the development of a stable system. These two processing approaches were merged with the concept of hybrid organic-inorganic sol-gels, in order to increase the single-layer thickness and reduce the propensity for cracking, based on the work of (Seco, Goncalves $et\ al.$, 2000).

An important aspect that arises particularly in the titania doped systems, is the competition between densification and crystallization as reported by (Keddie and Giannelis, 1990; Keddie, Braun $et\ al.$, 1994). Chemical composition and thermal treatment greatly affect the final structure and propensity of the film to crack. From a chemical standpoint, having a theoretical concentration higher than 20% presents many problems in this respect, especially when thermally treating the film to reduce the solvent concentration and porosity. The thermal processing is addressed in the next chapter.

Over the past 10 years or so, there has been a growing interest on hybrid organic-inorganic sol-gel systems (Gvishi, Narang $et\ al.$, 1997; Wright and

Sommerdijk, 2001) for a diverse range of applications, including photonics. One of the popular approaches is the use of organically-modified precursors. These precursors contain non-hydrolizable groups that achieve a reduction of connectivity in the network, which in turn increases the compliance, thus reducing cracking problems during the shrinkage stage of the sol-gel process (Brusatin, Guglielmi *et al.*, 1997; Seco, Goncalves *et al.*, 2000). The Fraunhofer Institut from Germany has developed a patented set of materials named Ormocers®, which combine inorganic silicon alkoxides with organic functionalities covalently bonded in a two-step process activated thermally or by UV radiation (Buestrich, Kahlenberg *et al.*, 2001; ORMOCER, 2003). Typical non-hydrolyzable groups have the form of Si–R, where R is an alkyl radical (Seco, Goncalves *et al.*, 2000).

Some inherent disadvantages of these hybrid compounds include high carbon content and high OH content, therefore resulting in larger optical losses due to absorption. There is ongoing research in trying to attenuate this problem by chemical routes (Atkins, Krolikowska *et al.*, 2000; Atkins, Charters *et al.*, 2001; Atkins and Charters, 2003). Yet, as reported by (Brusatin, Guglielmi *et al.*, 1997), in some systems the thermal processing at high temperatures (>500°C) mostly eliminates the organic components, leading to a system quite similar to its inorganic counterpart. This was the compelling reason to continue the research in this direction.

The following section describes the preparation procedure that was used for the second part of the material preparation portion of the research.

3.5.1. Preparation Procedure for Ti-doped Hybrid Silicate Sol-Gel

The three main compounds for this system consist of the inorganic silicate portion, provided by the use of TEOS, an organic portion, by the use of methyltriethoxysilane (MTES), and the Ti doping portion, by means of the alkoxide titanium isopropoxide (TPOT). Ethanol is used as the solvent.

The calculations of molar ratios and volumes required for preparation of the sol-gel are summarized in the following steps:

Step 1: Define the molar ratios X_{TEOS}, X_{MTES}, X_{TPOT}, X_{EtOH}, and X_{H2O}.

Step 2: Define the desired total mass m_T of sol to prepare.

Step 3: Calculate the total number of moles from the following equation:

$$NM_T = m_T \cdot \left[\frac{1}{X_A \cdot FW_A + X_B \cdot FW_B + X_C \cdot FW_C + X_D \cdot FW_D + X_E \cdot FW_E} \right] \quad (3.24)$$

where $A \rightarrow$ TEOS, $B \rightarrow$ MTES, $C \rightarrow$ TPOT, $D \rightarrow$ EtOH, and $E \rightarrow$ acidified H_2O.

Step 4: Calculate the number of moles for each compound with the following equation:

$$NM_{[\cdot]} = NM_T \cdot X_{[\cdot]} \quad (3.25)$$

Step 5: Determine the mass of each individual compound, with:

$$m_{[\cdot]} = NM_{[\cdot]} \cdot FW_{[\cdot]} = \left[NM_T \cdot X_{[\cdot]} \right] \cdot FW_{[\cdot]} \quad (3.26)$$

Step 6: Calculate the individual volumes:

$$V_{[\cdot]} = \frac{m_{[\cdot]}}{\rho_{[\cdot]}} \quad (3.27)$$

Step 7: Given a desired molarity N, calculate the volume of HCl:

$$V_{HCl} = \frac{N\left(\frac{1mol}{1eq}\right)FW_{HCl} \cdot 10^{-3}\frac{cm^3}{L}}{\rho_{HCl} - N\left(\frac{1mol}{1eq}\right)FW_{HCl} \cdot 10^{-3}\frac{cm^3}{L}} \cdot V_{H_2O} \qquad (3.28)$$

where V_{HCl} (cm³), V_{H2O} (cm³), N (eq/L), FW_{HCl} (g/mol), and ρ (g/cm³).

In some cases it is convenient to define the molar ratios of only the main alkoxide precursors. Most of the literature reviewed reports it in this way. If this is the case, the following formulas can be applied to find the molar ratios of the solvent and water, as well as the respective volumes.

Given the partial ratios X'_{TEOS}, X'_{MTES}, and X'_{TPOT},

$$X'_{TEOS} + X'_{MTES} + X'_{TPOT} = 1 \qquad (3.29)$$

and the overall alkoxide-solvent ratio, R_{sa}:

$$R_{sa} = \frac{NM_{EtOH}}{NM_{T1}} \qquad (3.30)$$

where the total number of moles of combined alkoxides is,

$$NM_{T1} = NM_{TEOS} + NM_{MTES} + NM_{TPOT} \qquad (3.31)$$

The water-alkoxide ratio R_{wa} is also another design parameter,

$$R_{wa} = \frac{NM_{H_2O}}{NM_{T1}} \qquad (3.32)$$

After some algebraic manipulation, which is not provided for the sake of briefness, the individual molar ratios for each reagent can be determined given: (1) partial ratios between alkoxides (three variables), (2) solvent-alkoxide ratio (one variable), and (3) water-alkoxide ratio (one variable). The following equations can be used,

$$X_{TEOS} = \frac{X'_{TEOS}}{R_{sa} + R_{wa} + 1} \tag{3.33}$$

$$X_{MTES} = \frac{X'_{MTES}}{R_{sa} + R_{wa} + 1} \tag{3.34}$$

$$X_{TPOT} = \frac{1 - \left(X'_{TEOS} + X'_{MTES}\right)}{R_{sa} + R_{wa} + 1} \tag{3.35}$$

$$X_{EtOH} = \frac{R_{sa}}{R_{sa} + R_{wa} + 1} \tag{3.36}$$

$$X_{H_2O} = \frac{R_{wa}}{R_{sa} + R_{wa} + 1} \tag{3.37}$$

These equations can be used now with the equations outlined in the procedure above to find the individual volumes to add to the mixture.

Once all the volumes are known, one can proceed to prepare the sol. Figure 3.14 presents a flow diagram of the process that was used for this research, and is a result of combining the process of System #1 with the works of (Guglielmi, Martucci *et al.*, 1998; Seco, Goncalves *et al.*, 2000). This process avoids the use of chelating agents (e.g., acetylacetone) to reduce the hydrolysis rate of TPOT, by high speed mechanical stirring and large dilution in EtOH prior to mixing with the pre-hydrolyzed TEOS and MTES portions.

A Mix TEOS +1/2 EtOH	- T = 293 K (room temp.) - t = 10-15 min
B Mix H_2O + 1/2 EtOH + HCl	- T = 293 K (room temp.) - t = 10 min
D Mix MTES + EtOH	- T = 293 K (room temp.) - t = 10 min
C Slowly drip (B) into (A) Stir vigorously	- T = 293 K (room temp.) - t = 2 hrs *optional reflux at T=338 K
E Slowly drip 0.1N HCl into (D) Stir vigorously	- T = 293 K (room temp.) - t = 2 hrs
F Slowly mix (E) into (C) Stir for 20 min	
G Mix TPOT + EtOH Stir vigorously	- T = 293 K (room temp.) - t = 15 min
H Slowly drip (G) into (F) Stir vigorously	- T = 293 K (room temp.) - t = 15-20 min
I Add remaining H_2O dropwise Stir vigorously	- T = 293 K (room temp.) - t = 2 hrs - Closed flask - Avoid solvent evaporation
J Filter and store in amber bottle	- Filters: 0.1 or 0.2 μm - Filter type: PTFE or solvent resistant
K Age for 24 hrs before deposition	– T = 293 K (room temp) – t = 24 hr – Atm: air – RH < 35%

Hybrid sol-gel
Dopant: Ti
Precursors:
 TEOS, MTES,
TPOT

Figure 3.14. Preparation procedure for hybrid sol-gel doped with Ti

3.5.2. Mixing Apparatus

As mentioned in Section 3.4.2, the alkoxide precursors used are highly reactive to water and moisture from the atmosphere. TPOT is even more reactive and volatile than TEOS and MTES. For this reason all the mixing was done under a controlled atmosphere with low humidity (30<RH<40%) and a flowing inert gas: N_2. The setup used for the pre-hydrolysis of TEOS is schematized in Figure 3.15a, and is the same of Figure 3.8. TEOS was pre-hydrolyzed and refluxed using this setup, as indicated by steps (A) through (C) in Figure 3.15. After reflux it was allowed to cool down to room temperature (~20°C), before proceeding with the process. Solution (D) was hydrolyzed in a separate flask in a similar manner, before being added drop by drop to the main flask containing the hydrolyzed TEOS solution (C), by means of the graded funnel shown in Figure 3.15a. This step took a few minutes, depending on the amount of sol to be prepared, and the flowrate of the nitrogen was reduced to a minimal. After this, the flowrate was slightly increased, the graded funnel removed for cleaning, and the main flask sealed, followed by reducing the gas flow rate to avoid evaporation.

Hydrolysis of MTES, corresponding to solutions (D) and (E) of Figure 3.14, was performed in a separate setup, as shown in Figure 3.15b. All the mixing was done at room temperature and in parallel to the hydrolysis of TEOS described above. No refluxing was done for this solution.

(a) setup for hydrolysis of TEOS

(b) setup for hydrolysis of MTES

(c) setup for dilution of TPOT

(d) final mixing setup
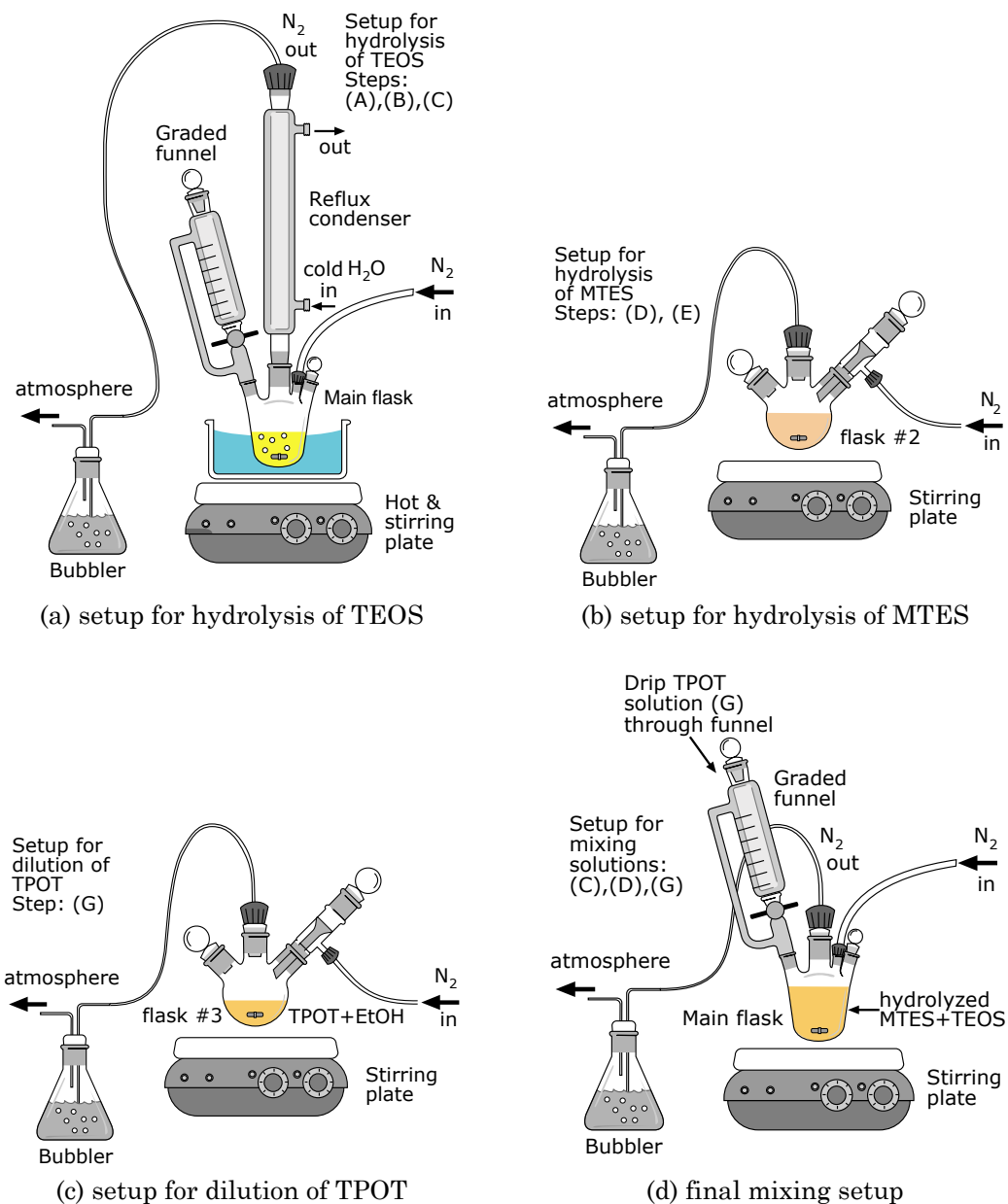
Figure 3.15. Configurations for synthesis of hybrid SiO_2-TiO_2 sol-gel

Solution (G) was also prepared in a separate and sealed flask, diluting TPOT with EtOH. EtOH was added first to a flask filled with flowing nitrogen

at a low flow rate, just enough to keep external air from entering the flask and avoiding evaporation. Then TPOT was added while stirring vigorously at room temperature. An illustration of the setup is shown in Figure 3.15c. After diluting TPOT in EtOH, solution (G) was slowly added to the pre-hydrolyzed mixture (E) dripping it through the graded funnel, as seen in Figure 3.15d. In a similar way, the final portion of water was added to reach the desired water-alkoxide ratio. The solution was mixed for 2 hours at room temperature, under nitrogen with a very low flow rate. The process continued as presented in Figure 3.14.

3.5.3. Experimentation with various molar ratios

The development of the preparation procedure described in the previous section was based both on the experience gained through the synthesis of System #1 (Section 3.4) and some preliminary experiments with the Ti-doped system. In a similar way as was done for System #1, the initial molar fractions were obtained from the literature. These were later modified based on experimentation. Table 3.7 presents a list of the chemicals used for the synthesis of this sol-gel system. The table includes the formula, formula or molecular weight, the manufacturer, purity level, and the density of each chemical. These properties were used to calculate the molar fractions using the formulas presented in Section 3.5.1.

Table 3.7. List of reagents used for hybrid Ti-doped silica sol-gels

Name	Formula	Source	Purity (%)	FW (g/mol)	Density (g/cm^3)
Tetraethoxysilane (TEOS) CAS: 78-10-4	$Si(OC_2H_5)_4$	Aldrich	99.999	208.33	0.9340
Methyltriethoxysilane (MTES) CAS: 2031-67-6	$C_7H_{18}O_3Si$	Aldrich	99.0	178.30	0.8950
Titanium IV-propoxide (TPOT) CAS: 3087-37-4	$C_{12}H_{28}O_4Ti$	Aldrich	98.0	284.26	1.0330
Ethyl alcohol (EtOH)	C_2H_5OH	Aldrich	9.98	34.0578	0.7893
De-ionized water	H_2O		NA	18.0152	0.9982
Hydrochloric acid, 70%vol	HCl	Aldrich	99.98	36.4606	1.1978

The molar fractions, water-alkoxide ratio R_{wa}, solvent-alkoxide ratio R_{sa}, normality for the catalyst HCl, and the design parameters (a,b,c,d,e), of the various mixtures that were prepared are presented in Table 3.8.

Table 3.8. Molar fractions for Ti-doped hybrid silicate sol-gel

	Parameters							Molar fraction (%)					Ratios	
	TEOS	MTES	TPOT	EtOH	H$_2$O	N		TEOS	MTES	TPOT	H$_2$O	EtOH	R$_{wa}$	R$_{sa}$
Exp	a	b	c	d	e	Init.	Fin.							
1	0.4	0.4	0.2	8	4	0.1	0.1	3.08	3.08	1.54	30.77	61.54	10.0	20.0
2	0.45	0.45	0.1	8	4	0.1	0.1	3.46	3.46	0.77	30.77	61.54	8.9	17.8
3	0.45	0.45	0.1	8	4	0.1	0.1	3.46	3.46	0.77	30.77	61.54	8.9	17.8
4	0.435	0.435	0.13	8	4	0.1	0.1	3.35	3.35	1.00	30.77	61.54	9.2	18.4
5	0.45	0.45	0.1	8	4	0.1	0.1	3.08	3.08	1.54	30.77	61.54	10.0	20.0
6	0.4	0.4	0.2	6	4	0.1	0.1	3.08	3.08	1.54	30.77	61.54	10.0	20.0
7	0.4	0.4	0.2	8	3	0.1	0.1	3.08	3.08	1.54	30.77	61.54	10.0	20.0
8	0.4	0.4	0.2	8	3	0.25	0.1	3.08	3.08	1.54	30.77	61.54	10.0	20.0
9	0.4	0.4	0.2	8	3	0.5	0.2	3.08	3.08	1.54	30.77	61.54	10.0	20.0

Observations

The list of mixtures of Table 3.8 was developed after preliminary experiments based on the molar fractions for purely inorganic sol-gels reported by (Syms and Holmes, 1994; Brusatin, Guglielmi *et al.*, 1997; Du and Almeida, 1997; Guglielmi, Martucci *et al.*, 1998). These initial experiments did not include the organic alkoxides, such as MTES. Precipitation of species during mixing, cracking of films during thermal processing, and non-homogeneous or "cloudy" films were frequently observed for these purely inorganic Ti-doped sol-gels. After this experience and in search for a sol-gel system that would avoid these difficulties, some experimentation was done based on the work of (Que, Sun *et al.*, 2001; Que, Zhou *et al.*, 2001). In their work they propose the use of an organically-modified silicon precursor (γ-glycidoxypropyltrimethoxysilane, GLYMO), in combination with TPOT as the titanium source, TEOS and ethanol, to produce a hybrid sol-gel suitable for low temperature applications. In addition to these chemicals, Que *et al.* use acetylacetone (acacH) as a chelating agent that reduces the hydrolysis rate of TPOT by steric hindrance. The use of an additional organic sources leads to films with high OH content, which as mentioned in Chapter 2 are a major source of optical loss.

The sol-gel mixtures following the process and molar ratios proposed by Que *et al.*, led to the synthesis of homogeneous mixtures, which in turn were able to be successfully spin-coated onto Si and quartz wafers. The films had good homogeneity and high refractive indexes in the order of 1.56 to 1.62, and thicknesses between 1 and 2 μm for a single layer. On the other hand, the quality of the surface was rather poor, had a wavy aspect, and remained mostly "tacky" or sticky even after thermal treatment. This led to the search for a

different type of sol-gel system that would avoid these difficulties as well, and this is the reason why the system of Seco *et al.* was selected.

After including MTES and modifying the preparation procedure based on (Seco, Goncalves *et al.*, 2000) more homogeneous solutions were obtained. This in turn resulted in films with fewer tendencies to crack; yet, the concentration of Ti alkoxide still played an important factor in cracking. Based on the literature and preliminary experiments, it was decided that the molar fraction of TPOT would be kept between 10 to 20%. This is shown in Table 3.8 for parameter *c*. This range assures an increase of the refractive index sufficient to allow two or three modes to be coupled in a film with a thickness of a few microns (e.g., 2 to 3 µm). For example, a single mode waveguide operating at a wavelength between 800 to 1600 nm, with a characteristic length of 2 to 5 µm, requires a core-cladding index difference of only 0.003 to 0.010 (Hunsperger, 2002).

Several factors come into play when selecting the appropriate molar fractions to produce this Ti-doped hybrid sol-gel system. Some of the most important factors include the R_{wa} and R_{sa} for pre-hydrolysis of both TEOS and MTES, the proportion of Ti species (molar fraction of TPOT) to the Si alkoxides (TEOS and MTES), the final water-alkoxide and solvent-alkoxide ratios, and the amount of catalyst HCl (normality) to begin the reactions. These factors are represented by the design parameters (*a,b,c,d,e*), the water-alkoxide ratio R_{wa}, solvent-alkoxide ratio R_{sa}, and normality N for the catalyst HCl. Some of these are dependent on each other, but still that means having six design parameters, in addition to process parameters such as refluxing temperature (if needed), mixing time, and the way the solutions are mixed together (e.g., drop by drop or a steady flow of liquid). This can become a rather complex problem involving

many experiments. So based on the experience from System #1 (Section 3.4), and on experimentation using the parameters and fractions suggested in Table 3.8, it was found that mixture #5 from this table produced consistent and reproducible results. Therefore the subsequent experimentation of film deposition, thermal treatment, and laser processing, for this particular system, was conducted with solutions based on mixture #5. This is described in subsequent chapters.

The following section describes the synthesis of a different hybrid sol-gel system. This can be seen as a third iteration on the Spiral and Stage-gate model.

3.6. System 3: Hybrid Photosensitive Doped Sol-Gels

Hybrid organic-inorganic sol-gels have the advantage of needing moderate processing temperatures. An additional feature that can be incorporated to certain types of these sol-gels is their ability to be polymerized by ultraviolet radiation, in a similar way as photo-polymers used in the semiconductor industry (e.g., photoresists). This makes hybrid sol-gels particularly attractive to be integrated with semiconductor-type processing techniques, such as photolithography (Najafi, Li *et al.*, 1995). Over the past years there has been an increasing interest in the sol-gel and photonics communities, to develop novel materials and processing technologies that incorporate these materials. Notable is the work of (Fardad, Andrews *et al.*, 1997), proposing a few-step novel sol-gel fabrication process for single- and multi-mode waveguides by means of photo-sensitive sol-

gel materials. This process is based on dip coating of the sol-gel film, followed by UV radiation exposure through a mask, and a development step to dissolve the unexposed regions. Several important works have followed, exploring a similar direction but with different doping materials and photoinitiators (Fardad, Touam *et al.*, 1997; Fardad, Andrews *et al.*, 1998; Andrews, Zhang *et al.*, 1999; Fardad and Fallahi, 1999; Atkins, Charters *et al.*, 2001; Fardad, Mishechkin *et al.*, 2001; Fallahi, Bedford *et al.*, 2002; Atkins and Charters, 2003; Blanc, Pelissier *et al.*, 2003).

As introduced in Section 3.3, the two sol-gel systems described in the previous sections contemplate only photothermal activation to increase the density, therefore increasing the index of refraction to define the light propagation path. Due to the difficulty of achieving thick sol-gel films, in combination to the small operating window for laser photo-thermal processing, a different route was explored. This route consisted in employing the sol-gel synthesis proposed by (Fardad, Andrews *et al.*, 1997), and using a laser direct-write processing approach to photopolymerize the sol-gel film.

These organically modified silicate hybrid systems are based on methacrylate and silicate networks photopolymerizable by photon induced free-radical polymerization. The photon activated polymerization process of acrylate monomers by crosslinking is well documented in the literature (Fouassier, 1995; Decker, 2002). In the different works of Fardad *et al.* no insight into the polymerization mechanisms of hybrid sol-gels was documented. Only recently (Park, Jung *et al.*, 2001) have provided a brief description of the photochemical process undergone by the photoinitiator only, by means of studying the infrared spectra using FTIR techniques. On the other hand, more updated and thorough

107

evidence was presented by (Soppera and Croutxe-Barghorn, 2003; Soppera and Croutxe-Barghorn, 2003), using similar FTIR techniques in addition to ^{29}Si-NMR. The reason why it is important to understand the mechanisms that occur during the photopolymerization process in the context of this research, is because the design parameters involved in such process play a key role in the successful manufacturing by direct-write of photosensitive hybrid sol-gel waveguides. For example, the hydrolysis and condensation of the inorganic species is directly influenced by the water-alkoxide ratio, which in turn affects the mobility of polymerizable functions (organic part) (Soppera and Croutxe-Barghorn, 2003). Therefore this mobility or lack of it, has an impact on the degree of polymerization, and subsequently affects the resulting mechanical, optical and chemical properties.

A brief introduction to the polymerization and photo-induced polymerization processes is provided below.

Photopolymerization: Basics

In simple terms, the process of linking small molecules, such as monomers, together to form larger molecules is known as polymerization (Jacobs, 1992). Monomers, oligomers or prepolymers can polymerize and crosslink when exposed to radiation (Fouassier, 1995). Different types of polymerization schemes exist depending on the type of polymer. Radical chain polymerization of vinyl monomers by UV laser radiation is a popular method in the Rapid Prototyping industry, for example in Stereolithography (SLA) (Jacobs, 1992).

Vinyl polymers are made from vinyl monomers, which are small molecules containing a carbon-carbon double bond. Acrylates and methacrylates are subsets of the vinyl family with a high degree of reactivity due to the functional groups attached to the C$=$C bond, which is easily attacked by free radicals. The free radicals act as catalysts, and are generated either thermally or photochemically, for example by photoinitiators which are good sources of free radicals. A popular hybrid sol-gel precursor is methacryloxypropyltrimethoxy-silane or MAPTMS, which consists of organic (methacrylate functionality) and inorganic (trimethoxysilane) parts.

The free radical polymerization process is characterized by three main phases: (1) initiation, (2) propagation, and (3) termination.

Initiation is characterized by a photochemical process, where free radicals are generated from the photoinitiator. Upon absorbance of light, the photoinitiator undergoes an excited-state process to form the reactive species (e.g., free radicals or R•) (Fouassier, 1995). Some of the most important characteristics of a good photoinitiator are a high absorbance at the particular wavelength of interest, and generated species with a high quantum yield. The nature of the photoinitiator also plays in important role in the final physicochemical properties of the film, as will be shown later.

Upon light exposure by photons with energy of $h\upsilon$, the radicals generated by the photoinitiator react with the monomers (M), and initiate a chain reaction, as depicted by the following equations (Fouassier, 1995):

$$I + h\upsilon \xrightarrow{k_d} 2R\bullet \tag{3.38}$$

$$R\bullet + M_1 \xrightarrow{k_i} M_1\bullet \tag{3.39}$$

where k_d and k_i are the rate constants for the initiator and initiation, respectively, h is Plank's constant, v is the frequency of the photon, and M_1 is the first monomer molecule.

Propagation is characterized by a chain reaction and monomer unit addition, which causes an increase in the molecular weight. This step occurs very rapidly, and is described by the next equation:

$$M_n \bullet + M \xrightarrow{k_p} M_{n+1} \bullet \tag{3.40}$$

where k_p is the propagation rate constant.

As the polymer chains continue to grow, less reactive species are available, thus leading to termination. Two common termination modes are by coupling or disproportionation, and can be expressed by

$$M_n \bullet + M_m \bullet \xrightarrow{k_{tc}} M_{n+m} \tag{3.41}$$

$$M_n \bullet + M_m \bullet \xrightarrow{k_{td}} M_n + M_m \tag{3.42}$$
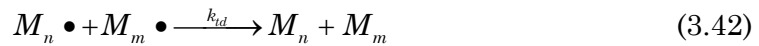
where k_{tc} and k_{td} are the termination rate constants by coupling and disproportionation, respectively.

Although this three reaction process seems like a simple scheme, (Soppera and Croutxe-Barghorn, 2003) have shown it to be useful in describing a big picture of the complex process of polymerization occurring during irradiation of the hybrid sol-gel. The above equations, together with the kinetic equations associated to them, will be further discussed in Chapter 5 in reference to laser photopolymerization and the dimensional accuracy.

Having presented an introduction to photopolymerizable sol-gels and a brief description of the mechanisms involved during this process, the next section presents the procedure used to prepare these sol-gels. Two sol-gel systems were

prepared containing Zirconium and Aluminum as doping or refractive index modifier agents.

3.6.1. Preparation Procedure for Hybrid Sol-Gel Doped with Zr

The organic-inorganic silicate network for the two photo-activated sol-gel systems was provided by the use of methacryloxy-propyltrimethoxysilane (MPTMS or MAPTMS). This first system used Zr as refractive index modifier. The Zr precursor employed was Zirconium(IV)-propoxide (ZPO). Since ZPO is highly reactive, methacrylic acid (MAA) was used as a chelating agent to help reduce the hydrolysis rate of ZPO, as suggested by (Coudray, Chisham *et al.*, 1997; Fardad, Andrews *et al.*, 1997; Saravanamuttu, Du *et al.*, 1998). MAA can also be polymerized due to its methacryl function and C$=$C bond. The photoinitiator that was selected for this first system was 1-hydroxycyclohexyl-1-phenylketone (Irgacure 184 or HCPK, by Ciba).

Before describing the preparation procedure, a series of suggested calculation steps are provided to determine the molar ratios and volumes required for preparation of the sol mixture. A convenient way to approach this system is to define the following design parameters.

Design Parameters:

(1) Set of final molar ratios for MPTMS, ZPO, and MAA, defined as: X_{MPTMS}, X_{TZP}, and X_{MAA}, respectively; where $0 \leq X_{[\cdot]} \leq 1$.

111

(2) Water-MPTMS ratio for initial pre-hydrolysis step: R_{wa}'. This relationship can also be expressed in terms of *equivalents*; for example: 0.75 *eq.* of 0.05M HCl.

(3) Molarity *M* or normality *N*, to react in the first pre-hydrolysis step. In this case the catalyst of choice was HCl.

(4) Final H_2O-alkoxide ratio: R_{wa} (this includes MPTMS and ZPO).

(5) Amount of photoinitiator expressed as weight percentage of the total solution: *wt*%. This can also be defined as concentration of photoinitiator [PI], usually in mili-mol/liter or m-M.

Once these design parameters have been specified, the following set of formulas can be used to calculate the volume and mass of reagents required for the preparation of the sol. The calculations are provided in a series of recommended steps, which can be easily programmed into a spreadsheet.

Step 1: Define the desired <u>final</u> molar ratio of MPTMS, ZPO, and MAA expressed either as:

$$\text{MPTMS} : \text{ZPO} : \text{MAA} \Rightarrow p : q : r \tag{3.43}$$

or with X_{MPTMS}, X_{ZPO}, and X_{MAA}, which must satisfy (where $0 \le X_{[\cdot]} \le 1$):

$$X_{MPTMS} + X_{ZPO} + X_{MAA} = 1 \tag{3.44}$$

To determine X_{MPTMS}, X_{ZPO}, and X_{MAA} based on (p,q,r) use the following equations:

$$X_{\text{MPTMS}} = \frac{p}{p+q+r} \;\; ; \;\; X_{\text{ZPO}} = \frac{q}{p+q+r} \;\; ; \;\; X_{\text{MAA}} = \frac{r}{p+q+r} \tag{3.45}$$

112

Step 2: Define the mass of Si precursor MPTMS: m_{MPTMS}, the molarity M or normality N for the acid catalyst HCl, and the water-MPTMS ratio R_{wa}'. With these values, the initial molar ratios for MPTMS (X'_{MPTMS}) and acidified water (X'_{NHCl}) are determined by:

$$X'_{MPTMS} = \frac{a}{1+a} \qquad ; \qquad X'_{NHCl} = \frac{1}{1+a} \tag{3.46}$$

where:

$$a = \frac{NM_{NHCl}}{NM_{MPTMS}} = \frac{1}{R_{wa}'} \tag{3.47}$$

The partial molar ratios to determine the amount of H_2O and HCl can be calculated with:

$$X'_{HCl} = \frac{M(\frac{1eq}{1000l})}{M(\frac{1eq}{1000l}) + \frac{\rho_{H_2O}}{FW_{H_2O}}\left(1 - \frac{MW_{HCl}}{\rho_{HCl}} \cdot M(\frac{1eq}{1000l})\right)} \tag{3.48}$$

$$X'_{H_2O} = 1 - X'_{HCl} \tag{3.49}$$

For HCl $N=M$ (for single the single proton acid).

Step 3: Determine the number of moles for each of the above components, by the following equations:

$$NM_{MPTMS} = \frac{m_{MPTMS}}{FW_{MPTMS}} \tag{3.50}$$

$$NM_{NHCl} = \frac{m_{MPTMS}}{FW_{MPTMS}}\left(\frac{1 - X'_{MPTMS}}{X'_{MPTMS}}\right) \tag{3.51}$$

$$NM'_{H_2O} = X'_{H_2O} \cdot NM_{NHCl} \qquad ; \qquad NM'_{HCl} = X'_{HCl} \cdot NM_{NHCl} \tag{3.52}$$

The volumes for step A of the preparation procedure (Figure 3.16) are determined as:

$$V_{MPTMS} = \frac{m_{MPTMS}}{\rho_{MPTMS}} \tag{3.53}$$

$$V_{H_2O}^{(A)} = \frac{m'_{H_2O}}{\rho_{H_2O}} = \frac{NM'_{H_2O} \, FW_{H_2O}}{\rho_{H_2O}} \quad ; \quad V_{HCl}^{(A)} = \frac{m'_{HCl}}{\rho_{HCl}} = \frac{NM'_{HCl} \, FW_{HCl}}{\rho_{HCl}} \tag{3.54}$$

Step 4: Having calculated the volumes required for Step A of the procedure, we now proceed to calculate the number of moles of the Zr alkoxide and chelating agent MAA:

$$NM_{ZPO} = \frac{X_{ZPO}}{X_{MPTMS}} \cdot NM_{MPTMS} \tag{3.55}$$

$$NM_{MAA} = \frac{X_{MAA}}{X_{MPTMS}} \cdot NM_{MPTMS} \tag{3.56}$$

and the volumes,

$$V_{TPZ} = \frac{m_{ZPO}}{\rho_{ZPO}} = \frac{NM_{ZPO} \cdot FW_{ZPO}}{\rho_{ZPO}} \tag{3.57}$$

$$V_{MAA} = \frac{m_{MAA}}{\rho_{MAA}} = \frac{NM_{MAA} \cdot FW_{MAA}}{\rho_{MAA}} \tag{3.58}$$

Step 5: In order to establish the amount of H_2O required to further hydrolyze the mixture, based on a desired final water-alkoxide ratio

$$NM_{H_2O}^{(D)} = R_{wa} \left(NM_{MPTMS} + NM_{ZPO} \right) - NM_{H_2O}^{(A)} \tag{3.59}$$

where the water-alkoxide ratio is:

$$R_{wa} = \frac{NM_{H_2O}^{(A)} + NM_{H_2O}^{(D)}}{NM_{MPTMS} + NM_{ZPO}} \tag{3.60}$$

and the volume of water to complete the hydrolysis is defined as:

$$V_{H_2O}^{(D)} = \frac{m_{H_2O}^{(D)}}{\rho_{H_2O}} = \frac{NM_{H_2O}^{(D)} \cdot FW_{H_2O}}{\rho_{H_2O}} \tag{3.61}$$

Step 6: The final part is to calculate the amount of photoinitiator to add to the mixture, in this case HCPK (Irgacure 184, by Ciba). Usually this is expressed as a weight percentage or *wt*%, either of the total mass of the mixture or the mass of photopolymerizable monomers. The mass of acrylate groups was chosen for this calculation. So the mass of photoinitiator is:

$$m_{\text{HCPK}} = \left(\frac{wt\%}{100}\right) \cdot \left(m_{\text{MPTMS}} + m_{\text{MAA}}\right) \tag{3.62}$$

The photoinitiator concentration [*PI*] in units of mili-mol per liter (mol·10^{-3}/L=mM) is calculated as follows:

$$[PI] = [HCPK] = \frac{NM_{HCPK}}{V_{MPTMS} + V_{ZPO} + V_{MAA} + V_{NHCl} + V_{H_2O}^{(D)}} \cdot 10^3 \quad \text{mM} \tag{3.63}$$

where the number of moles for the photoinitiator is determined as:

$$NM_{\text{HCPK}} = \frac{m_{\text{HCPK}}}{FW_{\text{HCPK}}} \tag{3.64}$$

From the previous calculation steps, all the quantities can be determined to proceed with the preparation of the sol, following the procedure presented in Figure 3.16.

Precursors used for preparation of this sol are equally reactive to water and moisture from the atmosphere, as in the previous two systems. Since preparation of this sol was done at room temperature and no refluxing was performed, all the mixing took place inside a glove box with flowing nitrogen, thus achieving a relative humidity between 30<RH<40%. The glove box was designed in-house for both mixture preparation and sol deposition. Figure 3.17

presents a series of four illustrations of the main steps involved in the preparation of the sol inside the glove box, following the procedure from Figure 3.16.

A
Mix MPTMS
+ 0.01M HCl
Stir for 1hr

- Stir vigorously
- Wait until exothermic reaction is complete: homogeneous transparent solution
- Cover flask from light
- Mix in N_2, with RH~40%

B
Mix ZPO
+ MAA
Stir for 15min

- Mix in separate flask
- Mix in N_2, with RH~40% (ZPO is highly reactive to moisture)

C
Slowly drip (B) into (A), stir 10 min

- Add (B) while stirring vigorously
- Add in small increments (e.g 50-100 μl)
- Cover flask from light (aluminum foil)
- Mix in N_2, with RH~40%

D
Add H_2O
Stir vigorously for 20 hrs

- Add H_2O until desired ratio, e.g. R_{wa}~2
- Add H_2O while stirring vigorously
- Add in small increments (e.g. 10-50 μl)
- Keep flask covered from light
- Mix in N_2, with RH~40%

E
Add HCPK
Stir vigorously for 2 hrs

F
Filter (0.2 μm) and store in the dark

Hybrid sol-gel
Dopant: Zr
Photoinitiator:
  Irgacure 184 (HCPK)

Figure 3.16. Preparation procedure for hybrid sol-gel doped with Zr

116

(a) setup for steps A and B

(b) setup for step C: drip B into A

(c) setup for step D: final H$_2$O

(d) setup for step E: add initiator
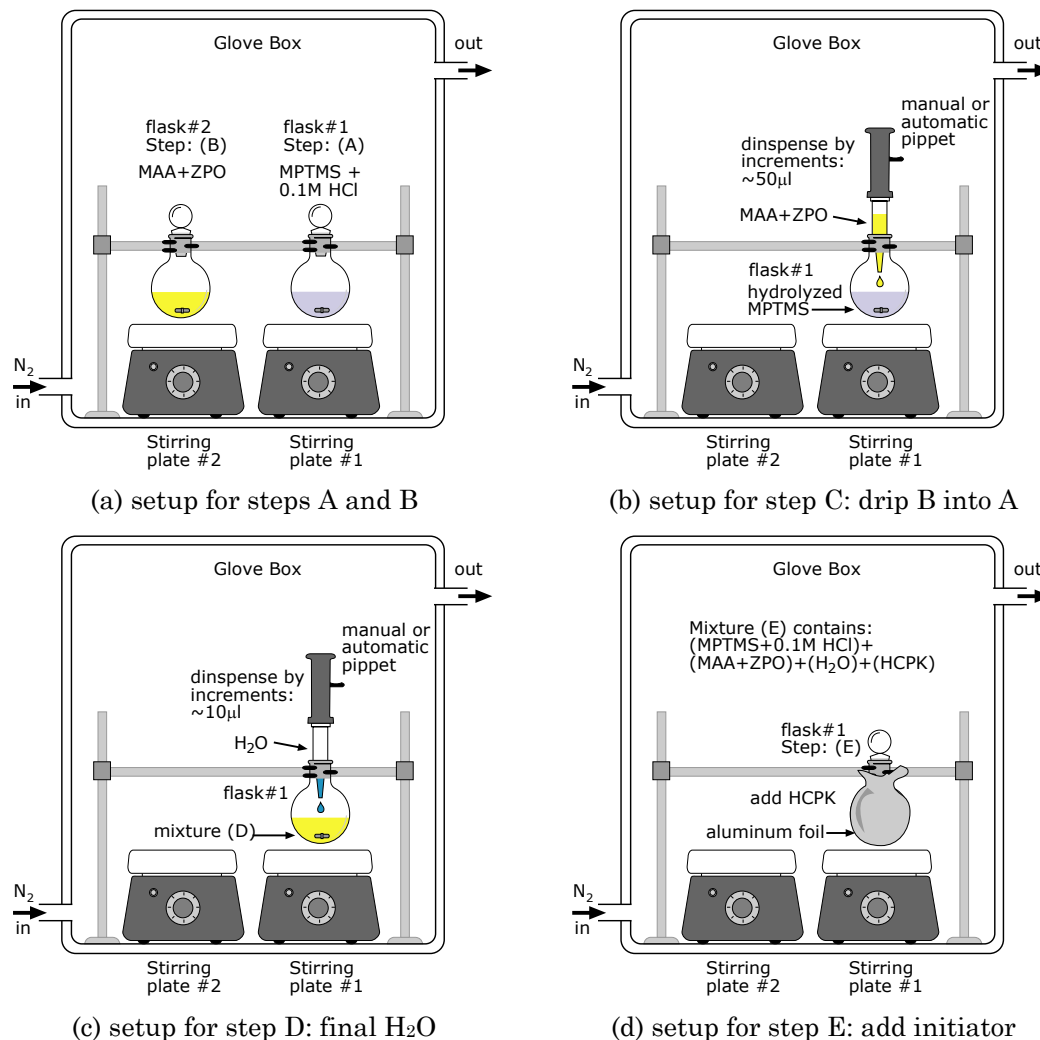
Figure 3.17. Configurations for preparation of Zr-doped hybrid sol

Some key issues to be considered for preparation of these sol-gel systems, which are based on experimentation and observation, are:

(1) Protection from light: The mixture, particularly after adding the photoinitiator (step E), is sensitive to light exposure. HCPK has a low absorbance in the visible range, compared to the UV, with a peak

between 240–325 nm, depending on the concentration (see spec sheet of Irgacure 184 by Ciba). Yet, longer lasting sols which produced more homogeneous films were obtained by blocking visible light during both the mixing process and the storage of the filtered solution. An amber UV filter was installed in all the lighting of the laboratory, and amber flasks covered with aluminum foil were used to store the sol.

(2) Aging of sol: As was learned from the preparation of purely inorganic silicate sol-gels (Section 3.4), the aging of the solution is crucial to obtain high quality films. During aging of the sol, further condensation of the network occurs and the viscosity of the solution increases, reaching optimum levels for spin coating in a period of 24 to 48 hours. Our observations are in agreement with the literature (Soppera and Croutxe-Barghorn, 2003).

(3) Drop-wise addition: A slow addition (e.g., drop by drop) of H_2O to MPTMS during pre-hydrolysis, or the MAA+ZPO mixture to the hydrolyzed MPTMS solution, was observed to be critical in avoiding precipitation or unreacted species. Initially, a manual Repette® (Jencons) dispenser with disposable tips (1.25, 2.5, 5.0, and 12.5 ml) was used. An automatic pipette, Research Pro® by Eppendorf, was later used, with 5 ml tips.

The following section describes the preparation procedure for the Al-doped hybrid photosensitive sol-gel.

3.6.2. Preparation Procedure for Hybrid Sol-Gel Doped with Al

The system containing Al as index modifier is prepared in a similar way than the above solution. Three main differences from the first photo-polymerizable system are the absence of methacrylic acid, the use of a somewhat different Al precursor that consists of a co-polymer alkoxide, and third, the use of HMPP (Darocur 1173, by Ciba) as photoinitiator. This system is based on the work of (Fardad and Fallahi, 1998; Fardad, Mishechkin *et al.*, 2001; Fallahi, Bedford *et al.*, 2002).

Various aluminum precursors have been presented in the literature, for example aluminum sec-butoxide. Three different aluminum butoxide precursors were tried and none produced reliable and consistent results, even under heavy dilution with isopropanol or ethanol, as suggested by (Najafi, Touam *et al.*, 1998). After some more research and talks with a manufacturer, United Chemical Technologies (UTC), an appropriate alkoxide was found. As a result Di-s-Butoxyaluminoxy triethoxysilane (BATES) was selected as the aluminum precursor.

For this second photopolymerizable system, the recommended design parameters to be specified are described next.

Design Parameters:

(1) Set of molar ratios for the alkoxide precursors MPTMS and BATES, defined as: X_{MPTMS} and X_{BATES}, respectively; where $0 \leq X_{[\cdot]} \leq 1$.

(2) Water-MPTMS ratio for initial pre-hydrolysis step: R_{wa}', expressed as molar ratio or in terms of *equivalents*: HCl *eq*.

(3) Molarity M or normality N, for pre-hydrolysis step of MPTMS catalyzed with HCl (note: for hydrochloric acid $M=N$).

(4) Final H_2O-alkoxide ratio (MPTMS+BATES): R_{wa}.

(5) Photoinitiator weight percentage from the total solution: $wt\%$.

Having defined the design parameters, and following a similar procedure as for the previous Zr sol-gel, the steps to calculate the volumes required for mixing are presented below.

Step 1: The partial molar ratios of MPTMS and BATES, expressed as:

$$\text{MPTMS} : \text{BATES} \Rightarrow p : q \tag{3.65}$$

or with X'_{MPTMS} and X'_{BATES}, which must satisfy:

$$X'_{MPTMS} + X'_{BATES} = 1 \tag{3.66}$$

The partial molar fractions X'_{MPTMS} and X'_{BATES} as functions of p and q, are determined from the following equations:

$$X'_{MPTMS} = \frac{p}{p+q} \quad ; \quad X'_{BATES} = \frac{q}{p+q} \tag{3.67}$$

Step 2: Define the mass of Si precursor MPTMS: m_{MPTMS}, the molarity M or normality N for the acid catalyst HCl, and the water-MPTMS ratio R_{wa}'. With these values, the initial or partial molar fractions for MPTMS (X'_{MPTMS}) and acidified water (X'_{NHCl}) are determined by:

$$X'_{MPTMS} = \frac{a}{1+a} \quad ; \quad X'_{NHCl} = \frac{1}{1+a} \tag{3.68}$$

where:

$$a = \frac{NM_{\text{NHCl}}}{NM_{\text{MPTMS}}} = \frac{1}{R_{wa}}' \tag{3.69}$$

To calculate the partial molar fractions for H_2O and HCl, the following equations are used:

$$X'_{\text{HCl}} = \frac{M(\frac{1eq}{1000ml})}{M(\frac{1eq}{1000ml}) + \frac{\rho_{H_2O}}{FW_{H_2O}}\left(1 - \frac{MW_{\text{HCl}}}{\rho_{\text{HCl}}} \cdot M(\frac{1eq}{1000ml})\right)} \tag{3.70}$$

$$X'_{H_2O} = 1 - X'_{\text{HCl}} \tag{3.71}$$

In the case of the catalyst HCl: $N=M$, for the single proton acid.

Step 3: Once the molar fractions are calculated, the next step is to determine the number of moles for each component, by means of the following equations:

$$NM_{\text{MPTMS}} = \frac{m_{\text{MPTMS}}}{FW_{\text{MPTMS}}} \tag{3.72}$$

$$NM_{NHCl} = \frac{m_{\text{MPTMS}}}{FW_{\text{MPTMS}}}\left(\frac{1 - X'_{\text{MPTMS}}}{X'_{\text{MPTMS}}}\right) \tag{3.73}$$

$$NM'_{H_2O} = X'_{H_2O} \cdot NM_{NHCl} \quad ; \quad NM'_{\text{HCl}} = X'_{\text{HCl}} \cdot NM_{NHCl} \tag{3.74}$$

Subsequently, the volumes required to prepare the solution of Step A from the preparation procedure of Figure 3.18, are determined by:

$$V_{MPTMS} = \frac{m_{MPTMS}}{\rho_{MPTMS}} \tag{3.75}$$

$$V_{H_2O}^{(A)} = \frac{m'_{H_2O}}{\rho_{H_2O}} = \frac{NM'_{H_2O} FW_{H_2O}}{\rho_{H_2O}} \quad ; \quad V_{HCl}^{(A)} = \frac{m'_{HCl}}{\rho_{HCl}} = \frac{NM'_{HCl} FW_{HCl}}{\rho_{HCl}} \tag{3.76}$$

Step 4: Once the volumes required for Step A (see Figure 3.18) have been calculated, the number of moles of the Al alkoxide BATES can be calculated simply by substituting in the next equation:

$$NM_{BATES} = \frac{X_{BATES}}{X_{MPTMS}} \cdot NM_{MPTMS} \tag{3.77}$$

while the volume of BATES is determined as,

$$V_{BATES} = \frac{m_{BATES}}{\rho_{BATES}} = \frac{NM_{BATES} \cdot FW_{BATES}}{\rho_{BATES}} \tag{3.78}$$

Step 5: The mixture requires a second addition of H_2O to fully hydrolyze the mixture. The amount of H_2O to be added is calculated based on the final water-alkoxide ratio:

$$NM_{H_2O}^{(C)} = R_{wa} \left(NM_{MPTMS} + NM_{BATES} \right) - NM_{H_2O}^{(A)} \tag{3.79}$$

where the water-alkoxide ratio is defined as:

$$R_{wa} = \frac{NM_{H_2O}^{(A)} + NM_{H_2O}^{(C)}}{NM_{MPTMS} + NM_{BATES}} \tag{3.80}$$

The volume of water to complete the hydrolysis can be computed with the following equation:

$$V_{H_2O}^{(C)} = \frac{m_{H_2O}^{(C)}}{\rho_{H_2O}} = \frac{NM_{H_2O}^{(C)} \cdot FW_{H_2O}}{\rho_{H_2O}} \tag{3.81}$$

Step 6: The last step of the calculations is to determine the weight percentage or *wt*% of photoinitiator, for this solution HMPP (Darocur 1173). This calculation was based on the total mass of photopolymerizable monomers, which corresponds to the mass of acrylate groups. The mass of HMPP can be calculated as:

122

$$m_{\text{HMPP}} = \left(\frac{wt\%}{100} \right) \cdot \left(m_{\text{MPTMS}} + m_{\text{BATES}} \right) \tag{3.82}$$

With the mass of HMPP the concentration of photoinitiator [*PI*] can be determined as follows:

$$[PI] = [HMPP] = \frac{NM_{\text{HMPP}}}{V_{\text{MPTMS}} + V_{\text{BATES}} + V_{\text{NHCl}} + V_{\text{H}_2\text{O}}^{(C)}} \cdot 10^3 \quad \text{mM} \tag{3.83}$$

where:

$$NM_{\text{HMPP}} = \frac{m_{\text{HMPP}}}{FW_{\text{HMPP}}} \tag{3.84}$$

The mixing process of the sol and the setup used for this solution was very similar to the previous system. The preparation procedure is shown in Figure 3.18. This is a relatively simple process compared to the ones described before, which makes this sol-gel system rather attractive.

Despite of the apparent simplicity of the preparation procedure, there are some important issues to consider for this sol-gel system. First, from the experimentation it was observed that this particular sol-gel, which uses BATES as the Al source, tends to be more sensitive to light. This reduces the life of the sol, and requires more care during the mixing process in order to minimize the contact with external light. This is solved by covering the mixing flask with aluminum foil during the entire process, and by covering as well the syringes used to transport and filter the sol. Another solution is to perform all the mixing in a UV filtered room. The sol is then transferred to an amber bottle previously purged with high purity nitrogen, and stored in the dark. The second thing to consider is the aging time of the sol. Within the first 24 hours after mixing, the

sol has a relatively low viscosity, and hydrolysis and condensation of species is still occurring (Soppera and Croutxe-Barghorn, 2003). After this period of time, the sol should be used within the first 3 to 4 days after preparation. These observations are consistent with reports by (Fardad, Mishechkin *et al.*, 2001), although they recommend that the sol be used immediately after the first 24 hours in order to reduce the surface roughness of the features photopolymerized by UV light.

The next section presents the different molar fractions that were explored for the two photosensitive systems.
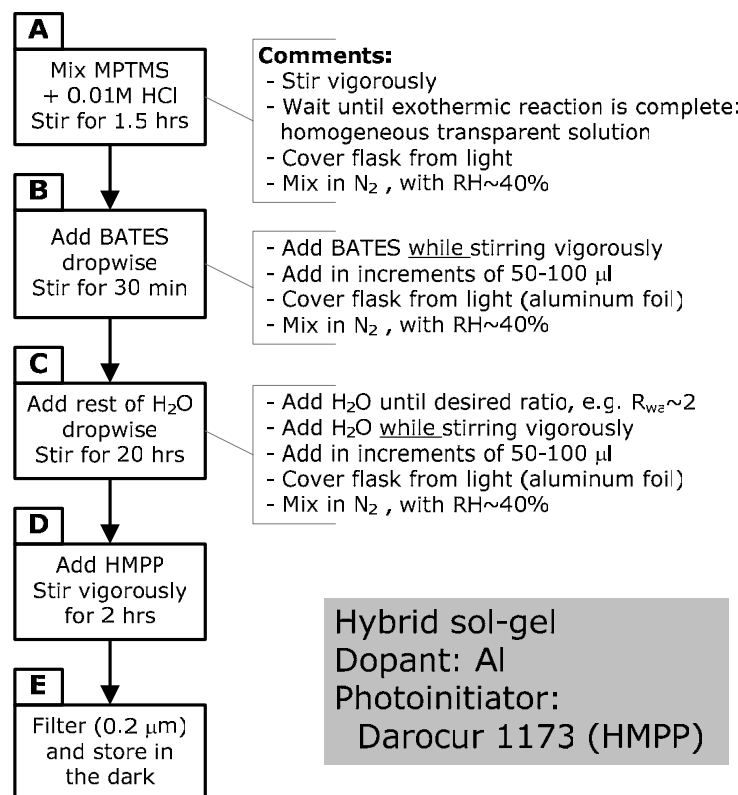
Figure 3.18. Preparation procedure for hybrid sol-gel doped with Al

3.6.3. Experimentation with various molar ratios

The previous two sections described in detail the experimental procedures, along with the equations required to calculate the molar fractions and volumes, needed to synthesize the Zr and Al doped hybrid sol-gels. These hybrid sol-gels use MPTMS as the main Si source, which is pre-hydrolyzed with acidified water. The full list of chemicals required for both Zr and Al doped hybrid systems is provided in Table 3.9. This table includes the compound's full name, formula, manufacturer, purity, and some useful properties.

Table 3.9. List of reagents used for Zr and Al doped hybrid sol-gels

Name	Formula	Source	Purity (%)	FW (g/mol)	Density (g/cm^3)
Methacryloxy propyl trimethoxysilane (MPTMS), CAS: 2530-85-0	$C_{10}H_{20}O_5Si$	Aldrich or Gelest	98.0	248.35	1.0450
Methacrylic acid (MAA), CAS: 79-41-4	$C_4H_6O_2$	Aldrich	99.0	86.09	1.0150
Zirconium(IV) propoxide (ZPO), 70 wt % in 1-propanol, CAS: 23519-77-9	$C_{12}H_{28}O_4Zr$	Aldrich	NA	327.60	1.0440
Di-s-Butoxyaluminoxy triethoxysilane (BATES), CAS: 68959-06-8	$C_{14}H_{33}AlO_6Si$	Gelest or United Chemical Tech.	NA	352.478	0.9882
2-Hydroxy-2-methylpropiophenone (HMPP, Darocur 1173) CAS: 7473-98-5	$C_{10}H_{12}O_2$	Ciba	97.0	164.20	1.0800
1-Hydroxycylohexyl phenyl ketone (HCPK, Irgacure 184) CAS: 947-19-3	$C_{13}H_{16}O_2$	Ciba	99.0	204.30	NA (powder)
Ethyl alcohol (EtOH)	C_2H_5OH	Aldrich	99.98	34.0578	0.7893
De-ionized water	H_2O		NA	18.0152	0.9982
Hydrochloric acid, 70%vol	HCl	Aldrich	99.98	36.4606	1.1978

During experimentation it was observed that the purity and manufacturer of the Si precursor played a key role in the successful synthesis of these hybrid sol-gels. Initial experiments were performed with MPTMS with ~97% purity from Aldrich, and during pre-hydrolysis the solutions experienced slow reactions. An additional problem was found after the sol was deposited on the substrate and subsequently exposed to UV light from the laser. Following these two steps the sample was immersed in a developing solution to remove the unexposed areas. This step of the process showed a poor repeatability, leaving traces of partially polymerized sol-gel bonded to the surface. After experimenting with new bottles of MPTMS from the same source, it was decided to change the manufacturer to Gelest, and the results improved substantially.

The first experiments with this class of sol-gels were done with the Zr-doped system. The initial molar fractions were obtained from the literature (Fardad, Andrews *et al.*, 1997; Saravanamuttu, Du *et al.*, 1998), and are presented in the upper part of Table 3.10, labeled as experiments 1,3 and 5. Because of certain conflicting data and preparation procedures from some of the cited references, it was decided to vary some of the parameters in a similar way as was done for System #1 (Section 3.4) and System #2 (Section 3.5). The parameters that were varied included the initial and final water-alkoxide ratio, the amount of catalyst HCl, the molar fractions of MPTMS, ZPO and MAA, and the concentration of photoinitiator. A full scale DOE was not pursued because of some problems encountered during the synthesis of this sol-gel system. These were mainly related to the manufacturer of the chemicals, as mentioned above, or to the preparation procedure, rather than to the molar fractions, as was the case for System #1.

126

Table 3.10. Molar fractions for hybrid Zr-doped sol-gel

	Molar fraction (%)			HCl		$\frac{[MPTMS]}{[H_2O]}$	$\frac{[Si+Zr]}{[H_2O]}$	PI wt%	[PI] (mM)	Initiator type
Exp	MPTMS	ZPO	MAA	M	a	R_i	R_f			
1	80.00	10.00	10.00	0.05	0.75	0.750	1.500	1.0	0.040	HCPK
2	80.00	10.00	10.00	0.05	1.50	1.500	1.500	1.5	0.076	HCPK
3	66.66	16.67	16.67	0.05	0.75	0.750	1.482	1.0	0.051	HCPK
4	66.66	16.67	16.67	0.05	1.50	1.500	1.465	1.0	0.051	HCPK
5	55.56	22.22	22.22	0.05	0.75	0.750	1.500	1.0	0.051	HCPK
6	55.56	22.22	22.22	0.05	1.50	1.500	1.500	1.5	0.076	HCPK
4.1	66.66	16.67	16.67	0.05	1.50	1.500	1.465	0.5	0.025	HCPK
4.2	66.66	16.67	16.67	0.05	1.50	1.500	1.465	1.0	0.051	HCPK
4.3	66.66	16.67	16.67	0.05	1.50	1.500	1.465	1.0	0.063	HMPP
4.4	66.66	16.67	16.67	0.05	1.50	1.500	1.465	2.0	0.127	HCPK
6.1	55.56	22.22	22.22	0.05	1.50	1.500	1.336	1.25	0.064	HCPK
6.2	55.56	22.22	22.22	0.05	1.50	1.500	1.336	1.50	0.095	HMPP

One of the main differences in the first set of experiments, labeled from 1–6 in Table 3.10, lays in the discrepancy between a and R_i. After these experiments were conducted, it was found that the best and more consistent results were produced when $a=R_i$. Additionally, the more balanced mixtures 4 and 6, which have higher ZPO content, produced mixtures that were more resistant during the post-processing operations. This was particularly true for the crucial chemical development step.

The second half of experiments from Table 3.10, represent replicas of mixtures 4 and 6 with variations in the concentration and type of photoinitiator [PI]. Both the concentration and type of photoinitiator are factors with greater importance during the laser processing stage; nonetheless, they also affect other aspects of the sol-gel features such as surface roughness and degree of polymerization. The most consistent results were obtained with mixtures 4.3

and 6.1. However, it is important to mention that results particularly for sol-gel System #3, must be analyzed by looking at the entire process: chemical concentration, film deposition, thermal treatment, and laser processing. It is difficult to evaluate a certain mixture until the process is completed.

In the case of the Al-doped hybrid sol-gels, the initial molar ratios for the compounds were similarly drawn from the literature. Experiment #1 from Table 3.11 was directly obtained from the work of (Fardad, Mishechkin *et al.*, 2001). The following experiments from Table 3.11 show slight differences mainly on the molar ratios between the silicon and aluminum alkoxides, as well as the concentration of photoinitiator HMPP. The difference between experiments #1 and #6 was the manufacturer of the alkoxides. Mixture #1 used a combination of MPTMS by Aldrich and BATES by Gelest, while mixture #6 consisted of MPTMS by Gelest and BATES by United Chemical Technologies. This last combination proved to be the more effective and consistent one.

After multiple experiments with the molar fractions and concentration of PI indicated in Table 3.11, consistent and repeatable results were obtained with mixtures #4 and #6. The greatest challenge for the successful use of this sol-gel

Table 3.11. Molar fractions for hybrid Al-doped sol-gel

Exp	Molar fraction (%)		HCl		$\frac{[MPTMS]}{[H_2O]}$	$\frac{[Si+Al]}{[H_2O]}$	PI	[PI]	Initiator
	MPTMS	BATES	M	a	Initial R_i	Final R_f	wt%	(mM)	type
1	80.00	20.00	0.01	1.33	0.75	2.0	0.75	0.0217	HMPP
2	80.00	20.00	0.01	1.33	0.75	2.0	0.75	0.0206	HMPP
3	71.43	28.57	0.01	1.00	1.00	2.0	0.75	0.0180	HMPP
4	71.43	28.57	0.01	1.00	1.00	2.0	0.75	0.0179	HMPP
5	71.43	28.57	0.01	1.00	1.00	2.0	0.75	0.0180	HMPP
6	80.00	20.00	0.01	1.33	0.75	2.0	0.75	0.0217	HMPP
7	71.43	28.57	0.01	1.00	1.00	2.0	0.75	0.0216	HMPP

combination is in preventing the sol from exposure to light before film deposition. Additionally, the best results were obtained when the sol is used within the first 48 hours after it is mixed and hydrolyzed, as explained in the procedure outlined in Figure 3.18. Basically what this means is that areas in the film not exposed to the UV laser can be successfully removed by the chemical development step. Also, the sol-gel films deposited by spin coating were homogeneous throughout the entire surface, thus avoiding some "islands" that had the tendency to appear as the sol begins to age.

The hybrid photosensitive sol-gels presented in this section have a great potential in both producing high quality materials with optical grade quality, and being incorporated into an automatic direct-write process.

3.7. Conclusions

This chapter has presented in detail the preparation procedures for three different types of sol-gel materials which constitute the underlying platform for the proposed direct-write process. Several of the key factors involved in the successful synthesis of these sol-gel materials were identified, both from a chemistry perspective and in terms of the processing parameters and conditions.

One of the main goals of this chapter was to provide a repeatable preparation procedure for each of the sol-gel systems, in an attempt to settle clear differences which are commonly obscured in the literature. The following chapter details the procedure for film deposition and thermal treatment of the sol-gels synthesized as presented in this Chapter 3.

Chapter 4. Material Deposition and Thermal Processing

4.1. Introduction

Deposition of the sol and thermal processing of the sol-gel film are the subsequent steps of the proposed process. Figure 4.1 presents the sequence of steps and highlights the two parts to be covered in this chapter. Each step has a significant impact on the quality of the sol-gel film and thus on the quality of the features to be defined in the later laser processing step. Therefore, the various parameters involved in these two steps must be characterized and controlled. The objective of this chapter is to present a detailed study of the design
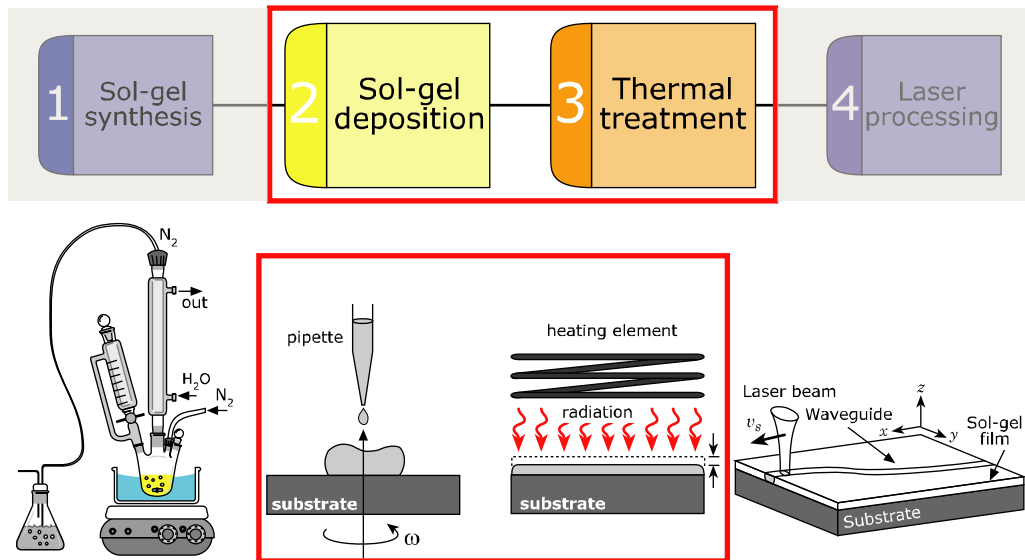
Figure 4.1. Flow chart of steps described in this chapter

parameters, and discuss the correlation to film quality and optical properties, such as refractive index.

Observing more close the film deposition and thermal processing steps, Figure 4.2 illustrates intermediate parts of these two steps. The first four steps correspond to the deposition by spin coating (Brinker and Scherer, 1990). From the initial release of the fluid, through the spin-up, spin-off, and evaporation, the sol-gel film undergoes large structural changes, yet the film still contains a large amount of solvent. Further condensation and evaporation, accompanied by yet even larger structural changes occur during the thermal processing of the sol-gel film. In order to obtain a film with a high degree of purity, a low level of porosity, a smooth surface (less than $\lambda/4$), and a desired thickness and refractive index, one must identify and control the critical parameters to achieve this goal.
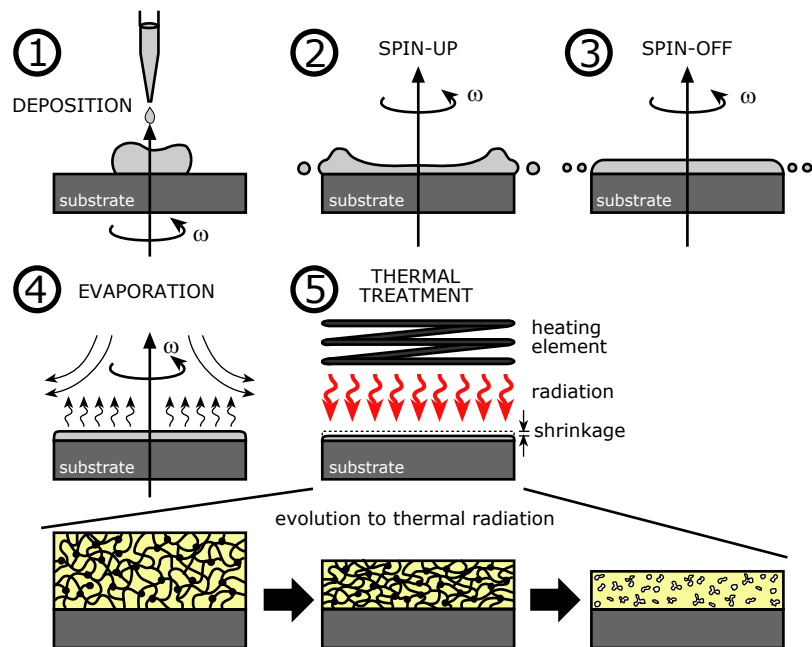
Figure 4.2. Evolution of sol-gel film fabrication; based: (Brinker, 1990)

Chapter 4 is organized as follows. It begins with a discussion on the theory and practice of deposition of sol-gels by the spin coating technique. A detailed description of the techniques developed for successful spin coating of sol-gels is provided, which includes some hardware modifications. This is followed by a discussion of the experimental procedure and experimental results for the deposition of the sol-gel systems proposed in Chapter 3. The second part of the chapter discusses the importance of thermal processing of the deposited sol-gel film. The design of the experimental equipment for thermal processing is described, and experimental results are presented.

4.2. Deposition of Sol-Gel Films: Theory & Procedures

Following the mixture preparation and solution aging, described in Chapter 3, the sol is ready to be deposited on the substrate. The two most common techniques for the deposition of sol-gel optical films are spin coating and dip coating, each having certain advantages over the other (Brinker, Hurd *et al.*, 1990; Klein, 1991; Brinker, Hurd *et al.*, 1992). For this research the spin coating method was selected for two main reasons. First, because it is a popular method compatible with microelectronics manufacturing, so vast literature and equipment are readily available. Second, in the context of designing an automated freeform fabrication machine, spin coating can be easily incorporated into a batch-type process. A description of the deposition procedure and theory of spin coating is given below.

4.2.1. Physics of Spin Coating

The main idea behind the spin coating process is to uniformly spread a solution on the substrate material by centrifugal forces. For the deposition by spin coating, the substrate is placed in a vacuum chuck and spun to the desired velocity. According to (Scriven, 1988), the process can be divided in four main stages: (1) deposition, (2) spin-up, (3) spin-off, and (4) evaporation (see Figure 4.2). Some of these stages may overlap, especially in sol-gel mixtures, which observe non-Newtonian behavior as the solvent evaporates and the viscosity drastically increases (Brinker and Scherer, 1990).

An estimate of final thickness can be calculated by (Meyerhofer, 1978):

$$h_f = \frac{K_s c_o^2}{\sqrt{\omega}} \tag{4.1}$$

where h_f is the final thickness, c_o is the initial concentration of solids in the mixture, ω is the rotational velocity, and K_s corresponds to a constant dependent on the solvent system.

Emslie *et al.* provided a more accurate description of the various phenomena involved in spin coating from a hydrodynamics perspective (Emslie, Bonner et al., 1958). They arrived at the following equation from a balance of centrifugal and viscous forces, combined with the continuity equation:

$$h(t) = \frac{h_o}{\sqrt{1 + \left(\frac{4\omega^2}{3\nu}\right)h_o^2 t}} \tag{4.2}$$

Equation (4.2) is not valid for non-Newtonian fluids, which is the case of sol-gels, where density and viscosity do not remain constant. Therefore a different equation must be used. From a process design perspective, we would like to predict the final thickness as a function of rotational velocity. Meyerhofer

provided an estimate of the final thickness of the film by introducing the evaporation rate of the solvent (Meyerhofer, 1978). He arrived at the following expression:

$$h_f = c_o \left(\frac{3 v_o e_s}{2(1 - c_o) \omega^2} \right)^{\frac{1}{3}} \qquad (4.3)$$

where e_s is the solvent's evaporation rate, v_o is the initial kinematic viscosity ($v = \eta/\rho$), and c_o the initial concentration of solids on the solution. The solvent's evaporation rate can be estimated by:

$$e_s = C_s \sqrt{\omega} \qquad (4.4)$$

In this equation C_s is a proportionality constant that must be determined for each system. All of these calculations assume laminar flow above the spinning substrate.

Since some of the above parameters are difficult to estimate, a simpler version of Equation (4.3) can be restated as (Syms and Holmes, 1994):

$$h_f = K \omega^{-\gamma} \qquad (4.5)$$

where K and γ are constants to be determined.

The above equation basically predicts an exponential decrease of the film thickness as the spin coating velocity is increased. This equation can be used to examine the influence of the velocity on the final thickness.

4.2.2. Deposition Procedure and Apparatus

Successful deposition of high-quality optical films is affected by a number of parameters. The most important parameters can be divided in four groups: (1) velocity profile, (2) environment, (3) physicochemistry of the solution, and (4)

deposition equipment. Some of the most important parameters and characteristics from each group are discussed next.

(1) Velocity Profile

In designing a velocity profile, the parameters to consider include the acceleration (initial or of any subsequent stage), dwell time (more than one can be used, depending on the solution), and the maximum velocities of each stage (if there are more than one, which is usually the case). Another important factor to consider is whether the deposition is done as *static* or *dynamic*. For static deposition, a puddle of solution is dispensed before spinning the sample. Dynamic deposition, on the contrary, is performed after spinning the sample at low speed, dispensing the fluid, and then accelerating the sample through the rest of the cycle. From experimentation, dynamic deposition provided the best results for all three types of sol-gels.

Different velocity profiles were used depending on the nature of the sol-gel mixture. For example, the inorganic sols have very low viscosity and high evaporation rate, so an acceleration stage combined with a steady dwell time provided the best results. Hybrid sols required a multi-step acceleration and dwell profile. Figure 4.3a shows the profiles used for the inorganic sol-gel (System #1), indicating the time for dynamic deposition with an arrow. On the other hand, Figure 4.3b shows a modified version of the spin coating profile used for the hybrid Ti-doped sol (System #2). For this profile the initial acceleration is much greater, to allow a rapid spreading of the sol, thus covering completely substrate's surface before gelling.
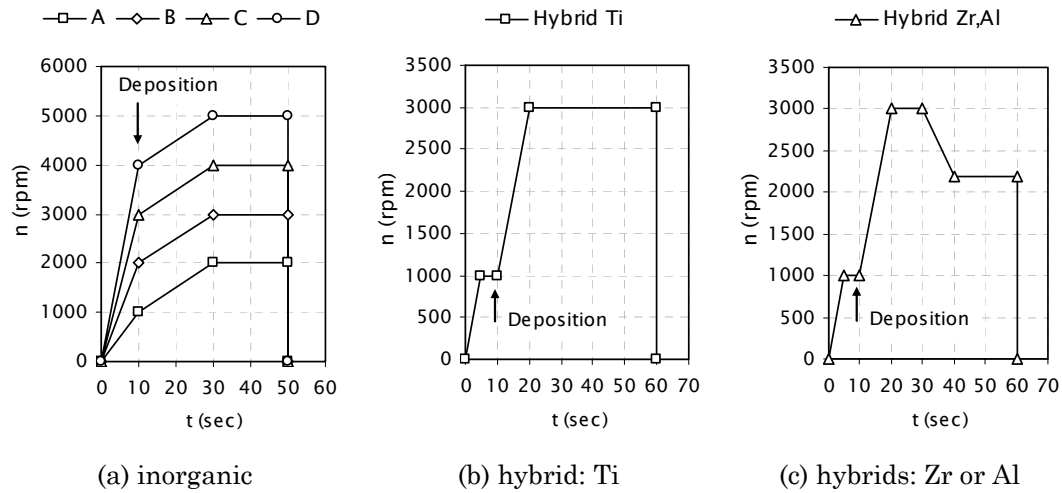
Figure 4.3. Spin coating velocity profiles

Due to the high organic component content in the hybrid sols of System #3, a different spin coating profile had to be designed. This profile is shown in Figure 4.3c, and it resembles the profile used for spin coating of photoresists (Plummer, Deal *et al.*, 2000). The main difference with this profile, resides in the deceleration after a small dwell period immediately after the main acceleration. This avoids a greater thinning of the film.

(2) Environment

The most important environmental factors include type of atmosphere, relative humidity, and exhaust rate. The relative humidity (RH) in the environment plays a key role in both proper spin coating and final physicochemical characteristics of the film. Consistent results were obtained with levels between: 30<RH<40%. Through experimentation it was observed that the inorganic sol-gels required a moderate exhaust rate to avoid saturation

from the solvent, keeping the flow as laminar as possible near the spinning substrate. High exhaust rates resulted in highly irregular films. On the other hand, the deposition of hybrid sol-gels, in particular the photopolymerizable type, was greatly benefited from a solvent enriched atmosphere. The use of inert atmospheres, such as N_2, produced good results for hybrid sol-gels, while the use of standard dry air or O_2 is more compatible with inorganic sol-gels. Another key factor is to avoid any particles to be introduced into the film during deposition. This was achieved by performing the deposition inside a glove box (Figure 4.4a).

(3) Physicochemistry of the Solution

The main physicochemical aspects to consider for sol-gel deposition include the viscosity of the sol and the type of solvent used to dilute the sol prior to deposition. Compared to other solutions deposited by spin coating (e.g., photoresists), sol-gels are characterized by a low viscosity and high evaporation rate, particularly inorganic sol-gels. Yet these two parameters are influenced by the chemistry of the sol; for example, the degree of connectivity of the silicate backbone, which increases as the condensation reactions progress. So they are greatly affected by the molar concentration of alkoxides, solvent, and H_2O. As seen from Equation (4.3), viscosity and evaporation rate, which depend on the type of solvent, will affect the final thickness of the film. Some popular solvents for sol-gel solutions include ethanol (EtOH), isopropanol (IPA), or tetrahydrofuran (THF).

The rheology of the sol also plays an important role during the release of fluid by the pipette for dynamic deposition. The low viscosity inorganic sols do

137

(a) Glove box   (b) Spin coater (detail)

Figure 4.4. Spin coater used for sol-gel film deposition.

not tend to adhere to the inner walls of the pipette tip, thus allowing a clean and complete release of the volume. On the other hand, based on observation, it was noted that hybrid sols have a greater tendency to adhere to the pipette and form bubbles, resulting in a continuous jet followed by residual bubbles being expelled. This caused the films to have "comets" or streaks in a radial direction. This problem was solved by using an automatic pipette (Research Pro pipette, Eppendorf), where the operator can predefine the speed during release, and select an operating mode where the stroke and blow-out stages are independently controlled.

(4) Deposition Equipment

Deposition of the sol-gel films was carried out in a programmable spin coater from Laurell Technologies (model WS-400A-GNPP-Lite), as shown in Figure 4.4b. As illustrated from the velocity profiles of Figure 4.3, an automatic
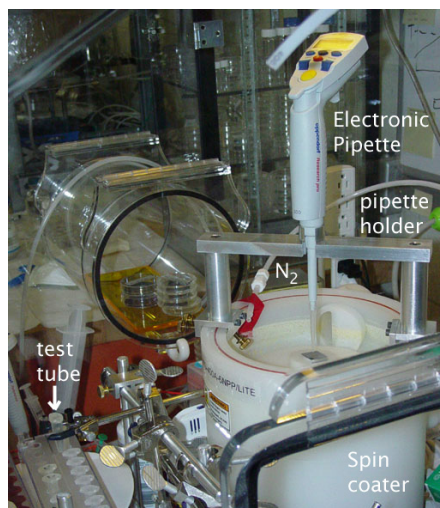
Figure 4.5. Assembly of automatic pipette and holder on spin coater

and programmable spin coater is more likely to achieve the profiles in a precise way, which is crucial for repeatability of the experiments. Furthermore, reducing human involvement in such tasks as in deposition of the sol-gel film is preferable, thus increasing the reproducibility and reducing errors or faulty samples. Human intervention during spin coating was not completely eliminated, due to lack of an automatic liquid dispensing device. However, the human error was reduced by incorporating into the spin coater a fixture that held the pipette in place and at the desired height during the dispensing of the liquid. Figure 4.5 shows the fixture and how it holds the pipette in place at the center of the sample. An ideal design would incorporate an automatic liquid handling and dispensing system, which is widely used in the microelectronics and photonics industries. This concept is proposed for the development of a fully automatic machine.

Figure 4.6. Different pipettes used for sol-gel deposition

Two additional elements to consider for successful sol-gel deposition are the pipette and tips. If no automatic dispensing equipment is available, various types of manual pipettes or semi-automatic pipettes can be employed. During this research several pipettes were tested and are shown in Figure 4.6. As mentioned above, more consistent results were achieved by employing an electronically controlled pipette.

The main advantages of using an automatic pipette are: (1) the volume of the liquid to be dispensed can be defined with great accuracy and with a typical resolution of 0.5 μL, (2) the speed or rate at which the liquid is dispensed can be controlled, thus reducing the risk of splashing while maintaining a constant jet of fluid, and (3) the fluid intake, release and blow-off stages are independently controlled, which reduces the likelihood of residual fluid to be accidentally dropped on the substrate. The second important element is the pipette tip. The most important factors of the tip to consider are the diameter of the release hole at the bottom of the tip, and the shape and size of the tip. Small diameters are more appropriate for low viscosity inorganic sol-gels, while tips with a larger form factor help reduce bubbles in hybrid sol-gels. Figure 4.6 shows the different tips used.

Table 4.1. Design parameters for sol-gel spin coating deposition

Velocity Profile	Environment	Physicochemistry	Equipment
• Acceleration • Dwell time • Deceleration	• Type: inert (N_2), oxygen enriched, solvent enriched	• Chemistry of sol • Viscosity • Solvent percentage • Solvent type	• Programmable spin coater • Pipette tip: hole diameter, shape of tip

Summary of Important Design Parameters

For process design purposes, the main design parameters described above for film deposition are summarized in Table 4.1.

Recommendations for Deposition Procedure

In addition to the design parameters presented above, following are some recommendations to consider during the deposition procedure of sol-gel films. These recommendations are based on observations from experimentation conducted during this research.

After mixing and aging, the sol is diluted in a solvent immediately before deposition, as explained above. It is crucial during this final step before deposition, to avoid any particles in the sol. This can be achieved by working in a clean room or in a glove box, and by filtering the solution immediately before deposition. When using pipettes, it is recommended to separate the diluted sol in small volumes and store them in sterile disposable test tubes. This avoids contamination of the entire sol. In addition to this, disposable pipette tips are recommended. Figure 4.7 illustrates the procedure to address these recommendations, starting from the dilution of the sol, to the filtering and separation of the fluid in

① Dilute sol-gel

Sol (a%) +
EtOH (b%)

Vial
Vol.~2.5ml
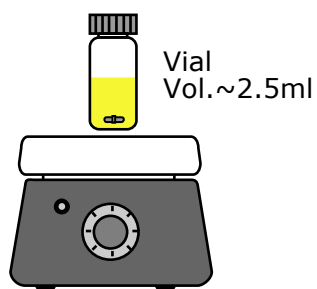
1- Add a% of sol
2- Add b% of solvent
3- Stir vigorously 10 min

② Filter and dispense

Syringe 2.5 ml

PFTE filter
0.2μm

Safe-Lock micro
test tube
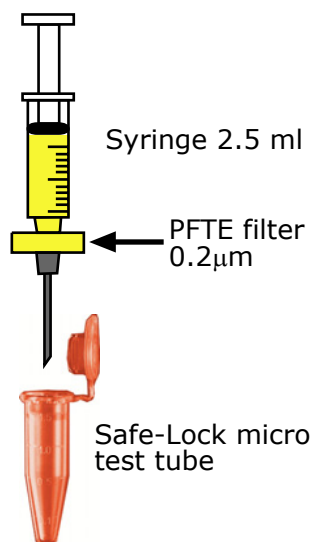
③ Split volume

Split volume in
2 or 3 tubes

④ Load liquid

⑤ Deposit

Electronic
pipette

pipette
holder

N_2

test
tube

spin
coater
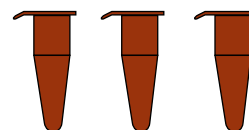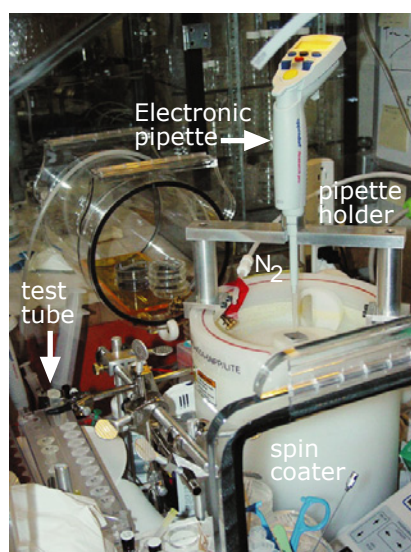
Figure 4.7. Final dilution, filtering and volume separation procedure

smaller volumes, and finally loading the sol into the pipette tip and depositing it
in the substrate.
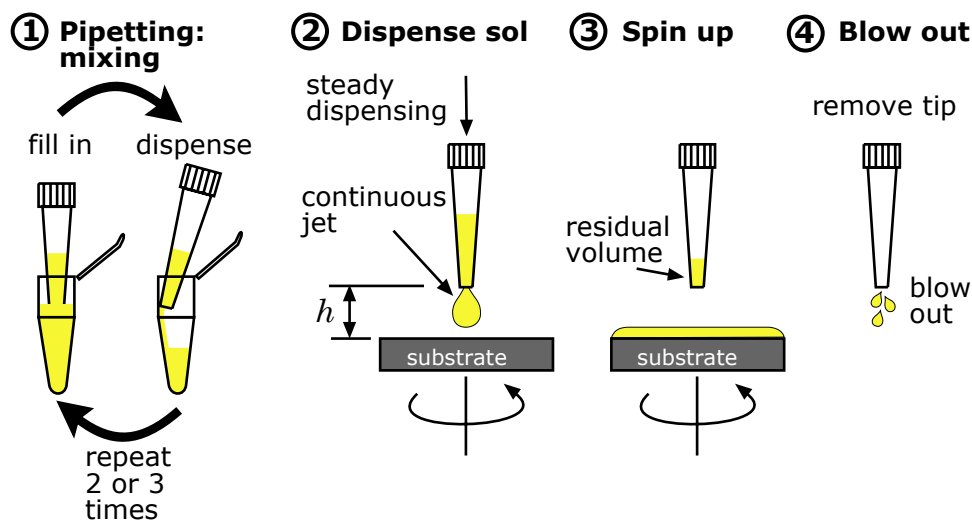
Figure 4.8. Manual pipetting process for sol deposition

Once the sol has been diluted, filtered and separated in smaller volumes, the next step is to load the fluid into the pipette tip and deposit it on the substrate. A recommended procedure for manual pipetting is illustrated in Figure 4.8. This procedure minimizes non-homogeneous films, in particular for high-viscosity hybrid sol-gels, reducing the development of streaks on the film.

The procedure starts with mixing the sol in the pipette tip, by loading and releasing the fluid a few times. Residual bubbles that build up on the loaded sol in the tip must be avoided. Then the substrate is spun, while the pipette is brought close to the substrate and held at a fixed height. A continuous jet of fluid is then released. Typically, a residual liquid remains in the tip, which is "blown out" after the pipette has been removed.

The following section presents a general experimental procedure and results from experiments related to spin coating of sol-gels.

143
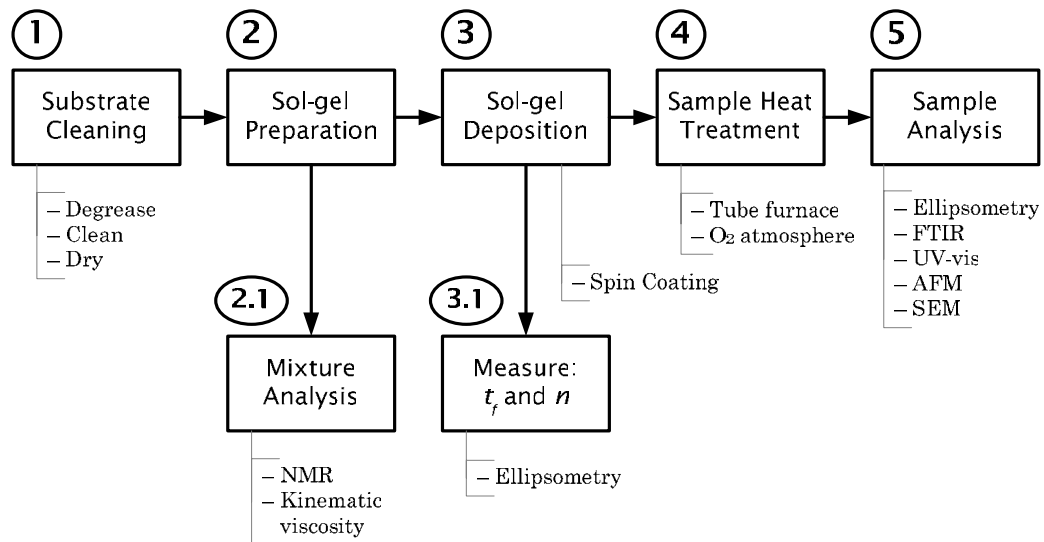
Figure 4.9. Experimental procedure for sol-gel films

4.3. Sol-Gel Deposition: Procedure and Experiments

This section outlines a general experimental procedure for deposition of sol-gel films, including details of the preparation and cleaning of substrate materials. The overall procedure followed is outlined in Figure 4.9, which is comprised by a substrate cleaning and surface preparation phase, mixture preparation phase, sol-gel deposition phase, heat treatment phase, and finally an analysis phase. The sol preparation was covered in detail in Chapter 3, while specifics on the thermal treatment procedures are covered in subsequent sections in this chapter. A detailed description of the individual phases is provided below.

4.3.1. Preparation of Substrate Material

The sol-gel films were deposited on the following substrate materials: silicon wafers, quartz wafers, borosilicate glass slides, and silicon wafers with an oxide layer. The Si-wafers were P-type (100) orientation, with a thickness of ~500μm, polished on one side, from Silicon Inc. Three standard Si wafer sizes were used: 100 mm, 70 mm, and 25 mm. The 100 mm wafers were cut into small 20x20 mm squares. Two types of quartz substrates were used: square microscope slides from GM Associates with a thickness of 1 mm, and round wafers from Marks Optics with a thickness of ~550 μm. The borosilicate substrates were standard microscope glass slides cut to 20 × 20 mm squares. The silicon wafers with a grown oxide layer were used for doped sol-gels, serving as the under-cladding for waveguiding. The characteristics of these silicon wafers are: thickness of the oxide layer 2.4 μm, wafer diameter 6", thickness ~6,000 μm, and manufacturer Silicon Inc.

The wafers were cleaved into smaller pieces according to the patterns shown in Figure 4.10. A manual diamond scriber from Terra Universal was used to mark the pattern on the wafer, which was later cleaved with the aid of glass cleaving tweezers.

Once the wafers were cut into smaller pieces, these substrates were cleaned thoroughly following a series of steps. A critical part for the deposition of high-quality films lies in the proper surface preparation. The following procedure was used for surface cleaning:

    1) <u>Degreasing</u>: The samples were placed in a beaker containing approximately 20 ml of trichloroethylene, which was then heated to 60°C until boiling, and refluxed for 10 minutes.

Cutting pattern for 6 inch wafer with oxide layer

Cutting pattern for 100 mm wafer
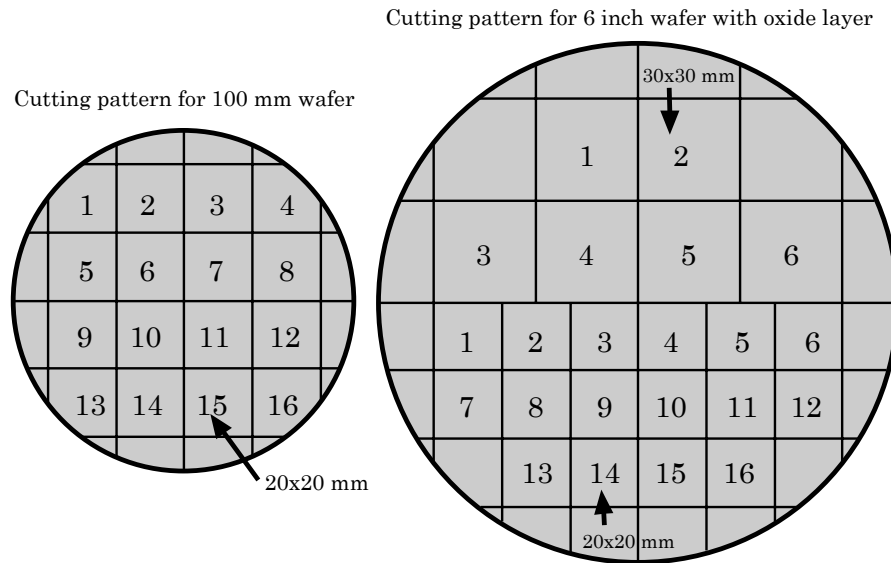
Figure 4.10. Cutting patterns for 100 mm and 150 mm wafers

2) <u>Rinsing</u>: The samples were then rinsed in an ultrasonic bath with high-purity acetone, isopropyl alcohol, and de-ionized water, subsequently, for 5 min in each substance.

3) <u>Drying</u>: The samples were then dried by using a heat gun and a continuous jet of nitrogen, ensuring no watermarks were left.

4) <u>Storage</u>: After cleaning the samples were carefully placed in Petri dishes and stored in a drying cabinet (RH~30%).

It is worth mentioning that there are more sophisticated cleaning techniques for wafers, particularly in clean rooms and micro-fabrication facilities. Yet if none of these are available, the procedures described above provide adequate results for experimental purposes.

4.3.2. Analysis Techniques

In order to characterize the samples and evaluate the results of sol-gel deposition experiments, various analytical techniques and devices were used. The main quantitative parameters of interest are the film thickness, index of refraction, and the morphology of the film's surface, which includes the surface roughness. On the other hand, additional qualitative aspects of film deposition include the presence of cracks or defects, as well as the number of layers that could be deposited for multi-layer films before cracking occurred.

Below is a brief description of the techniques and equipment used.

Variable-Angle Spectroscopic Ellipsometry

Variable-angle spectroscopic ellipsometry (VASE) is an optical non-destructive technique used to characterize the film thickness and index of refraction, among other properties (Woollam, Johns *et al.*, 1999). By measuring the amplitude and phase shift of the complex Fresnel reflection coefficients from a polarized beam, going from linearly polarized light to elliptical polarization, one can estimate through a series of algorithms and numerical fit to a model the properties of a film, such as thickness and index of refraction. This technique can be very precise (e.g., estimate the refractive index up to a fifth digit or more), yet it requires the film's surface to be very smooth. Since it provides an average estimate of the properties over the region covered by the beam's diameter, it also requires a high degree of homogeneity of the film for good readings. These factors make ellipsometry a challenging technique to apply in some cases.

In the case of this research, the ellipsometer used was a J.A. Woollam Co. model EC400. The wavelength range used was 300–1000 nm. The typical model used to fit the data consisted of three layers: (1) a silicon layer model with 0.5 mm in thickness, (2) followed by a model of a layer of SiO_2 representing the native oxide layer of approximately 4-10 nm, and finally (3) a Cauchy model for the sol-gel film. By using the Cauchy model, the software can fit the film thickness and refractive index over the spectral range. The software provides the Cauchy coefficients (*A,B,C*), which are used to determine the refractive index *n* by means of the following equation:

$$n(\lambda) = A + \frac{B}{\lambda^2} + \frac{C}{\lambda^4}$$
(4.6)

One parameter that is important to consider when using VASE is the root mean squared error (MSE), which is calculated by the software and is used to quantify the variation between the experimental data and the proposed model (Woollam, Johns *et al.*, 1999). Thus, this parameter must be minimized. As a rule of thumb, an MSE≤20 provides accurate estimates of *n* and t_f.

Atomic Force Microscopy

Atomic force microscopy or AFM is a highly accurate technique to characterize the morphology of a surface at scales close to the atomic level ($\overset{\circ}{A}$). Two common operating modes include the *tapping mode*, which is basically a non-contact non-destructive method, and a *contact mode*, which depending on the surface properties can alter the surface under inspection. For this research the tapping mode was selected. The device used was a Dimension 3100 with a

148

Nanoscope IV controller from Digital Instruments. Standard tapping mode silicon tips were used, with a natural frequency of 300 kHz.

For the tapping mode, the AFM operates by scanning the tip attached to the end of an oscillating cantilever across the sample surface. The cantilever is oscillated at or near its resonance frequency, and then the tip lightly "taps" on the sample surface during scanning, making contact with the surface. Scanned regions can cover up to 50×50 µm, with a step height preferably lower than 5 µm. This somewhat limits AFM to small scale measurements.

4.3.3. Defects in Sol-Gel Films

Common defects to avoid during spin coating of sol-gel films include "comets" or streaks caused by the presence of particles or other residues on the substrate. Another type of defect is the presence of uncoated areas on the substrate, as a consequence of a low volume of sol and in some cases augmented by the "wetability" characteristics of the substrate. It is quite common to observe in many sol-gel films, in particular for inorganic sol-gels, the development of cracks throughout the film. These cracks, which begin as micro-cracks, can be caused by particle defects or most commonly develop due to residual stresses induced during the evaporation stages of the film deposition process. The large structural changes observed during shrinkage of the film in the evaporation and thermal processing stages often result in the development and propagation of cracks. Figure 4.11 shows some common defects observed in sol-gel films.

(a) particles (x50K)   (b) inside of film (x10K)   (d) crack (x10K)
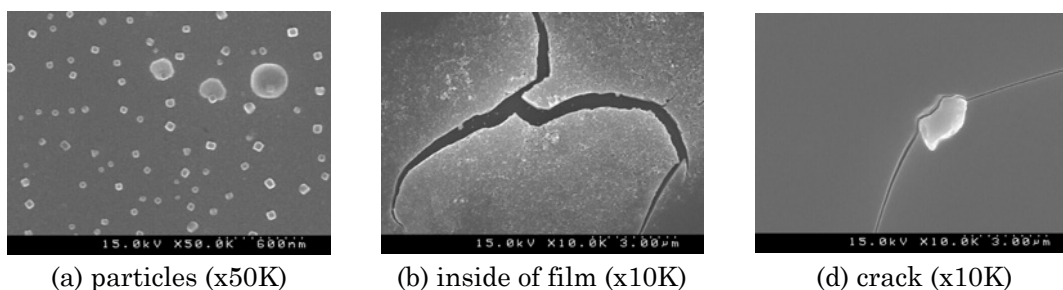
Figure 4.11. Pictures of common defects found on sol-gel films

Some solutions to these problems include the deposition in a certified clean room to avoid particles, the use of organically modified sol-gels which can be more compliant and reduce stress buildup, or rapid-thermal processing. These solutions will be discussed in more detail in later sections.

4.3.4. Deposition of Inorganic Silicate Sol-Gel Films – System #1

The deposition process and characterization of purely inorganic silicate sol-gels, which was the first system experimented, is well documented in the literature (Brinker, Hurd *et al.*, 1990; Brinker, Hurd *et al.*, 1992). So a number of experiments were performed first to corroborate the experimental results with the literature, and second, to characterize the material and processing parameters under the conditions of our experimental setup. As reported by (Guglielmi, Colombo *et al.*, 1992), a significant variability can occur not only by changing experimental conditions, such as the chemical concentration or spin coating parameters, but by changing the facility were the experiments are conducted.

The experiments focused on three main areas. The first area was to evaluate the effects of the spin coating velocity on the index of refraction and film

thickness, and at the same time corroborate the exponential relationship between spin velocity and thickness depicted in Equation (4.5). The second area of interest consists of characterizing the repeatability of the process by verifying the variability in n and t_f between samples and within a sample. A third area of interest is related to the chemical aspects of the sol, by assessing the influence of the water-alkoxide ratio R_{wa} and the percentage of solvent (EtOH) on n and t_f.

As noted in Chapter 3, several solutions were prepared with various molar ratios and preparation procedures. The influence of the viscosity of the sol was also established in Chapter 3. Once consistent results were achieved, the experimentation progressed to the study of the three areas mentioned above.

Figure 4.12 presents a summary of experimental results using mixture #7 of Table 3.5 ($X_{TEOS}=19.60$, $X_{H2O}=21.00$, $X_{EtOH}=59.40$, $R_{wa}=1.07$, $R_{sa}=3.03$).

The effects of the spin coating velocity are analyzed in Figure 4.12a. As predicted by Equation (4.5), the film thickness decreased exponentially as the spin coating velocity was increased. A more dramatic decrease in thickness was observed at low speeds; for example, a 50% change in velocity at low speeds (2000-3000 rpm) caused a thickness decrease of ~20%. On the other hand, a similar 50% increase from 4000–5000 rpm caused a 10% thickness decrease. From the same figure, but in the case of the index of refraction, an inverse behavior was observed, although a lower index was seen at 5000 rpm. This non-linear behavior for the refractive index is common and can be attributed to experimental errors during measurements with ellipsometry, or to a denser film produced at higher velocities, where the reduced thickness represents a shorter diffusion length for the solvent and residual water.

151

(a) effect of velocity

(b) variability between samples

(c) variability within a sample

(d) curve fitting
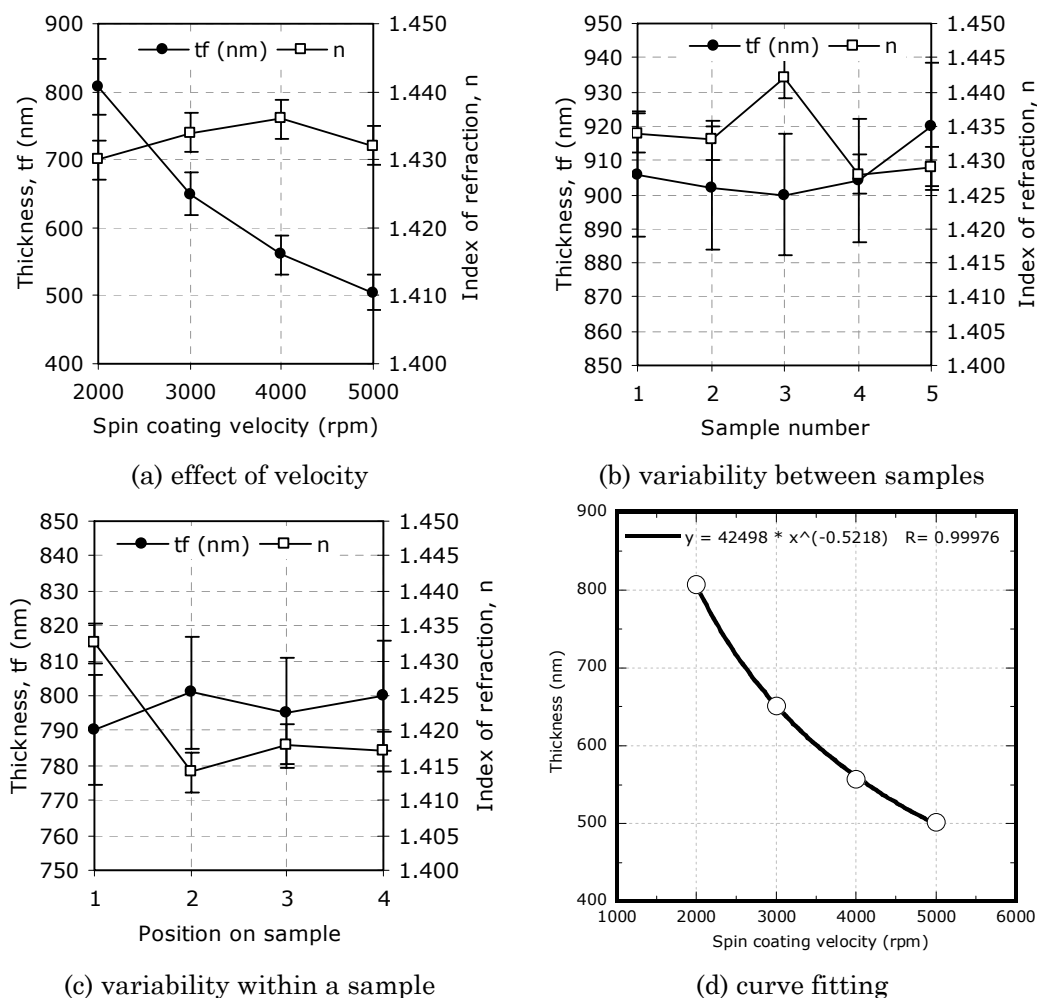
Figure 4.12. Various factors that affect spin coating of sol-gel films

Repeatability is an important factor in the development of a manufacturing process. This was studied by measuring the variability between samples with the same process parameters, and by the variability within the same sample. Figure 4.12b presents data for thickness and index of refraction for five samples produced with the same solution, spin coating velocity (2000 rpm), and dwell time (40 sec). The thickness stayed within ±10 nm range (~2%),

(a) effect of water-alkoxide ratio   (b) effect of solvent content
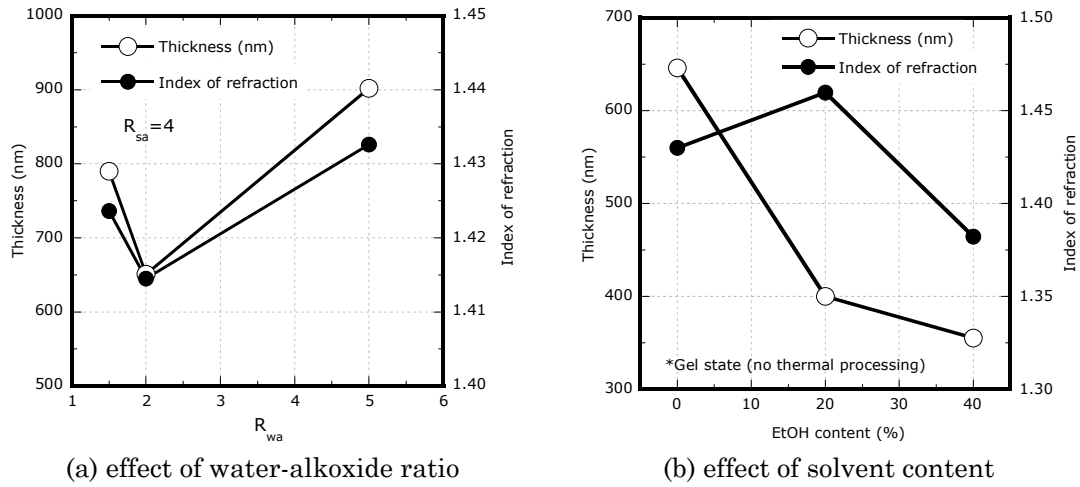
Figure 4.13. Effects of R_{wa} and %EtOH on inorganic sol-gel films

while the index of refraction had fluctuations of $\Delta n \approx 0.0125$ (~1%). Although these results are still not in the range required for industrial photonic applications, they represent a promising outcome which can be further improved.

The variability within a sample is studied in Figure 4.12c. For this case, the measurements were taken from outside to center of a square sample of 20×20 mm. From this plot the following can be concluded. The outer part of the sample had a thinning film with an expected higher index of refraction. The inner and center part of the film had a fairly stable thickness (~0.6%) and refractive index (~0.3%). These results are also promising.

From a chemistry perspective, the influence of the water-alkoxide ratio R_{wa} on the film thickness and refractive index is shown in Figure 4.13a. In this case, three different solutions were prepared changing R_{wa} while maintaining R_{wa} constant and equal to 4. From the plot it can be observed that t_f and n had similar trends as R_{wa} is increased. These results, though, have some discrepancy

153

from what was reported by (Fardad, Yeatman *et al.*, 1995), where the thickness always decreases with greater R_{wa} values.

As mentioned above, the sol is generally diluted with a compatible solvent before deposition, in order to control the viscosity. Figure 4.13b shows a plot of % of ethanol versus film thickness and refractive index. As expected, a higher percentage of solvent results in a thinner film. For this sol, a 20% increase in ethanol caused a ~39% decrease in thickness and a ~2% increase in refractive index. This plot helps illustrate the following point. Since TEOS and EtOH are chemically compatible (ethyl group), one would expect a small influence of the solvent on the refractive index, while allowing an independent change on the viscosity to control the film thickness. But as observed in Figure 4.13b, these two effects are not entirely independent. Several reasons might help explain this effect. On one side, the sol (liquid state) is in a chemically unstable state, where the viscosity is continuously increasing (Brinker and Scherer, 1990), as the hydrolysis and condensation reactions and their inverse reactions take place over time (see Equations 3.4–3.6). Therefore the presence of an excess of EtOH can affect these reactions and the final physicochemical properties of the film. On the other hand, the conditions of the environmental surroundings during deposition (i.e., humidity and chemistry) along with the boiling point of the solvent (for EtOH: ~78°C), play a key role in the solute-solvent chemical interaction.

An additional aspect of great importance in the fabrication of optical films and components is related to the morphology of the surfaces. This aspect was evaluated by taking measurements on the surfaces of various samples with an AFM scope. Figure 4.14 shows graphical renderings of AFM data from two different samples. These plots characterize the typical results of successful films

(a) sample 1: room temperature   (b) sample 2: heated at 150°C
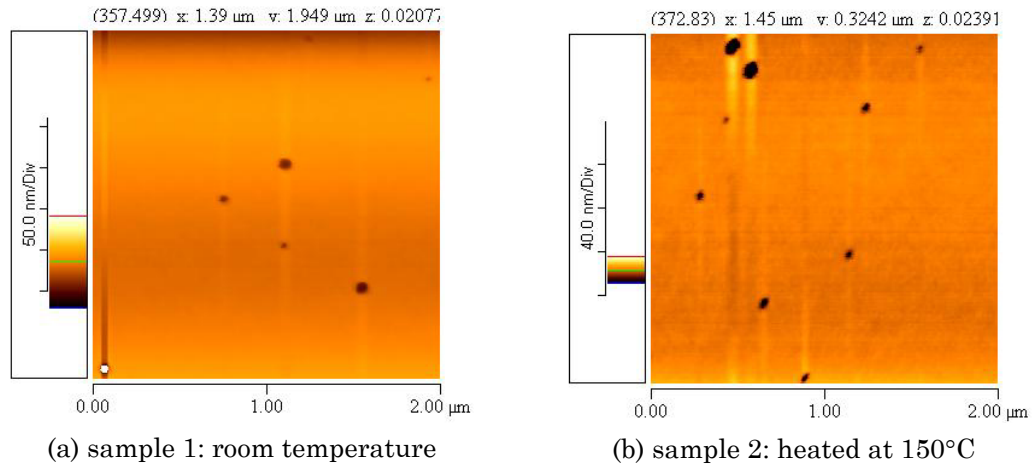
Figure 4.14. Results from AFM on inorganic silicate sol-gel films

fabricated once many of the difficulties previously discussed were addressed. As seen from these results the films are very smooth with RMS values of 7–25 nm, and show the presence of particles and defects due to a non-ideal environment.

Comments

A few comments and recommendations can be made based on the previous results for the deposition of inorganic silicate sol-gel films.

- The relationship between spin coating velocity and film thickness effectively exhibits an exponential behavior. As seen in Figure 4.12c, the least-squares fitting of experimental data to an equation of the form: $t_f = K\omega^{-\gamma}$, accurately represents the trend. The final equation is: $t_f = 42498 \cdot \omega^{-0.5218}$, with R=0.9998.

- The use of ethanol (EtOH) as a solvent to dilute the sol prior to deposition reduces the final film thickness. It is recommended to use

a small amount of EtOH (<30% vol) to avoid affecting the chemical composition of the sol and therefore the final refractive index.

- The final thickness for a single-layer inorganic silicate sol-gel film is well below the core characteristic length of single mode components (e.g., fibers or waveguides), typically 5–10 µm. This means that a multiple-layer approach must be followed in order to achieve this thickness. From the literature, and as it will be shown later, multiple layer sol-gel films are difficult to make, mainly because of residual stresses which cause cracking. One solution is the combination of a small film thickness and high-rate thermal processing, which requires a high capital investment.

4.3.5. Deposition of Hybrid Ti-doped Sol-Gel Films – System #2

Following a similar approach than for the inorganic silicate sol-gel films, the experiments conducted with a hybrid titanium-doped sol-gel explored two main issues: (a) achieving a crack-less film with a higher thickness, and (b) increasing the refractive index and the cladding-to-core index difference in order to achieve the guiding of light.

Based on the experience from the deposition of sol-gel system #1, the experiments for this sol-gel system focused on changing two parameters and measuring the effect on the film thickness and on the index of refraction. The first parameter was the spin coating velocity, which was varied between 2500 and 4500 rpm. The second parameter was the volume deposited by the pipette, being either 30 or 40 µL. For these experiments a total of two replicates were

conducted for each set of parameters, and the results were averaged and included the standard deviation. The sol-gel mixture corresponds to Exp. #5 of Table 3.9, and has the following molar fractions (%): TEOS=3.08, MTES=3.08, TPOT=1.54, H_2O=30.77, EtOH=61.54, R_{wa}=10.0, R_{sa}=20.0. The sol was diluted in ethanol, and the dwell time was 30 sec.

The addition of the organic alkoxide (MTES) to the solution had two main effects on the film. By reducing the connectivity of the silanol bonds the matrix was made more compliant and thicker films can be produced by either single-layer or multiple thin layers. The second effect is related to a slight increase in surface roughness. Because of this last effect, the sol was heavily diluted in ethanol (up to 50% vol) in order to produce films smooth enough and thin enough so that ellipsometry could be used (measurements presented in Figure 4.15).

The relationship between final film thickness and spin coating velocity for

(a) for 30 μl of Ti-hybrid sol   (b) for 40 μl of Ti-hybrid sol
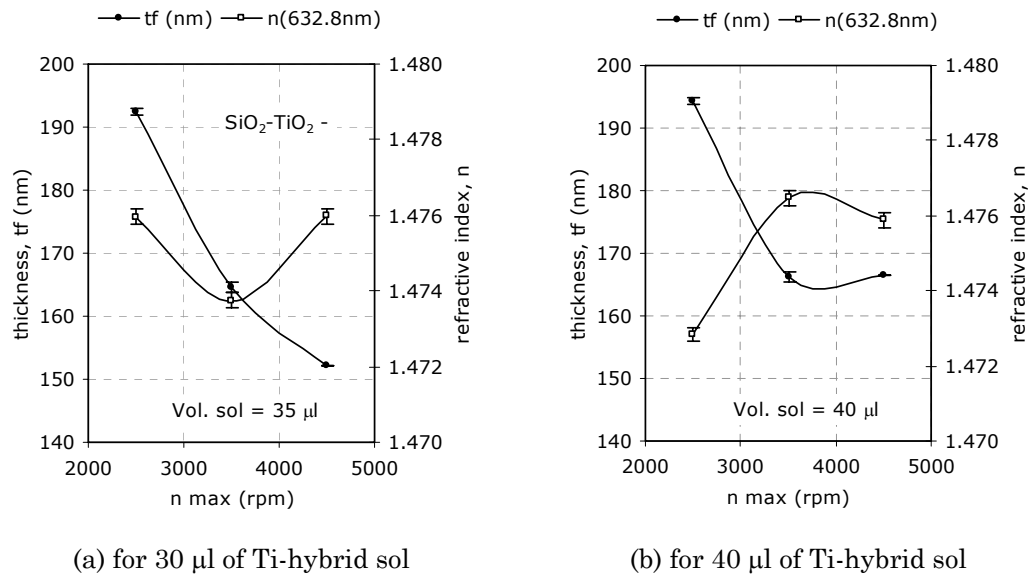
Figure 4.15. Effect of spin coating velocity and volume of sol

(a) curve fitting of thickness　　　　(b) AFM image of hybrid sol-gel film
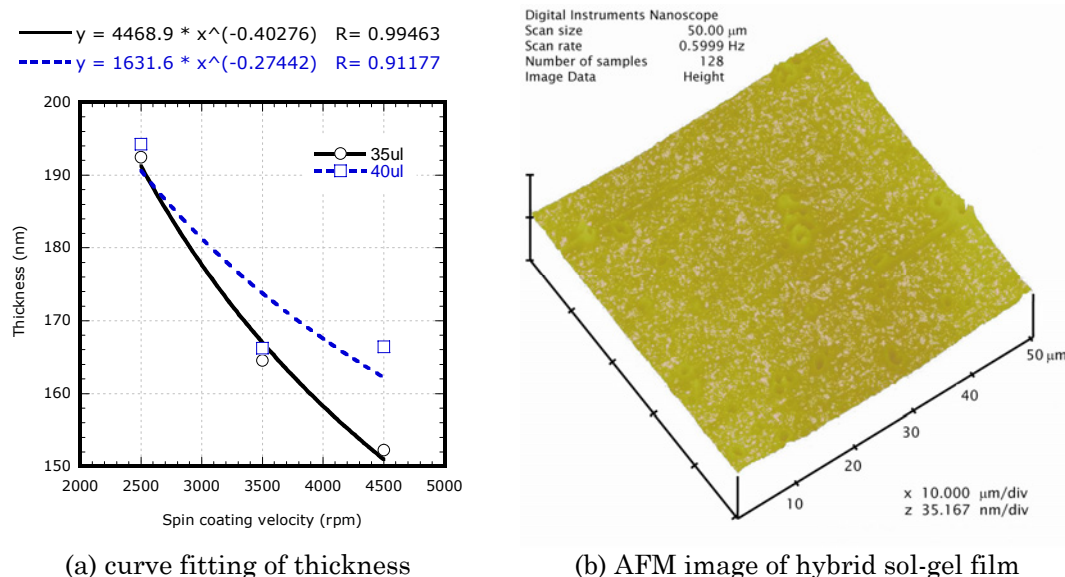
Figure 4.16. Spin coating results of hybrid sol-gel system #2

this type of sol-gel can also be approximated by the expression of Equation (4.5). Figure 4.16a shows a plot of the experimental values of the film thickness for three spin coating velocities and the respective curve fit for two deposition volumes (35 and 40 μl). A better fit is observed for the 35 μl case, though it appears that for the 40 μl case the trend is somewhat similar. The discrepancy can be attributed to variations in the spin coating process or the measurements in ellipsometry.

A plot of the surface obtained from AFM of a typical sample is shown in Figure 4.16b. The scanned area in this image is 50×50 μm. A typical surface roughness average for films with hybrid system #2 was in the range of: R_a=0.142–1.311 nm.

4.3.6. Recommendations for Spin Coating

Based on the experimental results presented in the previous sections, a set of general guidelines for the spin coating of sol-gels is presented. Figure 4.17 shows a set of graphics that summarize some of the past observations.

As seen from the experimental data, the relationship between the spin coating velocity and the film thickness can be described by a power equation (see Equation 4.5). As the velocity is increased, the film thickness is reduced. Additionally, as the sol is further diluted in solvent prior to deposition, the thickness curves are shifted downwards (Figure 4.17a). On the other hand, Figure 4.17b illustrates how the refractive index exhibits a minimal shift for small concentrations of solvent. The water-alkoxide ratio R_{wa} is a crucial parameter to control, since it affects the chemical reactions (hydrolysis and condensation) and also the physical properties t_f and n. Figure 4.17c exemplifies the trends for t_f and n (Fardad, Yeatman *et al.*, 1995).

Effect of spin coating velocity on film thickness

$t_f = K\omega^{-\gamma}$

% solvent

a
b
c

t_f $\qquad$ n_{sc} (rpm)

(a) t_f Vs. n_{sc}

Effect of spin coating velocity on index of refraction

a
b
c

% solvent

n_{sc} (rpm)

(b) n Vs. n_{sc}

Effect of water-alkoxide ratio on film thickness and refractive index

n

t_f

n_{sc} = constant

1 $\quad R_{wa} \quad$ 5

(c) t_f Vs. R_{wa}
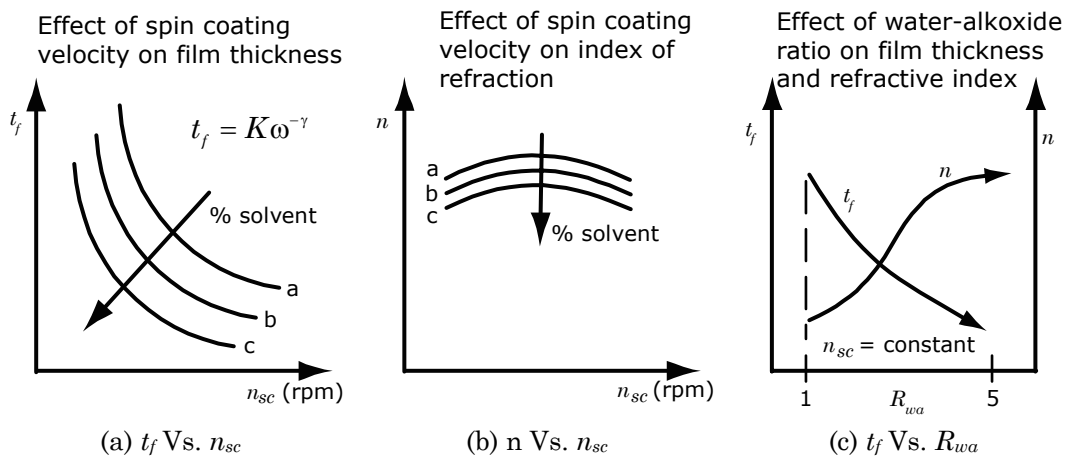
Figure 4.17. Trends in spin coating of sol-gel films

4.4. Importance of Thermal Processing

The result of a chemical synthesis by the sol-gel route under acidic catalysis of thin films or monoliths is a highly porous structure (Brinker and Scherer, 1990). Therefore the sol-gel structure is thermally processed in order to increase the density, while at the same time removing the organic components and promoting further condensation of the network. Figure 2.2 presented a graphical depiction of the evolution of the sol-gel network's microstructure as the temperature is increased.

As the temperature is increased, the organic solvent and residual water (byproduct or unreacted) are diffused out of the structure. In addition, the pores begin to collapse and the structure begins to shrink dramatically. Shrinkage values can reach 30–40%, or even more. From a macroscopic viewpoint, the refractive index of the bulk begins to shift. Residual stresses in the material are also induced during these large physical changes. In some instances, large residual stresses result in catastrophic failure or cracking of the sol-gel. Some of these physical changes were exemplified in Step 5 of Figure 4.2.

The thermal history has a great effect on the final structure and density of the sol-gel (Brinker, Scherer *et al.*, 1985). In this respect, and as pointed out in the work of Keddie and Giannelis, the heating rate, besides the maximum temperature, plays a key role in this structural evolution (Keddie and Giannelis, 1990; Keddie and Giannelis, 1991; Keddie, Braun *et al.*, 1994). This is even more important for sol-gel systems that present crystallization, which is the case of the Ti-doped sol-gel of System #2. When a fast heating rate is used in non-crystal-line systems, the resulting structure is less crosslinked, and therefore is easier to

sinter. The shrinkage is independent of the heating rate, while the viscosity depends on both the current temperature and the thermal history (Keddie, Braun *et al.*, 1994). For systems that exhibit crystallization this phenomenon becomes more complicated, and a competition between densification and crystallization is observed (Keddie and Giannelis, 1991). The combination of high heating rates and short dwell times is preferable for such sol-gel systems, as pointed out in the work of (Holmes, Syms *et al.*, 1993; Syms and Holmes, 1994) for multi-layer thick films. Typical heating temperatures can range between 400 up to 1200°C.

In contrast, the hybrid organic-inorganic sol-gels are processed at lower temperatures in order to preserve the organic polymeric components. The thermal cycle for the hybrid sol-gel films can include an 80–100°C pre-bake for a few minutes to stabilize the matrix and remove some residual solvent near the surface. This can be followed by a post-UV exposure step at ~105°C to harden the material and conserve good feature resolution, similarly to photoresists (Plummer, Deal *et al.*, 2000). A final hard-bake step at temperatures of 140–180°C is performed for several hours and in some cases under vacuum to drive off the residual solvent (Fardad, Mishechkin *et al.*, 2001). Diffusion of unreacted photoinitiator has also been pursued to leave a stable film (Bae and Park, 2001).

The physicochemical evolution of the sol-gel matrix is studied by spectroscopic techniques, such as Fourier Transform Infrared (FTIR) and UV-visible spectroscopy, and by electron microscopy techniques, including Scanning Electron Microscopy (SEM). FTIR, UV-vis, AFM, SEM and optical microscopy were employed in this research to study the behavior of the various sol-gel systems at different processing temperatures, with the main goal of designing an optimal or close to optimal thermal process.

From a processing standpoint, the observations made above translate to the need for controlling four main aspects of the thermal process:

1) Heating rate, $\Delta T / \Delta t$

2) Maximum temperature, T_{max}

3) Heating cycle or dwell times, t_{dwell}

4) Atmosphere during thermal treatment: O_2, N_2, He.

These are essentially the main *Design Parameters* (DPs) of the thermal process.

Some of the main challenges for the thermal processing phase are related to cracking and shrinkage of the film. Cracking of sol-gel films or monoliths is associated to the large shrinkage that occurs during thermal processing and to residual stresses at the evaporation stage of the film deposition. It can be controlled or avoided though a chemical approach: hybrid sol-gels, or a process control approach: rapid thermal processing. On the other hand, shrinkage is related to the chemical composition, as documented by (Fardad, Yeatman *et al.*, 1995; Du and Almeida, 1997), and to processing parameters such as the heating rate and maximum temperature.

From a Design Methodology perspective, the *Performance Metrics* (PMs) of the thermal process include:

1) Refractive index, n

2) Film thickness, t_f

3) Surface roughness (average), R_a

4) Crack-free film

A more detailed design of the thermal process should also consider the transformation temperatures, which can be characterized by techniques such as Thermogravimetric Analysis (TGA) and Differential Thermal Analysis (DTA)

(Brusatin, Guglielmi *et al.*, 1997; Que, Zhou *et al.*, 2001). These techniques, in combination with FTIR, UV-vis, and XRD, provide a full picture for the selection of the right combination of DPs.

4.5. Design of Thermal Process

The design of the thermal processing stage must take into account the optimization of the Performance Metrics (PMs) mentioned above, by manipulating and controlling the Design Parameters (DPs), also mentioned above. The embodiment of the thermal processing stage will thus be comprised by a set of stages of temperature versus time, in a certain atmosphere, and the equipment where the processing will occur. This section and the next will briefly discuss some of the DPs and how they are controlled, along with the equipment used during this research.

4.5.1. Atmosphere

The nature of the atmosphere surrounding the sol-gel film during thermal processing is equally if not more important that it is during the deposition stage. The interaction between the atmosphere and the film strongly depends on the temperature. In some cases the atmosphere can diffuse into the film or react with it, causing a negative impact on certain properties. For this reason, the selection of the appropriate atmosphere plays an important role in the fabrication of high quality optical films and components.

163

In the case of purely inorganic sol-gel films it has been reported that a nitrogen enriched atmosphere employed during thermal processing results in films with poor surface quality (Holmes, Syms *et al.*, 1993). By contrast, the use of a standard air or oxygen-based atmosphere produces films with a chemical composition highly similar to silica (SiO_2). The use of helium has been reported to produce films with very low surface roughness, because of the small size of the helium atoms (Klein, 1988; Bräutigam, Bürger *et al.*, 1989). The use of different gasses during low- and high-temperature stages has also been suggested. For example, Parrill has reported on the use of an O_2:N_2 mixture with 1:3 ratios for temperatures below 500°C, and N_2 only for temperatures above 500°C for inorganic silicate sol-gels (Parrill, 1994). Most of the studies found in the literature regarding structural evolution with temperature change, suggest the use of either standard air or O_2 with a low degree of humidity ($\leq 40\%$) (Almeida, Guiton *et al.*, 1990; Syms and Holmes, 1994).

On the other hand, for hybrid organic-inorganic sol-gel systems the use of an O_2 atmosphere inhibits the polymerization process, in particular for photoinduced polymerization (Young and Lovell, 1991; Fouassier, 1995). In this case, the oxygen molecules interact with photopolymerizing systems at the initiation and propagation stages. The presence of oxygen leads to the formation of an inhibition layer in which the diffusion rate of oxygen into the sample from the surrounding environment is more rapid than its consumption by the polymerization. For this reason, an inert atmosphere approach was pursued as the most available solution. Helium and nitrogen were chosen as inert gases for thermal processing of these hybrid sol-gels.

4.5.2. Temperature Profile

During thermal processing, the temperature profile over time plays a crucial role in controlling the structural changes of the sol-gel film. The temperature profile in general consists of a combination of three steps (see Figure 4.18a):

1) Heating. Characterized by a steady temperature increase, and defined by: heating rate $\Delta T_h/\Delta t$ and target temperature T_{max}. The heating rate has a strong relationship to structural changes, in particular to densification and crystallization.

2) Dwell. Characterized by a constant temperature period, and defined by: dwell time t_{dwell} and goal temperature $T_{dwell} = T_{max}$. Dwell time affects time-related structural changes, diffusion-driven processes, and plays a major role in stress release.

3) Cooling. Characterized by a continuous temperature decrease; it is defined by: $\Delta T_c/\Delta t$ and final temperature T_{final}. Cooling rate also has an effect on the structure, particularly affecting crystallization at high temperatures. A two-stage approach is thus recommended: (a) high cooling rate for high temperature ($\geq 400°C$), and (b) lower rates below that temperature.

Based on these three main elements, multi-stage thermal processes can be designed depending on the processing requirements. As mentioned above, a detailed design of a thermal cycle requires a thorough knowledge of the transformation temperatures, which can be obtained with the aid of techniques such as TGA, DTA, FTIR, and XRD.

Three typical thermal cycles for inorganic silicate sol-gels (System #1) are shown in Figure 4.18a. These profiles were used during preliminary experiments. As seen from the graph, there are two profiles with a heating rate of 4°C/min and T_{max}=(200,400)°C, and a high heating rate of 8°C/min with T_{max} = 800°C. On the other hand, Figure 4.18b shows a series of closely spaced profiles intended for a detailed study of the thermal evolution of the film, and it includes a low temperature "drying" step done at T_{drying}=150°C.

Inorganic silicate sol-gels similar to System #1, exhibit a decrease in refractive index and increase of the in-plane tensile stress due to elimination of residual water at temperatures below 800°C (Parrill, 1994). On the other hand, film thickness is strongly dependent on processing temperature T_{max}, and temperatures below ~900°C yield incompletely densified films (Syms and Holmes, 1994). These high temperatures can present an obstacle for the

(a) initial profiles

(b) profiles for heat treatment study
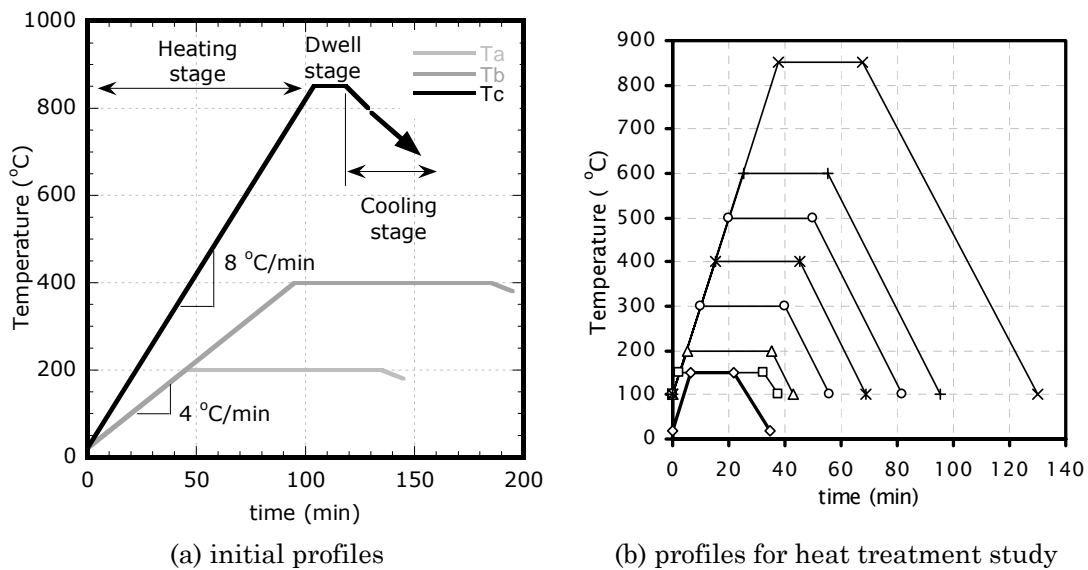
Figure 4.18. Examples of thermal processing cycles

166

(a) thermal cycles for System #2   (b) thermal cycles for System #3
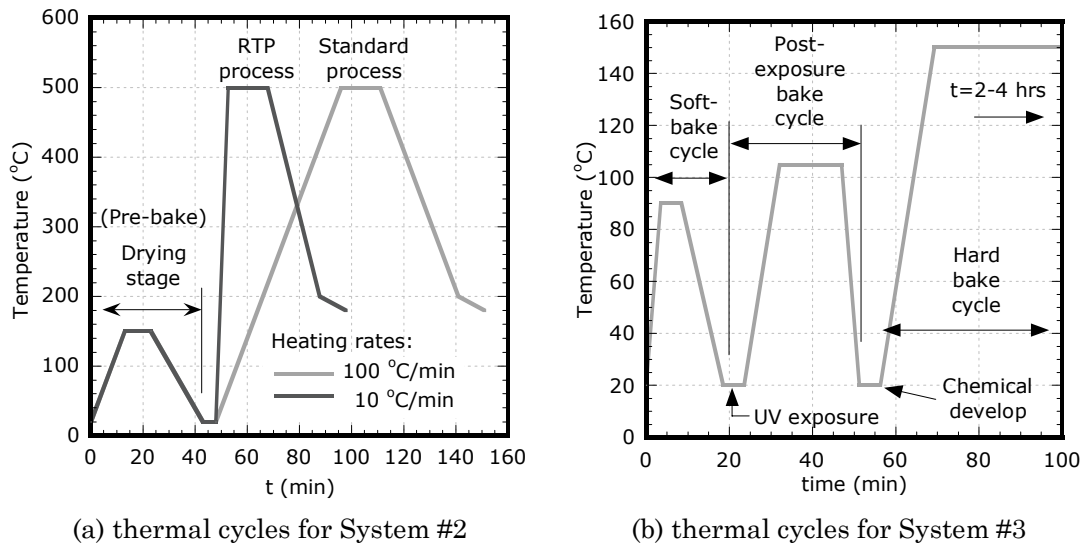
Figure 4.19. Thermal cycles for hybrid sol-gels

development of a freeform fabrication process, mainly from a hardware standpoint, due to the heavy insulation and costly corrosion and creep resistant requirements. Nonetheless, it is possible to operate at temperatures around 500°C, and still obtain good results (Guglielmi, Martucci *et al.*, 1998).

The design of the thermal process for a doped sol-gel system, such as for System #2 which is doped with titanium, must take into account the potential formation of unwanted phases. Such is the case of titania (TiO_2) and titania-silica (TiO_2–SiO_2) glasses, where Ti can form rutile or anastase phases (Keddie and Giannelis, 1991). The sol-gel System #2 also contains an organic component (MTES), which must be considered as well. Sol-gels derived from TEOS and MTES alkoxides can approach the structure of purely inorganic sol-gels if heated above ~650°C (Brusatin, Guglielmi *et al.*, 1997; Gallardo, Duran *et al.*, 2002).

Figure 4.19a illustrates typical thermal cycles for sol-gel films of System #2. Two different cycles are shown: (1) rapid thermal processing (RTP), and (2) standard process. Both cycles begin with a low temperature "drying" step with T_{dry} =150°C, typically performed under O_2 atmosphere. This step helps promote further condensation. After drying, the RTP process begins with a high heating rate step, in this case 100°C/min, followed by a short dwell and a tow-step cooling stage. Much greater heating rates can be achieved by industrial RTP furnaces found in the microelectronics industry. The hardware used in this research was limited to that heating rate as a maximum. The two-step cooling stage is intended to avoid crystallization by a high rate first phase, followed by a slower second phase, intended to reduce residual stress buildup.

Thermal processing for the photosensitive hybrid sol-gels of System #3 is performed at lower temperatures. Figure 4.19b illustrates a typical profile that consists of three cycles: (1) Soft Bake (SB) at low temperature and performed immediately after deposition to slightly harden the film, (2) Post-Exposure Bake (PEB) at medium temperature to improve feature resolution and adherence to substrate after UV-laser processing, and (3) Hard Bake (HB) at high temperature (<200°C) for a long period of time to remove residual solvent after the chemical development step. This procedure emulates a typical thermal cycle performed on photoresists used for microelectronics manufacturing (Plummer, Deal *et al.*, 2000; Campbell, 2001). The processing temperatures are based on the work of (Fardad, Andrews *et al.*, 1997; Fardad, Mishechkin *et al.*, 2001).

The next section describes the equipment used for thermal processing, including design modifications based on the thermal cycles described above.

4.6. Design of Thermal Processing Equipment

Based on the description of the various thermal cycles outlined in the previous section, three main requisites can be identified: (1) low temperature processing for drying and hybrid sol-gels (80–200°C), (2) rapid thermal processing for inorganic and hybrid sol-gel (200–900°C), and (3) mid-level thermal processing suitable for long periods of time for annealing purposes (200–950°C). In addition to these three requirements, there is the ability to control the atmosphere through various types of gases (O_2, N_2, He, or a mixture), as well as the capability of programming thermal cycles based on the three main elements described in Section 4.5.2. As a result three different furnaces were chosen and employed for thermal processing experimentation. Below is a brief description of each of the furnaces.

| (a) front view | (b) side view |
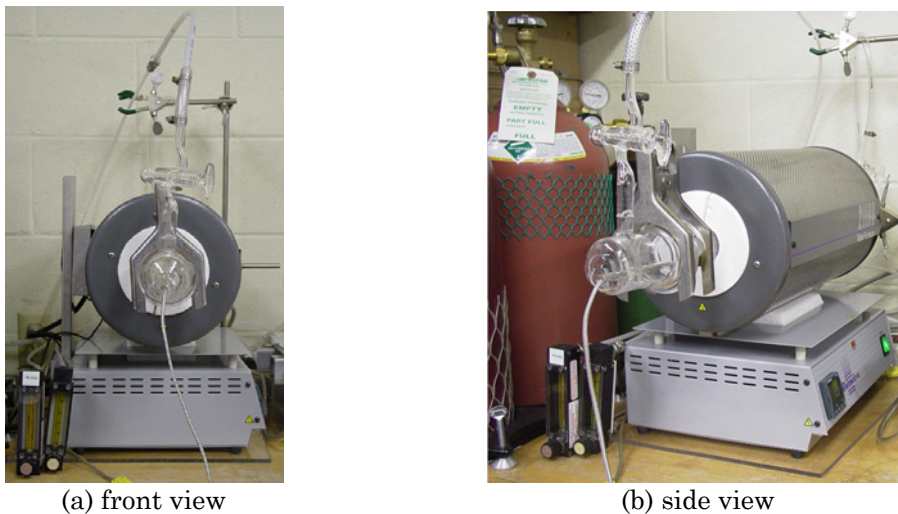
Figure 4.20. Tube furnace

4.6.1. Tube Furnace

Thermal processing at mid and high temperatures ($150 \leq T_{max} \leq 950°C$) with slow to moderate heating rates ($0.5 \leq dT/dt \leq 15°C$/min) was performed in a tube furnace; shown in Figure 4.20. The commercial furnace was modified in two main ways. First, a PID temperature controller by Eurotherm (model 2416) was installed, in order to achieve an accurate multi-stage control of the temperature profile over time. The controller was properly calibrated by the auto-tuning feature for low heating rates, and manually by a step response plot for high heating rates. The second modification involved the use of a thermocouple inserted at the middle of the processing quartz tube, to measure the temperature directly at the sample. Figure 4.21 illustrates the position of the thermocouple and the sample inside the quartz tube. In addition to this, the furnace was quipped with the capability of employing several transporting gases (He, O_2 or N_2) by means of a manifold and the gas entries welded to the front and back glass joints.
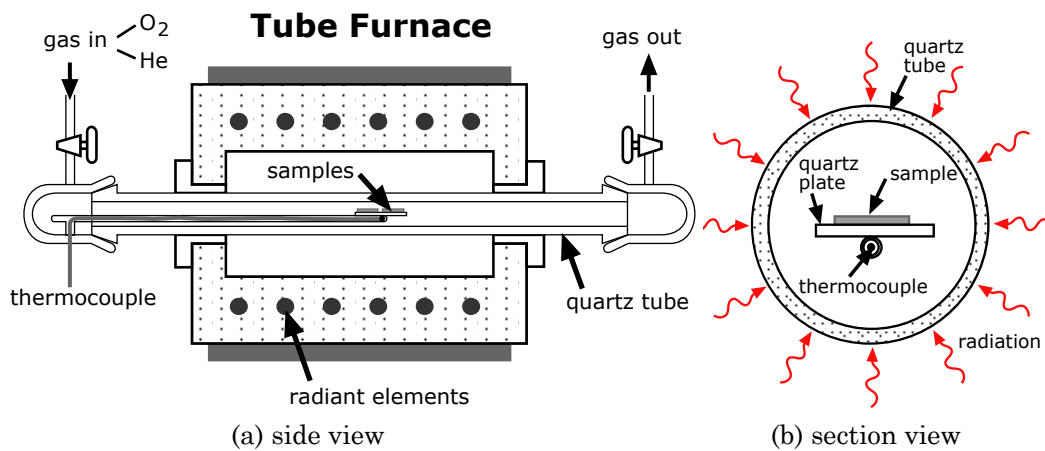
Figure 4.21. Schematic of tube furnace

4.6.2. Hot Plate

For the low temperature "drying" and softbake of the sol-gel films, a hot plate was designed to incorporate the requirements mentioned in Section 4.5.2. The hot plate is heated by two insert heating elements. The temperature at the center of the hot plate is measured by a thermocouple (type G), and controlled by a PID controller from Eurotherm. The hot plate was made of aluminum in order to transmit the heat rapidly and evenly. Atmosphere control is achieved by placing the hot plate inside a glass chamber, designed from glass flat joints, adapted with gas inlet and outlet for the same atmospheres as the tube furnace (He, O_2, and N_2). Figure 4.22 presents top and side views of the hot plate and temperature controller.
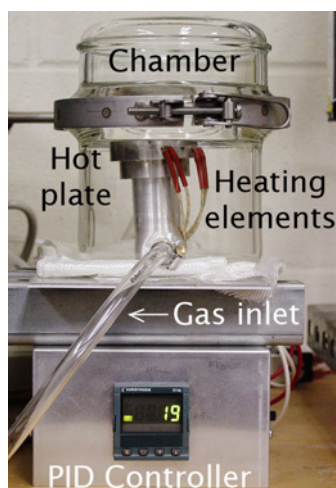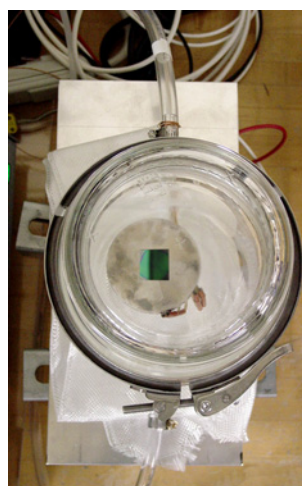
(a) side view   (b) top view

Figure 4.22. Hot plate with controlled atmosphere

4.6.3. Rapid Thermal Processing Furnace

For rapid thermal processing (RTP), a small experimental furnace was designed and built. Pictures of the RTP furnace are shown in Figure 4.23. The RTP furnace is comprised by a sealed processing chamber with a controlled atmosphere by a flowing gas (He, O_2, or N_2). Inside the chamber there is a quartz sample-holder that places the sample near the top quartz plate to receive the thermal radiation, leaving a small air gap to avoid turbulence near the sample's surface.

The high heating rate is achieved through a $MoSi_2$ coil (by Micropyretics Heaters International, Inc.) placed above the sealing quartz plate and surrounded by a dome-shaped cover of insulating material (alumina-silica, by Zircar Ceramics). This heating element can reach 1500°C in less than two minutes at maximum power; though the temperature of the sample is heated at a slower

(a) front view   (b) detail showing sample placement
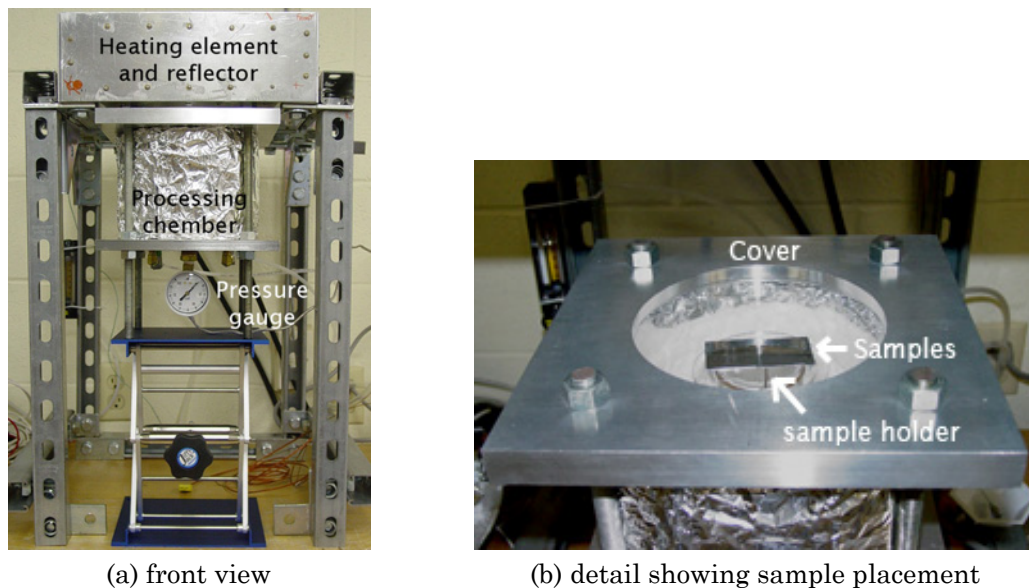
Figure 4.23. Rapid thermal processing furnace

rate (approximately 100–400°C/min), since the temperature drops quadratically with the distance. The MoSi$_2$ coil draws a maximum current of 100 Amp, which is provided by a high-power transformer and controlled by a solid state SCR connected to a PID controller, both by Eurotherm. Figure 4.24 presents a diagram of the RTP furnace, showing the different parts. A rapid response K-type thermocouple placed right below the sample senses the temperature, which is fed back to the PID controller. An R-type thermocouple is also used to monitor the coil's temperature and avoid overheating.

The heating rate obtainable by this experimental furnace is far below that of commercial devices, which can be up to 8000°C/min; yet it is high enough compared to the rates achieved by the tube furnace.
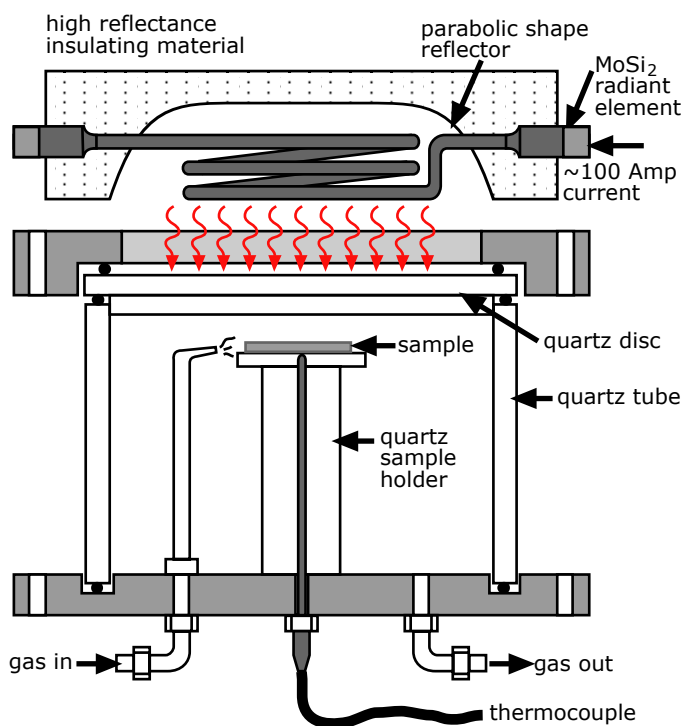
Figure 4.24. Schematic inner view of RTP furnace

4.7. Experimentation: Silicate Sol-Gels

This section presents experimental results of thermal processing of inorganic silicate sol-gels, corresponding to System #1. Three main effects are studied: maximum processing temperature, low temperature drying, and the heating rate to achieve multi-layer deposition.

4.7.1. Effects of Maximum Processing Temperature

As mentioned above, the design of an appropriate heat treatment process is crucial for the fabrication of uniform crack-free films. This can be observed by comparing Figure 4.25(a) and (b), where the highly porous nature of the as-spinned films is evident, while almost completely disappearing at high processing temperatures (~800°C). An important tool to help define the heat treatment profile is a TGA analysis. Figure 4.26 shows the results of a TGA for an inorganic sol, which was left to dry at normal atmospheric conditions and then crushed into a fine powder with a mortar. The change in weight takes place in three stages: (1)

(a) 20°C	(b) 600°C
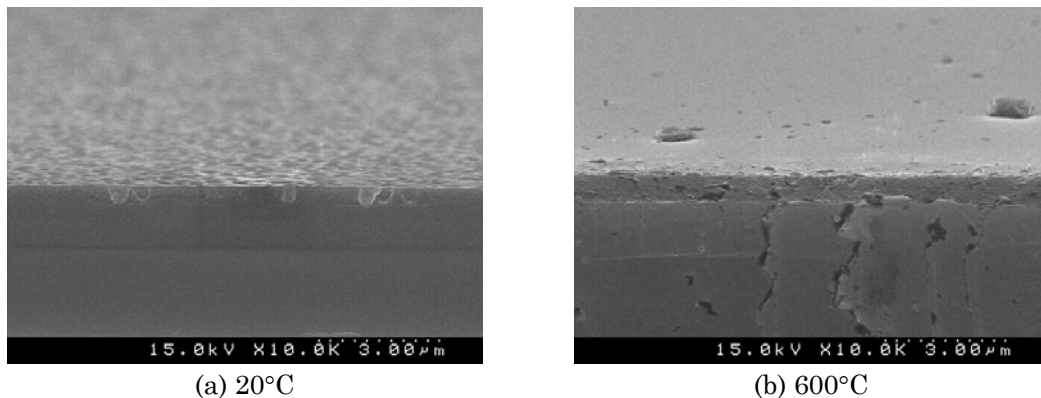
Figure 4.25. SEM images of inorganic sol-gel films comparing porosity
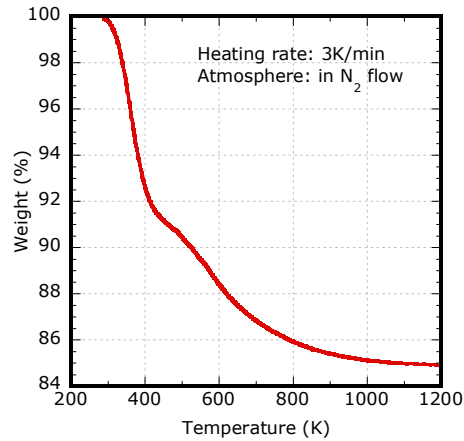
Figure 4.26. TGA plot for inorganic silicate sol-gel

T<400 K, (2) 400<T<530 K, and (3) T>530 K. During the first stage, the rapid decrease in weight is mainly attributed to the evaporation of water and the volatilization of remaining ethanol.   In the second stage, a slower weight reduction rate is attributed to the combustion of organic compounds (Primeau, Vautey *et al.*, 1997). The final stage is characterized by a slight increase weight reduction rate and then it gradually decreases until it stabilizes at ~84%. This result suggests sintering followed by viscous flow of the SiO_2 structure.

Figure 4.27 presents plots of the film thickness and refractive index versus temperature for two different mixtures (7 and 18). The main difference between these mixtures is the water-alkoxide ratio: R_{wa}(#7)=1, R_{wa}(#18)=1.6.   As seen from the graph of Figure 4.27a, the film thickness decreases as the temperature is increased, occurring at similar rates for both mixtures.   Not shown in this graph, a large decrease in thickness occurs between room temperature (~20°C) and ~120°C, where the thickness decreases ~30%, mainly due to

175

(a) thickness   (b) index of refraction
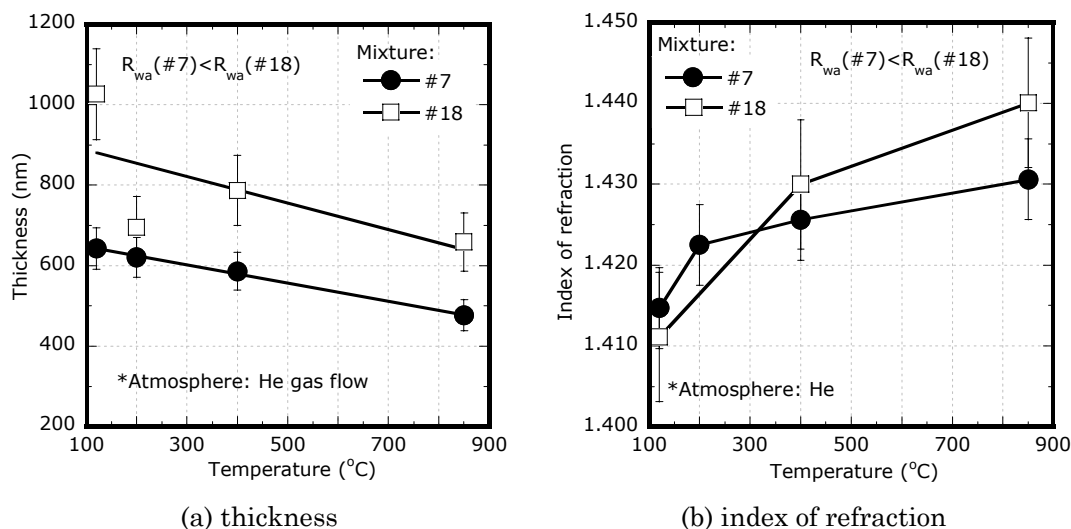
Figure 4.27. Temperature effects on two silicate sol-gel compositions

solvent evaporation. This result is consistent with the TGA graph of Figure 4.26. The change in refractive index with temperature is shown in Figure 4.27b. In this case, the refractive index exhibits a different behavior at low temperatures (<200°C) than at high temperatures (≥400°C). Above 400°C a slower increases rate is observed, as the sol-gel film is densified by viscous flow. The main difference observed between these two mixtures is that a greater water content on the mixture results in a thicker film and higher refractive index.

Continuing with the thermal processing analysis for the inorganic sol-gel, Figure 4.28 presents the FTIR analysis results for three different temperatures. Some of the main peaks are identified and labeled. These plots reveal the presence of a high organic content at room temperature. Also, it can be observed that the peak of the transverse optic (TO) component of the asymmetric stretching mode (Almeida, 1998) becomes more visible and exhibits a shift towards higher wavenumbers as the temperature is increased. On the other

176
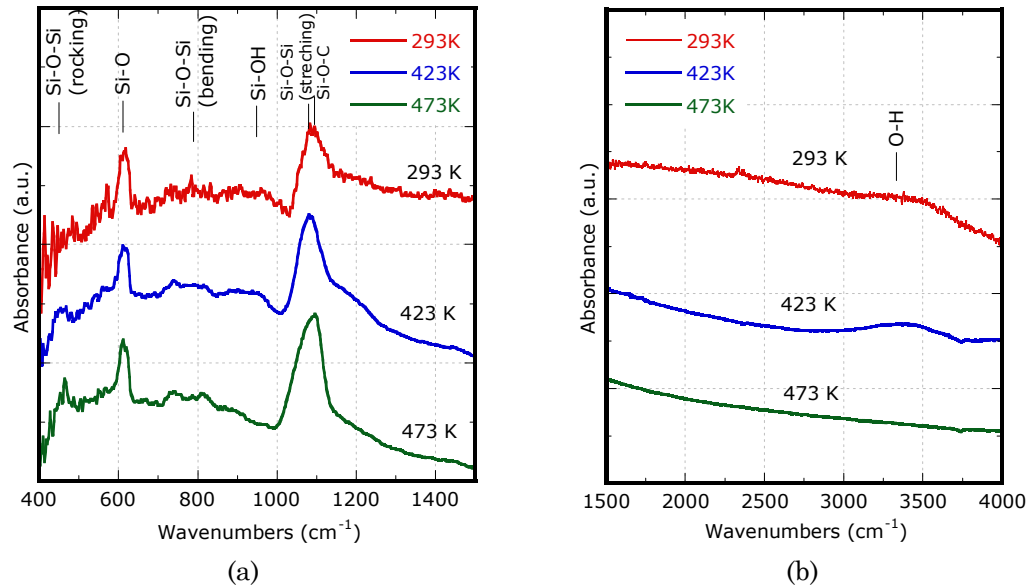
Figure 4.28. FTIR absorbance spectrum for three different processing temperatures for silicate sol-gel mixture #7

hand, the broadband around 3400 cm^{-1} begins to banish at high temperatures. This band is related undesired hydroxyl groups (OH$^-$), which are associated to absorption optical losses.

4.7.2. Effects of Drying

An important part of designing a thermal process suitable for a freeform fabrication approach is to investigate the option of low temperature processing. For this reason, an intermediate "drying" step at mid- to low-temperature was studied. From preliminary experiments for the successful fabrication of crack-free multi-layer films and based on the results presented by (Guglielmi, Martucci *et al.*, 1998), a low temperature step was proposed to be added prior to high-temperature sintering, in order to aid in the further condensation and cross

177

branching of the sol-gel. This low-temperature step consists basically in placing the sample in a hot plate with controlled atmosphere (see Figure 4.22) immediately after the film deposition by spin coating, and heating the sample to 150°C for a few minutes. A $2^1 \cdot 3^1$ DOE was developed for this study, where the DPs are: (1) Atmosphere ={No drying, He, O_2}, and (2) T_{max} ={400,880} °C. A total of six runs and a replicate for each resulted in 12 experiments. The experimental conditions are shown in Table 4.2.

For this study the mixture labeled as DOE#3 from Chapter 3 (see Figure 3.12) was employed. This mixture was prepared by the two-step hydrolysis procedure that was developed, employing the following ratios: Step 1 → R_{wa}=1, R_{sa}=3; Step 2 → R_{wa}=2, R_{sa}=3. The mixture was labeled as #25.

The low-temperature "drying" step was performed in a hot plate under He or O_2, with a temperature of 150°C for 15 minutes. After this, the samples were heated at $\Delta T_h / \Delta t$ =8°C/min until the desired temperature T_{max}, and held there for 20 min under O_2. Then the temperature was ramped down to 200°C at a rate of

Table 4.2. Parameters for drying study on silicate sol-gel films

Sample ID	T_{drying} (°C)	Drying atm.	T_{max} (°C)	Baking atm.	Thickness, t_f (nm)	Refractive index, n	MSE
25-st2-1-1	150	He	400	O_2	638.14	1.4029	21.76
25-st2-1-2	150	He	400	O_2	646.82	1.4029	20.67
25-st2-2-1	150	He	880	O_2	539.79	1.4165	7.97
25-st2-2-2	150	He	880	O_2	495.34	1.4146	19.30
25-st2-3-1	150	O_2	400	O_2	515.09	1.4047	19.59
25-st2-3-2	150	O_2	400	O_2	482.15	1.4036	17.07
25-st2-4-1	150	O_2	880	O_2	495.09	1.4198	19.46
25-st2-5-1	--	--	400	O_2	522.90	1.4036	20.59
25-st2-6-1	--	--	880	O_2	469.65	1.4171	5.22

4°C/min. Table 4.2 shows the various conditions, together with the values for thickness and index of refraction. A graph of these last two parameters for each experimental condition is shown in Figure 4.29c.

FTIR transmission spectroscopy was employed to compare these samples, and the results are presented in Figure 4.29a. The transmittance (T) data obtained from FTIR was converted to absorbance (A) by the following formula:

$$A = -\log_{10}(T) \tag{4.7}$$

The following observations can be made based on the absorbance plots of Figure 4.29a (Note: this figure shows only the ranges of interest where most of the structural information is found, according to Almeida, 1998). The peak for

Main Peaks (cm^{-1})				
Sample ID	Si-O-Si TO mode	Si-OH stretching	Si-O bending	O-H stretching
25-ST2-1-1	1076	964	800	3444
25-ST2-2-2	1078	none	798	none
25-ST2-3-2	1074	962	800	3446
25-ST2-4-1	1076	none	798	none
25-ST2-5-1	1074	962	502	3444
25-ST2-6-1	1081	none	800	weak

(b) peaks from FTIR

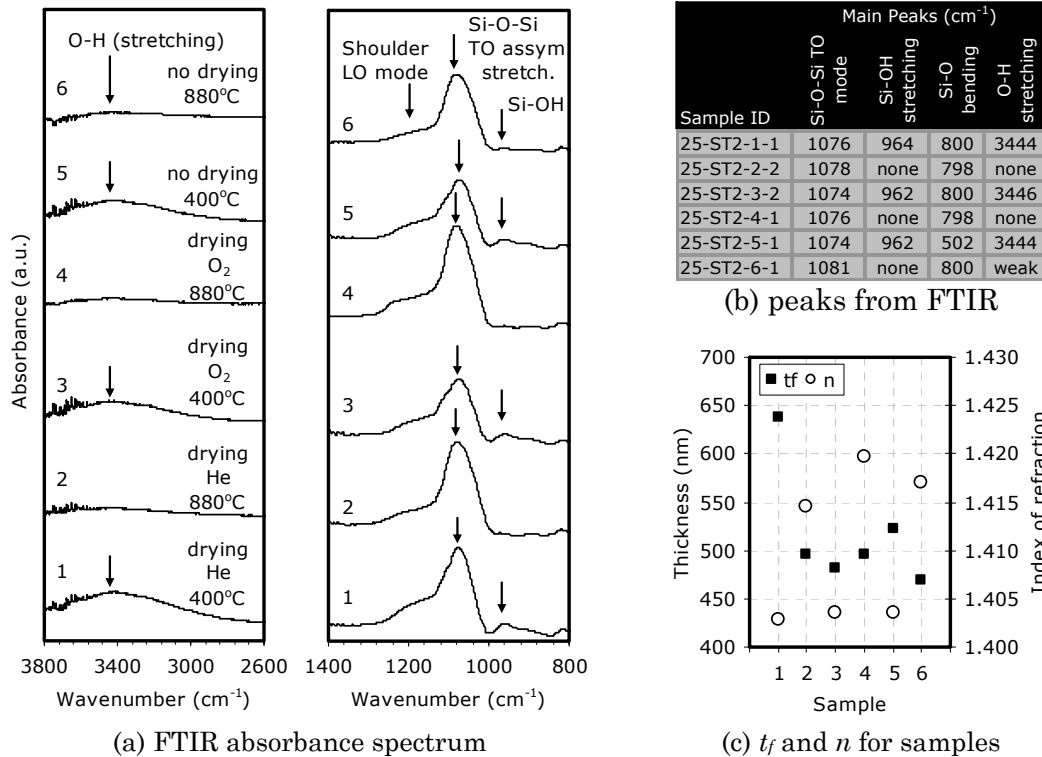(a) FTIR absorbance spectrum

(c) t_f and n for samples

Figure 4.29. Effects of temperature and atmosphere on silicate sol-gel

179

the transverse optic (TO) asymmetric stretching mode for Si–O–Si, centered on ~1970 cm^{-1}, exhibits a substantial increase and slight shift for each group of samples going from 400°C to 880°C. For sample 4 (drying in O_2, T_{max}=880°C), the TO peak is ~8% higher than for sample 2 (drying in He, T_{max}=880°C), and ~24% higher than for sample 6 (no drying, T_{max}=880°C). A strong TO peak has been associated with a network that has low porosity (Almeida, Vasconcelos *et al.*, 1994; Almeida, 1998). This result suggests that the low-temperature drying step with oxygen is beneficial to obtain a low porous network. Peaks for the Si–O–Si bending mode (~800 cm^{-1}) shift slightly to lower wavenumbers for samples heated at higher temperatures. This shift has been correlated to stress relief phenomena (Ramkumar and Saxena, 1992; Ramkumar, Ghosh *et al.*, 1993).

In samples heated at 400°C there is a broad band around 3400 cm^{-1} corresponding to O–H stretching in H_2O, which is evidence of remaining H_2O in the film. This shoulder almost completely disappears for samples heated at

Table 4.3. FTIR peak's analysis for drying experiments (system #1)

	Sample					
	25ST2.1.1	25ST2.2.2	25ST2.3.2	25ST2.4.1	25ST2.5.1	25ST2.6.1
	Drying	Drying	Drying	Drying	No drying	No drying
	He	He	O_2	O_2	---	---
Group	440°C	880°C	440°C	880°C	440°C	880°C
SiC$_6$H$_5$	667	667	667	667	667	669
Si-O-Si Bending	800	798	800	798	802	800
Si-O-Si Stretching	1076	1078	1074	1076	1074	1082
Shoulder LO mode	1207	1213	1201	1243	1201	1214
Si-OH	964	No peak	962	No peak	962	No peak
OH-Bonds	Weak	No peak	Weak	No peak	Weak	Weak
Iso-thiocyanates	2360	2360	2360	No peak	2361	2360
Si-O-Si Rocking	444	449	445	451	442	449
SiO-OH	Weak	Weak	Weak	Weak	Weak	Weak

880°C. This is desired for optical communications, since hydroxyl groups are generally associated with attenuation loss. In sample 4, it is also observed that there is no presence of SiC_6H_5, appearing around 667 cm^{-1}. The peak at ~960 cm^{-1} is related to the Si–OH stretching mode (Almeida and Pantano, 1990). This peak is absent in samples heated to 880°C, irrespective of whether the sample was dried in O_2 or He. Table 4.3 provides a summary of the peaks and the corresponding group found for each sample.

The shoulder on the high frequency portion of the TO peak, between 1200–1140 cm^{-1}, has been associated to the longitudinal optic (LO) component of
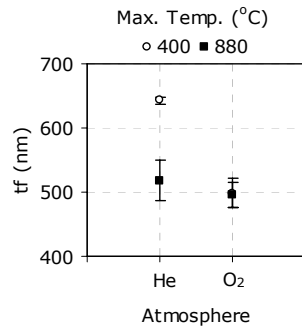
(a) effect of atmosphere on film thickness
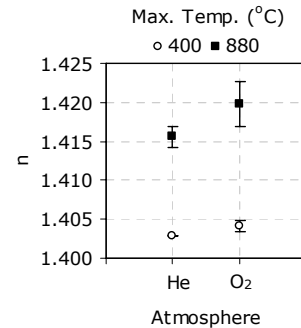
(b) effect of atmosphere on refractive index
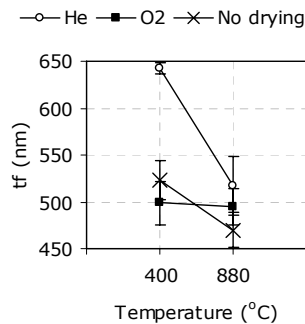
(c) effect of maximum processing temperature on film thickness
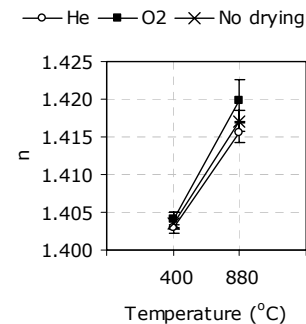
(d) effect of maximum processing temperature on refractive index

Figure 4.30. Effects of thermal processing parameters – silicate sol-gel

the Si–O–Si (Almeida and Pantano, 1990). As seen from Figure 4.29a, for every set of samples the increase in T_{max} resulted in an attenuation of the LO mode. As suggested by (Gallardo, Duran *et al.*, 2002), this effect occurs during sintering of the SiO_2 structure; noting that this observation is valid only for the case of normal incidence FTIR. So the LO mode provides some important information about the porosity of the film.

Drying in O_2 results in no formation of C–H bonds (related to the ethoxy groups, OCH_2CH_3), which are found in the range of 1400–1800 cm^{-1} (not shown in Figure 4.29a), while on the rest of the samples they are still present.

Figure 4.30 provides a series of plots that summarize the effects of the individual design parameters (atmosphere, T_{max}) on the performance metrics (film thickness and refractive index). These plots, along with the FTIR spectra, provide a more comprehensive picture of the effects on the drying step. Overall, results from the plots of Figure 4.30 reinforce the observations made from the FTIR, where the drying step in oxygen produces a denser film that exhibits less shrinkage in the region between 400–880°C.

4.7.3. Multiple Layer Deposition

Inorganic silicate sol-gels made by spin-coating tend to have a thickness between 200–700 nm for a single layer. This thickness is far from the minimum required for single mode wave propagation; for example, for λ=638 nm and Δn=0.01, $t_{f\ min} \approx$ 0.8–1.2 μm (Righini and Pelli, 1997; Hunsperger, 2002). For this reason, multiple layers must be deposited in order to achieve this minimum thickness.
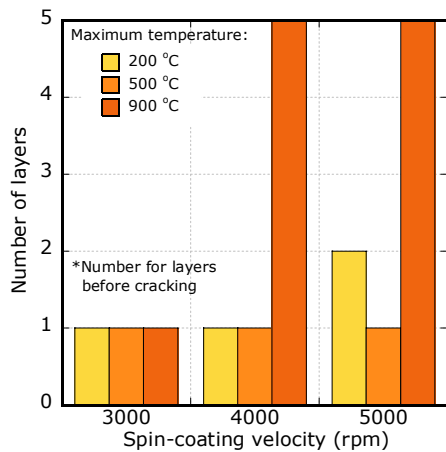
(a) effect of spin coating velocity of maximum number of layers
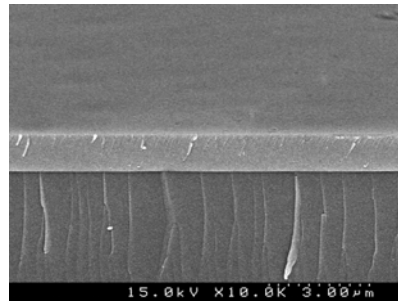
(b) SEM image of a multi-layer film

Figure 4.31. Multi-layer silicate sol-gel film

The deposition of subsequent layers of inorganic silicate sol-gel represents a technical challenge because of the development of cracks in the film due to residual stresses, or impurities in the form of particles. Extensive research has been reported on this issue (Ramkumar, Ghosh *et al.*, 1993; Syms, 1994; Syms, 1994; Syms and Holmes, 1994). Some solutions to the multi-layer deposition problem have involved the use of rapid thermal processing (RTP) or a series of clever modifications to the deposition and thermal processing cycles.

A series of experiments were performed changing the spin coating velocity and the maximum processing temperature, and observing the number of layers deposited prior to cracking of the film. For these experiments the sol labeled as Mixture #7 from Table 3.5 was used, and the samples were placed in the tube furnace of Figure 4.20. The results are depicted in the bar chart of Figure 4.31a, where it is observed that low spin coating velocity, regardless of the temperature, results in cracking after the first layer is deposited. As the deposition velocity is

increased, more layers can be deposited. This is due mainly to the fact that low velocity produces thicker films, and increased residual stresses. Figure 4.31b shows an SEM image of a successful multi-layer silicate sol-gel, with a final thickness of ~2μm, manufactured at 4500 rpm and T_{max}=850°C.

In summary, the successful deposition of crack-free multi- or single layer inorganic silicate sol-gel films requires high spin coating velocities that produce thinner films (small diffusion path, and lower residual stresses), and high temperatures (>500°C, preferably 900°C) achieved at high rates (>20°C/min).

4.8. Experimentation: Ti-doped Hybrid Sol-Gel

Following a similar procedure as for the inorganic silicate sol-gel, the current section presents experimental results for the thermal processing of titanium-doped hybrid sol-gel (System #2). As mentioned in Section 4.5.2, because of the addition of titanium in the sol-gel System #2, there is a potential formation of unwanted phases as a result from crystallization of TiO_2 in the form of anastase or rutile. So this section explores the effects of the maximum processing temperature on the structure of the sol-gel film.

4.8.1. Effects of Maximum Processing Temperature

To study the effects of the maximum temperature on the hybrid titanium-doped sol-gel, six different target temperatures were chosen and replicates of each experiment were produced. The mixture chosen for these experiments corresponds to #5 in Table 3.9. The sol was diluted in ethanol to 50%, and 200 μl

Table 4.4. Results for heat treatment study of Ti-doped hybrid sol-gel

			t_f (nm)		n		error (%)	
Exp	Samples	T_{max} (°C)	avg	stdv	avg	stdv	t_f	n
1	H1p2, H2p2	200	274.77	47.12	1.4702	0.0013	17.15	0.09
2	H1p3, H2p3	300	270.82	46.80	1.4662	0.0016	17.28	0.11
3	H1p4, H3p4	400	229.65	3.31	1.4633	0.0032	1.44	0.22
4	H1p5, H3p5	500	212.07	0.54	1.4824	0.0052	0.26	0.35
5	H2p6, H3p6	600	211.82	36.02	1.5008	0.0001	17.01	0.01
6	H2p7, H3p7	850	170.95	30.70	1.5239	0.0004	17.96	0.02

were spin coated on 50 mm silicon wafers at 2500 rpm. The coated wafers were dried at 150°C for 10 minutes in O_2, according to the results from the previous section. After this low temperature stabilization step, the samples were cleaved into smaller pieces and thermally treated to the target temperature. Every sample was analyzed by FTIR and ellipsometry techniques.

The target temperatures were: T_{max}={200,300,400,500,600,850}°C; while the heating rate for all experiments was $\Delta T_h/\Delta t$=8°C/min, and the atmosphere was O_2 for the ramp-up stage and He for the rest of the process.

Table 4.4 presents a summary of results obtained from ellipsometry for the six processing temperatures. The table includes average and standard deviation for film thickness and refractive index for the six temperatures and their respective replicates. As seen from this table, the film thickness has the largest error or uncertainty when averaged among samples, while the refractive index has a good numerical fit. This is evidence of the challenge it is to achieve consistent repeatability in sol-gel films.

(a) FTIR absorbance spectrum   (b) ellipsometry data
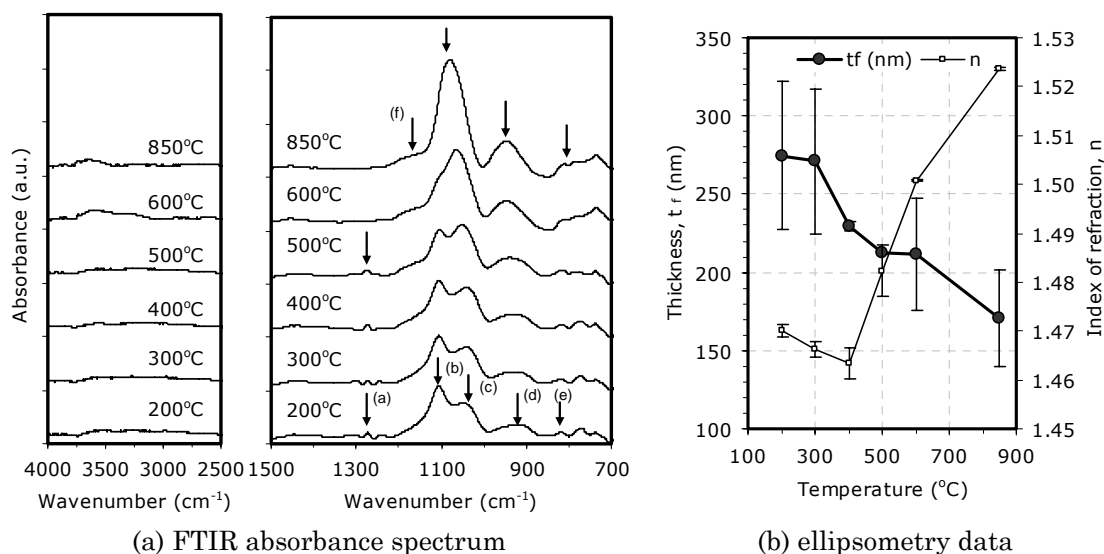
Figure 4.32. Effects of T_{max} on hybrid Ti-doped silicate sol-gel

A graph of the results from ellipsometry is presented in Figure 4.32b, which plots the variation of t_f and n with T_{max}. As expected, the thickness gradually decreases as T_{max} is increased. However, it is worth noting that the decrease in thickness is not as smooth as reported by (Seco, Goncalves *et al.*, 2000), but it can be divided in three main regions, which is similar to the observations made for an undoped hybrid system with the same precursors (MTES and TEOS) presented by (Gallardo, Duran *et al.*, 2002). The reduction in thickness is attributed to densification by the reduction or elimination of the film porosity. On the other hand, the refractive index exhibits a slight decrease at low temperatures ($T_{max} <400°C$), and gradually increases after this temperature.

The structural changes in the film as the temperature is increased were monitored by FTIR spectroscopy. Results for the absorbance at each temperature are reported in Figure 4.32a, for the spectral ranges where most of

186

Table 4.5. FTIR peak's analysis for Ti-doped hybrid sol-gel

Label	Group	Evolution of peaks (cm^{-1}) Temperature					
		200°C	300°C	400°C	500°C	600°C	850°C
(a)	Si-CH$_3$ (residual methyl)	1274	1274	1274	1276	none	none
(b)	Si-O-R stretching of ethoxys	1106	1106	1105	1104	~1102	None
(c)	Si-O-Si transverse optic mode (TO)	1047	1040	1040	1051	1065	1080
(d)	Si-O$^-$ stretching in Si-O-Ti(4$^+$)	927	927	929	938	949	948
(e)	Si-O-Si symmetric stretching						
(f)	Si-O-Si longitudinal optic (LO), or shoulder						

the structural information of interest is found. In this figure, arrows indicate the location of the main peaks of interest with their respective labels. Table 4.5 lists the main peaks and their respective values at each temperature.

As observed in Figure 4.32a, the inclusion of organic components into the sol, adds a number of peaks that persist even at moderate temperatures (<600°C). Such is the case for residual methyl groups bonded to silicon, (a) Si–CH$_3$, which appear near 1275 cm^{-1}. Another peak that appears at low temperatures is attributed to Si–O–R stretching vibrations, where R is an alcohol group, in a region near ~1100 cm^{-1} and overlapping the Si–O–Si band, just as discussed by (Brusatin, Guglielmi *et al.*, 1997). In Figure 4.32a, this peak can be clearly seen at temperatures below 600°C, caused in part due to the high EtOH content required for dilution of Ti species in order to avoid precipitation. After this temperature it vanishes and is overtaken by the Si–O–Si TO mode peak, which becomes sharper at high temperatures. The presence of this

(a) Si–O–Si TO component of asymmetric
    stretching mode

(b) Si–O stretching in Si–O–Ti⁴⁺
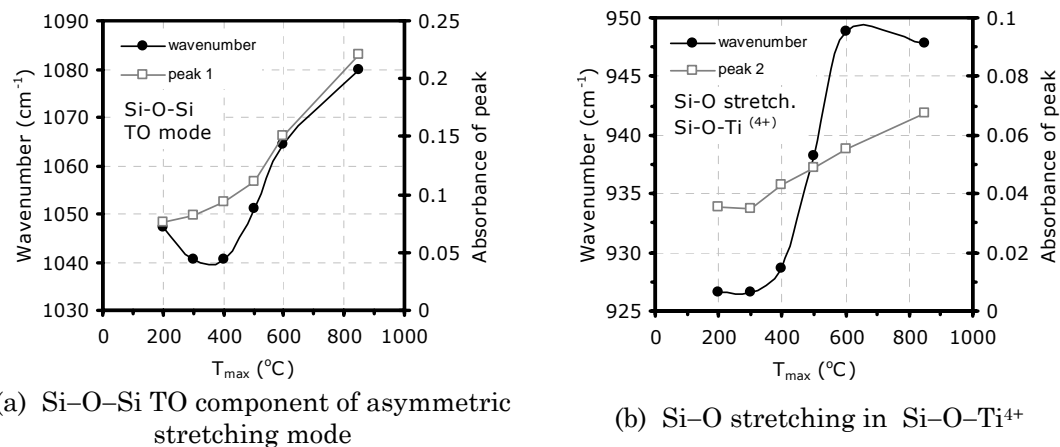
Figure 4.33. Shift of primary peaks with temperature

undesirable Si–O–R peak can be diminished perhaps by lowering the R_{sa} ratio, although this aspect was not fully investigated in this research.

The transverse optic (TO) component of the asymmetric stretching mode of Si–O–Si, which peaks between ~1030–1075 cm⁻¹, was monitored as it shifts and increases in absorbance as the temperature is raised. Figure 4.33a presents a plot of the evolution of the absorbance and wavenumber of the TO peak with temperature. It is clear from this plot that both the magnitude of the peak and the wavenumber increase sharply as the temperature is increased. The increase of this peak is the result of further condensation of the Si–O–Si network. In a similar fashion, Figure 4.33b shows the increase in absorbance and wavenumber as the temperature is raised for the Si–O stretching in Si–O–Ti⁴⁺. For this case, the increase in the peak's absorbance is more modest, while the wavenumber shift is still substantial. As suggested by (Seco, Goncalves *et al.*, 2000), the condensation of the Si–O–Si network and the accompanying wavenumber shift and peak increase are at times interrupted whenever a Si–O–Ti is formed.

The Si–O–Si LO component of the asymmetric stretching mode, or shoulder, is not evident at low temperatures due to overlap with the Si–O–R stretching vibrations of the ethoxy groups. At temperatures above 400°C it becomes more evident, and its intensity decreases with temperature. As mentioned before, the importance of this peak is that it has been directly correlated to porosity in the network; thus a decrease in absorbance is evidence of a desirable reduction in porosity at temperatures above 500°C.

In summary, moderate processing temperatures around 500°C results in the removal of undesired species, while promoting condensation and initiation of viscous sintering that reduces the film porosity. An ideal processing temperature lays in the range of 900°C, to fully remove the undesired alcohol, water, and OH related species, while obtaining a structure that closely resembles that of a purely inorganic sol-gel network.

Considering a freeform fabrication process, temperatures near 900°C might not be easily implemented in an integrated system. Therefore, one solution is to decouple the high-temperature treatment and leave it as a post-processing operation. Two alternatives are presented in a following sub-section.

4.8.2. Effects of Heating Rate

It was mentioned previously that in the case of Ti-doped silicate sol-gels, the heating rate is an important parameter to avoid crystallization and therefore cracking of the film. The results for the inorganic silicate sol-gel (system #1) presented in the preceding section, in conjunction with the research by (Keddie and Giannelis, 1991), provides a solid starting point for defining the heating rate

for sol-gel system #2. So these lessons where immediately implemented in the experimental process for system #2 without following a detailed systematic study. Only a few observations pertaining the heating rate will be made, which are based on experimentation.

For the fabrication of crack-free multi-layer films using sol-gel system #2, control of the cooling rate, particularly at high temperatures (500–900°C), appeared to have a greater impact on the development of cracks. Although a too slow heating rate (for example 1–4°C/min, for our furnaces), in particular for subsequent layers, also resulted in cracking. This can be explained by the analogy to Time-Temperature Transformation (TTT) or Continuous Cooling Transformation (CCT) diagrams, where certain crystalline structures can be avoided by adjusting the heating and cooling rates. Therefore, suggested heating rates are above 20°C/min, while the cooling rates can be 10–20°C/min at least until the temperature has reached ~300°C, after which a more moderate cooling rate should be used: 1–5°C/min.

4.8.3. Proposed Thermal Process for System #2

Based on the experiments for the sol-gel system #2 described above, in conjunction with results found in the literature, two alternatives are proposed for the thermal cycle to treat the sol-gel film. The two cycles are shown in Figure 4.34, along with a flow diagram of the sequence of steps for each cycle.

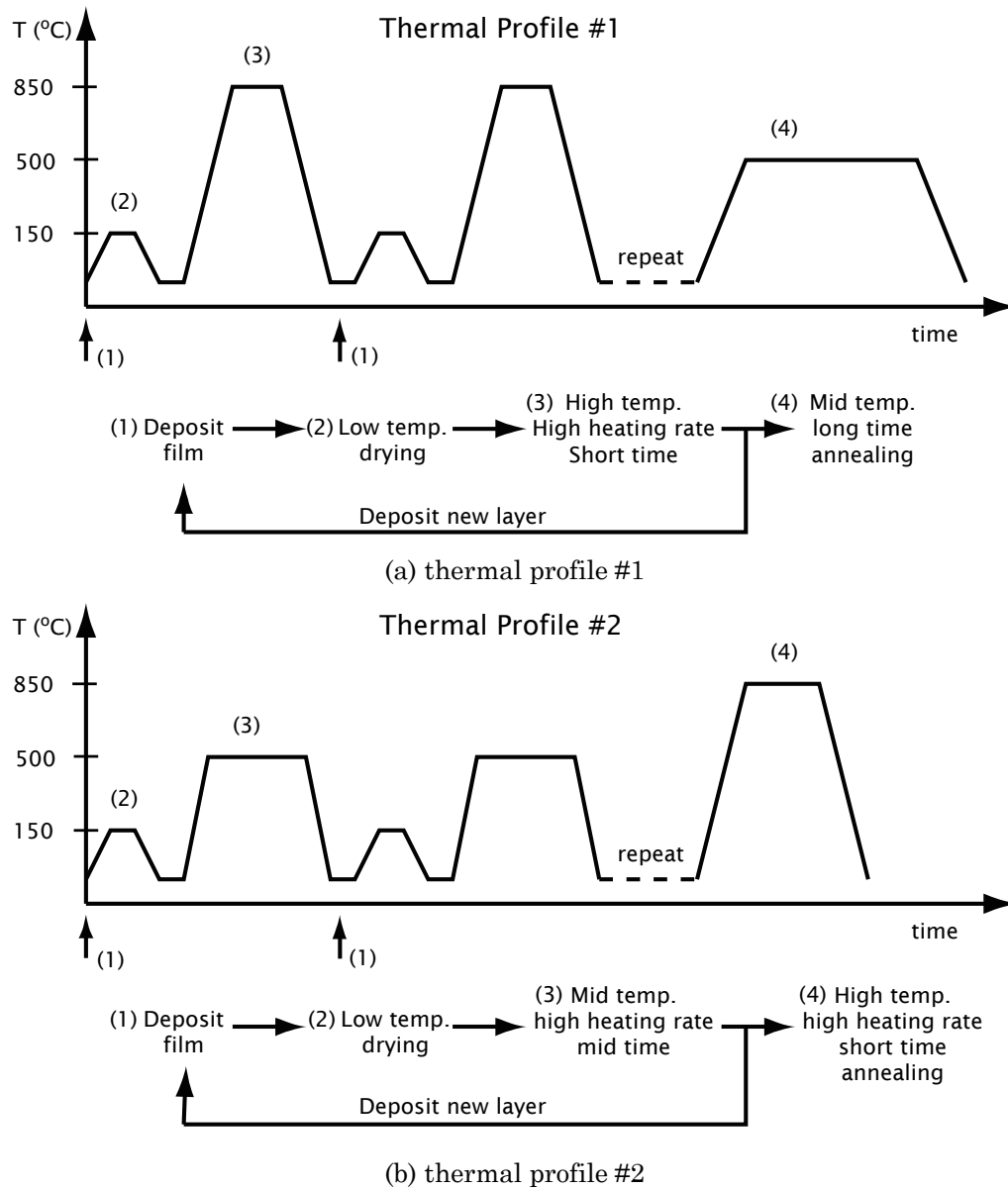(a) thermal profile #1

(b) thermal profile #2

Figure 4.34. Proposed thermal cycles for sol-gel system #2

Thermal profile #1 (Figure 4.34a) begins with the low temperature drying step that follows immediately after the film deposition. The second step is performed at a high temperature and high heating ratio, for a short period of

191

time. The subsequent layer deposition is followed by repeating the two steps in the thermal cycle. This process is repeated until the desired and calibrated final thickness is obtained. After the final layer has been deposited, the whole specimen is subjected to a mid-temperature step for a longer period of time in order to relieve some of the stresses induced during spin coating and RTP processing. This thermal cycle is suitable if the RTP process can be incorporated into the whole direct-write process.

Alternatively, thermal cycle #2 (Figure 4.34b) consists of a series of low-temperature drying and mid-temperature steps for each layer, and a final high temperature and high heating rate step. This final high-temp step can be performed in a separate processing chamber that can withstand these high temperatures without interfering with the layer-based manufacturing process, all performed at moderate temperatures (400–550°C).

4.9. Thermal Processing of Hybrid Sol-Gel System #3

Thermal processing of sol-gel system #3 is significantly different that that of the previous two systems. To begin with, the processing temperatures are substantially lower (<200°C); secondly, an additional thermal step is present in the cycle after UV exposure. A sample of the thermal cycle for system #3 was shown in Figure 4.19b. Another difference for this system is the presence of an intermediate chemical processing step to "develop" or remove the unexposed areas of the sol-gel film. Figure 4.35 provides a more detailed picture of the thermal and chemical processing required for sol-gel system #3. This figure
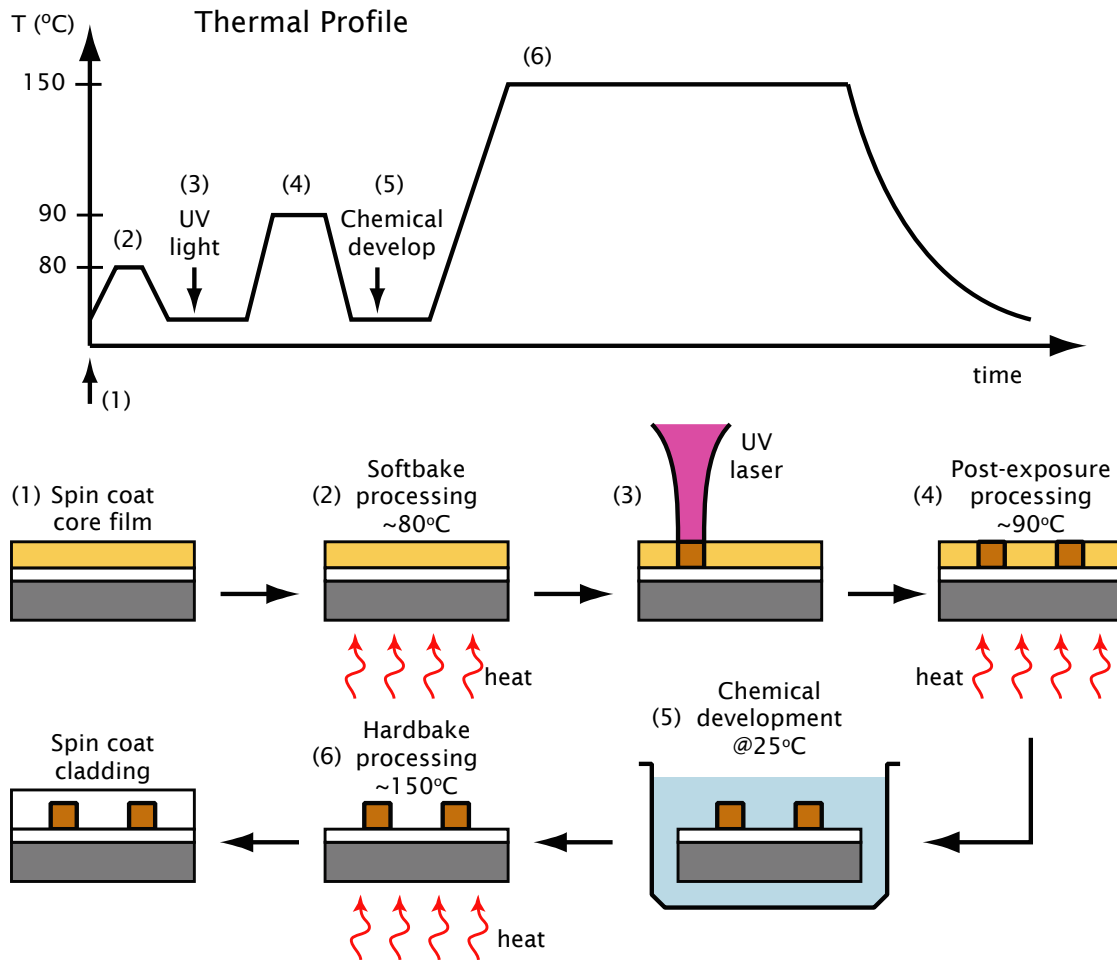
Figure 4.35. Thermal cycle for sol-gel system #3

shows the temperature-time profile for each step, and a corresponding illustration to clarify the whole process.

As mentioned in Section 4.5.2, the thermal cycle consists of three steps:

1) Soft-Bake (SB): performed immediately after sol-gel deposition to increase the strength and reduce the tacky nature of the film. Temperature: 80–90°C. Dwell time: 5–10 min. Atmosphere: N_2 or He.

2) Post-Exposure Bake (PEB): performed after UV exposure to improve the strength and adhesion of the laser scanned feature to the substrate. Temperature: 90–100°C. Dwell time: 5–10 min. Atmosphere: N_2 or He.

3) Hard-Bake (HB): performed after chemical development, with the objective to remove unwanted organic residuals and increase strength and refractive index. Temperature: 140–180°C. Dwell time: 60–240 min. Atmosphere: N_2, He, or vacuum (~10 mTorr).

These three steps can be identified in Figure 4.35 by the numbers: (2), (4) and (6).

For system #3, the three thermal processing steps play a fundamental role in order to obtain smooth features that are properly bonded to the substrate material. All three steps must be examined in conjunction to the UV laser exposure step, because the appropriate combination of temperature and UV dose must be found for a determined sol-gel mixture. One possible scenario is when the SB temperature is too high, causing an unsuccessful removal of all the unexposed sol-gel. By contrast, if the SB temperature is too low, the film is more prone to having undesired particles adhere to the surface. Another scenario is when the PEB temperature is too low, or in some cases this step is completely omitted, the UV exposed region might become detached from the substrate in certain sections or completely. Figure 4.36 shows a set of SEM images of some of these common defects encountered in sol-gel system #3.
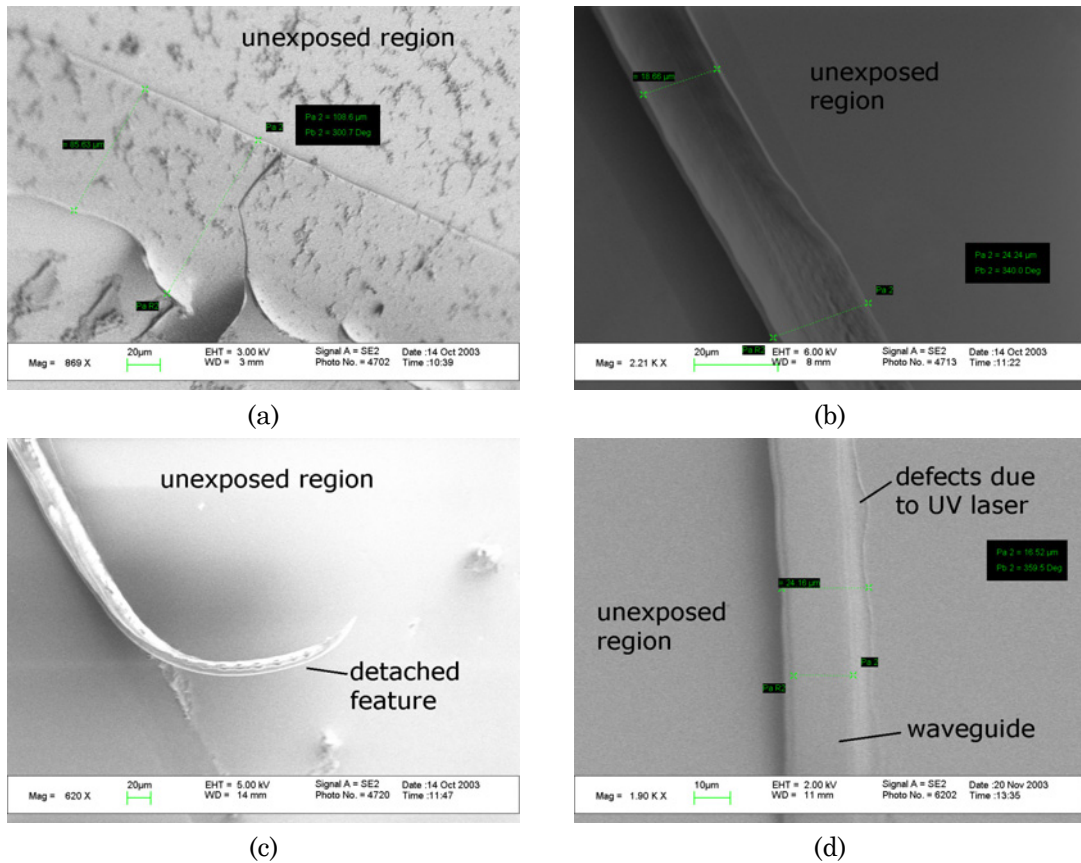
Figure 4.36. SEM images of typical defects of sol-gel system #3

In order to address some of these issues, a series of experiments were conducted observing the effects of the temperature for the SB and PEB steps, as well as examining the effect of the atmosphere (i.e., relative humidity) on the sol-gel features. The two different sol-gel mixtures described in Chapter 3 (Zr and Al doped) were studied. The experiments consisted basically in changing the processing temperature for the SB and PEB steps, writing straight lines with a UV laser across the sample, developing the sample in a solution of isopropanol and 4-methyl-2-pentanone (5:1), and observing the features in the microscope.

The experimental conditions are summarized as follows:

- SB: T_{SB} = {80,90,95}°C; t_{SB} = 5 min; atmosphere: He

- PEB: T_{PEB} = {90,95,105}°C; t_{PEB} = 5 min; atmosphere: He

- HB: T_{HB} = {150}°C; t_{HB} = 120 min; atmosphere: He

The results varied somewhat for the Zr or Al doped hybrid sol-gels, but similar trends can be established for the design of the overall thermal cycle. In the case of the Al-doped hybrid sol-gel, the film appeared to be more resistant to high soft-bake temperatures without affecting much the successful removal of unexposed material. On the other hand the PEB step is necessary and beneficial particularly for the Al-doped hybrid sol-gel in order to improve the strength and bonding to the substrate, avoiding the defect shown in Figure 4.36c. Nonetheless the PEB step does not solely guarantee a proper bonding to the substrate. This also requires an appropriate level of photopolymerization that reaches all the way through the lower part of the film, which in turn depends on the extinction coefficient and the fluence delivered by the laser. Figure 4.37 shows a waveguide that was successfully developed.
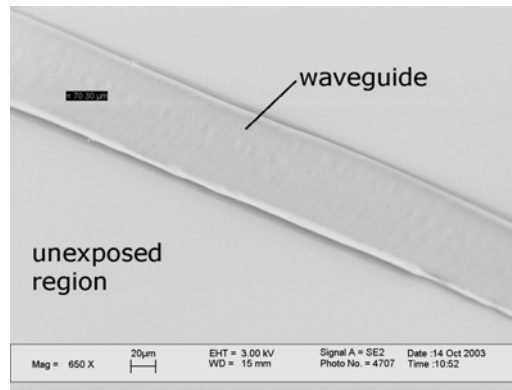
Figure 4.37. SEM image of a successfully developed sol-gel waveguide

Two additional parameters that play crucial roles for good feature development are the humidity of the atmosphere and the time between film deposition and the PEB step. Because of the small thickness of the hybrid sol-gel film (2–10 μm), the diffusion length is small, thus allowing further condensation and evaporation of residual solvent and water. If the humidity is too low (<30%) or the time between spin coating and PEB is too large, traces of unexposed sol-gel adhere scattered throughout the surface, as shown in Figure 4.36a. For both Al and Zr doped hybrid sol-gels, it was found out that the humidity during UV laser exposure should be kept between: 40<RH<50%. The time between film deposition and PEB should be kept below 3 h, for maximum dissolution of the unexposed areas. In a fully automatic direct-write machine this would be

(a) soft bake   (b) post UV exposure bake
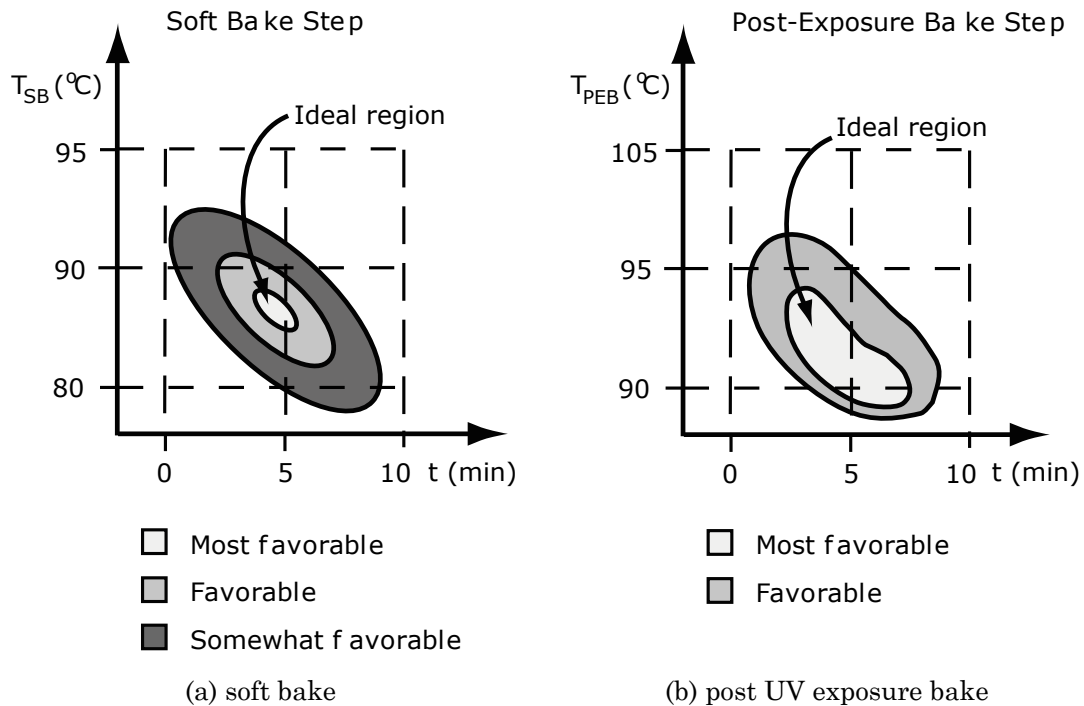
Figure 4.38. Suggested processing regions for the SB and PEB steps

performed immediately, and every step conducted under controlled humidity, thus reducing the occurrence of these two defects.

Figure 4.38 illustrates the favorable regions for processing time and temperature for the soft bake and post-exposure bake steps, based on experimental observations. The regions indicated in these figures are approximate, yet provide an overall picture for more detailed studies.

In summary, the thermal processing of the hybrid photopolymerizable sol-gels is conducted at lower temperatures, which in a sense is advantageous for a fully automated freeform fabrication machine. Also, for the design of the thermal cycle for these sol-gels, special attention must be put on the strict control of the humidity of the atmosphere that surrounds the sample, as well as in keeping the time between film deposition and PEB to a minimum. Thermal processing for sol-gel system #3 is closely related to the UV laser exposure and to the chemical development steps. Temperatures that are outside an optimal region for either of the thermal processing steps have the tendency to produce defects in the substrate and waveguide, such as the ones mentioned above.

4.10. Conclusions

This chapter has provided a comprehensive description of the two initial steps involved in the proposed manufacturing process. Detailed experimental procedures were provided for the successful deposition by spin coating of the three sol-gel systems presented in Chapter 3. Similarly, extensive experimental

results were provided to support the design of the thermal processing cycles that follow the film deposition step. Most importantly, this chapter has aimed at conveying the message on how these two steps can be integrated into a fully automated process based on the premises of freeform fabrication and direct-write technologies. Full integration of the process will become clearer in subsequent chapters.

Chapter 5. Laser Processing

5.1. Introduction

After film deposition and thermal treatment (Figure 5.1), the next step in the proposed direct-write process involves the use of a laser to define the features in the film by means of photothermal or photophysical activation. The current chapter describes in detail the laser processing step, first by presenting the goals and objectives to be achieved with this particular method, following a similar procedure as was done for the previous steps in Chapter 2. Secondly, a brief review on laser-matter interaction is provided, which helps identify the key parameters to be controlled during laser processing. Next, a chronological
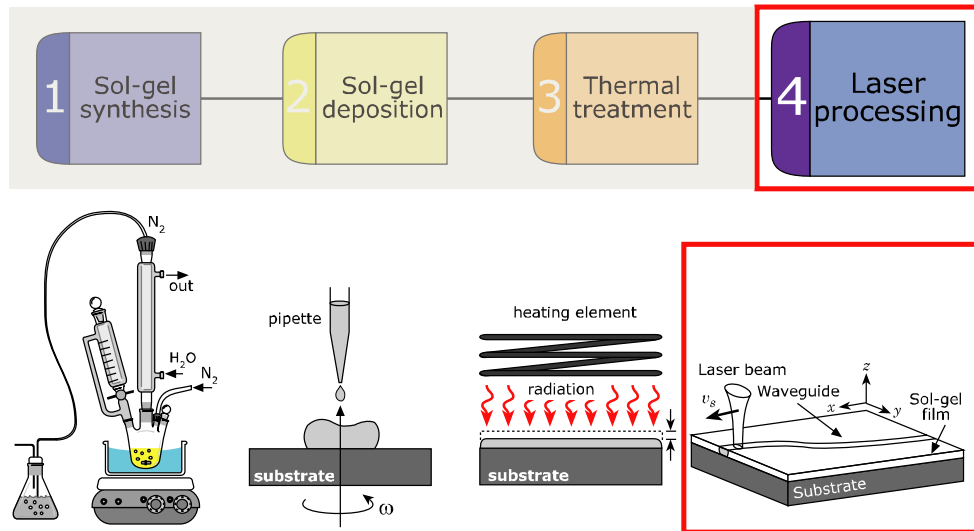
Figure 5.1. Current step in proposed direct-write process

review is provided of the various prototype laser processing setups. Finally, experimental results are presented and discussed.

5.2. Objectives and Characteristics of Laser Processing

Referring back to Chapter 2, several options were presented to address the *material shaping* subsystem of the direct-write process (see Figure 2.13 and Table 2.4). The use of a laser was selected for the following reasons: (1) a laser represents a powerful and concentrated energy source; (2) this concentrated energy source can be readily manipulated in space and the energy controlled by parameters such as scan speed or laser power; and (3) it may be integrated into a flexible automated process with CAD/CAM capabilities.

Along with these advantages come some disadvantages of using a laser, which are mainly related to spatial resolution and the processed area. These aspects tend to limit the feature's size and resolution, together with a larger per-part manufacturing time when compared to lithographic methods. On the other hand, the improved efficiency, broad range of available wavelengths, and reduction in cost, has made lasers an attractive element of manufacturing systems (Bäuerle, 2002; Piqué and Chrisey, 2002). Additionally, the positioning systems, such as XYZ stages or galvanometer mirrors, have also experienced an increase in accuracy, speed, and cost. The combination of these elements makes the use of lasers attractive for manufacturing components that prove to be difficult or impossible to make by other methods, particularly for complex three-dimensional shapes (Beaman, Barlow *et al.*, 1997).

A laser can induce physical or chemical changes, or both, on a material. Laser processing can be divided in three main types (Bäuerle, 2000):

(1) Photothermal. This type of laser processing occurs when the rate of thermalization is greater than the excitation rate, and it is fully characterized by temperature and enthalpy.

(2) Photochemical. The changes induced by this type of laser processing occur mainly in a non-thermal fashion. It manifests itself in a number of ways, such as changes in concentration, dissociation of species, or surface modification.

(3) Photophysical. This type of processing occurs when both thermal and chemical activation processes are induced. Photopolymerization is an example where physical and chemical changes occur.

For this research, the two important types considered are photothermal and photophysical processing. Although most of the work in this research, particularly for laser processing, is based on experimentation and the integration of various techniques, the main decisions were based on theoretical concepts. Such is the case for laser processing, where the heat transfer theory and kinetics of photopolymerization were incorporated into the decision-making process.

From a *Design Methodology* approach, we can identify a set of design parameters (DPs) and performance metrics (PMs) for laser processing. Typical examples of DPs and PMs are listed in Table 5.1. The DPs are divided in two main groups: *laser* and *material*. The laser parameters listed in Table 5.1 are those generally available in commercial lasers. Some important parameters include whether the laser is continuous wave (CW) or pulsed, the shape and

Table 5.1. Typical DPs and PMs for laser processing

Design Parameters **DPs**	**Laser**	Laser power, P_ℓ [W]
		Beam waist (radius), w_o [μm]
		Scan speed, v_s [cm/s]
		Wavelength, λ [μm]
	Material	Molar extinction coefficient, ε $[\mathrm{M^{-1}cm^{-1}}]$
		Absorption coefficient, α $[\mathrm{cm^{-1}}]$
		Reflectance, R
		Concentration of photoinitiator, $[PI]$ [mM]
Performance Metrics **PMs**	**Geometrical**	Line width, w_L [μm]
		Cross section shape,
		Surface roughness (average), R_a [nm]
	Physical	Density, ρ $[\mathrm{g/cm^3}]$
		Index of refraction, n

mode of the beam (e.g., Gaussian TEM$_{00}$), and the wavelength which is critical for a proper absorption by the material being processed. With respect to the material, the parameters listed in Table 5.1 include some of the properties that can be altered chemically, for example to enhance the absorption of the material at a specific wavelength.

In the case of the PMs, these are composed by two sets of properties which can be quantified in order to optimize the solution or reach a certain goal. The PMs associated to geometry are important in order to characterize the feature size and resolution, and evaluate the repeatability of the process. On the other hand, the PMs associated to physical properties, such as the increase in density and change in refractive index, are related to the characterization and performance of the component being manufactured. For example, maintaining a

uniform change in the index of refraction throughout the component has direct impact on the attenuation and losses of the optical signal being transmitted. These will be discussed in more detail in Chapter 6.

In summary, the key objectives to achieve, in order to characterize the success of the proposed manufacturing process in terms of laser processing are: (1) to control the refractive index by maintaining uniform and predictable distributions across the entire geometry; (2) to control of surface roughness by minimizing it; and (3) to control the geometry or shape of the features.

5.2.1. Characteristics of Laser Processing

This section will describe briefly the properties of a laser beam as well as some of the most important characteristics of laser-matter interaction in the scope of photothermal and photophysical processing. As mentioned above, a laser is a highly coherent source of electromagnetic energy, with wavelengths ranging from the ultraviolet (UV) to the infrared (IR) spectrum. For the proposed direct-write
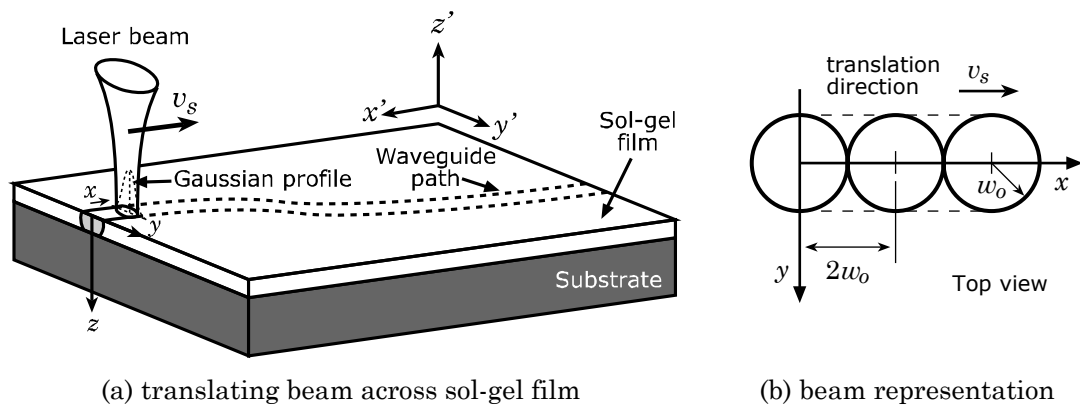

(a) translating beam across sol-gel film   (b) beam representation

Figure 5.2. Laser-matter interaction: moving laser beam

process, the laser beam is scanned over the working area, interacting with the sol-gel film. Figure 5.2 presents an illustration of the interaction between the moving laser beam and the sol-gel film to generate the desired optical path.

Intensity and Absorption Characteristics

In many cases, the lasers used for industrial applications have a Gaussian distribution profile for the cross-section of the irradiance $I(x,y)$, in units of (W/cm^2). In some reports found in the literature, the irradiance is incorrectly referred to as intensity. The main difference is that irradiance refers to the total radiant power (or energy flux) incident over a surface divided by the surface area, while the intensity is defined as the radiant energy flux per unit solid angle [W/sr] (Welch, van Germet *et al.*, 1995). Figure 5.3a shows the irradiance distribution of a fundamental mode (TEM$_{00}$) Gaussian beam, while Figure 5.3b shows a surface plot of the irradiance for a beam with w_o=5μm and P_l=10 mW. For a position exactly at the surface of the material, the irradiance of the beam can be described by the expression (Jacobs, 1992):

$$I(x,y,0) = I(r,0) = I_o \exp\left(-\frac{2r^2}{w_o^2}\right) \tag{5.1}$$

where: $r^2 = x^2 + y^2$, and w_o corresponds to the "Gaussian half-width", which occurs at $1/e^2$ of the maximum irradiance I_o. The total power by the laser beam acting over the surface area Γ is thus defined as:

$$P_\ell = \int_{r=0}^{r\to\infty} I(r,t)\,d\Gamma = \int_{r=0}^{r\to\infty} I_o \exp\left(-2r^2/w_o^2\right) 2\pi r\,dr = \frac{\pi}{2} w_o^2 I_o \quad [\text{W}] \tag{5.2}$$

For single photon interaction, the energy of a radiant source is absorbed by the material following what is known as the Beer-Lambert law (von Allmen

(a) parameters of beam	(b) irradiance plot for Gaussian beam
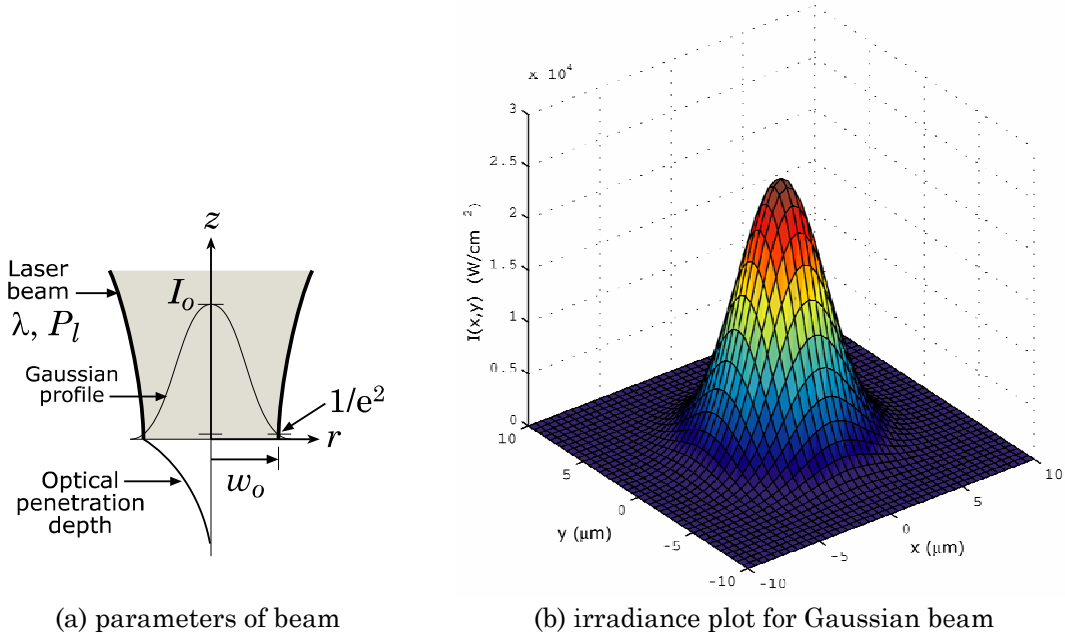
Figure 5.3. Gaussian beam: profile and parameters

and Blatter, 1995). This law results from the combination of Beer's law of absorption, which states that:

$$dI = -I\varepsilon[A] \; dz \tag{5.3}$$

where z corresponds to the length of the path in (cm), $[A]$ is the molar concentration of chemical A in (M=mol/l), and ε is the molar absorptivity in ($M^{-1}cm^{-1}$). Integrating equation (5.3) gives to the standard expression:

$$I(z) = I_o e^{-\varepsilon[A]z} \tag{5.4}$$

On the other hand, Lambert's law relates the decay in intensity I (erg cm^{-2} sr^{-1} s^{-1}) to position z, and the linear extinction or absorption coefficient α (cm^{-1}), derived from the radiative transfer equation (Siegel and Howell, 1992). This results in the following expression (Rubahn, 1999):

$$\frac{dI}{dz} = -\alpha I \tag{5.5}$$

**Figure 5.4. Absorption coefficient for crystalline SiO$_2$. Adapted from:
(von Allmen and Blatter, 1995)**

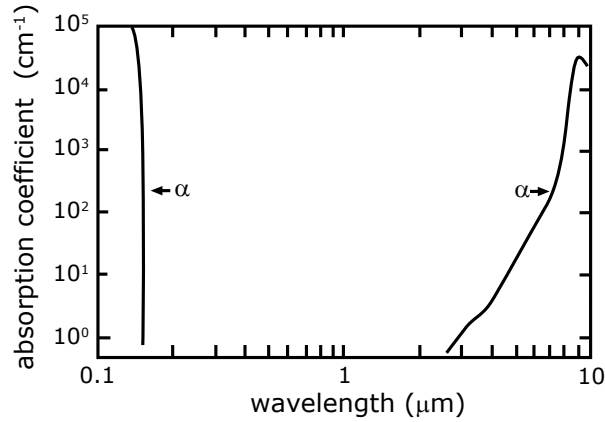Integrating Eq. (5.5) results in an equation that describes the exponential decay of the electromagnetic wave, as it propagates through the material (Plummer, Deal *et al.*, 2000). Thus solving the integral for the case when α is a constant, results in:

$$\int \frac{dI}{I(x,y,z)} = \int (-\alpha)dz \Rightarrow I(x,y,z) = I_o(x,y)\exp\left(\int_0^z -\alpha(z')dz'\right) \qquad (5.6)$$

$$I(x,y,z) = I_o(x,y)\exp(-\alpha z) \qquad (5.7)$$

A representation of this expression is shown in Figure 5.3a, indicated on the lower part of the figure by the *optical penetration depth*. Typically Beer's law is employed in chemistry applications, for example in UV-vis spectroscopy, while Lambert's law can be seen in radiation heat transfer. Both expressions were presented because of the two cases of laser-matter interaction considered (i.e., photothermal and photophysical).

From Equation (5.7) it can be seen that the penetration of the laser beam into the material strongly depends on α, which varies between materials and can be adjusted or "tuned" depending on the application. The absorption coefficient

also depends on the wavelength λ of the incident beam or wave. A material with similar properties as the silicate sol-gels is crystalline SiO_2. Figure 5.4 shows the spectral response of α Vs λ, adapted from (von Allmen and Blatter, 1995). This figure shows that SiO_2 has strong absorption in the low UV and deep IR regions, which should be considered when selecting the wavelength of the laser.

The inverse of the absorption coefficient is known as the absorption length l_α, or the optical penetration depth, and is defined by:

$$l_\alpha = \alpha^{-1} \tag{5.8}$$

For example, amorphous SiO_2 has an optical penetration depth of $l_\alpha \approx 40\mu m$ at $\lambda = 10.6\mu m$ (Bäuerle, 2000), which corresponds to the typical operating wavelength of a CO_2 laser. For silicate sol-gel films the penetration depth has been reported to be $l_\alpha \approx 1.5 - 10\mu m$ (Shaw and King, 1990; Chia, Hench et al., 1994). These previous values for l_α are larger than the typical thickness of a silicate sol-gel film ($100 \leq t_f \leq 1200$ nm), so before a substantial decay in irradiance occurs the beam fully penetrates the thin film. The optical penetration depth can be compared to the heat penetration depth l_h, for the photothermal case, which is defined as the depth where the surface temperature decreases by a factor of e, or by the following expression (Bäuerle, 2000):

$$l_h = 2\sqrt{\frac{kt_i}{\rho c_p}} = 2\sqrt{\kappa t_i} \tag{5.9}$$

where k denotes the thermal conductivity (W·m^{-1}·K^{-1}), ρ the density (kg·cm^{-3}), c_p is the heat capacity of the material (J·kg^{-1}·K^{-1}), κ represents the thermal diffusivity (m^2·s^{-1}), and t_i is the interaction time (sec). The interaction time can be approximated by considering the time it takes the beam to travel the distance equivalent to its diameter:

$$t_i \approx \frac{2w_o}{v_s} \tag{5.10}$$

In most cases $l_h \gg l_\alpha$, where the interaction times are in the order of mili-seconds or smaller, even for non-metals or insulating materials such as glasses. So for cases where $l_h \gg l_\alpha$ or the laser dwell time is considerably small (10^{-9} s), it is safe to assume pure surface absorption, thus neglecting the irradiance decay into the material (Bäuerle, 2000). On the other hand, for polymers such as PMMA, the absorption coefficient α has much larger values sharply increasing below the visible range and going into the UV, which results in smaller penetration depths. For example, PMMA at $\lambda = 400$ nm has an $\alpha = 400$ cm^{-1}, thus resulting in a length of: $l_\alpha = 25$ μm; or for $\lambda = 193$ nm the absorption length is approximately: $l_\alpha = 5$ μm (Bäuerle, 2000). This length is in the typical range for the thickness of the sol-gel films that were described in Chapter 4, so the assumption of pure surface absorption is somewhat limiting for this case.

For photopolymerization, the absorption coefficient α becomes a more complex function that depends on factors such as the concentration of the individual species in the film: photoinitiator, solvent, inorganic species, etc. It is also a function of time as the polymerization reaction takes place, and can be described by assuming first order kinetics (Plummer, Deal *et al.*, 2000). Thus an accurate characterization of the spatial and temporal distribution of α is required, which is critical in applications such as lithography for microelectronics manufacturing. A similar degree of importance can be seen for the accurate fabrication by laser direct-write techniques in hybrid sol-gels, such as System #3.

Photothermal Characteristics

A complete representation of an incident laser beam, with a Gaussian TEM$_{00}$ mode profile acting as a constant heat source over a surface with homogeneous material properties, is described by the following expression:

$$Q(x,y,t) = I_o \exp\left(-\frac{2r^2}{w_o^2}\right) \cdot (1-R)\alpha \exp(-\alpha z) \qquad (5.11)$$

where $Q(x,y,t)$ is the source term with units (W/m^3), and R is the reflectance of the material (Rubahn, 1999).

For the photothermal case, a mapping of the temperature field $T(\mathbf{x},t)$ in the material induced by the source term of Eq. (5.11) is desired. As mentioned in Chapter 2, the change in density of the sol-gel material has a direct correlation to the change in refractive index. Thus the shape and extent of the change in the refractive index can be understood in terms of the temperature field induced by the translating moving beam. From a theoretical standpoint, the temperature field can be calculated by solving the heat equation with appropriate boundary and initial conditions. Neglecting heat transfer by convection and radiation, the heat equation for a coordinate system that is fixed to the moving source can be
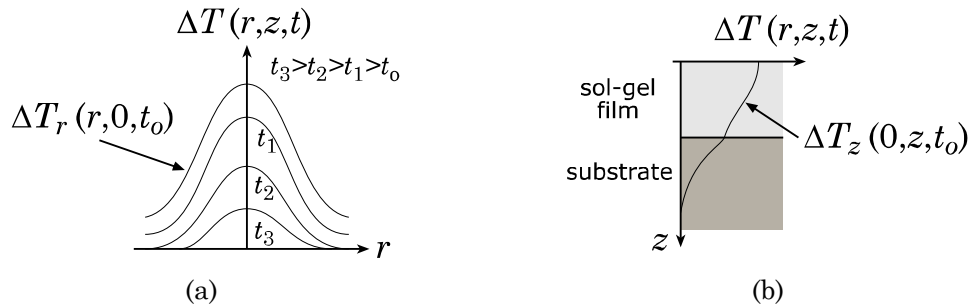

Figure 5.5. Temperature distributions due to laser irradiation

described as (Carslaw and Jaeger, 1986):

$$\rho c_p \frac{\partial T(\mathbf{x},t)}{\partial t} - \nabla\left[k\nabla T(\mathbf{x},t)\right] + \rho c_p \mathbf{v}_s \nabla T(\mathbf{x},t) = Q(\mathbf{x},t) \qquad (5.12)$$

Closed-form analytical solutions to Equation (5.12) are not easily found. In many cases a numerical approach must be taken, for example by employing finite differences or finite elements techniques. Considering the case of a stationary Gaussian beam, Figure 5.5a shows a typical temperature distribution at the surface on the radial direction r as it progresses with time. A Gaussian shape of the temperature profile in the radial direction is expected. Figure 5.5b shows the temperature increase going into the material (z direction), noticing a discontinuity in the temperature field at the sol-gel/substrate interface due to the change in material properties, particularly the thermal conductivity k.

The temperature profiles on the (x,y,z) directions will have a direct impact on the spatial distribution of the refractive index $n(x,y,z)$. Therefore the irradiance profile of the laser beam also has a direct impact on $n(x,y,z)$. For a Gaussian beam profile, the refractive index results in a graded index profile (Chia, Hench *et al.*, 1994), which in some cases might not be desired. The beam shape can be altered through optics to produce a more even and flat temperature profile, for example with a "doughnut" shaped beam (TEM*01 mode) (Charters, Luther-Davies *et al.*, 1999).

Referring back to the temperature distribution into the material depicted in Figure 5.5b, a rough estimation of the thermal time constant τ_T for heat propagation in the sol-gel film and silicon substrate can be calculated by:

$$\tau_T = \frac{\Delta^2}{4\kappa} \qquad (5.13)$$

where Δ is the characteristic length, and κ the thermal diffusivity (Welch, van Germet *et al.*, 1995). As an example we can consider a sol-gel film with t_f=600nm and a silicon wafer with t_{Si}=400μm, with diffusivities of 0.009 $cm^2 \cdot s^{-1}$ and 0.5 $cm^2 \cdot s^{-1}$, respectively (Shaw and King, 1990; Bäuerle, 2000). The time constants result as:

$$\text{Sol-gel film:} \quad \tau_T = \frac{\left(6 \cdot 10^{-5} \text{ cm}\right)^2}{4\left(9 \cdot 10^{-3} \text{ cm}^2/\text{s}\right)} \approx 0.1 \text{ μs} \tag{5.14}$$

$$\text{Silicon wafer:} \quad \tau_T = \frac{\left(4 \cdot 10^{-2} \text{ cm}\right)^2}{4\left(5 \cdot 10^{-1} \text{ cm}^2/\text{s}\right)} \approx 0.8 \text{ ms} \tag{5.15}$$

Comparing these two quantities we can see that heat propagates rapidly through the sol-gel film, and the silicon wafer with a much greater diffusivity acts as a heat sink. This is an important observation to consider when selecting an appropriate operating range for the laser power and scan velocity.

An additional parameter that combines the laser power with velocity and geometrical aspects of the beam is known as the *fluence*. The fluence ϕ_ℓ is defined as the energy density of an optical source acting on a surface (Welch, van Germet *et al.*, 1995). The average fluence can be estimated by the following expression:

$$\phi_\ell = \frac{P_\ell}{A_\Gamma} \cdot t_i = \frac{P_\ell}{A_\Gamma} \cdot \frac{2w_o}{v_s} = \frac{2P_\ell}{\pi w_o v_s} \quad \left[\frac{\text{J}}{\text{cm}^2}\right] \tag{5.16}$$

where A_Γ is the area of the laser beam on surface Γ.

Photophysical Characteristics

For photopolymerization processing of hybrid sol-gels a somewhat different approach is required for cases when the temperature increase effects

212

are much smaller compared to the laser-induced polymerization. In this case, a different quantity is studied, which is the radiant exposure $H(x,y,z,t)$ (Jacobs, 1992; Welch, van Germet *et al.*, 1995). The radiant exposure can be related to the polymerization kinetics in order to optimize factors such as penetration depth through laser power, interaction time, and concentration of photoinitiator (Lee, Prud'homme *et al.*, 2001). The radiant exposure at a point P in the material with coordinates (x_p, y_p, z_p) is defined as the integral over time of the irradiance; that is:

$$H(x,y,z,t) = \int I(x,y,z,t)dt \quad [\text{J}/\text{cm}^2] \tag{5.17}$$

Considering first a point on the surface and a moving laser beam in direction x at a constant velocity v_s, the exposure is defines as:

$$H(x,y,z=0) = \int_{-\infty}^{+\infty} I[x(t),y,z=0]dt \tag{5.18}$$

where the irradiance on the surface ($z=0$) from Equation (5.1) is:

$$I[x(t),y,z=0] = \frac{2P_\ell}{\pi w_o^2} \exp\left(-\frac{2\left(x(t)^2 + y^2\right)}{w_o^2}\right) \tag{5.19}$$

Following the procedure described by (Jacobs, 1992), the integral of Eq. (5.18) can be rewritten in terms the scan velocity:

$$v_s = \frac{dx}{dt} \Rightarrow dt = \frac{1}{v_s}dx \tag{5.20}$$

and the exponential term of Eq (5.19) can be separated in two terms, the time-dependent and independent parts,

$$\exp\left(-\frac{2\left(x(t)^2 + y^2\right)}{w_o^2}\right) = \exp\left(-\frac{2x(t)^2}{w_o^2}\right) \times \exp\left(-\frac{2y^2}{w_o^2}\right) \tag{5.21}$$

Substituting Equations (5.19),(5.20) and (5.21) into (5.18), and solving the integral, the following expression is obtained:

$$H(x,y,0) = \int_{-\infty}^{+\infty} \frac{2P_\ell}{\pi w_o^2} \exp\left(-\frac{2\left(x(t)^2 + y^2\right)}{w_o^2}\right) dt$$

$$= \sqrt{\frac{2}{\pi}} \cdot \frac{P_\ell}{w_o v_s} \exp\left(-\frac{2y^2}{w_o^2}\right) \qquad (5.22)$$

Incorporating now the attenuation in the z direction, from Eq. (5.7), into the result of Eq. (5.22), a general expression is obtained for the radiant exposure due to a Gaussian laser beam with power P_ℓ translating in the x direction at a constant velocity v_s. This results in the following equation (Jacobs, 1992):

$$H(y,z) = \sqrt{\frac{2}{\pi}} \cdot \frac{P_\ell}{w_o v_s} \cdot \exp\left(-\frac{2y^2}{w_o^2}\right) \cdot \exp(-\alpha z) \qquad (5.23)$$

This steady-state approximation is plotted in Figure 5.7, for the following parameters: $P_\ell = 10$ mW, $w_o = 5$ μm, $v_s = 0.1$ cm/s, and $\alpha = 200$ cm^{-1}. Figure 5.6a shows a surface plot of the radiant exposure, while Figure 5.6b presents a
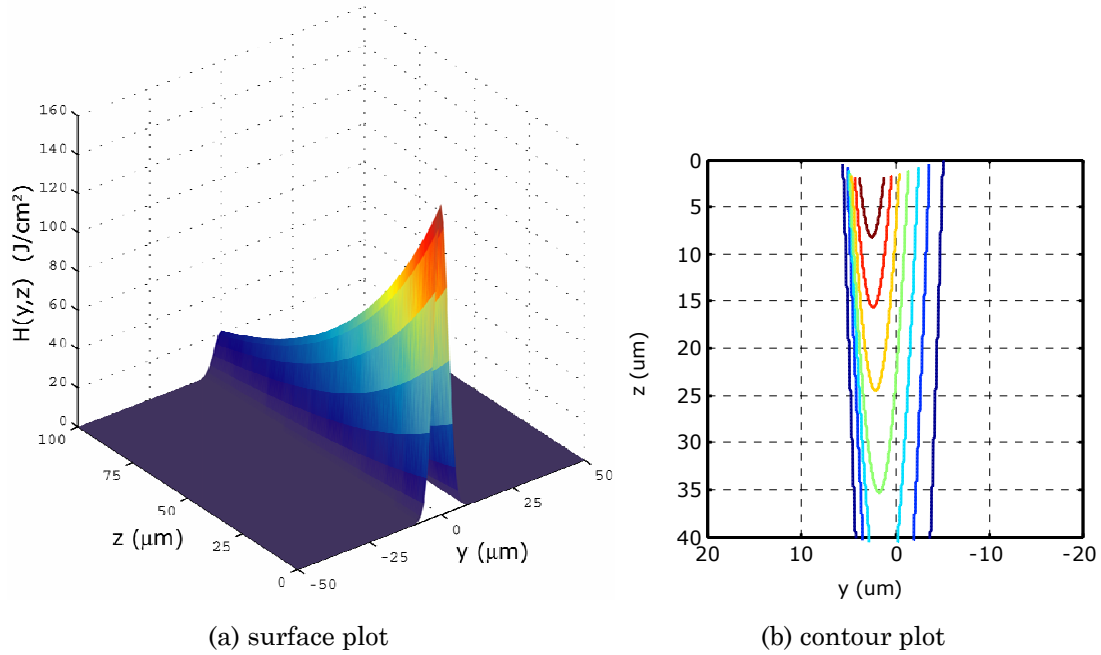

(a) surface plot   (b) contour plot

Figure 5.6. Plots for radiant exposure H(y,z)

214

contour plot in the *YZ* plane. These figures clearly illustrate the shape of the energy as it penetrates the material, following a parabolic profile in the *YZ* plane and exponentially decaying in the *z* direction. These plots are important since they provide insight into the shape of the features manufactured by laser direct-write. The shape or topology of the feature takes an even greater importance in micro- and nano-scale applications as compared to traditional SLS or SLA processing, which are typically performed in the meso- and macro-scales.

For this research, the *line spread* (*y*-direction) is somewhat more important than the *cure depth* (z_c) for two reasons: (1) the film thickness tends to be equal or smaller than the spot size ($2w_o$), and (2) an increase in laser power or interaction time at constant w_o has a greater impact on the feature's size on the *y*-direction. Lee *et al*. investigated the effects of photoinitiator concentration [*PI*] and critical radiant exposure H_c on the cure depth z_c for the SLA process (Lee, Prud'homme *et al.*, 2001). A similar approach is discussed later in the chapter but addressing the line spread.

Two important properties for the photopolymerization of hybrid sol-gels are the molar absorptivity or molar extinction coefficient ε ($M^{-1}cm^{-1}$) and the molar concentration of photoinitiator [*PI*] (M=mol/l). The selection of the type of photoinitiator depends on several aspects. An important one is the wavelength range at which it is designed for maximum absorption. Figure 5.7a shows the absorption spectrum for HCPK, as used in Chapter 3. On the other hand, Figure 5.7b shows the typical absorption spectrum for the hybrid sol-gel of System #3 with different concentrations of the solvent (EtOH), indicating the wavelengths of the two lasers used for experimentation. Absorption in these two wavelengths is strong. A more detailed discussion is provided later in the chapter.
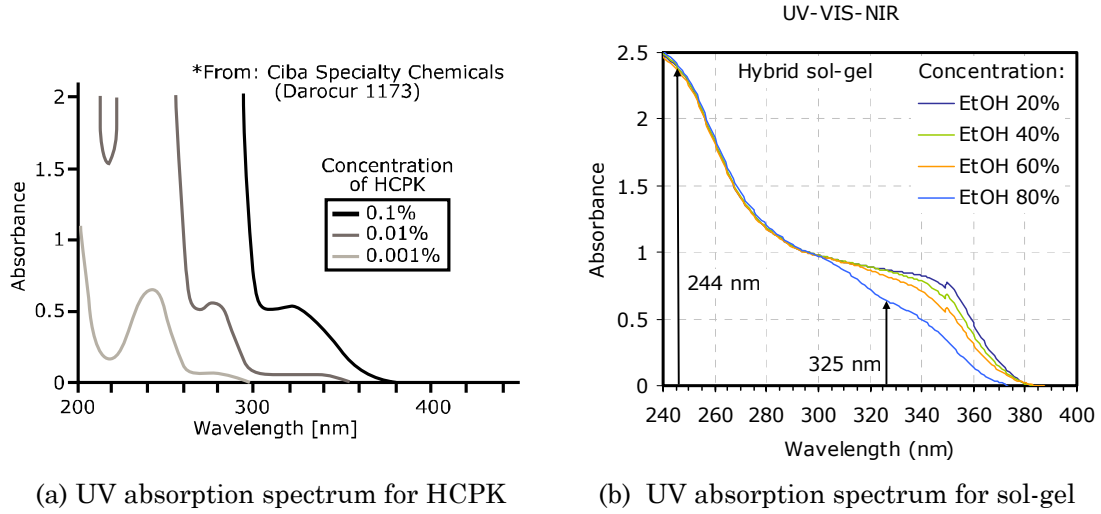
(a) UV absorption spectrum for HCPK

(b) UV absorption spectrum for sol-gel

Figure 5.7. Absorption characteristics for the UV spectrum

5.2.2. Important Aspects of Gaussian Beam Optics

In addition to identifying the main elements of laser photothermal and photophysical processing, it is important to mention some additional aspects related to the propagation and focusing of the laser beam. These aspects are important because of the interrelationship between feature's size and shape and the power distribution and diameter of the laser beam. Design and redesign of the laser stations must consider some of the physical limits imposed in optical setups.

One of the main factors to consider regarding the laser is the so called *spot size* or beam diameter ($d_o = 2w_o$). The spot size will directly affect the dimensions of the features manufactured by laser direct-write. The spot size is bound by what is known as the diffraction limit. The diffraction limit for the minimum spot size diameter d_{diff} for a Gaussian beam is defined as (Steen, 1998):

$$d_{diff} = 2.44 \cdot \frac{f\lambda}{d_{in}} \tag{5.24}$$

where, f is the focal length of the focusing lens, d_{in} is the diameter of the beam entering the lens, and λ is the wavelength of operation for the laser. Equation (5.24) shows that the wavelength of the laser is directly proportional to the beam diameter, thus limiting the minimum spot size. For this reason the minimum spot size of a UV laser (e.g. Argon-ion) can be made theoretically smaller than that of an IR laser (e.g. CO_2 laser).

A more realistic version of Equation (5.24) includes a correction factor, M^2, for divergence of the beam as it propagates. Figure 5.8a illustrates a diverging beam as it propagates. The corrected equation is thus (Steen, 1998):

$$d_o\big|_{\min} = \frac{4}{\pi} \cdot \frac{M^2 f \lambda}{d_{in}} \qquad (5.25)$$

where the ratio f/D is also known as the f-number or $f/\#$, used to characterize a lens (Moore, Davis *et al.*, 1991).

Equation (5.25) predicts a spot size that can be infinitely minimized as the focal length is reduced. This is not the case for real optics, which suffer from the phenomenon called *spherical aberration* (Fowles, 1989). This effect is shown in Figure 5.8c. The contribution of diffraction and aberration effects predict a more realistic spot size. Thus the total spot size is (II_VI, 2004):

$$d_o\big|_{total} = d_o\big|_{diff} + d_o\big|_{abe} \qquad (5.26)$$

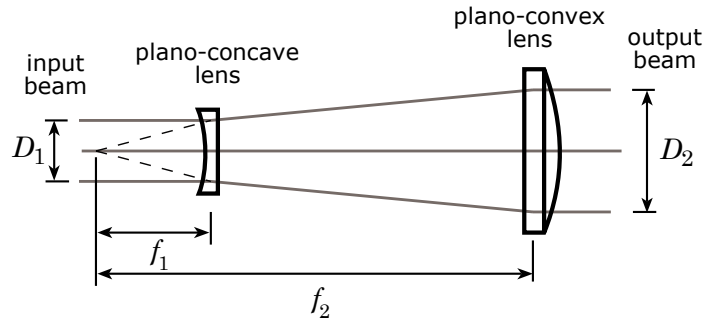$$d_o\big|_{total} = \frac{4}{\pi} \cdot \frac{\lambda f}{d_{in}} M^2 + \frac{k d_{in}^3}{f^2} \qquad (5.27)$$

where k is a function of the index of refraction and lens geometry.

Figure 5.9 presents a series of plots of Equation (5.27) for ZnSe lenses with different focal lengths. The following parameters were considered: $\lambda=10.6$ µm (for CO_2 laser), $M^2=1.2$, and $k=0.0286$.
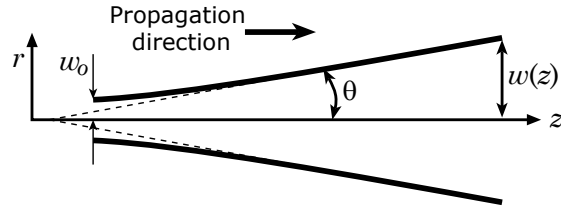
(a) divergence of beam from exit of laser cavity

(b) Galilean type beam expander
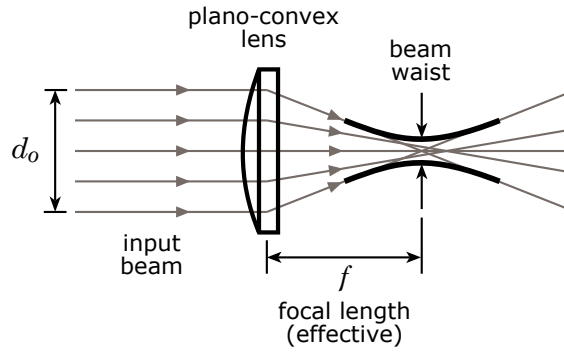
(c) focusing of collimated beam with plano-convex lens

Figure 5.8. Propagation and focusing of Gaussian beam

The minimum for each of the curves of Figure 5.9 is obtained by differentiating Equation (5.27) with respect to the input diameter d_{in}, solving for d_{in}, and substituting is back into Equation (5.27). The minimum d_{in} results as:

$$d_{in}\big|_{\min} = \left(\frac{4}{\pi} \cdot \frac{\lambda f^3 M^2}{3k} \right)^{1/4} \tag{5.28}$$

Figure 5.9. Output diameter due to diffraction and aberration
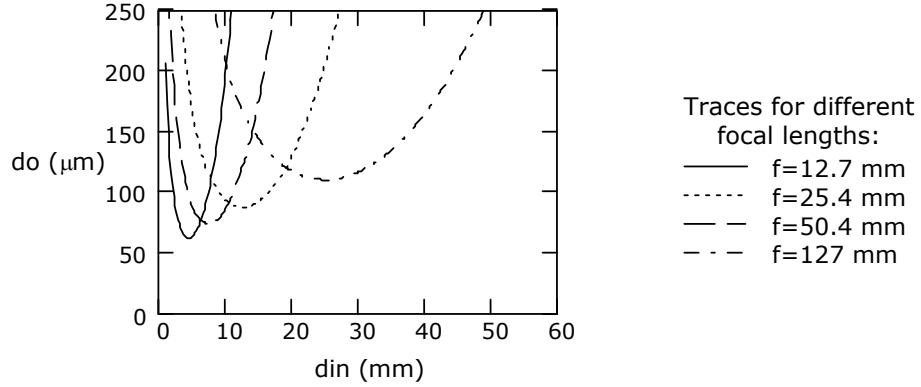
To find the minimum spot size, Equation (5.28) is substituted in (5.27). As seen from Figure 5.9, the curves for d_o get narrower as f decreases.

The divergence of a Gaussian beam as it propagates in the z-direction coming out of the laser cavity is shown in Figure 5.8a. The beam waist increases according to the following equation (Siegman, 1986):

$$w(z) = w_o \left[1 + \left(\frac{\lambda z}{\pi w_o^2} \right)^2 \right]^{1/2} \tag{5.29}$$

As the beam propagates, the far-field divergence angle for a Gaussian beam is defined as (Young, 2000):

$$\theta = \frac{\lambda}{\pi w_o} \tag{5.30}$$

In general, a laser with low M^2 is preferred. This means: $M^2 \to 1$ (Steen, 1998). CO_2 and Argon$^+$ lasers have M^2 values in this range.

Two important aspects can be identified from these properties of Gaussian beam propagation, and related to the design of the laser processing step. First, the diverging beam needs to be collimated, and second, the beam is focused on the sol-gel film to direct-write the features. Two main elements are

219

required to achieve this: a beam expander and a focusing lens. The beam expander re-collimates the beam and expands it by a specified factor. The amplified and collimated beam is then focused through a lens, typically a plano-convex or an achromat doublet. Another important element for the optical train is the spatial filter, which is comprised by a small aperture or pinhole and focusing optics, such as a microscope objective (Moore, Davis *et al.*, 1991). The spatial filter removes unwanted noise and higher order modes.

For this research, the Galilean-type beam expander was used for either IR or UV lasers. Figure 5.8b shows a diagram of the Galilean beam expander. The following relationship describes the increase in beam diameter:

$$\frac{d_2}{d_1} = \frac{f_2}{f_1} \tag{5.31}$$

where, d_1 is the input beam diameter, f_1 the focal length of the plano-concave lens, f_2 the focal length of the plano-concave lens, and d_2 is the output beam diameter as it exits the expander.

With respect to the focusing lens, plano-convex lenses were used to focus the beam to the desired spot size. Figure 5.8c shows a diagram of a plano-convex lens focusing the incoming beam with diameter d_o to the diffraction limited beam waist w_o.

These two elements, along with a spatial filter for some cases, were used in this research. The properties described above are worth mentioning since the lasers used in this research behave closely like a Gaussian beam, and the parameters involved helped in the design of the optical trains.

5.2.3. Comments

In summary, this section has covered some of the important aspects related to laser processing for both photothermal and photophysical cases, along with important properties of Gaussian beam propagation. The key design parameters and performance metrics have also been discussed. In general, the most important aspects of laser processing to control are its position in space, the scan velocity, the power or irradiance, shape and beam waist, and the proper selection of wavelength according to the optical absorption characteristics. From a freeform fabrication perspective, the control of the position in space of the laser beam was performed following a CAD/CAM approach, where the trajectories are computer generated directly from a 2D or 3D computer model of the geometry. This in itself is the most important characteristic of the proposed manufacturing process, and is what differentiates it from the more traditional processes described in Chapter 2, which rely heavily on masks.

The following section discusses the design of the laser stations for experimentation with laser direct-write of sol-gel films.

5.3. Design of Laser Direct-Write Stations

Following the spiral-stage gate design methodology presented in Chapter 2, and once the objectives, performance metrics, and design parameters had been identified, the next stage of the process was to perform a series of experiments with laser processing of sol-gel films. The procedure consisted in designing a prototype laser station, followed by a series of experiments, then evaluating the

results and proceeding with a redesign and refinement of the setup. A total of four laser processing stations were used throughout this research. A brief description of each prototype station is provided below in a chronological order.

The main functional requirements (FRs) for the design of the laser processing station for the proposed direct-write process are shown in the first column of Table 5.2. The second column presents the proposed solutions that were actually implemented in the prototype stations.

From the FRs of Table 5.2, a set of general subsystems for the laser processing station are identified as: (1) laser (type), (2) beam shaping optics, (3) laser power controller, (4) translation of beam, and (5) processing unit. These

Table 5.2. Requirements and proposed solutions for laser processing

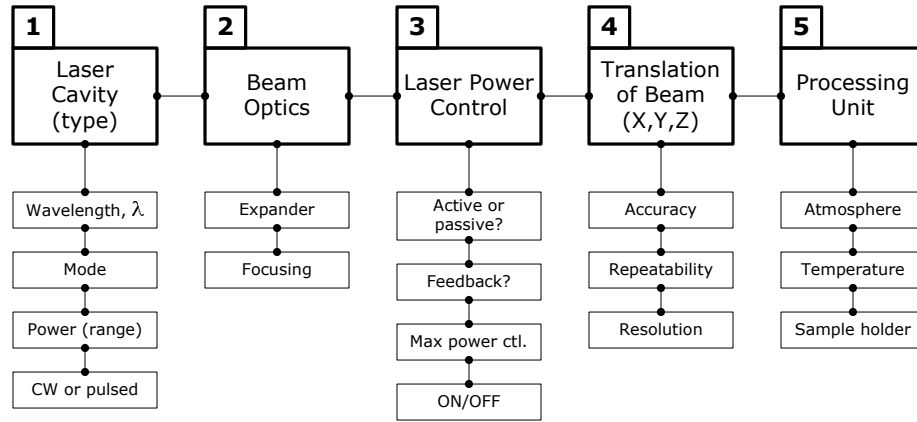| Functional Requirements	Embodiment solutions
Control position, velocity and acceleration, of laser beam in space	Move laser beam • Galvanometer mirrors Move sample • Translation stages: XY
Wavelength of laser	IR range: • CO_2 laser (λ=10.6 μm) UV range: • HeCd laser (λ=325 nm) • Ar^+ laser (λ=244 nm) • Solid state-diode pumped (λ=256 nm)
Irradiance distribution of laser	Gaussian distribution • Single mode TEM_{00} • Multimode
Laser power	Continuous wave (CW) lasers. Power ctl.: • PWM controller • Neutral density filters
Beam waist w_o	Control of Focal Length (FL)
Atmosphere	• Atmospheric conditions • Controlled atmosphere (inert)

Figure 5.10. Main subsystems for laser processing

subsystems are rearranged, and each of its main elements depicted in Figure 5.10. The different laser processing stations developed throughout this research are comprised by these five basic subsystems. Each experimental station has different embodiment solutions, as it will be shown below, and each station is a refined version of the previous ones, where the modifications are based mainly on the experimental results.

In the beginning chapters a series of objectives were identified based on some of the crucial aspects of optical communications. Two of the fundamental objectives from a manufacturing standpoint that were to be addressed by this work include: *feature size* and *property uniformity*. These two aspects are particularly affected by the laser processing step of the proposed direct-write process. In order to identify the set of parameters related to laser processing that affect these two properties, a cause-effect diagram was put together for each. Figure 5.11 shows the cause-effect or fishbone diagrams, with branches based on the main subsystems of Figure 5.10. Some of the parameters are

related to material properties, which are mainly controlled following the procedures of Chapters 3 and 4. On the other hand, several parameters have a strong relation with the actual design of each of the main subsystems involved. For example, the feature size is dependent on the wavelength of the selected laser, or the property uniformity depends on the accuracy and stability of the beam translational subsystem.

As seen from Figure 5.11, there are a large number of parameters that affect each of these objectives. Therefore, an important objective of this chapter is to identify the significance of these parameters and provide a set of guidelines for the successful implementation of the proposed direct-write process.

Below is a brief description of the various prototype laser processing stations developed during this research, presented in chronological order.
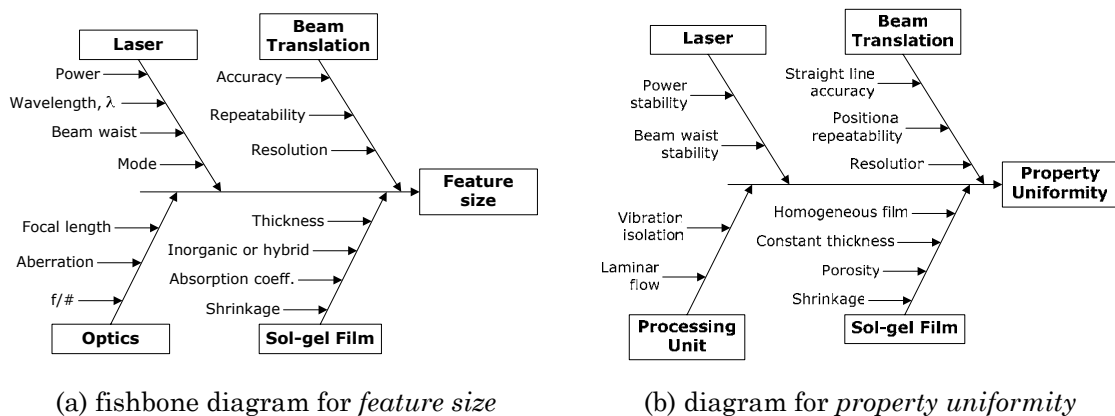

(a) fishbone diagram for *feature size*   (b) diagram for *property uniformity*

Figure 5.11. Cause-effect diagrams for two important objectives

5.3.1. Alpha 1: CO_2 Laser and Galvanometers

Current SLS technology uses galvanometer mirrors to translate the laser beam (typically a CO_2 laser) over the part bed in an *XY* plane. For this reason this was the first selection for the Alpha 1 station: to experiment with familiar and proven technology. The embodiment solutions for the Alpha 1 station were based on the fundamental subsystems presented in Figure 5.10. Following this scheme, Table 5.3 presents the embodied solutions for each subsystem.

A schematic diagram of the optical bench (top view) designed for the Alpha 1 station is presented in Figure 5.12. As observed from this figure, a HeNe laser was used as a *sighting laser* for alignment purposes and to track through a CCD camera the position of the beam at the focal plane prior to any direct-write operation with the CO_2 laser beam. Pictures of the actual Alpha 1 station are shown in Figure 5.13. The position of the laser beam is controlled through a pair of galvanometer mirrors, which can independently move the beam

Table 5.3. Embodiment solutions for Alpha 1 station

|		
1	Laser type	CO_2 laser (Synrad) as heating source, nominal power= 50 W, CW, d_l=3.5 mm, single mode TEM_{00}
2	Beam shaping optics	$10\times$ beam expander, and focusing lens (D=50.8 mm, f=305 mm) (II-VI Inc.)
3	Laser power control	External PWM controller (Synrad), TTL on/off access, duty cycle control: 5-95%
4	Translation of beam	Galvanometer mirrors and servo-controller (General Scanning DE2000)
5	Processing unit	Stainless steel high-vacuum chamber, multi-port, adjustable position of sample (z-direction), controlled atmosphere with high purity nitrogen and high vacuum capabilities, ZnSe top viewport for CO_2 laser. Non-isolated rigid structure
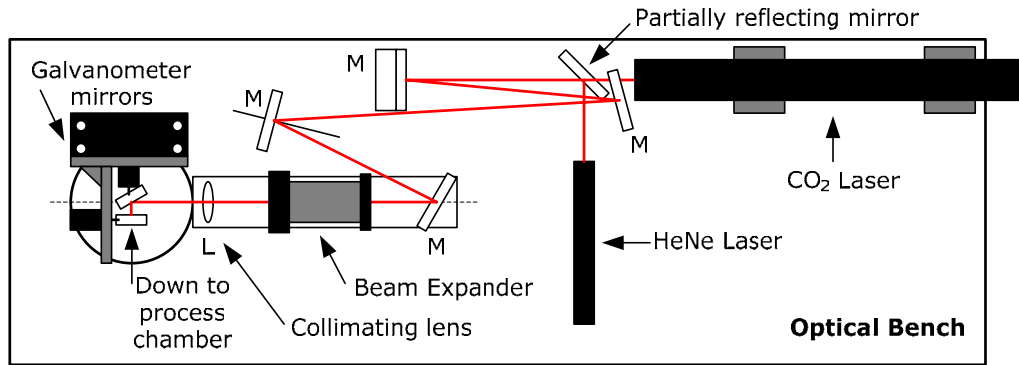
Figure 5.12. Schematic of optical bench for Alpha 1 station

in the X and Y axis. The galvanometer system, a DE2000 model by General Scanning, has a linear resolution defined by the following expression (Das, 1998):

$$LSB = 2l_{sc} \cdot \frac{\tan(20°)}{65536} \qquad (5.32)$$

where *LSB* is defined as the smallest linear motion the scanners can execute along each axis (in or μm), and l_{sc} is the scanning radius or distance from the galvo mirror to the work plane (in or cm). The rectangular grid is divided in 65536 (2^{16}) points along each axis, and each scan head has a rotational freedom of ±20° (Das, 1998).

For the current design (see values from Table 5.3), and from Equation (5.32), the resolution is approximately ≈3μm for each axis.

The software used to control the scanners was designed and developed by Suman Das (Das, 1998). In the software, the user provides the geometry to be scanned as 2D "slices". The geometry can be processed as a vector or contour file, and the user can select between raster scanning (uni-directional or bi-directional) and contour scanning. In addition, the user can select the following processing parameters: (a) scan spacing (spacing between successive vectors), (b)

226

step size *SS* (magnitude of each step as a multiple of *LSB*), (c) step period *SP* (time taken to translate the beam one *LSB* unit, in µsec). The scanning velocity can thus be determined through the following equation (Das, 1998):
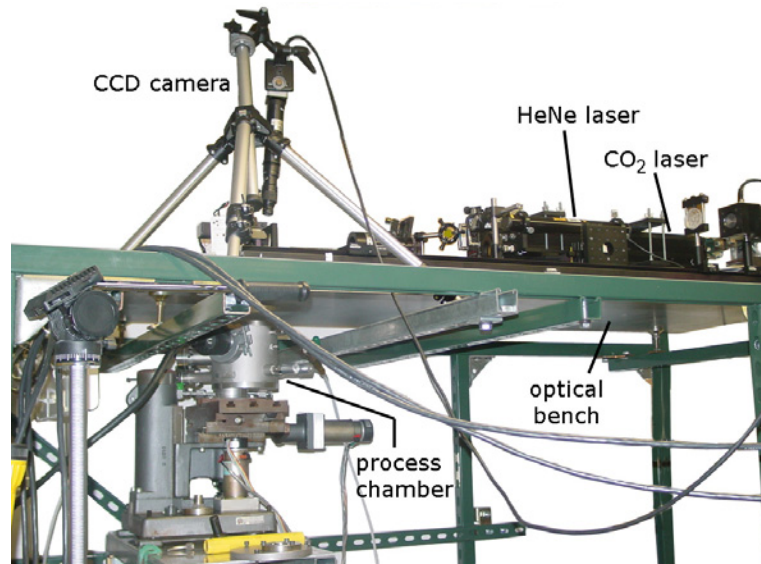
(a) process chamber and optical bench
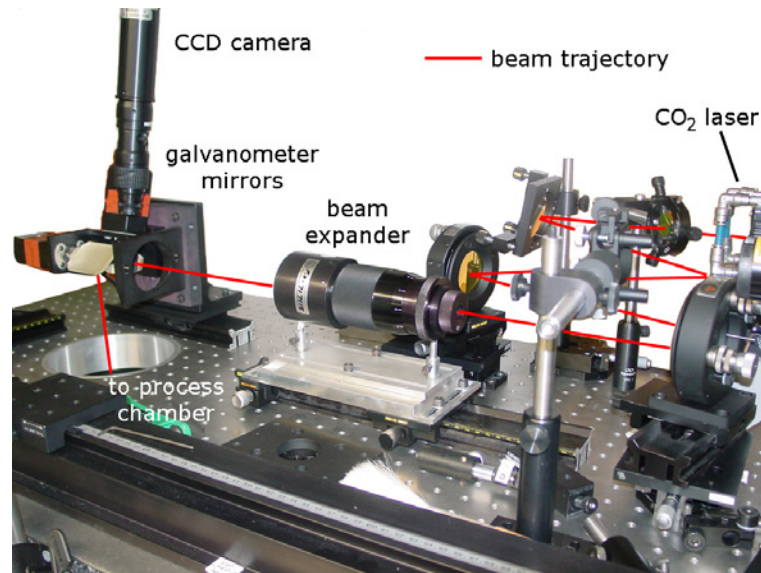
(b) optics bench

Figure 5.13. Alpha 1 station

$$v_s = \frac{SS \times LSB}{SP \cdot 10^{-6}} = \frac{2l_{sc} \tan(20°) \cdot 10^6}{65536} \cdot \frac{SS}{SP} \qquad (5.33)$$

For the DE2000, the range of allowed values is: SS={1–32767} LSB units, and SP={210–65534} µs.

With the DE2000 scanners a fast and moderately accurate beam positioning system is provided. The next process choice was the selection of a CO_2 laser, which was done for two main reasons. From Figure 5.4, it can be observed that the absorption of crystalline SiO_2 is high in the far IR, particularly at λ=10.6 µm, which corresponds to the wavelength of the CO_2 laser, making this type of laser appropriate for thermal processing. The second reason is that this laser was readily available in the laboratory, and it constitutes a low power, low cost, and easily controlled laser for initial experimentation. The CO_2 laser used for this station was a 50 W (nominal), CW, TEM_{00}, by Synrad.

Since silica has a high absorption at λ=10.6 µm, the optics required to position and focus the CO_2 laser beam must be made or coated with a material with lower absorption. ZnSe is an adequate material for this application. For the Alpha 1 station ZnSe was the material of choice for lenses, mirrors, and the viewport for chamber, all of these manufactured by II-VI Inc.

Control of the laser power was performed through a PWM controller with a trigger input signal, and manual selection of the power set point. The PWM controller was also from Synrad. The main characteristic of this controller is that it produces a square signal with a 200 µs period, plus a tick signal of 1 µs duration at the same period (see Figure 5.14b). The power is controlled by changing the pulse width from 5 to 95% of the total period. One drawback from this controller is that the power is adjusted through a knob or dial
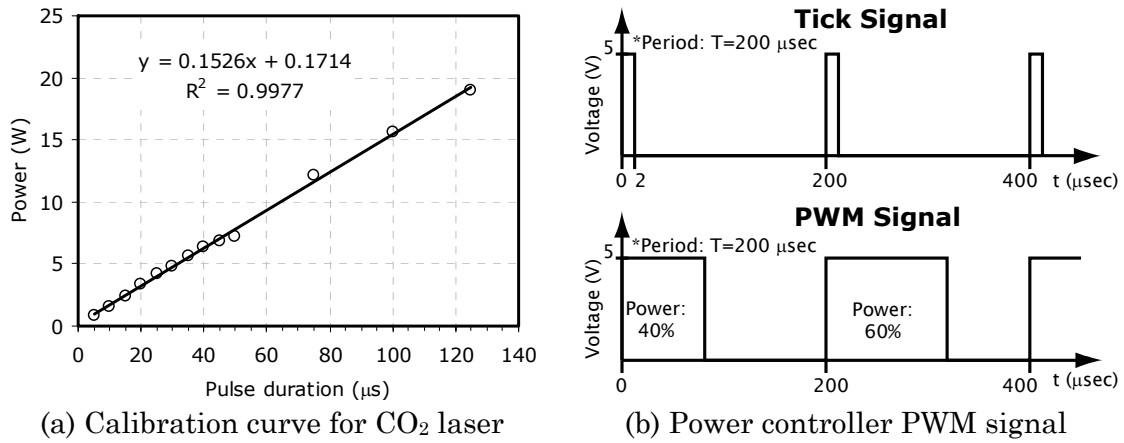
(a) Calibration curve for CO_2 laser　　(b) Power controller PWM signal

Figure 5.14. Calibration of CO_2 laser: power Vs pulse duration

(potentiometer) in a passive way; so no active or feedback control is possible, only on/off through the trigger.

The CO_2 laser output power was calibrated versus the pulse duration with the aid of an oscilloscope and a power meter (placed at the focal plane). Figure 5.14a shows the calibration curve with the corresponding linear fit and the squared of the residuals. The power stability over time remained at approximately ±2.5%, which is somewhat high if a high performance application is to be achieved. The CO_2 laser used performed better both in terms of stability and linearity if used between 15–80% of its full power (full pulse width).

With respect to the minimum spot size, the beam passes through a long focal length lens before it is translated by the scanners in the working plane (see diagram in Figure 5.12). Because of the long focal length of the focusing lens, the minimum spot size as described by substituting Equation (5.28) into (5.27), is larger than the one achievable by a shorter f. This is shown clearly in Figure 5.9. So considering the correction by diffraction, divergence, and aberration, the
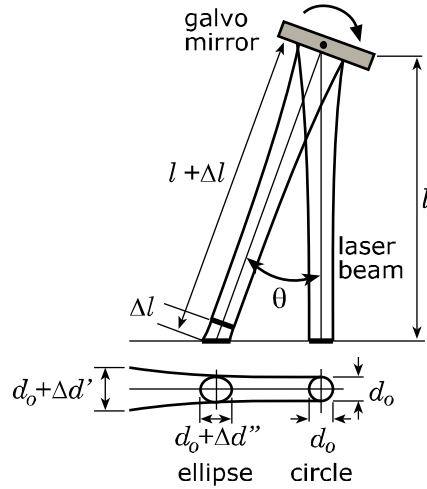
Figure 5.15. Beam distortion with galvanometer mirrors

minimum theoretical spot size achievable for this setup is ~137 μm at $1/e^2$, which is quite large as compared to the dimensions of both the sol-gel film thickness and a typical single mode waveguide.

One drawback of using galvanometer mirrors is the distortion of the spot shape with rotation. This distortion is illustrated in Figure 5.15. As the circular cross-section is rotated and the length increases, the shape of the cross section at the working plane becomes a distorted ellipse and the beam is defocused as the angle of rotation is increased. For long focal lengths, which is the case for common SFF applications (e.g. SLS and SLA), this beam distortion is minor. On the other hand, the manufacture of features in the micro-scale requires higher dimensional tolerances, particularly for optical applications. This beam cross-section deviation became apparent with experimentation, but the galvanometer mirrors were still used as a starting point.

Control of the atmosphere surrounding the sample was addressed by using a processing chamber, as shown in Figure 5.13a. The process chamber had controlled atmosphere with nitrogen and low vacuum capabilities, a sample holder with adjustable height, and a ZnSe viewport for the incoming CO_2 laser.

5.3.2. Alpha 2: CO_2 Laser and Galvanometers

Based on the experiments conducted with the Alpha 1 station, some modifications were implemented for the Alpha 2 station. The three main issues addressed were: (1) reducing the spot size, (2) redesigning the user interface to control the scanners, and (3) control the laser power by software with added functionality. More emphasis was put on the overall *systems design* part of the project. Table 5.4 lists the embodiment solutions for the Alpha 2 laser station.

In order to improve the beam quality and reduce the spot size two things were implemented. First, the number of elements in the optical path was reduced, as seen in Figure 5.16a. Second, the scan radius l_{sc} was reduced and a

Table 5.4. Embodiment solutions for Alpha 2 station

1	Laser type	CO_2 laser (Synrad) as heating source, nominal power= 50 W, CW, d_l=3.5 mm, single mode TEM_{00}
2	Beam shaping optics	10× beam expander, focusing lens: plano-convex (D=38.1 mm, f=127 mm), and beam 50% splitter (II-VI Inc.)
3	Laser power control	Software PWM controller programmed in LabVIEW, TTL on/off signal, duty cycle control: 5-95%
4	Translation of beam	Galvanometer mirrors and servo-controller (General Scanning DE2000)
5	Processing unit	Sample holder, open atmosphere. Non-isolated rigid structure
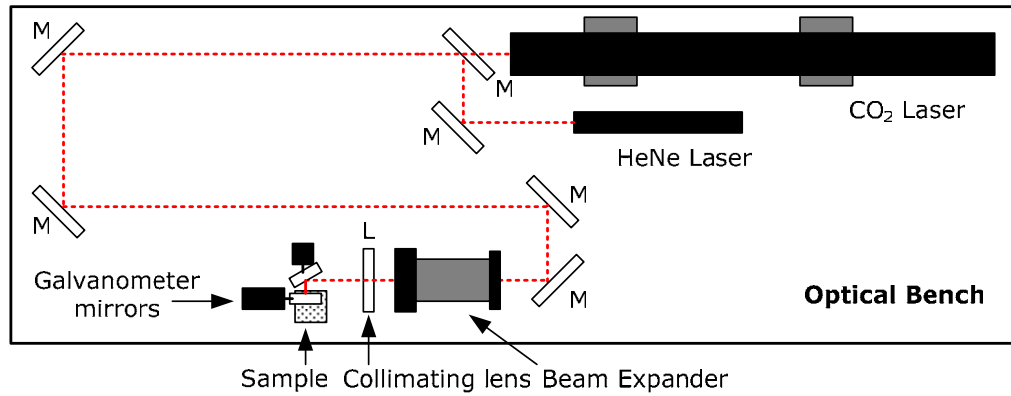
(a) schematic of optical bench (top view)
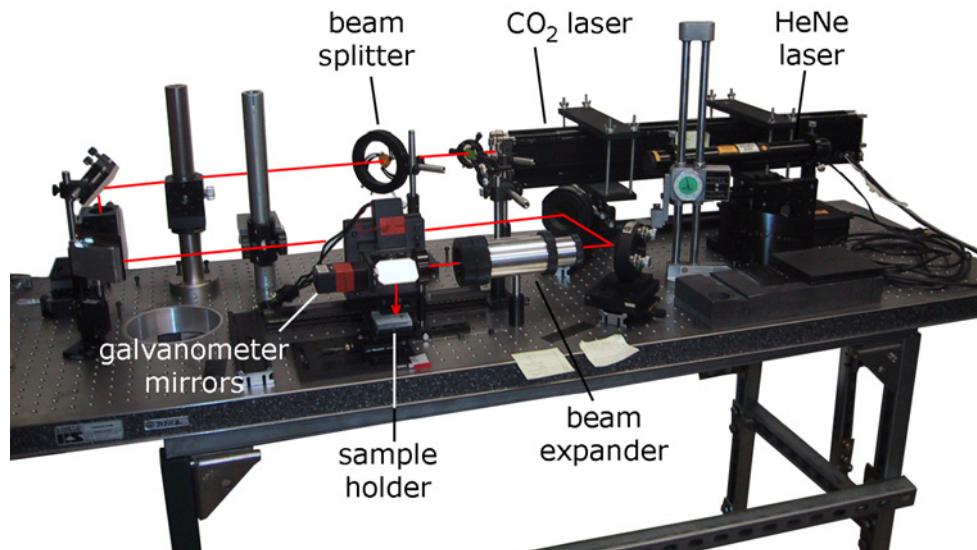
(b) picture of Alpha 2 station

Figure 5.16. Alpha 2 station

shorter focal length lens was used. The theoretical minimum spot size was reduced to $d_o \approx 110$ μm with a focal length of $f=127$ mm.

One of the goals of this research was to create the platform for a fully automated direct-write machine. To move in this direction and using standard elements, the user interface to control the laser processing step was redesigned

and implemented in LabVIEW. The LabVIEW interface was designed to incorporate three main elements:

(1) *Geometry*: design or import the 2D geometry to be traced by the laser.

(2) *Scanner control*: translate the geometrical input into the code executed by the DE2000 controller, allowing the user to define the scanning parameters such as the scan step, scan period, etc.

(3) *Laser power control*: allow the user to define a power profile (P_l Vs t) that can be synchronized with the geometry as it is executed and controlled by the laser motion unit, in this case by the DE2000.

These three elements were fully implemented through software, programmed in LabVIEW (v7.1) by Ms. Guohua Ma, doctoral student of the LFF research group. Figure 5.17 shows a series of screen shots of the LabVIEW interface. The screen shot of Figure 5.17a is welcome screen, which is followed by the "Generate Geometry" screen in Figure 5.17b. This screen allows the user to import a file that contains the 2D geometry as a vector or contour file. The user also has the option to generate the geometry directly in the interface, based on simple geometries such as a series of points, straight or curved lines, circles, or splines. After the geometry has been defined, there is a third screen (not shown) in which the user executes a function that translates the geometry into a series of commands in the code of the DE2000 controller, appending the code into a new file. In a fourth screen, shown in Figure 5.17c, the user can assign values to a series of parameters that control the scan speed and the option of repeating the commands several times. After selecting the scanners' parameters, the user

can define in a new screen (not shown) the laser power profile. In this case, the user has the option of selecting the power profile from a library (constant, ramp, parabolic, trapezoidal) or typing in a table the power level and time parameters. In the final screen, presented in Figure 5.17d, the user can verify all of the parameters, execute the program, and verify in real-time the execution of the program.

For this Alpha 2 station, the PWM power controller of the laser was replaced by a software version, which can generate the pulse pattern and change
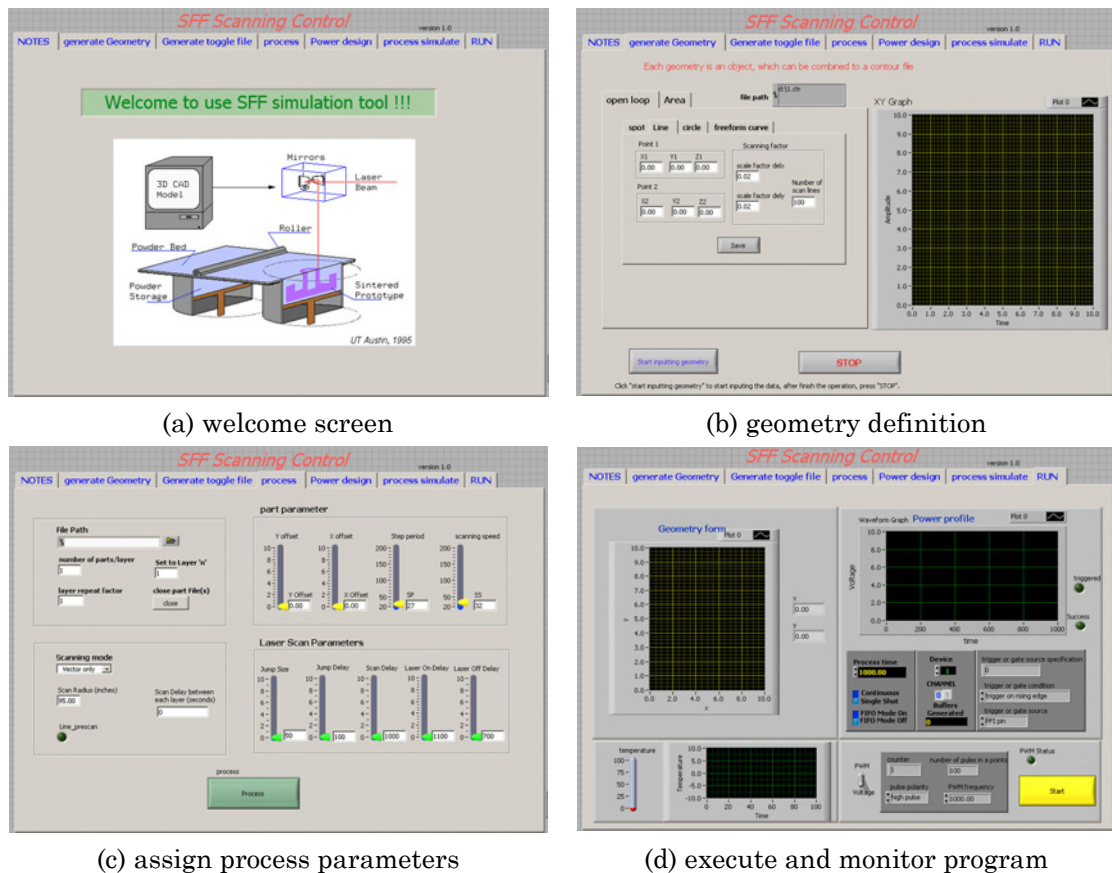

(a) welcome screen

(b) geometry definition

(c) assign process parameters

(d) execute and monitor program

Figure 5.17. LabVIEW interface for laser motion and power control

the pulse width according to the power level defined by the user. In the LabVIEW interface, when the user defines the power profile P_l Vs t, the time is assigned as relative to the total time required to execute the geometry. This total time is divided by the number of steps, and the result must be higher than the 200 μs period of the tick signal required by the laser to operate in optimal conditions.

The LabVIEW interface is executed in a PC (Dell Dimension 4800, Pentium IV, 512 MB RAM). The PC communicates to the DE2000 controller through the LPT1 port (parallel) and to the laser through a DAQ card (model: PCI-MIO-16E-4, by National Instruments). The DAQ card sends the TTL PWM signal (voltage V=0–5 Volts, period T=200 μs) to the laser to control On/Off condition and power level.

In general, the LabVIEW interface was designed mainly for research purposes, to test the overall concept of building parts of the proposed direct-write process to be fully automated and controlled by a PC. Simple and off-the-shelf components were selected based on a modest budget and equipment already owned by the LFF lab.

One of the problems that emerged from the implementation of the software version of PWM control was that the laser could not maintain a continuous wave output, behaving like a pulsed laser. Two main issues were found to cause this problem. First, a PC with Microsoft Windows as its operating system is interrupt driven, so "real-time control" is not realistically achieved, particularly for cases of rapidly changing signals such as the 200 μs period of the PWM signal. Second, the data transmission time between the PC to the DE2000

controller through the LPT1 port was much longer as compared to the PCI DAQ board and laser. This poor synchronization was partially solved by improving the code and including time delays, but it was decided that independent controllers can communicate faster between themselves through direct signals. One alternative is to use more recent real-time DAQ boards, which act as independent master computers. This option was not pursued.

For this station no atmosphere control was pursued and the sample was exposed to atmospheric conditions, as seen in Figure 5.16a.

5.3.3. Alpha 3: CO_2 Laser and XY Stage

A major overhaul of the laser processing station was pursued and named Alpha 3 station, as a third iteration of this prototype. The main changes to this new station consisted of: (1) implementing a different embodiment solution to the

Table 5.5. Embodiment solutions for Alpha 3 station

1	Laser type	CO_2 laser (Synrad) as heating source, nominal power= 50 W, CW, d_i=3.5 mm, single mode TEM_{00}
2	Beam shaping optics	$10\times$ beam expander, focusing lens (D=38.1 mm, f=127 mm), and beam splitter (50%) (II-VI Inc.)
3	Laser power control	Hardware: PWM controller (in house) with TTL on/off access, and PC duty cycle control: 5-95%
4	Translation of beam	• Hardware: XY translation stages (Parker-Daedal 404LXR), linear servomotors, working area 250×250 cm, encoder resolution 0.5 μm, max. velocity 1 m/s, positional repeatability $=\pm1.0$μm • Software: CompuMotor motion control interface
5	Processing unit	Sample holder, open atmosphere. Optical bench (Kinetic Systems) with rigid structure

subsystem responsible of the *beam translation*, (2) modifying the beam optics subsystem as a consequence of the previous step, (3) implementing a hybrid strategy of hardware and software for the laser power control to solve some of the problems encountered in the Alpha 2 station, and (4) completely redesigning the processing unit, in particular the structure that supports the laser station.

For this Alpha 3 prototype station, the scanners and DE2000 controller of the galvanometer mirrors were replaced by two translation stages (x and y direction) that would move the sample instead of the beam. This modification was made to allow the use of a focusing lens with a smaller focal length, thus reducing the spot size, and to maintain a uniform beam profile or cross-section throughout the whole part being manufactured. After an extensive evaluation of commercial XY translation stages, including cost-benefit, it was decided to purchase two linear servo-motors from Parker Hannifin Daedal Division that could be assembled as an XY stage. The servo motors are the 404LXR with a total working area of 250 cm × 250 cm, 1.5m/sec maximum velocity, 0.5μm encoder resolution, positional ±1.0μm repeatability, 12μm positional resolution, and straight line resolution of 14μm. Each linear servomotor is powered by independent Parker Gemini drivers, and both synchronized through the Parker 6K2 two-axis controller. The 6K2 controller is connected to a PC through an Ethernet cable. The motion programs are developed in the MotionPlanner software and then transferred and executed by the 6K2 controller.

There are two additional features that played an important role in the selection of this configuration. First, the 6K2 controller has digital onboard inputs and outputs, so the controller can be interfaced with other devices. This feature is particularly useful for the laser power control. Second, geometry

generated in standard CAD software such as AutoCAD or Solid Works, can be imported through the CompuCAM software, as DXF or STL files. CompuCAM then can generate the motion code interpreted by the 6K2 controller, thus making the interface more user-friendly. The user can design the optical component in standard CAD software, import it through CompuCAM, assign the motion control parameters, such as velocity and acceleration of the servomotors, and execute the program through a simple LabVIEW interface.

The use of this XY stage required the translation of the sample instead of the beam. Thus the beam optics was modified so the laser could be directly focused on the working plane. Two optical benches were employed, one with the laser and optics, and the second for the XY stage. Figure 5.18 presents a schematic of the Alpha 3 station, indicating the beam path and working area of the XY stage.

The structure was fully redesigned to accommodate the new requirements of two optical benches and the XY stage plus controller. The structure was built from scratch with simple Uni-truss beams with the help from one undergraduate student, Carlos Villalobos, and one master's student, Vinay Sriram. The full
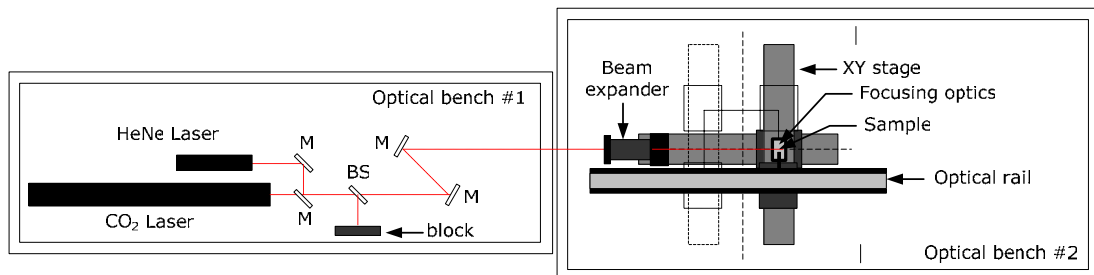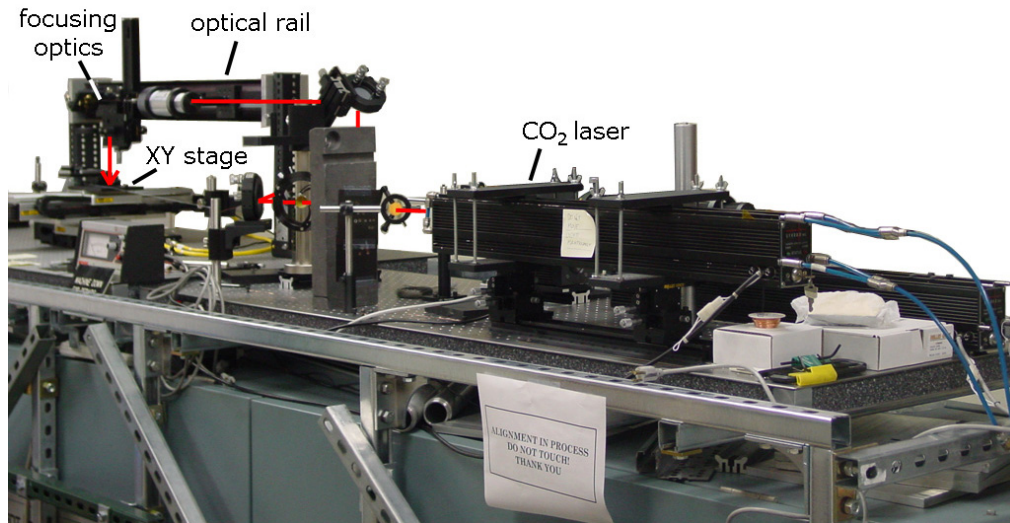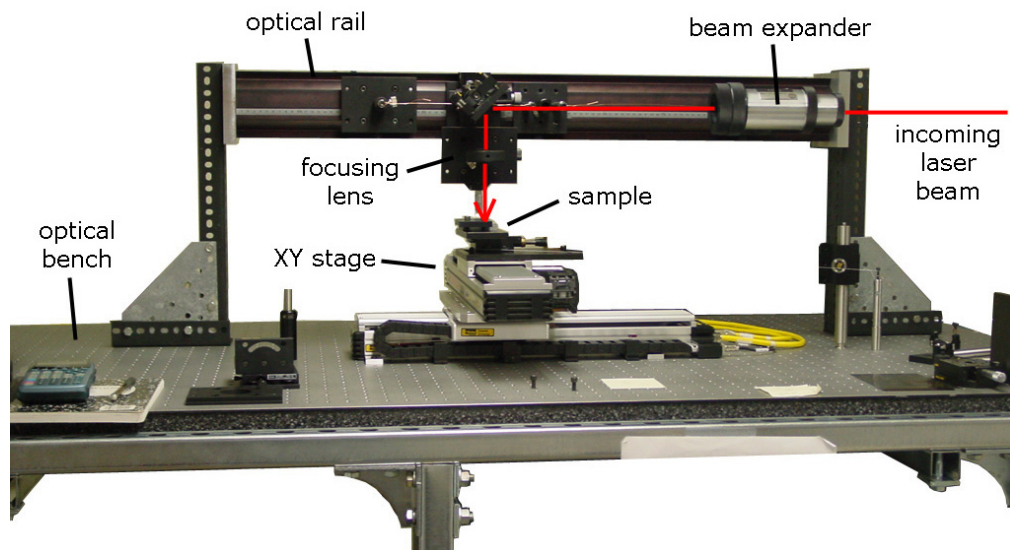

Figure 5.18. Schematic of Alpha 3 station

238

assembly of this first prototype with the XY stage is shown in Figure 5.19.

The sample holder consisted of a simple anodized aluminum plate from Thorlabs, and a set of adjustable jigs. The sample was exposed to atmospheric

(a) optical bench #1 & 2

(b) optical bench #2
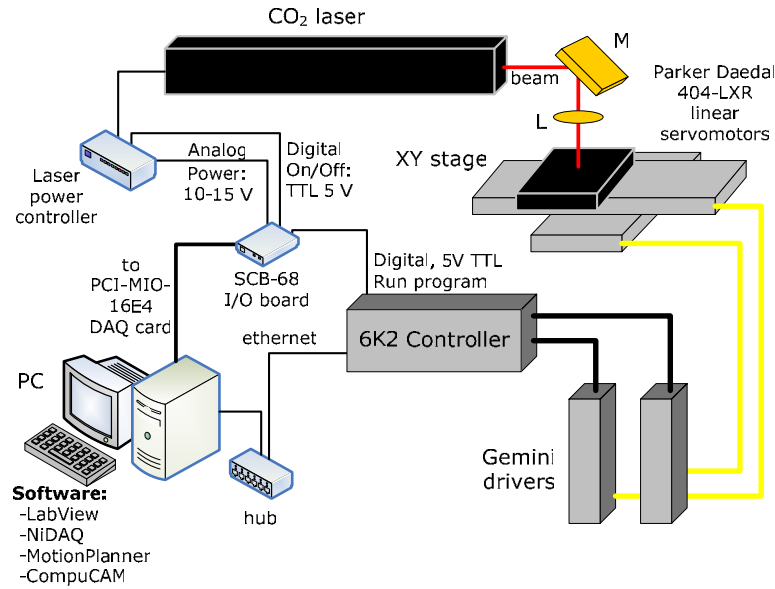
Figure 5.19. Alpha 3 station

conditions, which is not optimal, but for this prototype version it was considered sufficient.

The laser power control was performed by both hardware and software. The hardware portion basically was aimed at recreating the electronics of the original PWM controller, with the addition of two input signals to control the pulse width and the On/Off trigger signal. The software portion was designed in LabVIEW as a simple virtual instrument (*vi*), with parts of the code from the software for the Alpha 2 station. The LabVIEW *vi* allows the user to design the power profile from a library of options (constant, ramp, trapezoidal, parabolic, or by manual input through a table). The user can execute the program either manually (independent from the XY stage controller), or just execute the motion program and define the ON and OFF periods in the program so the 6K2 controller can send the signal directly to the hardware portion of the laser controller.

Figure 5.20a shows a wiring diagram depicting the connections between the components employed in the Alpha 3 station. The LabVIEW *vi*'s for the design of the power profile and the monitoring and interface to the power controller are shown in Figure 5.20a and b, respectively.

The power controller (Figure 5.21b) was designed based on a similar version by Mohammed Shaarawi. It consists of a function generator, capable of generating a clean square wave with a period of 200 μs by adjusting a resistor and selecting a capacitor. The output signal goes to a voltage comparator IC, which receives the input voltage from the LabVIEW *vi*. The output then goes to an AND logic gate that receives the On/Off input from the 6K2 controller

through the LabVIEW *vi* to turn the laser on or off. The tick signal is generated

by an oscillator IC, which provides the required T=200 μs and Δt=1 μs signal.

(a) wiring diagram for Alpha 3 station
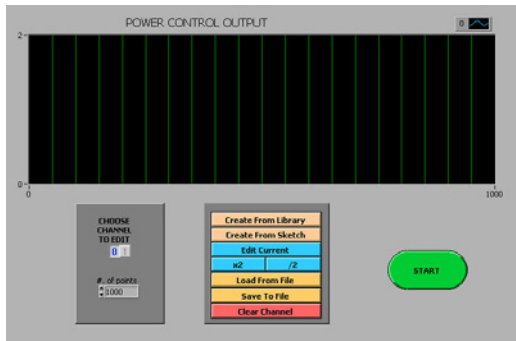
(b) *vi* for design of power profile
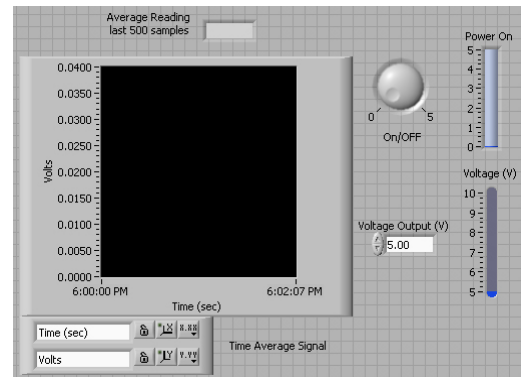
(c) *vi* for monitoring of output voltage for power control

Figure 5.20. Wiring diagram and LabVIEW interface for Alpha 3

<table>
<tr><td>(a) XY stage control board</td><td>(b) laser controller</td></tr>
</table>
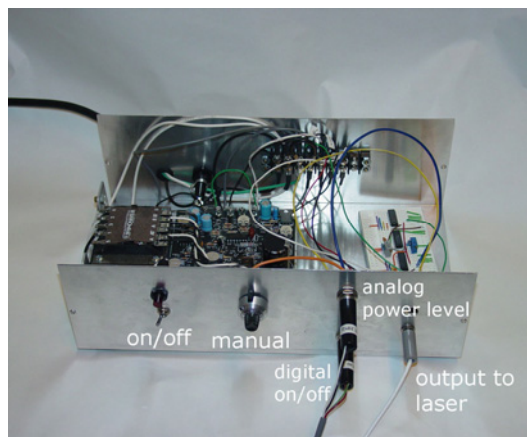
Figure 5.21. Hardware control connections for Alpha 3 station

5.3.4. Beta 1: HeCd UV Laser and XY Stage

The development of the Alpha 3 station was a major advance for the project. The next step involved a refined iteration of this station, incorporating a UV laser for photophysical processing and a more controlled atmosphere. These were the two main changes that constituted what was named as the Beta 1 station, following a *Design Methodology* jargon. Table 5.6 lists the embodied solutions for the Beta 1 station.

The optical setup for Beta 1 was redesigned to incorporate the IR and UV lasers, which use entirely different optics. First, the full setup was installed on a single optical bench. For the main optical rail installed above the XY stage, the

supporting pillars were changed for rails with greater stiffness from Thorlabs. This optical rail supported the main components of the optical trains for both laser systems. The design and assembly of the structure and optical train was done in conjunction with Michael Mignatti, graduate student from the LFF lab.

The lasers installed in this station were the previous CO_2 laser by Synrad, as the IR source, and a HeCd laser from Ominchrome (see Table 5.6), as the UV source. The lasers were installed above each other by means of an elevated plate, as seen in Figure 5.22.

Table 5.6. Embodiment solutions for Beta 1 station

|		
1	Laser type	• HeCd laser (Omnichrome 2056), nominal power= 8mW @325 nm and 25mW @424 nm, CW, d_l=1.5 mm, multi mode • CO_2 laser (Synrad) as heating source, nominal power= 50 W, CW, d_l=1.5 mm, single mode TEM_{00}
2	Beam shaping optics	• CO_2 laser: 10× beam expander, focusing lens (D=38.1 mm, FL=25.4 mm), and beam splitter (50%) (II-VI Inc.) • HeCd laser: collimating set, beam expander, focusing lens (D=25.4 mm, FL=25.4 mm), band pass filter (Optics for Research, Edmund Optics and OptoSigma)
3	Laser power control	• CO_2 laser: PWM controller (in house) with TTL on/off access, and PC duty cycle control: 5-95% through LabVIEW • HeCd laser: passive control, neutral density filters (Optics for Research and Edmund Optics)
4	Translation of beam	• Hardware: XY translation stages (Parker-Daedal 404LXR), linear servomotors, travel 250 mm, maximum velocity 1.5m/sec, encoder resolution =0.5μm, positional repeatability =±1.0μm, positional resolution =12μm, straight line resolution =14μm, • Software: CompuMotor motion control interface,
5	Processing unit	Sample holder in enclosed controlled atmosphere. Optical bench (Kinetic Systems) with vibration isolators (Kinetic Systems)

The HeCd laser is a refurbished laser selected to test the whole laser processing concept, based on a modest budget. This laser is multimode with two wavelengths: 325 nm and 424 nm. The nominal power at 325 nm is 8 mW, while at 424 nm is 25 mW. Because of the multimode nature of this laser, and the poor M^2 value (M^2=14), the beam greatly diverged with distance and it was difficult to focus to a small spot size. The optical train was designed taking this aspect into consideration. This optical train has a theoretical minimum spot size of ≈13 μm.

The optical train for the UV laser consists of five main elements, which in sequential order are presented in Table 5.7.

The Beta 1 laser station is protected by sheets of plexi-glass supported by a structure of aluminum beams, as seen in Figure 5.22a. To protect the sample from dust particles and the ambient humidity during laser processing, a small chamber was designed to be placed on the XY stage. This chamber has a thin quartz cover plate, when used with the UV laser, and a ZnSe window for the CO_2 laser. The chamber can be purged with nitrogen through inlet and outlet ports, designed to maintain a steady and slow laminar flow.

Table 5.7. Optical elements for UV laser of Beta 1 station

Element	Description
F1	band-pass filter, to filter out the λ=424 nm component of the beam
L1	plano-convex lens (D=25 mm, f=50 mm), to re-collimate the beam
BE	beam expander, which consists of two lenses, L2 and L3
L2	plano-concave lens (D=25 mm, f=−50 mm), to expand the beam
L3	plano-convex lens (D=25 mm, f=250 mm), to re-collimate the beam
L4	plano-convex lens (D=25 mm, f=25 mm), to focus the beam
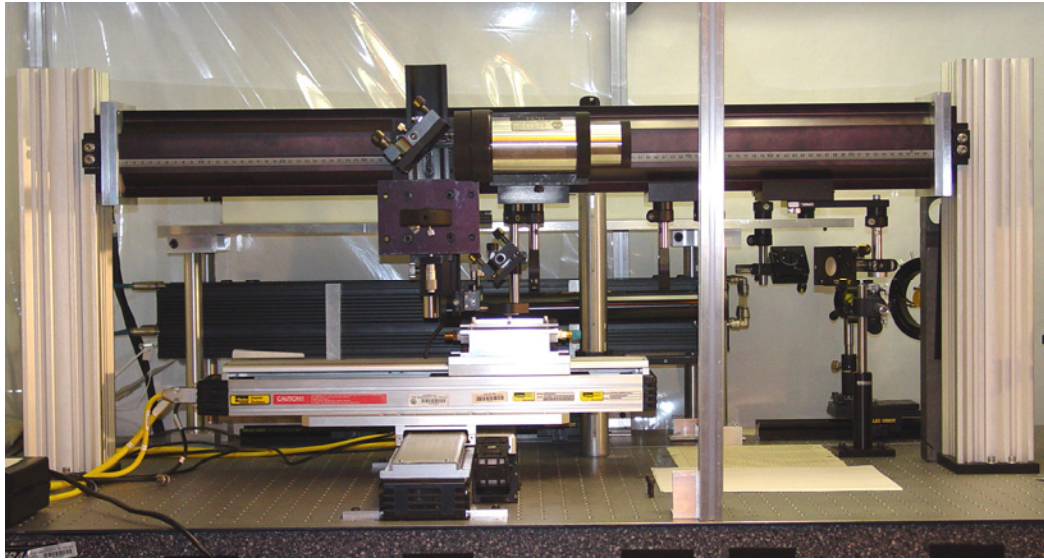
(a)
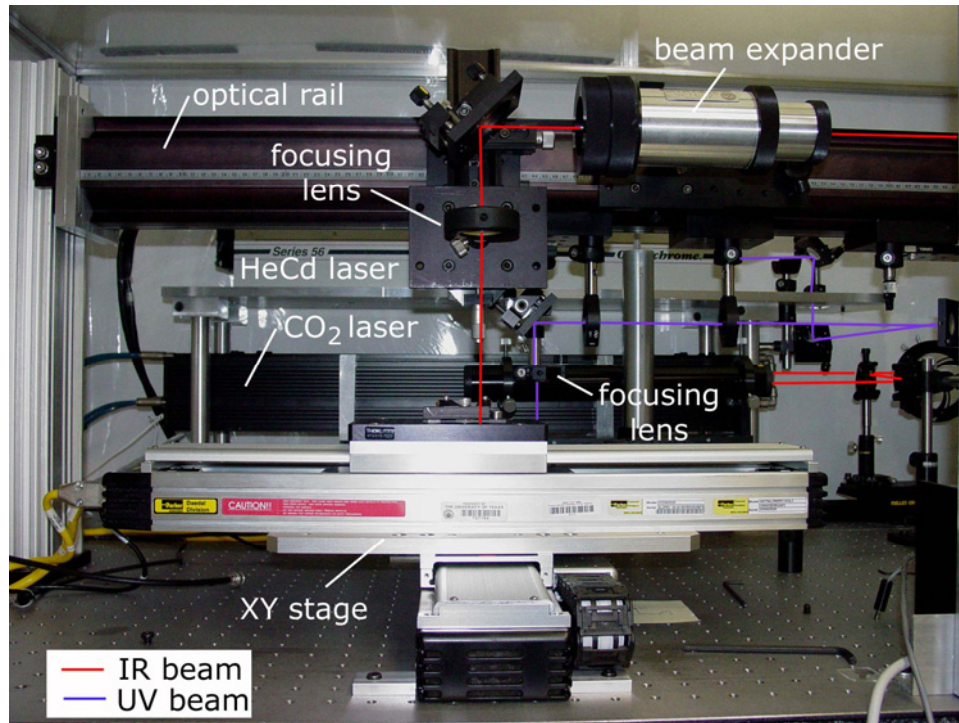
(b)

Figure 5.22. Beta 1 station

Four vibration isolators from Kinetic Systems were installed on the optical bench to suppress vibrations from equipment of neighboring labs.

With respect to the power control of the HeCd laser, this is done in a passive way through a series of neutral density filters, which attenuate the laser's irradiance. Three neutral density filters from OptoSigma were used with transmittances of: 50, 12.5, and 0.1%, respectively. The control of fluence delivered to the sample is done mainly though the velocity control of the XY stage.

The XY stage is controlled in the same way as described for the Alpha 3 station.

5.3.5. Experimental Setup for Laser Processing with UV laser at 3M

Ideally, the Beta 2 station would be equipped with a laser capable of producing a spot size in the range of single mode optical waveguides, that is 5–10 μm. Since such laser was not available, we were able to conduct equivalent experiments at 3M's Corporate Research Lab in Austin, Texas. The system used consists of a frequency doubled Argon$^+$ laser that operates at λ=244 nm (model: SabreFRED, by Coherent), a single translation stage (x-direction), and an optical train capable of focusing the beam down to d_o=5 μm. Figure 5.23 shows a diagram of the experimental setup. No picture of the physical system is shown.
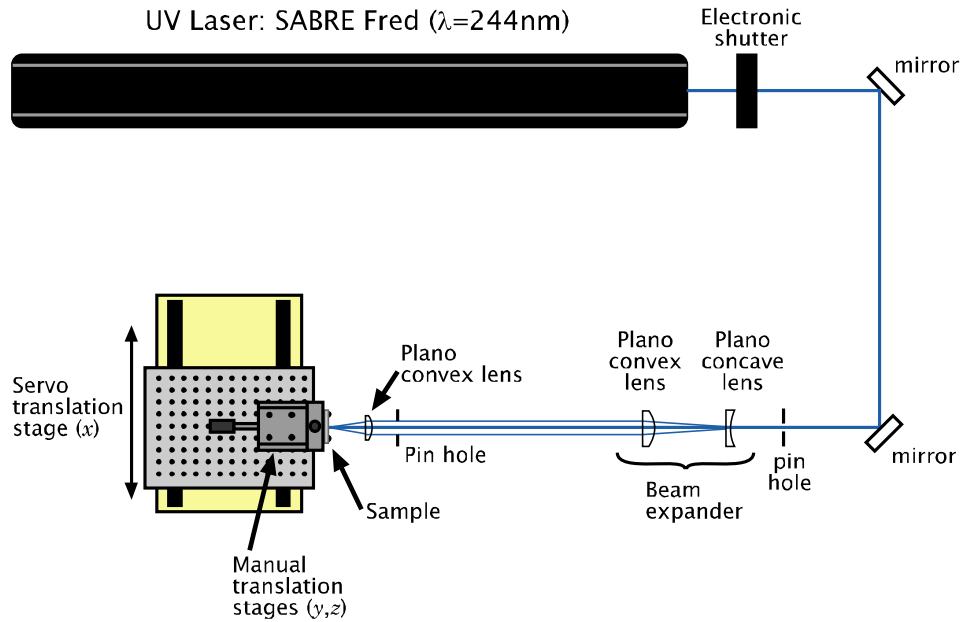
Figure 5.23. Experimental setup for laser processing at 3M-Austin

5.4. Experimentation and Analysis of Results

This section presents a summary of the experimental results with the prototype laser processing stations described above. The first experiments were conducted with the CO_2 laser; then followed by the use of the HeCd and Ar^+ lasers. The experimental results are presented in this same order.

5.4.1. Photothermal Processing – CO_2 Laser

As mentioned at the beginning of this chapter, the CO_2 laser was used as a concentrated heat source for photothermal processing of the sol-gel film with the objective of increasing locally the refractive index. The experiments involved the

use of the Alpha 1, 2, and 3 stations. The results presented below were primarily conducted with the Alpha 2 station.

The first step was to find the position of the focusing lens that produced the minimum spot size at the working plane. This was performed by adjusting the position of the lens and scanning a straight line on a piece of marking paper. Several lines were scanned and the width was measured with an optical microscope. After the best position for the focusing lens was found, some tests were conducted with a real sol-gel sample to corroborate the working position.

The laser processing step was only done on samples with crack-less sol-gel films. The experiments were done on purely inorganic silicate sol-gel films; using a mixture equivalent to DOE#5 (see Table 3.6). Translation of the beam for this station was done with the scanners and galvanometer mirrors, and controlled through the LabVIEW interface.

The design parameters for this set of experiments are the following:

- Laser power, P_l= 0.6–36 W (calibrated output power)

- Spot size (theoretical at working plane), $d_o \approx 110$ μm

- Wavelength (CO_2 laser), λ=10.6 μm

- Scan speed, v_s= 0.0013–13206.5 cm/s

Following a similar approach as for the synthesis of sol-gel films, at the beginning of the experiments a screening design (of experiments) was conducted. This involves selecting a broad range of values for the design parameters. At this point there is little knowledge on the ideal range for the DPs, so the use of plots such as the one shown in Figure 5.24 are quite useful for quickly locating a working space. The graph of Figure 5.24 plots a set of curves for fluence versus

(a) constant scan velocity   (b) constant interaction time
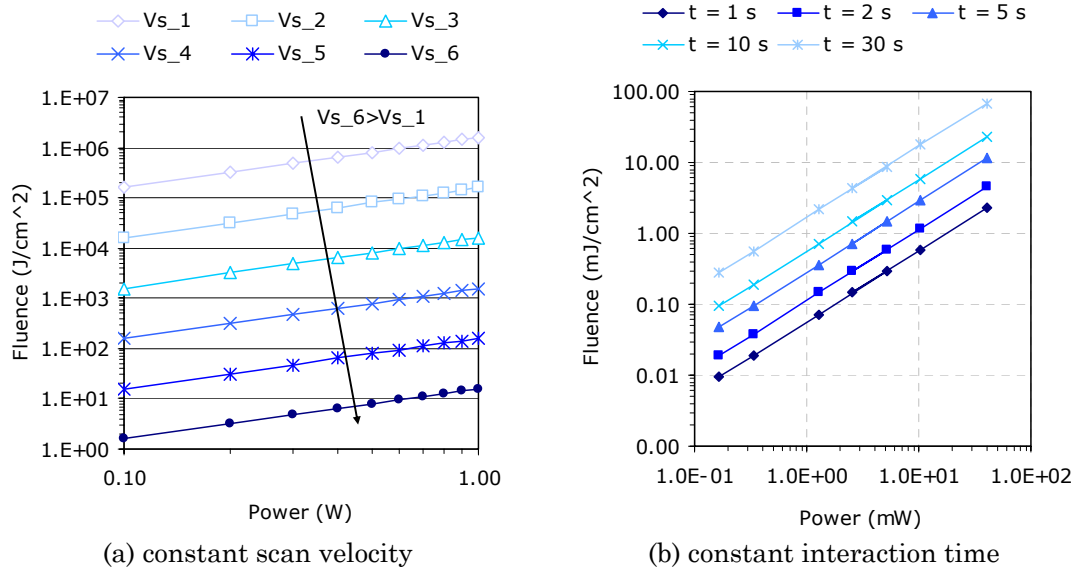
Figure 5.24. Working curves for experiments with Alpha 2 station

laser power at different scan velocities in log-log scale. The fluence is calculated with Eq. (5.16). The corresponding scan velocities are: v_{s1}= 0.001 mm/s, v_{s2}= 0.01 mm/s, v_{s3}= 0.1 mm/s, v_{s4}= 1.0 mm/s, v_{s5}= 10 cm/s, and v_{s6}= 100 cm/s.

The ID number for the sol-gel mixture for these experiments is #22-4, which is based on the mixture DOE#5 (see Table 3.6). The film deposition was done by spin coating with ω_{max}=2000 rpm and a total dwell time of 50 sec. The samples when then baked at T_{max}=250°C for 90 min under O_2 (grade 5.0 from Praxair). The substrates used were borosilicate glass slides, and were cleaned using the procedure described in Chapter 4.

Once a high quality film is produced, it can be used to conduct several tests by scanning various lines with different experimental conditions or DPs. For this sol-gel mixture, a total of ten samples were prepared. Ten lines were scanned through each sample with varying experimental conditions.

(a) sample: 22-4-1-1-E-2

(b) sample: 22-4-1-1-E-3

(c) sample: 22-4-1-1-E-6

(d) sample: 22-4-1-1-E-10
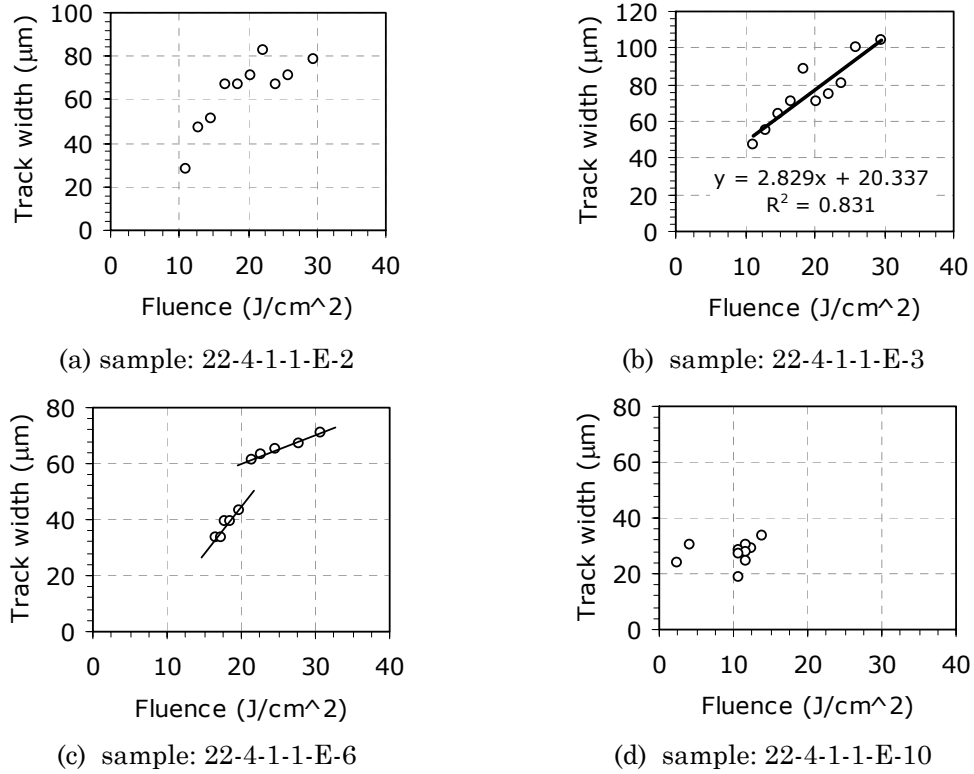
Figure 5.25. Line width Vs fluence for various experiments

Results from four samples are shown in the plots of Figure 5.25. The plots show the measured track or line width versus the fluence, which is calculated according to Equation (5.16). The track width was measured with an optical microscope.

Figure 5.25a and b show the results for samples 22-4-1-1-E-2 and 22-4-1-1-E-3, respectively. These two plots illustrate the screening design, where the fluence is varied over a broad range (~100–260 J/cm^2). The main difference between these two samples is the number of points used that divide the power profile curve P_l Vs t. As mentioned above, this was precisely a point of conflict that caused instabilities in the laser's output power. The greater the number of

points to interpolate the power curve, the greater the number of computations required, therefore causing a wider time delay between execution of the geometry by the scanners and the start of the power control scheme. This was corrected for sample 22-4-1-1-E-6, shown in Figure 5.25c. Also for sample 22-4-1-1-E-6, the laser power was increased to a region where the power remains more stable. This corresponds to the mid-region of the calibration curve (Figure 5.14). As seen from Figure 5.25c, the results follow a closer linear relationship over two visibly different regimes.

A step further was to operate the laser over its mid power region, while maintaining the same fluence levels by adjusting the scan velocity, and replacing the software PWM power controller by the hybrid software/hardware scheme, as described above. A beam splitter was installed to split the laser power by 30–70%, in order to operate the CO_2 laser in the optimal low-drift region. Sample 22-4-1-1-E-10 was prepared based on these changes, and the results for

(a) line width Vs fluence, showing the region of best results

(b) influence of scan velocity and laser power on the line width
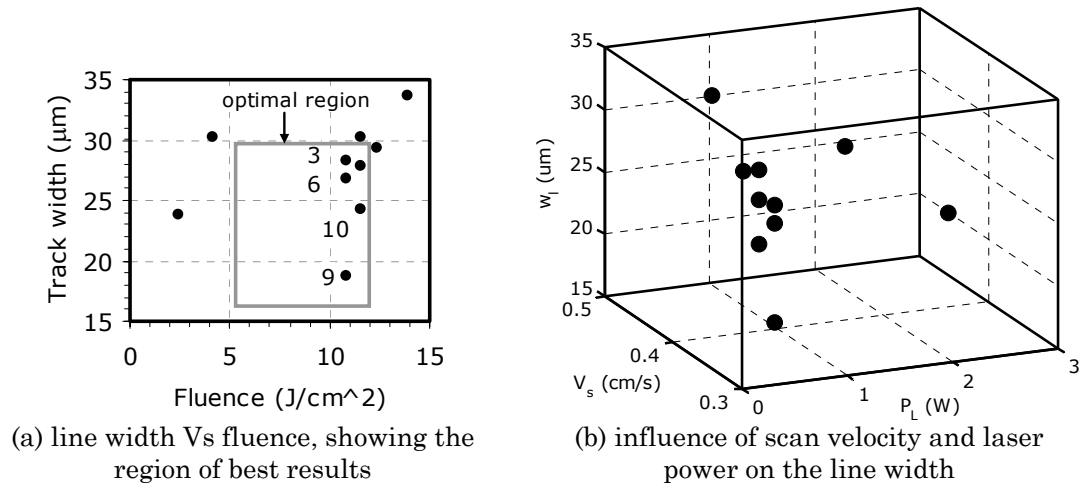
Figure 5.26. Plots for sample 22-4-1-1-E-10 showing no-damage region

(a) 22-4-1-E-2 track 5

(b) 22-4-1-E-9 track 1

(c) 22-4-1-E-10 track 5

(d) 22-4-1-E-10 track 6
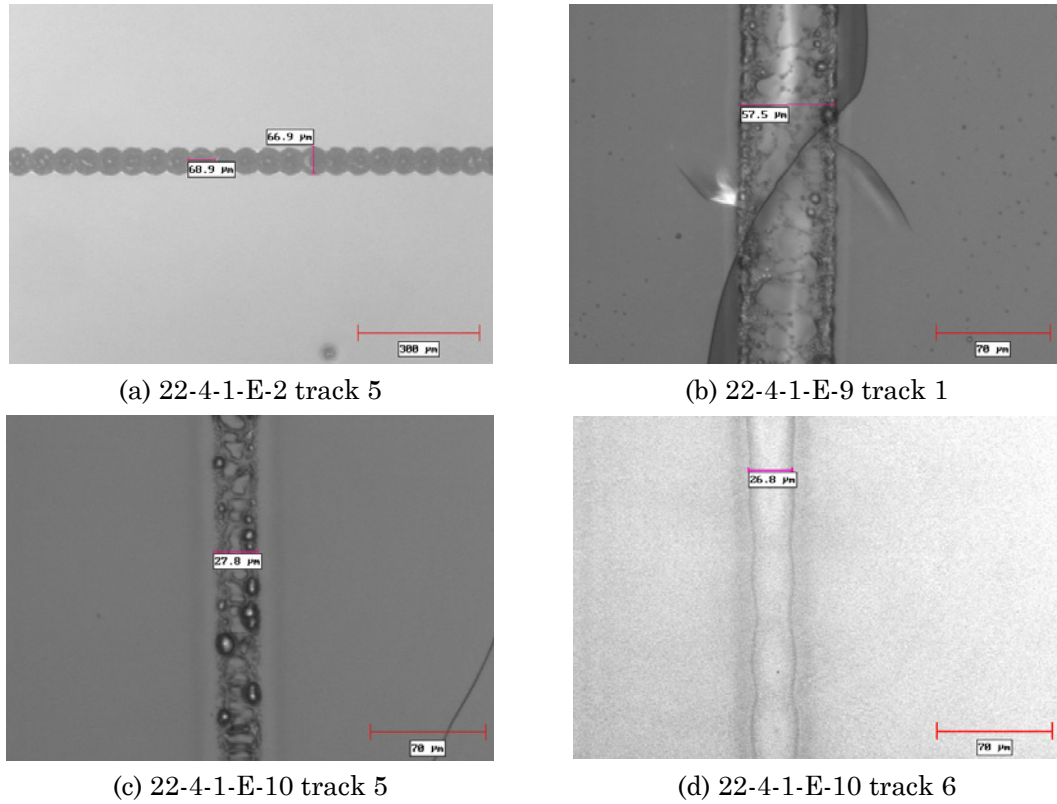
Figure 5.27. Pictures of experiments with CO$_2$ laser and Alpha 2 station

the line width are shown in Figure 5.25d and as a close-up in Figure 5.26a. As seen from these plots, a relatively small fluence level is required to achieve smaller line widths.

In addition to achieving a certain line width, it is also important to operate at a fluence level that is below the damage threshold, where the sol-gel film begins to melt and vaporize, and causing permanent damage to the surface (Shaw and King, 1990). Similarly, a minimum fluence level is required to achieve a substantial temperature increase, which in turn changes the refractive index in a significant way. Figure 5.27 shows optical micrographs of typical laser

direct-write tracks for the samples mentioned above. The laser-pulsing effect caused by the software implemented PWM is clearly shown in Figure 5.27a, through the continuous and overlapping spots where the laser was on a rapid on/off state. Figure 5.27b and c show melting, catastrophic failure of the sol-gel film, and permanent surface damage because of high fluence values; yet these images show a trend towards the ideal no-damage region.

A sol-gel film that was slightly densified with the CO_2 laser is presented in Figure 5.27d. The change in properties is so small that some post-processing

(a) output diameter from plano-convex ZnSe lens for various focal lengths

(b) rotation angle of scanners Vs position x on working plane

(c) percentage increase in scan length with position x on working plane

(d) percentage increase in beam waist with position x on working plane
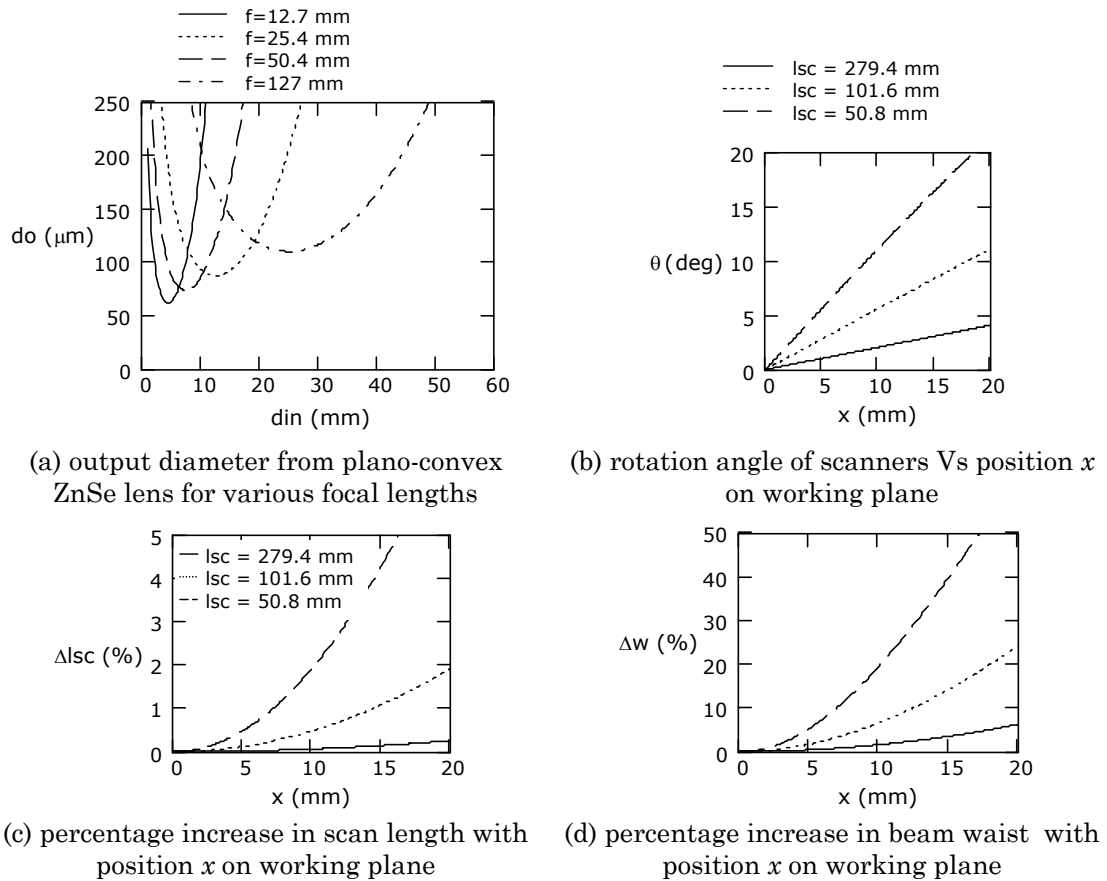
Figure 5.28. Design curves for optics and Gaussian beam in Alpha 2

was applied to the image, in order to "develop" the actual track.

As mentioned in Section 5.3.1, in addition to the relationship between line width and fluence, is the relation between the spot's size and shape and the line width. This was discussed in terms of the beam distortions suffered because of the rotating galvanometer mirrors, which cause a change in scan length, and therefore in spot diameter by defocusing the beam. This is particularly notorious for short focal and scanning lengths. In order to characterize the impact of the spot size distortion with the increase in scan length as the galvanometer mirrors are rotated to scan the beam across the working plane to define the geometry, a series of plots are presented in Figure 5.28. These plots simulate the increase in scanning length as the galvos rotate. Figure 5.28b shows the linear relationship between the scanning position and the angle of rotation of the galvo for three scanning length. Similarly, Figure 5.28c and d show the percentage increase of the scanning length and beam waist with the position in the x-direction, both being nonlinear as illustrated in Section 5.2.2.

Table 5.8 summarizes some important results for three sets of cases. As seen from this table, for small scanning distances the percentage increase in beam waist is small for the three scanning lengths between 50.8 and 279.4 mm. In comparison, the defocusing effect of the beam is greatly enhanced at larger

Table 5.8. Variation of beam waist with scan length and scanning length

	Δw (%)		
l_{sc} (mm)	$x =2$ mm	$x =5$ mm	$x =10$ mm
279.4	0.06	0.40	1.60
101.6	0.27	1.70	6.63
50.8	0.86	5.27	19.58

scanning distances and in particular for short scanning lengths l_{sc}. Subsequently for designs that implement scanners, a longer scanning length and a focusing lens with longer focal length should be used in order to minimize the beam distortion, thus sacrificing the minimum spot size achievable.

These problems can be solved, at least partially, by maintaining a fixed scanning length, equal to the focal length, and translating the part instead of the beam. This was one of the main reasons for making transition to the XY stage. Pictures from some experiments with the Alpha 3 station with equivalent parameters and sol-gel film as for the Alpha 2 station are shown in Figure 5.29,
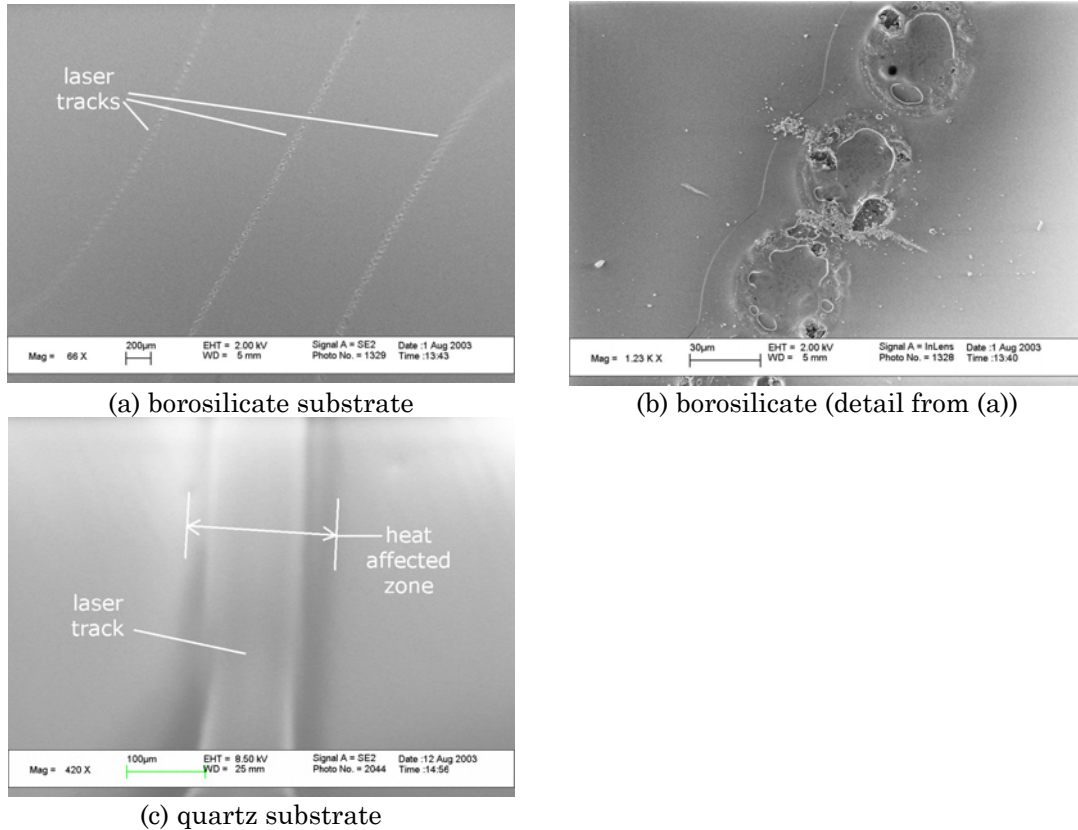

(a) borosilicate substrate

(b) borosilicate (detail from (a))

(c) quartz substrate

Figure 5.29. Photothermal processing with the Alpha 3 station

for borosilicate and quartz substrates. Figure 5.29b shows a detail of Figure 5.29a, depicting similar phenomena as observed for the Alpha 2 station. This surface damage is attributed mainly to the CO_2 laser and the increased absorption of the substrate of borosilicate. On the other hand, for a quartz substrate, which also has high absorption at $\lambda=10.6$ μm, the results are somewhat improved, as can be evidenced in Figure 5.29c.

5.4.2. Photothermal Processing – Argon-Ion Laser

In continuing with the concept of photothermal processing of the sol-gel film to increase locally the refractive index, a series of experiments were conducted with an $Argon^+$ laser at 3M and the system described in Section 5.3.5. The primary objective of these studies was to compare the results between a UV an IR laser for the types of sol-gel under investigation. Absorption properties of sol-gels or silica, as noted in Section 5.2.1, are different in the IR and UV regimes. This can be beneficial for the laser direct-write of optical waveguides, since only a small increase in refractive index is required to permit single- or multi-mode wave propagation by total internal refraction (see Chapter 2). Additionally, lasers operating at $\lambda=244$ nm, such as the Argon-ion SabreFRED, are the industry standards for manufacturing of Bragg gratings on Ge-doped optical fibers. This is performed through the photosensitization of the Ge-doped core by a UV source, which is a similar process to the one being investigated (Kashyap, 1999).

SEM images from preliminary experiments on inorganic silicate sol-gel films are shown in Figure 5.30. These images reveal a similar challenge as for the use of CO_2 lasers, which is to find the small operating window of laser power,

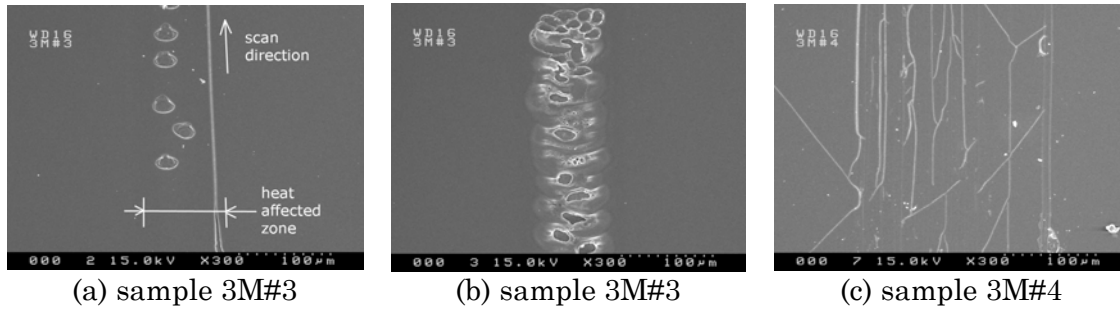| (a) sample 3M#3 | (b) sample 3M#3 | (c) sample 3M#4 |

Figure 5.30. Photothermal experiments with Argon-Ion laser on inorganic silicate sol-gel films

scan velocity and spot size to increase the temperature locally enough to induce the desired change in properties (e.g., density, refractive index), while reducing cracking and ablation, as observed in the images of Figure 5.30.

A second set of experiments was conducted in films from sol-gel System #2. The Ti-doped hybrid organic/inorganic sol was deposited on silicon wafers with a buffer oxide layer of ~5μm thick and quartz slides. As mentioned in Chapter 4, the thickness achieved by this sol-gel system (t_f=1.2–2μm) is greater than for the purely inorganic silicate type, and can transmit a single mode wave at 632.8 nm (HeNe line). The thin films produced by this system, with the procedures described in Chapter 3 an 4, have a high refractive index (1.48-1.51), good optical quality and surface roughness ($<\lambda/4$). These characteristics are particularly beneficial in order to test the proposed process.

The experimental procedure for this system was similar to that of the previous section, beginning by investigating the fluence range. A total of 27 lines were scanned across this sample. The DPs used for this set of experiments are:

- Laser power, P_l= {28,71.5,152} mW (calibrated output power)

- Spot size (theoretical at working plane), d_o=5.183 µm, with a degree of uncertainty of +10 µm, based on the results
- Wavelength (Argon-Ion laser), λ=244 nm
- Scan speed, v_s= 0.5–10.0 mm/s

The sample used for this discussion was prepared from mixture DOE5 of the sol-gel system #2. The sol was diluted in 40% EtOH, and 10 layers were spin coated at 2500 rpm for 40 seconds on a 25×25 mm quartz slide (GM Assoc.)

The experiments were divided in two main groups, defined by adjusting the z-position by Δz=+50 µm apart. Figure 5.31 presents experimental results for
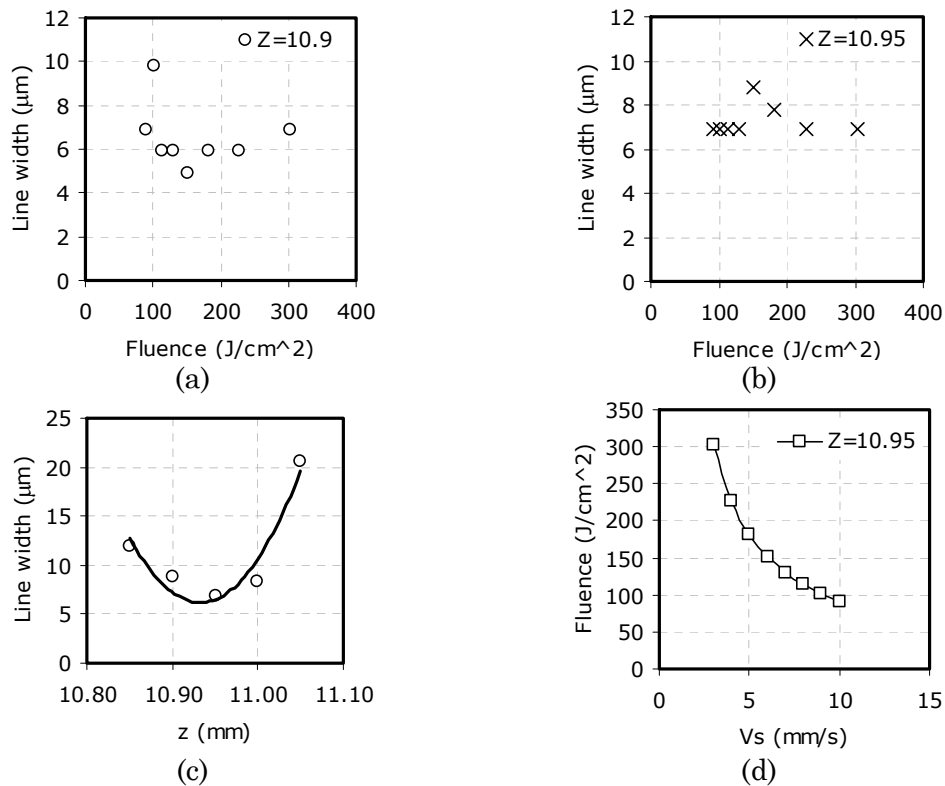
Figure 5.31. Photothermal processing with Argon^{+} laser (sample 3M#32)

(a) line 3	(b) line 3 (green filter)
(c) line 15	(d) line 18
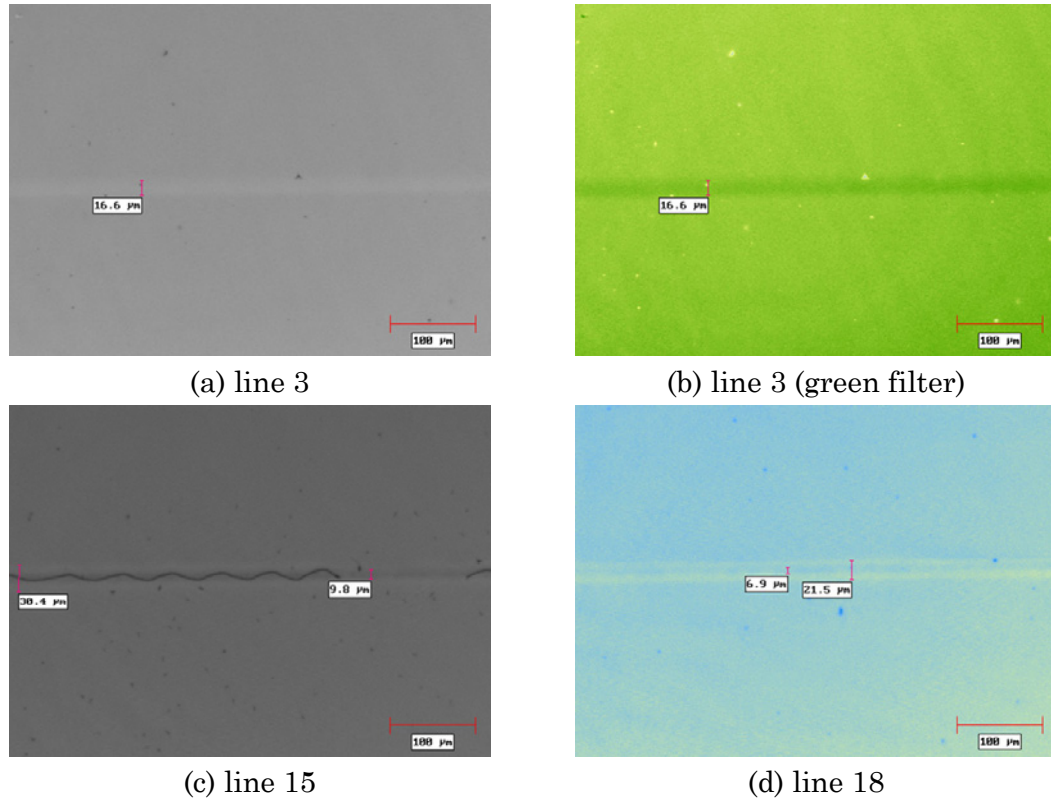
Figure 5.32. Micrographs for photothermal processing of sample 3M#32

one particular sample.

Figure 5.31a and b show plots for the line width versus the fluence, for each of the two main groups, respectively. These results are non-conclusive and represent a good example of the degree of uncertainty of measuring the line width in buried channel waveguides. These graphs are complemented by pictures taken with an optical microscope, and shown in Figure 5.32. As seen in Figure 5.32a, the area affected by the moving laser has a slightly brighter tone of grey. In some cases the interface between the *heat affected zone* (HAZ) and the rest of the matrix is difficult to distinguish. In these cases a green filter is

259

applied, and a higher contrast image is obtained, such as the case in Figure 5.32b for the same scanned line as in Figure 5.32a. In some cases a blue filter yielded better contrast, such as in Figure 5.32d.

With the help of these contrasting filters, a better sense of the best focal position was obtained. Figure 5.31c depicts a plot of the line width versus the z-position. The data follows a parabolic trend, as expected, clearly locating the best focal position.

For the second set of experiments with z=10.95 mm (Figure 5.31b), the lowest line width falls almost 2μm higher than for the set at z=10.90 mm (Figure 5.31a), though being closer to the ideal focal length and with the same fluence conditions. But observing the micrographs for the second set reveals samples with cracks and damaged tracks because of higher real fluence, which is due to the more tightly focused beam. Figure 5.32c illustrates this point.

In conclusion, in order to have a proper prediction and mapping of the fluence values for a working region, it is crucial to have a proper characterization of the beam diameter. Because of the quadratic dependence of the irradiance on the beam diameter (see Equations (5.1) and (5.2)), the focal length must be identified and maintained within a margin of 5%. If a translation stage is used, the "straightness" tolerance should be less than 40μm, in order to maintain a constant beam diameter.

5.4.3. Photophysical Processing – HeCd Laser

The experimental results for laser processing presented thus far have provided great insight in identifying some of the key parameters that must be controlled.

However, the straight line ridge or channel waveguides produced lack the dimensional requirements for actual light coupling; consequently testing the proposed process could not be accomplished. This was one of the main reasons why a different approach was pursued through photopolymerization of hybrid organic/inorganic sol-gels, based primarily on the sol-gels proposed by (Fardad, Andrews *et al.*, 1998; Fardad, Mishechkin *et al.*, 2001). The use of a UV laser immediately allows a reduced beam waist by an order of magnitude as compared to the CO_2 laser, due to the diffraction properties of light (shorter wavelength).

The type of sol-gel used for these experiments corresponds to sol-gel System #3, as presented in Chapter 3. In particular, experiments described in this section involved the use of the Zr-doped hybrid sol-gel. The Beta 1 station was used for laser processing, with the HeCd laser as the UV light source.

The samples were prepared from mixture #1 of the Zr-doped sol-gel of System #3. The sol was diluted in 30% EtOH, then a single thick layer was deposited by spin coating at 3000 rpm for 50 seconds on 30×30 mm substrates, cut from a 6" silicon wafer with a buffer oxide layer of ~5μm thick (Silicon Inc.) After UV exposure the samples were developed in isopropanol for 30 seconds. Detailed deposition and thermal treatment procedures are found in Chapter 4.

Experimentation with laser processing of these hybrid sol-gel films was performed following a similar methodology as for the previous sol-gel systems. A set of straight lines was scanned across the entire film, with varying DPs. The DPs for these experiments were as follows:

- Laser power, P_l= 8 mW @λ=325 nm & 25 mW @λ=424 nm (nominal output power), reduced by neutral density filters
- Laser type, HeCd multi-mode laser, with $M^2 \approx 14$

- Spot size (theoretical at working plane), $d_o \approx 15$ μm, with a degree of uncertainty of +5 μm, based on the results

- Wavelengths (HeCd laser), $\lambda = 325$ nm

- Scan speed, $v_s = 0.01–1.50$ mm/s (XY stage, Parker)

In addition to the straight lines, more complex geometries were investigated, in pursuit of the development of the integrated direct-write process. The shape of a Texas longhorn and a directional coupler were manufactured as
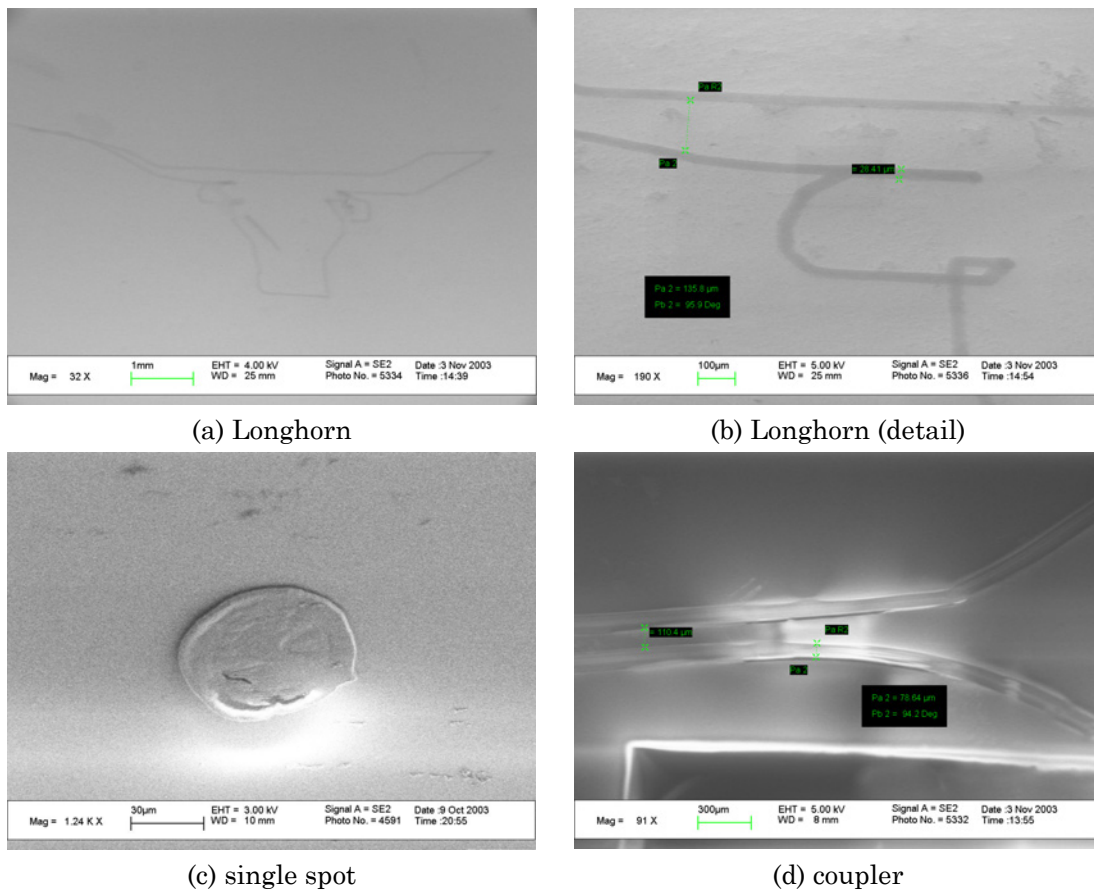

(a) Longhorn

(b) Longhorn (detail)

(c) single spot

(d) coupler

Figure 5.33. SEM images of geometries scanned with the Beta 1 station

part of these experiments. Figure 5.33 presents a set of SEM images of the UT longhorn (a, b) and one image of a directional coupler (d). The directional coupler has a spacing of 110.4 μm and a line width of 78.6 μm, while the overall dimensions of the coupler spanned to 10 mm long by ~4mm wide. These dimensions are clearly not comparable to a real coupler, where the spacing is in the order of λ/4, yet these two figures represent our first attempt to experiment with more complex geometry that demonstrates the potential of SFF and direct-write techniques.

On the other hand, Figure 5.33c shows an SEM image of a spot or disk of sol-gel, which was created by exposing the fixed beam over a defined period of time. A series of spots similar to this one were fabricated varying parameters such as laser power, exposure time, and focusing length. These spots are useful to quickly find the best focusing length, to characterize the beam shape at the working plane, and to determine ideal power and exposure time conditions.

With respect to the straight lines scanned across the film with varying parameters, Figure 5.34 depicts a plot of the cross section of a portion of one sample. The cross section profile was measured with a surface profilometer Dektak3. A total of 4000 data points was collected across 400 μm, with a 0.1 μm resolution (or 100 Å). Figure 5.34a shows the cross section of four lines, from a total of 16 lines that were scanned on sample TSTUV4. To investigate the kind of shape produced by the multimode laser, Figure 5.34b zooms into line 1. The height and width of line 1 can be clearly noted from this figure. A thickness of ≈2μm for a single layer is a substantial improvement as compared to films from sol-gel System #1. In order to visualize the actual shape of the laser-defined line,
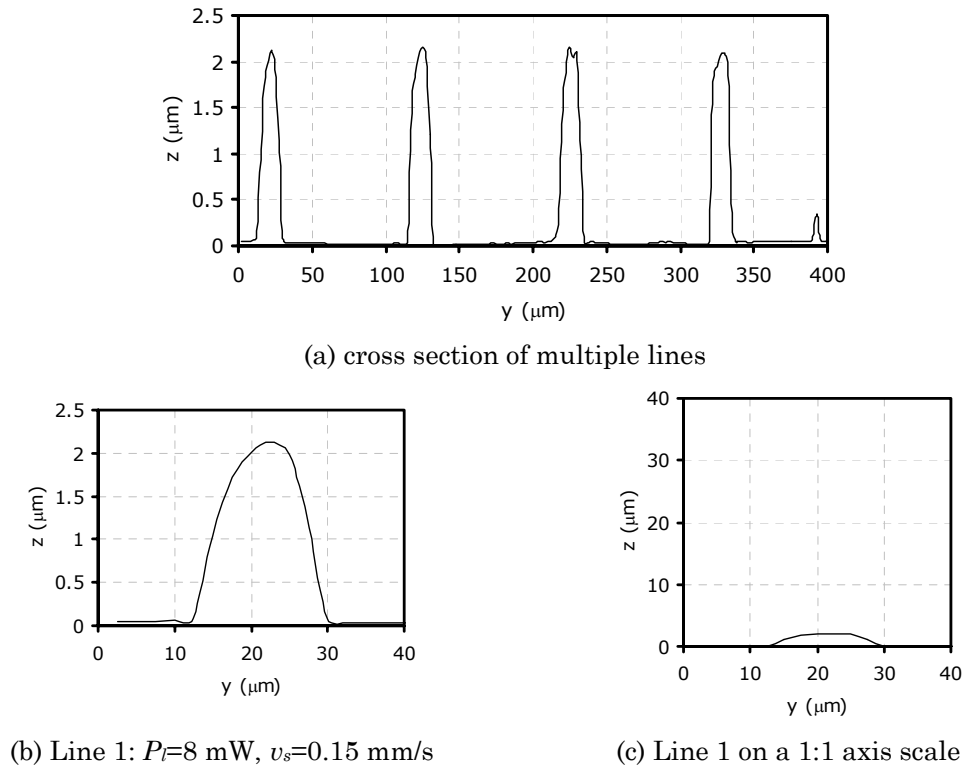
(a) cross section of multiple lines

(b) Line 1: P_l=8 mW, v_s=0.15 mm/s

(c) Line 1 on a 1:1 axis scale

Figure 5.34. Cross section of tracks for sample TSTUV4

Figure 5.34c shows the profile on a 1:1 axis scale. This 18×2 μm profile is far from an ideal 1:1 cross section desired for optimal waveguiding.

Overall, the smallest height to width ratio obtained was 8.7:1. Even though a smaller feature was not produced, parts of the overall objectives are achieved through this Beta 1 station; that is, a flexible and rapid process to direct-write geometries imported from CAD files on sol-gel thin films with good optical quality. An additional accomplishment from these sets of experiments was to show the feasibility of the photophysical processing of the hybrid sol-gel of System #3. This served as a starting platform to evaluate the influence of other parts of the process, such as the thermal cycles and developing solution, as

discussed in Chapter 4. With respect to the feature size, this is an aspect that has not been fully solved up to this point, primarily due to the lack of a high quality UV laser that can be integrated to the Beta 1 station. For this reason, further research was continued in the 3M UV system, and is described below.

5.4.4. Photophysical Processing – Argon-Ion Laser

Experimentation with a high-quality UV laser was performed using the system described in Section 5.3.5. The main goal of these experiments was to produce straight channel waveguides with dimensions capable of guiding light, therefore providing clear evidence of the feasibility of the proposed direct-write process. Over 60 samples were prepared using the sol-gel System #3, with Zr or Al doping. The factors explored in these samples included the same as for previous cases, such as laser power, scanning velocity, and focusing distance. In addition to these standard factors, other aspects investigated involved the concentration and type of chemical for development, development time, time from deposition to UV exposure to chemical development, and the optimization of the thermal cycle.

Results in this section will focus on samples prepared with Al-doped sol-gel from System #3, and the effects of exposure (H_{max}) on the line width. Some comments and recommendations regarding the other aspects investigated will be briefly discussed below.

The DPs for these experiments include the following:

- Laser power, P_l= 325 mW (nominal maximum power), reduced by neutral density filters to P_l=0.050–0.250 mW
- Laser type, Ar^+ laser, single TEM_{00} mode, with $M^2 \approx 1.2$

- Spot size (measured at working plane), $d_o \approx 10.8$ µm, with a degree of uncertainty of $+10$ µm, based on the results
- Wavelength (Ar^+ laser), $\lambda = 244$ nm
- Scan speed, $v_s = 0.01$–10.0 mm/s (single translation x-stage)
- Chemicals for development step: concentration and type (Isopropyl alcohol and 4-methyl-2-pentanone or Hexone)

The samples were prepared in our laboratory with a spin coater inside a glove box with controlled environment. After deposition of the sol, the sample was thermally treated in a hot plate with controlled environment of N_2, then covered with aluminum foil to shield it from light, and immediately taken to 3M's facility for UV laser exposure. Laser exposure was conducted by placing the sample in a single translation stage (Figure 5.23) under standard atmospheric conditions.

Instead of presenting results from all sixty samples, the discussion will focus on the sample labeled as 3M#70. This sample was prepared with Al-doped sol-gel from System #3, from mixture 5 (Table 3.11), diluted in 80% EtOH before depositing 250 µl of sol on a Si-wafer with a 2.4µm oxide layer, and a spin coating velocity of 3000 rpm for 40 sec. The sample was thermally treated following the cycle presented in Figure 4.35. A total of 27 lines were scanned on the sample, varying the scan velocity between 2–8 mm/s, the laser power at 0.100 and 0.158 mW, and the focal distance in three positions 50 µm apart. Table 5.9 presents a summary of parameters and results for selected lines. The maximum exposure H_{max} was determined from Eq (5.23) at $y=0$ and $z=0$. The line width L_w was measured with an optical microscope and with a profilometer Dektak3.

266

Table 5.9. Parameters for sample 3M#70

Line	P_l (mW)	v_s (mm/s)	d_o (μm)	H_{max} (J/cm²)	L_w (μm) microscope	L_w (μm) profilometer
1	0.158	2.0	11.34	1.112	12.4	10.0
2	0.158	3.0	11.34	0.742	10.9	9.0
3	0.158	4.0	11.34	0.556	10.4	9.0
4	0.158	5.0	11.34	0.445	10.4	8.5
5	0.158	6.0	11.34	0.371	9.4	8.5
11	0.158	6.0	10.94	0.384	8.9	–
20	0.100	4.0	11.34	0.351	9.9	–
23	0.100	4.0	10.94	0.364	9.4	–
25	0.100	2.0	10.80	0.737	9.4	–
26	0.100	4.0	10.80	0.368	6.9	–

For these experiments a better characterization of the laser beam was obtained by having access to a beam profilometer by Beam Scan Inc. The beam diameter at $1/e^2$ was adjusted to minimum measured values of 10.80 μm and 12.06 μm for the vertical and horizontal directions, respectively.

Figure 5.35 shows a comparison between a plot of the cross-section and its corresponding image from an optical microscope for three lines of sample 3M#70. These images and data from Table 5.9 show that as the scanning velocity is increased while the power is held constant (i.e., decreasing H_{max}), the resulting line width decreases as well. The images and cross section plots from Figure 5.35 reveal small line widths and smooth lines, which are a great improvement when compared to the results of the previous section (see Figure 5.34). The cross section plots reveal a characteristic topology with rounded edges that resembles an inverted-parabolic profile. Additionally, the width-to-height aspect ratio is 1.8:1–2.1:1 for the maximum width at the bottom, and 1.3:1–1.5:1 at the mid point. This is a significant improvement when compared to the 8.7:1 ratio for the previous experiments with the Beta 1 station and the HeCd multi-mode laser.
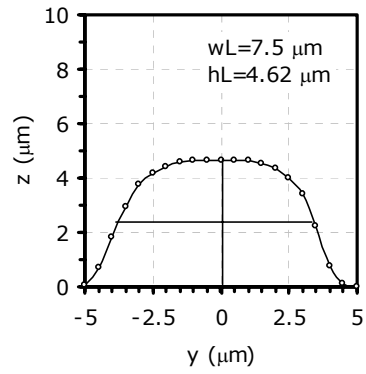
(a) line 1
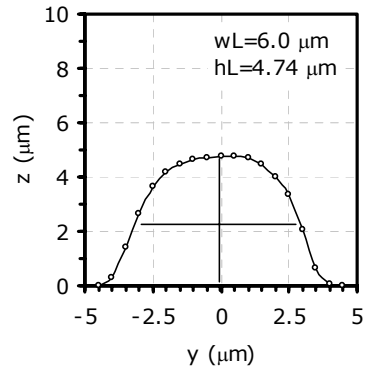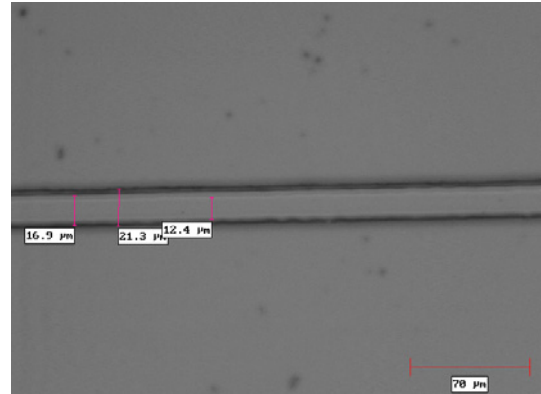
(b) line 5
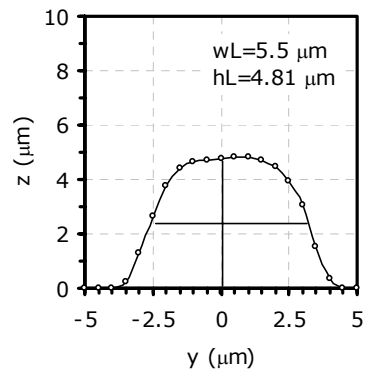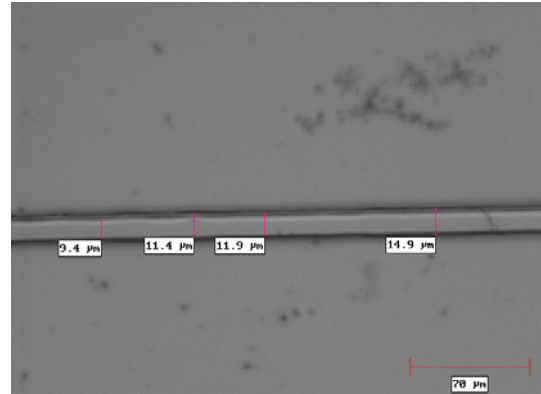
(c) line 23
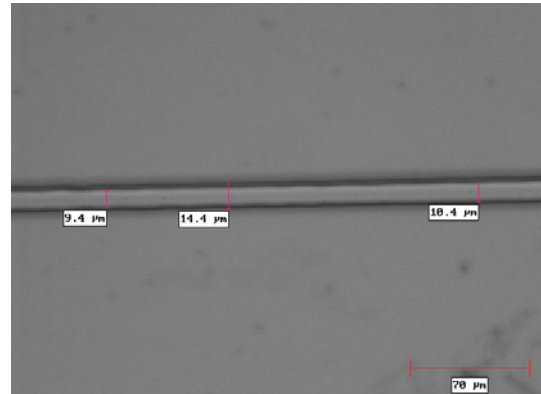
Figure 5.35. Line cross-section and top view image for sample 3M#70
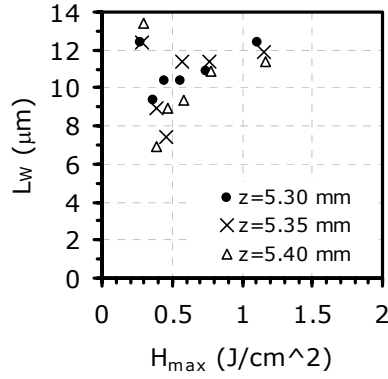
(a) Sample: 3M#70, P_l=0.158 mW, corrected for d_o
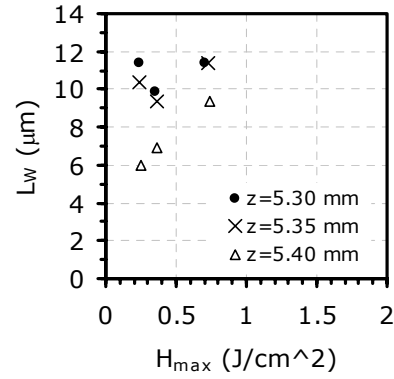
(b) Sample: 3M#70, P_l =0.100 mW, corrected for d_o
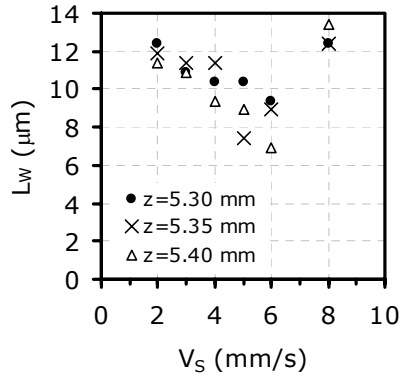
(c) Sample: 3M#70, P_l=0.158 mW
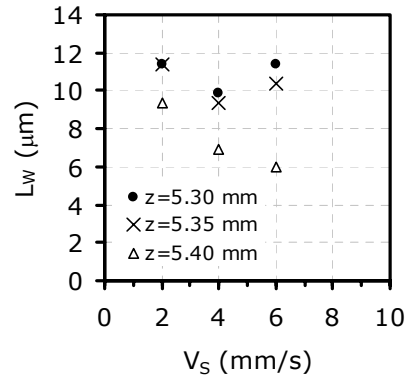
(d) Sample: 3M#70, P_l=0.100 mW

Figure 5.36. Effects of maximum exposure and scan velocity on L$_w$

The experiments in sample 3M#70 can be divided in two main groups by the laser power P_l={0.158,0.100} mW, each with three subgroups for focal distance Δf={0,+50,+100} μm. Figure 5.36 presents plots of line width versus maximum exposure and scanning velocity for the two main groups. For both cases of laser power, these figures show similar trends: as H_{max} is decreased, the line width decreases, for all three positions of Δf. On the other hand, this trend has a non-linear behavior and shows a rare increase in line width for H_{max}<0.3 and P_l=0.158 mW. Also, it is noted that the minimum line with for all cases is

obtained with $H_{max} \approx 0.25$, $P_l=0.100$ mW, and $\Delta f=+100$ μm (z=5.40 mm). Recalling Equation (5.23), H_{max} is inversely proportional to scan velocity v_s. The line width, as seen in Figure 5.36c and d, shows a similar behavior when compared to v_s.

The results presented in the plots of Figure 5.36 were corrected for the beam diameter d_o, considering that the smallest beam diameter occurs at $\Delta f=+100$ μm (z=5.40 mm), and has an experimental value of $d_o=10.80$ μm. In the other two positions, the beam is calculated to diverge to $d_o=10.94$ μm (z=5.35 mm) and $d_o=11.34$ μm (z=5.30 mm), respectively. Focal position has an important effect on the line width due to a change in diameter, which causes in turn a change in irradiance (inverse quadratic dependence) and exposure (inverse linear dependence).

Referring to Equation (5.23), the expression for $H(y,z)$ predicts a parabolic profile, as it propagates into the film. Although this equation was derived for photopolymers in SLA, there is reason to believe that photosensitive sol-gels behave in a similar manner (Soppera and Croutxe-Barghorn, 2003); therefore the line width can be predicted in advance. For photopolymers in SLA, Jacobs defines a critical exposure H_c at the "gel point", at which the resin transitions from liquid to solid. Thus defining a cross-linked boundary in Equation (5.23) at $y=y_c$ and $z=z_c$, the resulting cross-section profile is parabolic. Exposure values within this boundary result in a cross-linked polymer.

Following a similar procedure as presented in (Jacobs, 1992), and combining it with the polymerization kinetics approach of (Lee, Prud'homme *et al.*, 2001), we can determine an expanded version for $H(y,z)$ and estimate the line-width, therefore verifying if the hybrid sol-gel used has a similar behavior. The full procedure is not provided, but is can be shown that the following

equation represents the parabolic profile as a function of the processing parameters (e.g., P_l, v_s, w_o) and first-order polymerization kinetics constants (e.g., initiation, termination, etc.). Therefore, assuming a laser beam with a Gaussian irradiance distribution that decays exponentially according to Beer's law, the expression results as:

$$\left(\frac{2}{w_o^2 \ln 10} \right) y^2 + \left(\varepsilon [PI] \right) z = \frac{2}{\ln 10} \ln \left(\frac{H_{\max} [PI]^{1/2}}{\alpha_p \beta_p} \right) \qquad (5.34)$$

which has a parabolic form, and where α_p and β_p are defined as:

$$\alpha_p^2 = \frac{k_t}{k_p^2 \phi \varepsilon} \left[\ln \left(1 - p_c \right) \right]^2 \qquad (5.35)$$

$$\beta_p^2 = \frac{hcN_{av}}{\lambda \pi \sqrt{2\pi}} \cdot \frac{P_\ell}{w_o^2} \qquad (5.36)$$

The expression for α_p depends entirely on kinetics aspects, where k_t is the kinetic rate constant for termination, k_p represents the kinetic rate constant of propagation, ϕ is the quantum yield of the photoinitiator with a concentration of $[PI]$ and molar extinction coefficient ε (Lee, Prud'homme *et al.*, 2001). On the other hand, β_p is a function of the laser processing parameters, where h is Plank's constant, c is the speed of light, N_{av} is Avogadro's number, and λ is the laser's wavelength.

Considering the case at the critical transition point where $H(y,z) = H_c$, and substituting $y = y_c$ and $z = 0$ into Equation (5.34), results in:

$$2 \frac{y_c^2}{w_o^2} = \ln \left(\sqrt{\frac{2}{\pi}} \frac{P_\ell}{w_o v_s H_c} \right) \qquad (5.37)$$

where the critical exposure H_c is equivalent to (Lee, Prud'homme *et al.*, 2001):

$$H_c = \frac{\alpha_p \beta_p}{[PI]^{1/2}} \qquad (5.38)$$

Therefore, the line width $L_w = 2y_c$ can be determined from Equation (5.37):

$$L_w = w_o \cdot \left[2\ln\left(\sqrt{\frac{2}{\pi}} \frac{P_l}{w_o v_s H_c} \right) \right]^{1/2} = w_o \cdot \left[2\ln\left(\frac{H_{max}}{H_c} \right) \right]^{1/2} \tag{5.39}$$

This expression predicts a linear relationship between L_w and w_o.

Now, the results shown in Figure 5.36a for the line width versus H_{max} plot for the case of d_o=11.34 µm (z=5.30 mm), which correspond to the first five lines in Table 5.9, are converted to a semi-logarithmic plot. Figure 5.37a presents the semi-log plot for line-width measurements taken with the optical microscope, and mid and bottom data with the profilometer. The results as shown in this semi-log plot have a fairly linear behavior (R^2>0.892).

As proposed by Jacobs, the critical point corresponds to the intersection of the curve fit data for the cure depth C_d with the abscissa (y axis), where H_{max}=H_c (Jacobs, 1992). Since no data for the cure depth was obtained, only for the line width as presented in Figure 5.37a, the average of the squared difference between the predicted L_w (Equation (5.39)) and the experimental data (Table 5.9) was minimized to determine the critical exposure H_c. For the same three

(a) Sample: 3M#70, P_l=0.158 mW, z=5.30 mm, d_o=11.34 µm

(b) Sample: 3M#70, P_l=0.158 mW, z=5.30 mm, d_o=7.5 µm
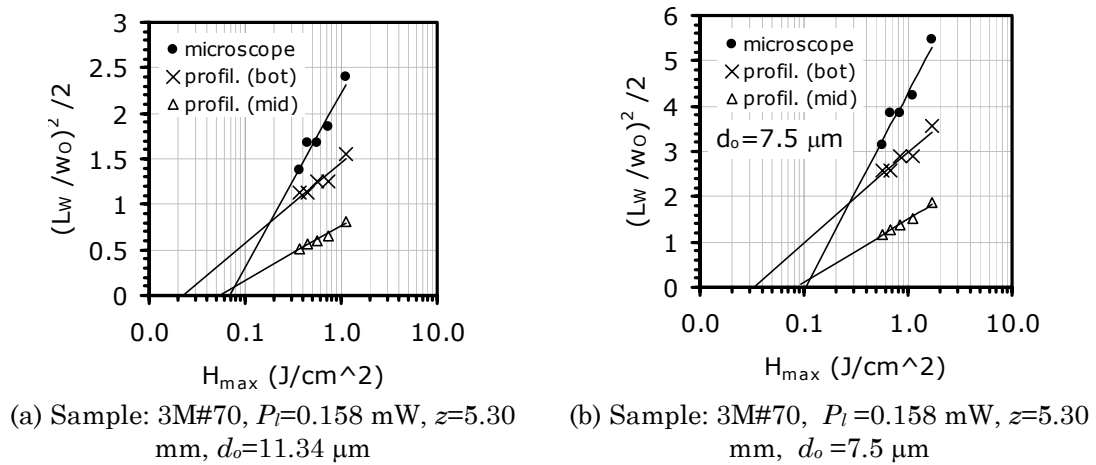
Figure 5.37. Curve fit of experimental data for line width, L_w

(a) α=3000 cm⁻¹   (b) α=3000 cm⁻¹

(c) α=1000 cm⁻¹   (d) α=1000 cm⁻¹

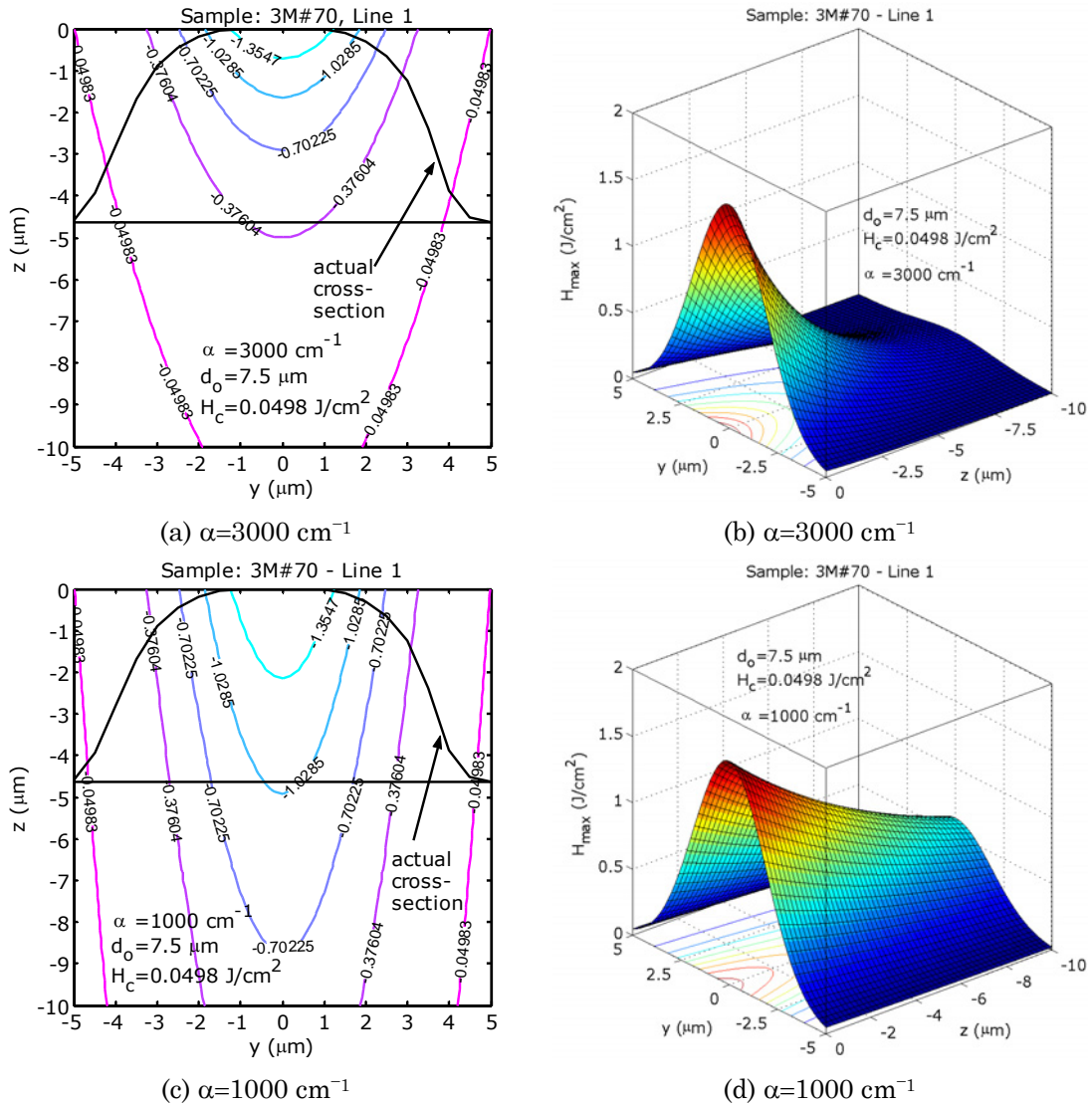**Figure 5.38. Comparison between model and experiment for line 1**

measurement data, the critical exposure is: H_c=0.0155 J/cm² (microscope), H_c=0.0498 J/cm² (profil. bottom), and H_c=0.2058 J/cm² (profil. mid-point).

Comparing the line width and shape for sample 3M#70 line #1 to the exposure distribution $H(y,z)$, particularly for $H(y,z)=H_c$, with an unknown value

273

for α, there is a substantial mismatch between experiment and mathematical model. For this line, the beam diameter is d_o=11.34 μm (z=5.30 mm). Considering this beam diameter, the absorption coefficient α would have to be in the order of 5000 ($l_α$→2 μm) to match the line theoretical value for L_w to the maximum experimental value from profilometry. On the other hand, if the spot size is reduced to d_o=7.50 μm, α can be reduced to ~1000 ($l_α$→10 μm) to fit the experimental data. Figure 5.38 presents contour plots for $H(y,z)$, comparing the cross-section profile from profilometry (placed underneath the z=0 plane) to the exposure distribution for two cases of the absorption coefficient (α=3000cm^{-1} and α=1000cm^{-1}) and a reduced spot size of d_o=7.50 μm. The contour plots indicate the case for $H(y,z)=H_c$=0.0498 J/cm^2.

By superimposing the exposure distribution to the actual line profile, a great discrepancy between these two is perceived, regardless of the absorption coefficient or beam diameter. The actual cross section depicts an inverted parabola with a flat top and rounded edges. Some possible explanations of this discrepancy are:

- The actual beam diameter at the working plane is smaller than what the beam profilometer was able to measure.

- Below the sol-gel film (with a t_f≈5 μm), there is a 2.4 μm buffer oxide layer (under-cladding), and below that the silicon wafer. The optical penetration depth of Si-c at λ=250 nm is $l_α$≈6 nm, and the reflection coefficient at normal incidence is R≈0.61 (Bäuerle, 2000). These values suggest that there is a great possibility that a portion of the Argon-ion laser beam (λ=244 nm) is being reflected back, therefore contributing to this inverse parabolic shape of the cross-section profile.

274

- The chemical development step in 95% isopropyl alcohol and 5% Hexone causes the rounded edges. This is known to happen in photoresists (Campbell, 2001).

Therefore, for a proper prediction of the line width, future work must consider these aspects in more detail. Nevertheless, Figure 5.39 presents some
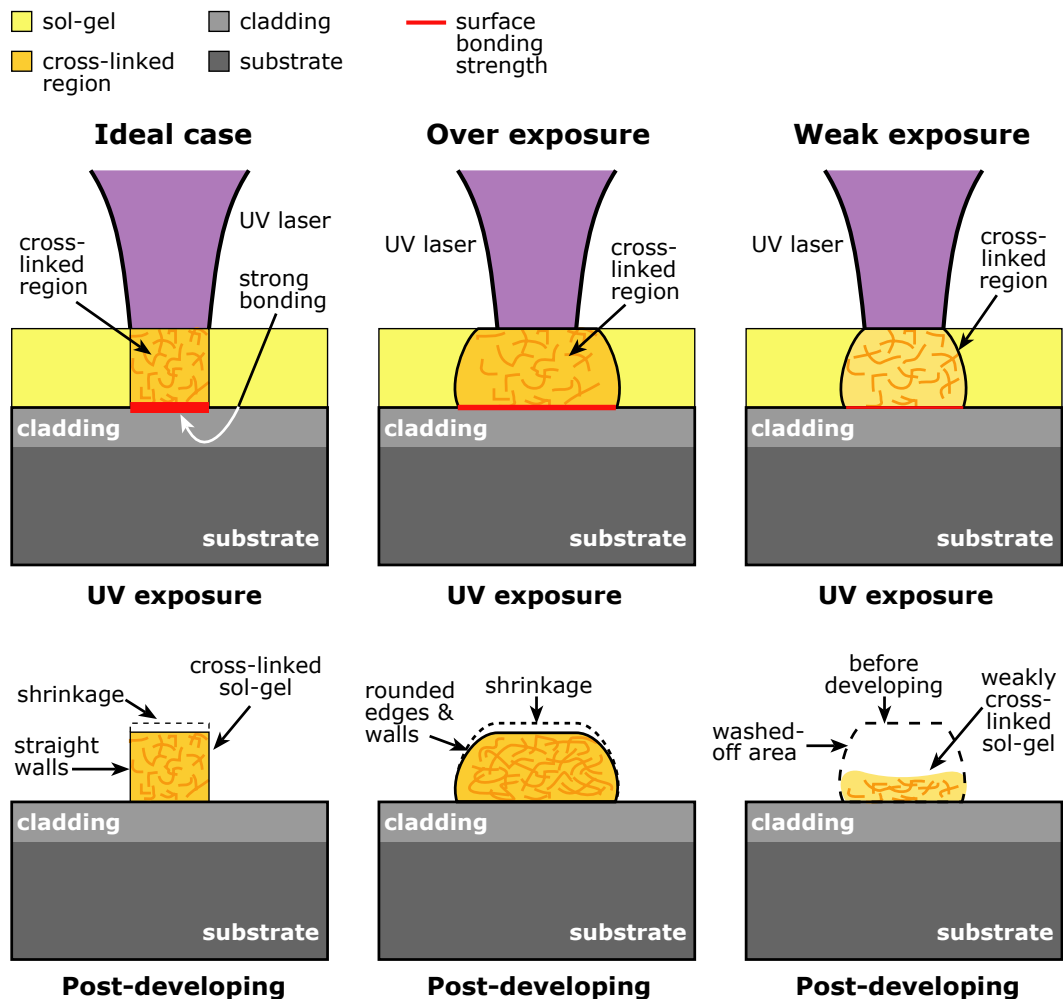

Figure 5.39. Direct-write with UV laser: three cases

275

qualitative recommendations based on the experimentation with this sol-gel. Three basic cases are depicted in this figure. In the first ideal case, the laser polymerizes an area with square cross-section that is strongly bonded to the cladding surface, and experiences little shrinkage and distortion after chemical development. The two other cases consider the over exposure (low scan velocity or too high laser power) or weak exposure (fast scan velocity, low interaction time, or low laser power). Each case shows the typical cross section of the scanned track. The DPs involved must be optimized to produce a cross-section that resembles that of the ideal case.

Even though the cross section has not been fully optimized at this point, the dimensions and shape of the tracks produced with a high quality UV laser on a hybrid sol-gel of System #3 show a promising improvement from the initial results. These tracks can be used to test the process by coupling light into them, which is the purpose of the next chapter.

5.5. Conclusions

This chapter has provided a detailed description of the design of the laser processing prototype stations, and an extensive account of experimentation with photothermal and photophysical laser processing of various sol-gel films. This chapter has emphasized the goal of the design of an automatic direct-write machine, and laid some of the groundwork towards this goal. This was pursued particularly by adopting a Systems Design approach, and demonstrating how the individual elements of the laser processing step are connected.

Experimental results from this chapter have provided recommended operating ranges for fluence or exposure for the photothermal and photophysical laser processing of three very different sol-gel systems. Also, the importance of an adequate characterization and control of the spot size at the working plane has been highlighted. This is perhaps one of the most important aspects to control in order to produce high-quality features and a repeatable process by means of laser processing.

Some degree of mathematical modeling has been presented for different aspects of laser processing, with the goal of supporting the experimental findings and as guidance tools for design purposes.

Finally, this chapter has presented experimental results of straight ridge waveguides with good surface properties and cross-section aspect ratio suitable for light coupling. The light coupling and optical characterization of these waveguides are presented in the following chapter.

Chapter 6. Demonstration of Technology

6.1. Introduction

Part of the initial research objectives was to demonstrate the feasibility of the proposed process, by evaluating the light-guiding characteristics of the fabricated waveguides. The purpose of this chapter is to show this feasibility through a series of experimental results of light coupling into simple slab and straight channel waveguides produced by the direct-write process. Two methods of light coupling were investigated: transverse or end-fire coupling and prism coupling. The end-fire technique provided more conclusive results. For this reason only the results from this method are presented in this chapter. The experimental equipment used is briefly described, followed by experimental results.

6.2. End-fire Light Coupling

Chapter 4 described the characterization of the sol-gel films were by a number of standard techniques. These included variable angle ellipsometry for thickness and index of refraction measurements, atomic force microscopy (AFM) for surface roughness and film morphology, and a profilometry to measure the cross-sectional profile of the laser scanned region.

This chapter focuses on demonstrating the feasibility of the process by coupling light into simple waveguides. Light from a HeNe laser (632.8 nm) was coupled into the waveguide by means of transverse coupling, also known as the end-fire technique. Figure 6.1 presents a diagram of the optical setup, which
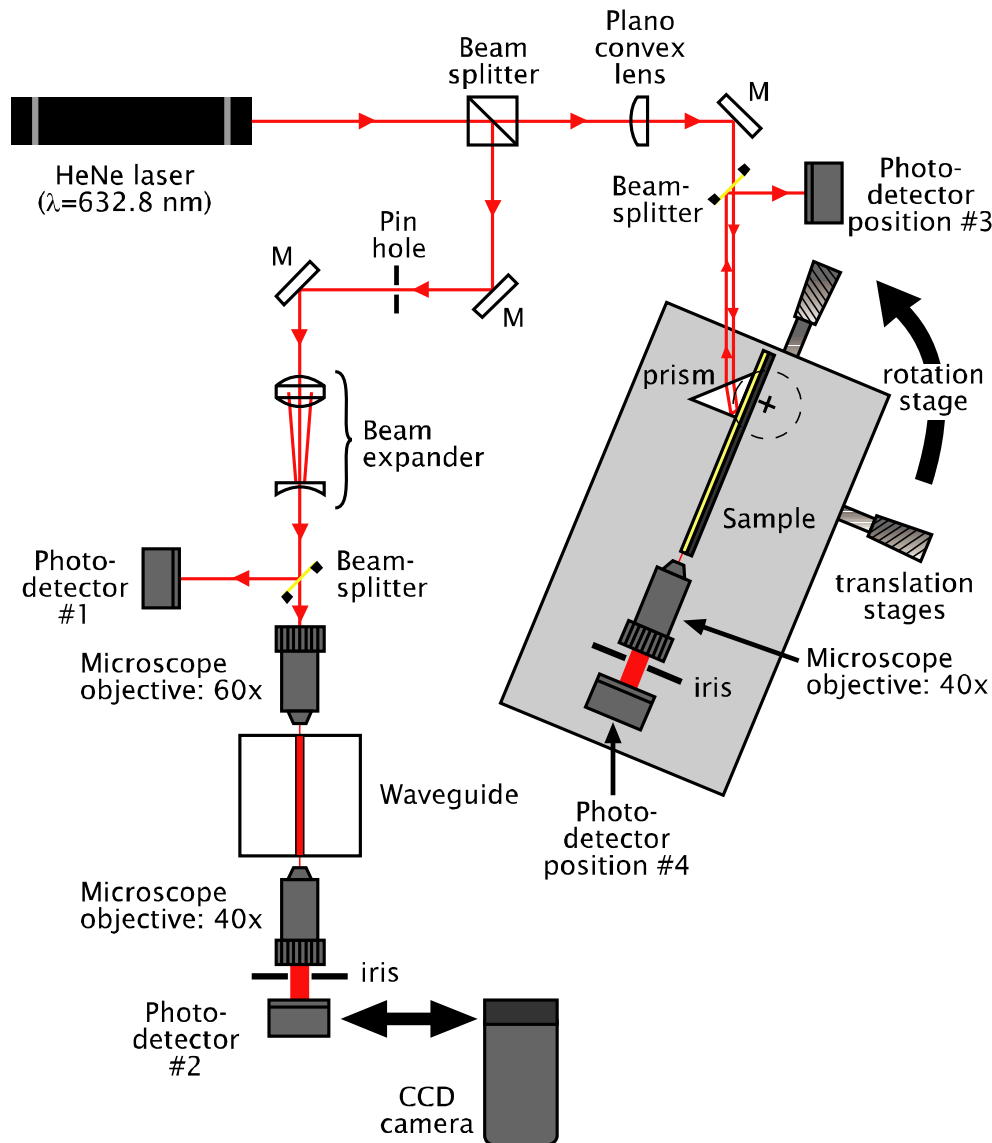

Figure 6.1. Diagram of optical setup for waveguide characterization

includes the end-fire (left) and prism-coupling (right) setups.

6.2.1. Design of End-Fire Coupling Module

For the end-fire configuration of Figure 6.1 (left), polarized light from a HeNe laser was coupled into the waveguide by means of a microscope objective (60x) that focuses the light directly into the polished edge of the waveguide. Then the light was extracted at the other end of the sample using another microscope objective (40x), and observed using a CCD camera mounted to the objective. The CCD camera can be replaced with a photodetector connected to a power meter to record the optical losses. An estimate of the attenuation loss was obtained by comparing the power at photodetector #1, which comes from a 50:50 pellicle beam splitter, to the power collected at photodetector #2 at the end of the waveguide. There are inherent coupling losses associated to the microscope objective-waveguide interface, yet they were assumed to be within the experimental error and resolution of the power meter.

A second CCD camera was placed above the waveguide in order to align the specific channel waveguide to the incoming beam from the microscope objective. Figure 6.2 shows a picture of the actual setup, indicating the main components. The waveguide is mounted on a MicroBlock™ three-axis flexure stage with differential micrometer actuators by Melles Griot. This position stage has a resolution of 50 nm. On the other hand, the microscope second objective (40x) and CCD camera assembly was positioned with a XYZ stage assembly from Newport. This stage has a resolution of 0.5 μm.
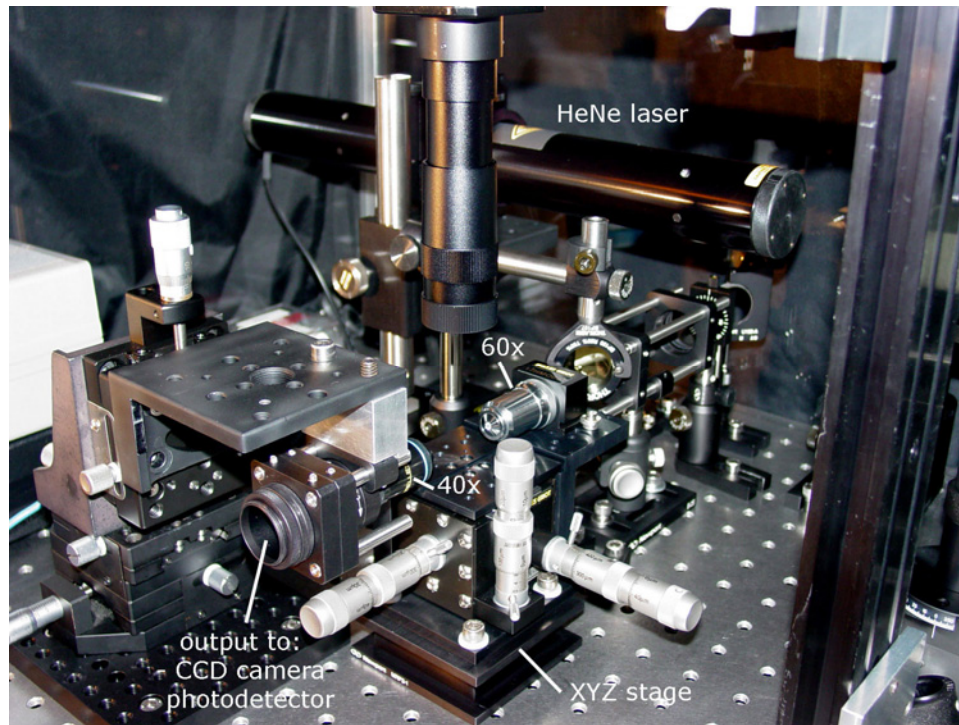
Figure 6.2. Experimental setup for end-fire coupling

6.2.2. Experimental Results

The results of this section will focus on one particular sample. This sample was prepared from sol-gel System #3, doped with Zr. Figure 6.3a presents an image taken with an optical microscope showing the laser scanned track after chemical development. The characteristics of the sample are the following:

- Sol-gel mixture: system #3, Zr-doped, mixture #DOE4

- Dilution: 15% EtOH–85% sol

- Spin coat velocity: 3000 rpm for 50 sec; Volume: 300 μl

- Substrate: Si-wafer with 2.4 μm oxide layer

- Thermal cycle: soft bake at 80°C for 5 min, post-exposure bake at 92°C for 5 min, hard bake at 130°C for 120 min; all under ultra-high purity He

- Chemical development: 95%IPA–5% Hexone, for 30 sec

- Sample ID: 3M#36

- Laser processing: Argon-ion laser, d_o=10.8 μm (experimental)

- Maximum exposure for line#15: H_{max}=22.34 J/cm² for d_o=5 μm and H_{max}=10.34 J/cm² for d_o=10.8 μm. Figure 6.3b depicts a graph with the experimental conditions and results.

- Track dimensions for line #15: L_w≈9.8 μm, t_f≈6.2 μm
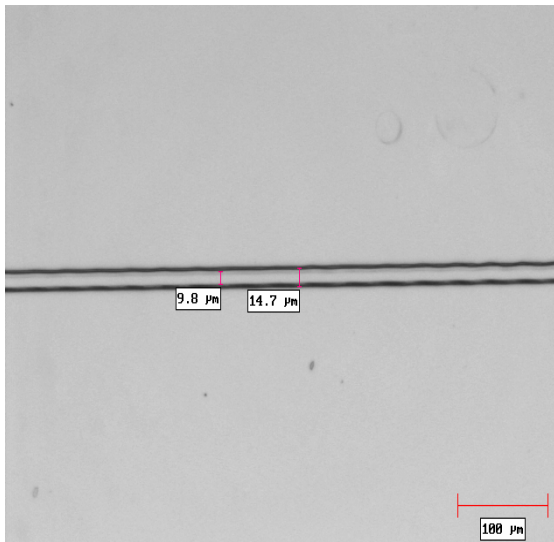
(a) image of line #15
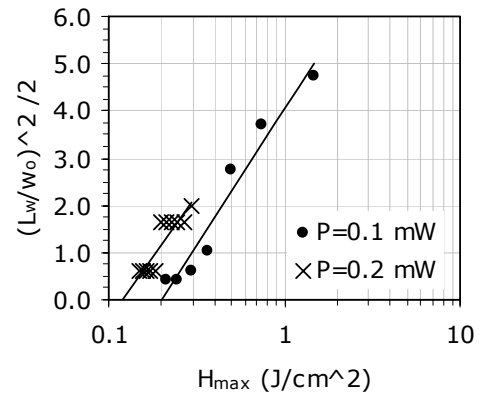
(b) exposure Vs line width

Figure 6.3. Results and conditions for sample 3M#36

Figure 6.4a shows a close-up picture of the end-fire configuration with light from the HeNe laser being coupled into the laser-defined sol-gel waveguide. To complement this image, Figure 6.4b shows a top view picture of the same end-fire setup, where the light is being coupled from the right through the microscope objective. This last image shows how light is coupled into one of the multiple waveguides (straight lines). It also shows how light is quickly scattered and the signal quickly weakens. This is due mainly to imperfections in the waveguide, both interior and exterior, through inclusions and surface defects caused during the laser direct-write process. The losses were estimated in the range of ~2.5 dB/cm, which is still far from a desired <1dB/cm, but remains promising.

On the other side of the waveguide, light is collected by a CCD camera (as shown in Figure 6.5a), and captured into a computer, where the image is automatically converted into a bitmap (Figure 6.5b). The bitmap can then be post-processed to estimate the light intensity profile, which in turn can be used to approximate the spatial distribution of the refractive index.

Figure 8a presents an image taken with the CCD camera at the end of the laser-defined waveguide. The image is presented without any alterations. As seen from the picture, the light intensity has an ellipsoidal shape, which is expected because of the difference between thickness (~5 μm) and width (~8 μm). This is further confirmed when the light intensity is visualized in a surface plot, as depicted in Figure 6.5c. Scattered light is eliminated for this step by means of and iris and image processing.
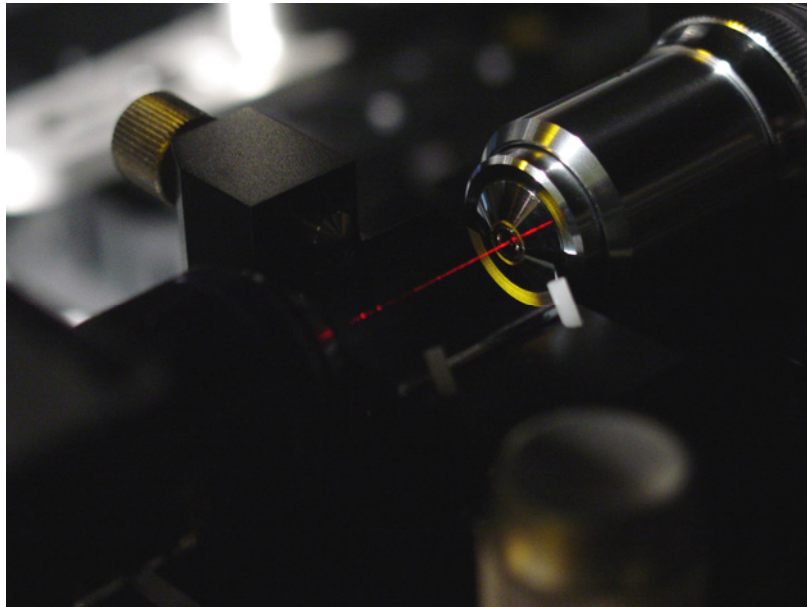
(a) side photograph of end-fire coupling
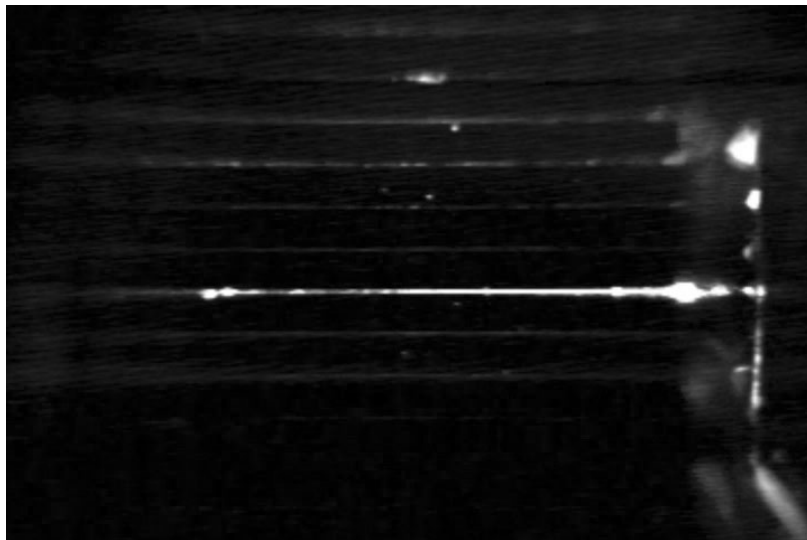
(b) top view from CCD camera #2

Figure 6.4. Photographs of end-fire coupling

(a) near-field image at exit of waveguide
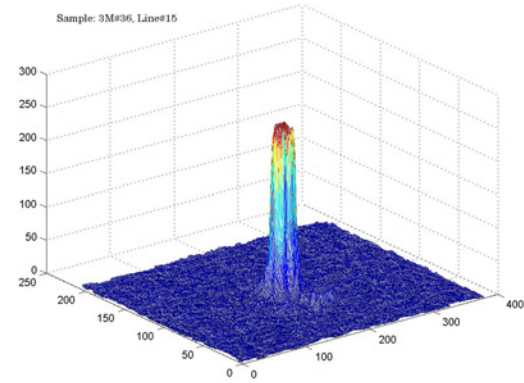
(b) raw data from bitmap
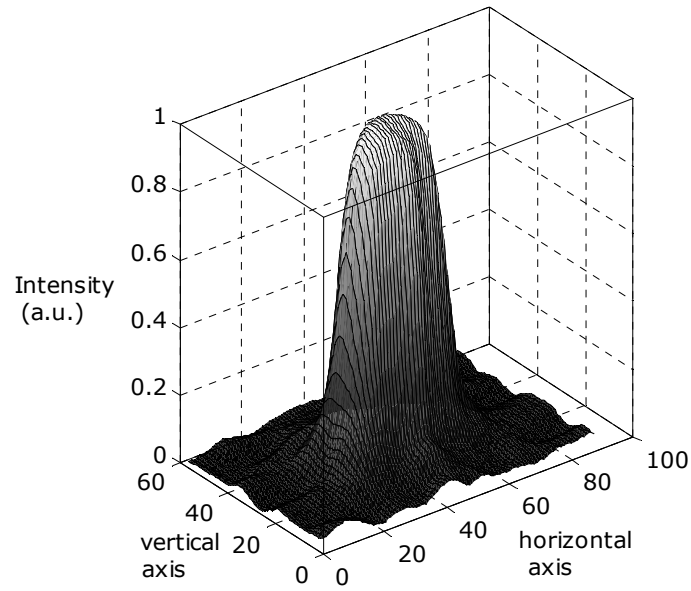
(c) surface plot of smoothed data

Figure 6.5. Results of near-field image from end-fire coupling

The refractive index difference for the vertical and horizontal directions at the central axis of the intensity plot (Figure 6.6a) can be calculated by employing the propagation-mode near field method proposed by (Morishita, 1986). After

performing some curve smoothing operations on the light intensity data, the index difference in both directions was determined and is plotted in Figure 6.6b.
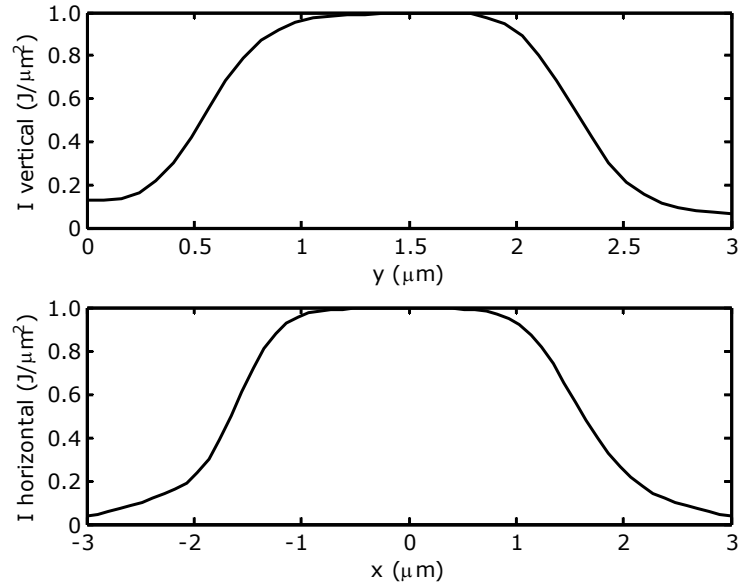
(a) smoothed data for intensity in vertical and horizontal directions
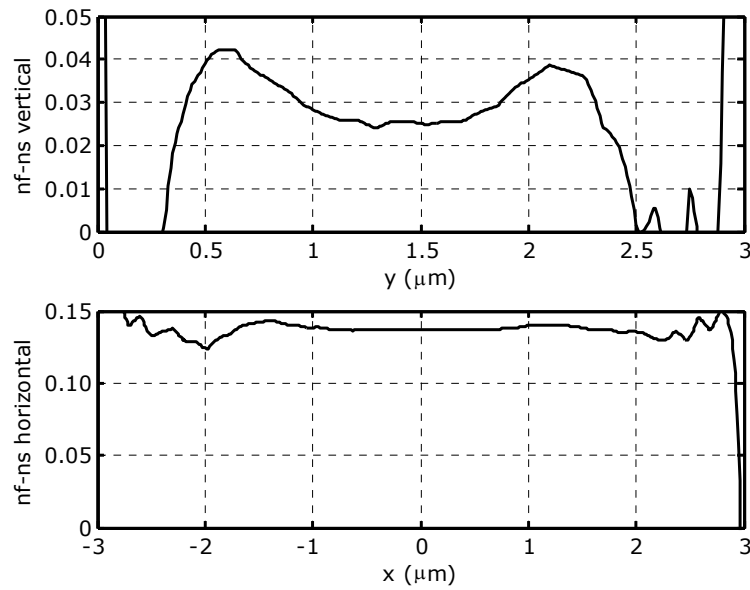
(b) numerical approximation for index difference

Figure 6.6. Numerical calculations for intensity and index difference

One of the drawbacks of the method proposed by Morishita is that it requires numerical differentiation of the second order, so it is particularly sensitive to small variations in the data. This is clearly seen in the jittery data of the approximated Δn for both directions (horizontal and vertical), in particular once approaching the edges of the waveguide. In this edge region the fit is neither stable nor reliable. We are working on resolving this issue by both improving the image acquisition hardware and software, as well as the numerical differentiation techniques.

6.3. Conclusions

This chapter presented results for the light coupling by the end-fire technique into a laser scanned channel waveguide. Light was successfully coupled into the waveguide, and estimation of attenuation loss was provided. The results from this chapter provide a strong case for the success of the proposed direct-write process. These results can be improved by optimizing even further the process, conducting the experiments in a clean room, and modifying the irradiance profile of the laser, so that it provides an even distribution across the width.

Chapter 7. Conclusions and Future Work

Based on the experimental results presented in Chapter 6, the successful coupling of light into a channel waveguide fabricated with the proposed process, it can be said that the major objective of this dissertation was achieved. The following sections provide an overview of the main results, and include a discussion on possible future avenues for research.

7.1. Overview of Proposed Direct-Write Process

Direct-write and freeform fabrication technologies challenge conventional manufacturing processes in many fields, by having the promise of producing near net-shape parts rapidly from a CAD model to a physical object. Manufacturing products that can go beyond prototyping purposes is the current test of these techniques. Therefore, research in the development of novel processes or advancing current ones must consider: (a) a systems design approach that can lead to modularity and quick identification of emerging technologies, (b) a research intensive process that takes into consideration from the early stages of the design process the specific market for the product, and (c) a fundamental understanding of the material properties and how these can be controlled and altered by SFF techniques.

The work presented in this dissertation has been guided by these three principles. Yet it has allowed, in a relatively short period of time and with little

knowledge in the field of sol-gel processing, a rapid and systematic advance towards the development of a stand-alone fully automatic direct-write machine. The juxtaposition of design methodology techniques and more traditional statistical experimental techniques (e.g., DOE), can spur innovation. The use of methodologies such as the Spiral and Stage-Gate model, which are generally applied in very complex avionics and automotive systems, can provide the research and design team of Direct-Write and SFF processes with a useful tool for managing complex systems that usually involve numerous parameters.

One of the goals of this dissertation was to provide a detailed account of the procedures involved in each of the four steps that comprise the proposed process: (1) sol-gel synthesis, (2) sol-gel deposition, (3) thermal processing, and (4) laser processing. This was done for two main reasons. First, to provide a repeatable and robust process, which can be further improved in the next series of iterations. And second, to serve as a case study of the application of design methodology techniques in research- and science-intensive areas, such as SFF and direct-write, which tend to be dominated by a materials science approach.

The work in this dissertation demonstrated that it is possible to produce high optical quality films with various types of sol-gels, and after post-processing
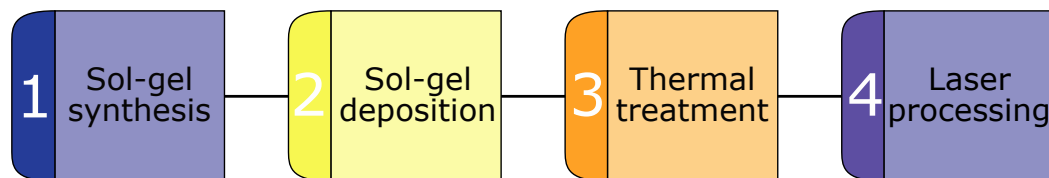
Figure 7.1. Basic steps of the proposed direct-write process

289

operations, these films can be used as the starting material for laser direct-write.

The following sections provide observations for each of the fundamental steps involved in the proposed direct-write process, as presented in Figure 7.1.

7.1.1. Process Design

The proposed direct-write process is a direct result of applying the Reverse Engineering and Redesign methodology proposed by (Otto and Wood, 1998) to the standard SLS process, while investigating alternative solutions to the functions or subsystems of the generic direct-write process.

By performing a reverse engineering study of the SLS process and after a comparison with similar layer-based manufacturing techniques in the microelectronics and photonics fields, three fundamental processing steps emerged: (1) material deposition, (2) material shaping, and (3) material treatment. The interaction between these three systems as part of a CAD/CAM system constitutes the basic architecture of the proposed direct-write process. By defining the architecture, the groundwork is established for the potential development of an automated machine that can be used in commercial applications.

7.1.2. Sol-Gel Synthesis

The selection of materials synthesized by the sol-gel process for the proposed direct-write technique emerged from the analogy of a pre-sintered high optical quality material, and from a literature review that showed a broad community of researchers with similar objectives. Once the set of materials was selected, the

main goals were to produce films with optical-grade quality and provide a robust and repeatable procedure for preparing this material. Because the ability to produce high-quality sol-gel films is the single most crucial aspect of the process, detailed preparation procedures have been presented in this work. These preparation procedures are the result of fundamental processes taken from the literature, modified by our own experimentation to convey a repeatable process.

Three different types of sol-gel materials were used throughout this research, which are based on inorganic and hybrid organic/inorganic silicate sol-gel systems. These include the inorganic silicate sol-gel system, the hybrid titanium doped organic-inorganic silicate sol-gel system, and the photosensitive hybrid Zr and Al doped organic-inorganic silicate sol-gel system. Various key factors involved in the successful synthesis of these sol-gel materials were identified. Some of these factors are related to the chemistry aspects of sol-gel synthesis, such as molar concentration, molar absorptivity, and solubility, among others. However, the most important factors affecting the development of a robust process are mainly related to the processing parameters and conditions; for example, relative humidity during the synthesis, reflux temperature, mixing order of compounds, or mixing time. Essentially, this entails the control of the hydrolysis and condensation reactions.

In general, as the control of the processing parameters was improved, the synthesis of the sol-gels also improved substantially. Maintaining an inert atmosphere with relative humidity between 30–40% is key to successful sol-gel synthesis.

The synthesis of sol-gels focused on two aspects: the synthesis procedure that would yield consistent results, and finding the molar ratios that lead to solutions with the appropriate viscosity and films that do not crack during thermal processing. During this process it was discovered that for inorganic systems, a pre-hydrolysis step for approximately half of the mixture helps to avoid any phase precipitation, even in undoped systems. After this initial step, the molar concentrations can be modified to the desired final values. The pre-hydrolysis step corresponds to the minimum theoretical value required for the hydrolysis of the silicon alkoxide (i.e., $R_{wa}=2$ and $R_{sa}=3$). For the second step, concentrations that lead to mixtures with good spinability include: ($R_{wa}=1.5$, $R_{sa}=4$), ($R_{wa}=2$, $R_{sa}=3$), and ($R_{wa}=2$, $R_{sa}=4$).

Incorporation of dopants can be achieved by combining different metal alkoxides prior to the hydrolysis and condensation process. When combining different types of alkoxides for doping purposes, one of the key issues during hydrolysis and condensation is the differences in chemical reactivity that often lead to undesired phase segregations. For example, in this research titanium isopropoxide was employed as the Ti precursor, which is observed to be more reactive than the silicon alkoxides, such as TEOS. Again, a pre-hydrolysis step provided the best results, in conjunction with a drop-wise addition of a highly diluted mixture of the doping precursor. It is possible to control the reactivity through chemical modifications employing suitable chelating agents such as glycols or organic acids. The addition of such agents can affect negatively the optical properties, by increasing the attenuation losses due to an increment of

hydroxyl groups. Therefore, addition of reaction retarding agents must be studied in detail.

For mixed of doped systems, one alternative is the heavy dilution in solvent of the highly reacting alkoxide, in combination with the pre-hydrolysis of the slower reacting alkoxide. This approach was used to prepare the titanium-doped sol-gel system #2. In the case of the Zr-doped hybrid sol-gel (System #3.1), methacrylic acid (MAA) was added due to the high reactivity of the zirconium precursor, zirconium-IV-propoxide. On the other hand, for the aluminum doped hybrid sol-gel (System #3.2), the use of a functionalized co-polymer and alkoxide, in this case Di-sec-Butoxyaluminoxy-trithoxysilane (BATES), avoided completely the need of MAA.

The chemical composition and the synthesis procedure also have significant effects on the subsequent deposition process. In the case of deposition by spin coating, viscosity is a key parameter for successful deposition, and it depends strongly on the chemical composition and preparation procedure, as shown in Chapter 2. For purely inorganic sol-gels, good spinability was observed for viscosities of 2.5–4.8 cP. The viscosity of the hybrid sol-gels is a more complicated factor. Although it was not studied in detail, the low solubility of these sol-gels results in a different deposition process in order to fully coat the substrate. Solvent evaporation is far from complete after deposition by spin coating, therefore requiring thermal treatment.

The content of water to hydrolyze the solution greatly affects the structure and optical characteristics of the films. This is true for both inorganic and hybrid sol-gels. In particular, the index of refraction depends strongly on

the water content remaining in the films (physi- and chemisorbed water). For the inorganic silicate system, the effect of the H_2O:TEOS molar ratio on the thickness and index of refraction of the films was examined, and a strong non-linear relationship was observed. The increase of water to alkoxide ratio R_{wa} increased both thickness and index of refraction. Yet, values of R_{wa} greater than 4 produced films with a greater amount of segregated phases and exhibited a higher degree of cracking when exposed to thermal treatment.

7.1.3. Deposition and Thermal Treatment

The deposition and thermal treatment steps serve as a test of the successful synthesis of a certain sol-gel. A comprehensive description of these two steps has been provided, as parts of the proposed manufacturing process. One important aspect of this part of the research was to demonstrate how these two steps could be integrated into a fully automated process based on the premises of freeform fabrication and direct-write technologies.

Detailed experimental procedures were provided for the successful deposition by spin coating of the three sol-gel systems presented in Chapter 3. Similarly, extensive experimental results were provided to support the design of the thermal processing cycles that follow the film deposition step.

For the deposition of purely inorganic silicate sol-gels, some of the technological barriers that limit the final achievable thickness of multi-layer films to ~2.4 µm were identified. The results obtained are in agreement with published literature in the field over the past decade and a half. The main factor

to control is the level of residual stress after deposition of the inorganic silicate sol-gel.

Purely inorganic sol-gels produce high quality films (smooth, homogeneous, and low OH⁻ concentration), yet the processing temperatures required for full densification and residual stress relaxation are high (~900°C).

The effect of spinning velocity on the thickness and index of refraction of the spin-coated film was studied for both inorganic and hybrid sol-gels. For all three systems, the thickness was observed to decrease with increasing spinning velocity, following an exponentially decreasing behavior. On the other hand, the index of refraction slightly changes as the spinning velocity is increased.

As mentioned above, the viscosity of the sol-gel solutions strongly affects the morphology and thickness of the film. Control of the viscosity can be achieved by the further addition of a solvent, such as EtOH, immediately before deposition. The thickness of the spin-coated films decreases significantly with an increase in EtOH content. For inorganic silicate sol-gels, the index of refraction was found to increase with 20% EtOH–80% sol, and then decrease with 40% EtOH–60% sol.

The thermal treatment of the sol-gel film is necessary to help consolidate the film and remove undesired byproducts residing in the pores of the structure. The thermal process must avoid the development of cracks in the film due to undesired particles, residual stresses induced during the solvent evaporation, and the competition between densification and crystallization during thermal treatment.

For the successful fabrication of multi-layer inorganic silicate sol-gel films, the following observations can be made:

- The maximum temperature for the heat treatment strongly affects the thickness and morphology of the film. The thickness of the film decreases with increasing heat treatment temperature, while the index of refraction increases. Heating below 500°C mainly drives off excess solvent and water contained in the pores, while heating above 850°C causes viscous sintering of the sol-gel matrix and elimination of OH ions.

- In order to fabricate crack-free multi layer films, the recommended thermal processing temperature is above 900°C.

- The presence of inclusions in the sol or in the substrate promotes film cracking in subsequent steps. Therefore, the use of a clean room is highly recommended.

- The maximum thickness in multi-layer deposition increases linearly with an increasing number of deposited layers. The thickness of one layer is 250–700 nm, depending on the percentage of solvent (generally 20–40% EtOH).

- The index of refraction slightly increases as the number of deposition layers is increased, except for the fifth deposition.

- Rapid thermal processing is recommended in order to fabricate the thicker films quickly.

For inorganic silicate sol-gels, the addition of an intermediate drying step at low temperature resulted in a reduction of the chemi- and physisorbed water

on the film. This step was shown to promote further condensation of the sol-gel film. Therefore this heat treatment step is recommended immediately after the deposition of the film at low temperatures (~150°C) for a few minutes (~10-15 min) under a high-purity atmosphere. In the case of hybrid Ti-doped sol-gels (System #2), this step was also shown to be beneficial.

For the hybrid Ti-doped sol-gel of System #2, it was shown that temperatures of up to 550°C removed most of the inorganic compounds. It was also shown how the sol-gel' structure began to resemble a fully inorganic glass when the film was thermally treated at ~900°C.

Hybrid organic-inorganic sol-gels present a clear advantage over those purely inorganic with respect to film thickness and thermal processing. Hybrid sol-gels can easily produce films with a thickness of ≥2 μm, for a single layer. Thermal processing of these sol-gels is performed at substantially lower temperatures (T_{max}→180°C).

In the case of hybrid sol-gels synthesized for photopolymerization, lower temperatures were used (<250°C). The thermal cycle of these sol-gels closely resembled the heat treatment process used for photoresists. General steps followed for these procedure included: soft bake after deposition (80°C), post-exposure bake after UV laser processing (90–95°C), and a hard bake step for the final consolidation of the film (~150°C).

7.1.4.   Laser Processing

The final step of the proposed process consists of the use of a laser to directly pattern the geometry on the sol-gel film using SFF and CAD/CAM techniques.

In particular, two laser processing approaches were investigated: photothermal and photophysical. The photothermal approach was pursued for inorganic silicate sol-gels with a CO_2 infrared laser and for the hybrid Ti-doped sol-gel with an Argon-ion UV laser. On the other hand, photophysical processing, in particular photopolymerization, was investigated with hybrid organic-inorganic silicate sol-gels doped with Zr or Al, and the use of HeCd and Argon-ion UV lasers. This research provided a detailed description of the design of three prototype laser processing stations, and an extensive account of experimentation with photothermal and photophysical laser processing of the three sol-gel systems investigated.

Design of the prototype laser stations was conducted from a *systems design* perspective, to demonstrate the interaction between the individual elements of the laser processing step. Part of the goal was to establish the basic architecture for the design of an automatic direct-write machine.

Experiments with laser processing were conducted with the three sol-gel systems. The results from these experiments provided recommended operating ranges for fluence for the photothermal or photophysical laser processing of each sol-gel system. In addition to the operating power and scan velocity levels, these experiments demonstrated the effects of the spot size at the working plane on feature size and cross section shape. The results also emphasized the importance of having an optimal characterization and control of the laser beam's dimensions and energy distribution at the working plane. The beam diameter and energy distribution of the laser will determine in great measure the quality and size of the features, and are key elements for a repeatable process.

298

The evolution and redesign of the laser processing stations was done after experimentation with a particular sol-gel system. The first two iterations began with the use of a CO_2 laser and galvanometer mirror scanners to trace the two-dimensional geometry over inorganic silicate sol-gel films. Two main problems were identified for these stations. First, because of diffraction and spherical aberration effects, the use of a CO_2 laser with $\lambda=10.6$ μm had a limited minimum spot size of ~110 μm (for $f=127$ mm), which is more than an order of magnitude larger than the film thickness ($t_{f\,max}\approx2.4$μm). Second, the combination of rotating galvanometer mirrors and lenses with short focal length, results in a substantial distortion of the laser beam's cross section at the working plane (e.g., the sol-gel film's surface), by producing an ellipse-like shape and a defocused beam. Therefore it was concluded that a laser with shorter wavelength was required, as well as a different method of moving the beam.

In the subsequent redesigned laser station, an XY translation stage with 0.5 μm resolution was used, in conjunction with a HeCd UV laser ($\lambda=325$ nm). The final set of experiments was conducted with a single translation stage, but with a higher quality Argon$^+$ UV laser ($\lambda=244$ nm). This allowed the reduction of the spot size to $5<d_o<10$ μm, which in turn resulted in smaller features that are compatible with single mode optical fibers. Light was successfully coupled into straight channel waveguides fabricated with this laser on hybrid organic-inorganic Al-doped sol-gel films.

For the photothermal laser direct-write of the silicate sol-gel films with a CO_2 laser of $d_o\approx110$ μm, the fluence range that minimized track width and damage of the film was found to be: $5.5<\phi<11.5$ J/cm^2. This range is in

agreement with previous reports by (Shaw and King, 1990; Taylor, Fabes *et al.*, 1990; Guglielmi, Colombo *et al.*, 1992). The depth of the laser densified region varies depending on the laser power and scan speed. Typical depths were between 400 and 1200 Å. The laser power and scan speed used to produce this image was 0.75 W and 0.15 cm/s, respectively. Also, the width of the channels resulted in approximately twice the laser spot size, assuming $d_{o\ min} \approx 80$ μm. This is largely due to thermal diffusion.

In the case of photothermal laser direct-write of Ti-doped hybrid sol-gel films (sol-gel System #2) on quartz wafers with an Argon-ion laser, the fluence range obtained that minimized track width and surface damage was: for $d_o \approx 15$ μm $\rightarrow 60.7 < \phi < 86.7$ J/cm^2, and for $d_o \approx 5.2$ μm $\rightarrow 175 < \phi < 251$ J/cm^2. For this particular case, the quartz substrate played an important role in obtaining such high fluence values, since it is mostly transparent at $\lambda = 244$ nm. Even though the thermal diffusivity for quartz (or amorphous SiO_2) is expected to be similar than the silicate sol-gel film, most of the energy is transmitted directly through the film and into the quartz substrate, while a small fraction is absorbed. Also, at normal incidence the reflectance is maximum; therefore some additional energy is lost.

Finally, for the photophysical processing of hybrid organic-inorganic silicate Al-doped sol-gels, with an Argon-ion laser operating at $\lambda = 244$ nm, straight ridge waveguides with good surface properties and cross-section aspect ratio suitable for light coupling were fabricated. Considering a spot size of $d_o \approx 10.8$ μm, the exposure range that produced small and smooth features was: $0.35 < H_{max} < 0.74$ J/cm^2.

The aspect ratio (line width to line height) was consistently improved, starting from (9.5:1) for the best inorganic silicate sol-gel, to (2.9:1) for the best case of the hybrid Ti-doped sol-gel system, to (18:1) for the Zr-doped hybrid sol-gel and the HeCd laser of the Beta 1 station, to a very best of (1.3:1) for the Al-doped hybrid sol-gel with the Argon-ion UV laser. The progress in the improvement of the aspect ratio, size of the line width, shape of the cross section, and the smoothness of the tracks, shows great promise for even further perfection of these aspects and for the proposed technology in general.

Additionally, CAM software is used to generate the motion profiles defined from a CAD model of the laser's trajectory. The power of the CO_2 laser is controlled through software developed in LabVIEW, which interacts with the XY-stage's controller. Precise control of the laser power and duty cycle allow for specific geometries and patterns to be written onto the film.

The resultant refractive index profile is largely governed by the beam profile of the incident laser, which in this case was 94% pure Gaussian, achieved after beam correction. Gaussian profiles are generally measured by the beam half-width, which is the point where the average power drops to approximately 14% (Siegman, 1986). With a given spot-size, most of the power will therefore be at the center of the spot, decaying exponentially outward. The densification process is mainly photo-thermal, and the largest change in refractive index will occur at the center of the beam/film interface. The scan speed and laser power play an important role in shaping the refractive profile, as slow scan speeds allow for significant thermal diffusion from the beam center, and therefore the resulting refractive profile is wider than the spot size. Additionally, as the

densification process is physical in nature, there is likewise a physical change in the film as of localized shrinkage.

7.1.5. Recommended Direct-Write Process

A broad objective of the current work was to present a generic laser direct-write process that could be applied for the fabrication of optical components based on thin films produced by the sol-gel process. The idea is that different types of sol-gel materials could be used depending on the type of component to be manufactured. Therefore, depending on the type of sol-gel, a different laser could be used for either photothermal or photophysical processing.

Based on the experimental results presented, one particular laser direct-write process stands out by having provided the most consistent results, and the features with the right dimensions for light coupling. For this reason, this process is recommended for future work. The recommended process is presented in Figure 7.2, and is based on the synthesis and deposition of sol-gel System#3, using the aluminum-doped hybrid sol-gel. As shown in this figure, two basic types of devices are proposed. First, planar 2D devices are fabricated by laser photopolymerization, and the residual material is removed by chemical development. The second class of devices includes multi-layer 3D devices or planar devices, where no material is removed, and the photoinitiator is simply out-diffused by thermal treatment in low vacuum. This second class of devices was not demonstrated in this research, but there is evidence in this work and in the literature that this could be achieved.
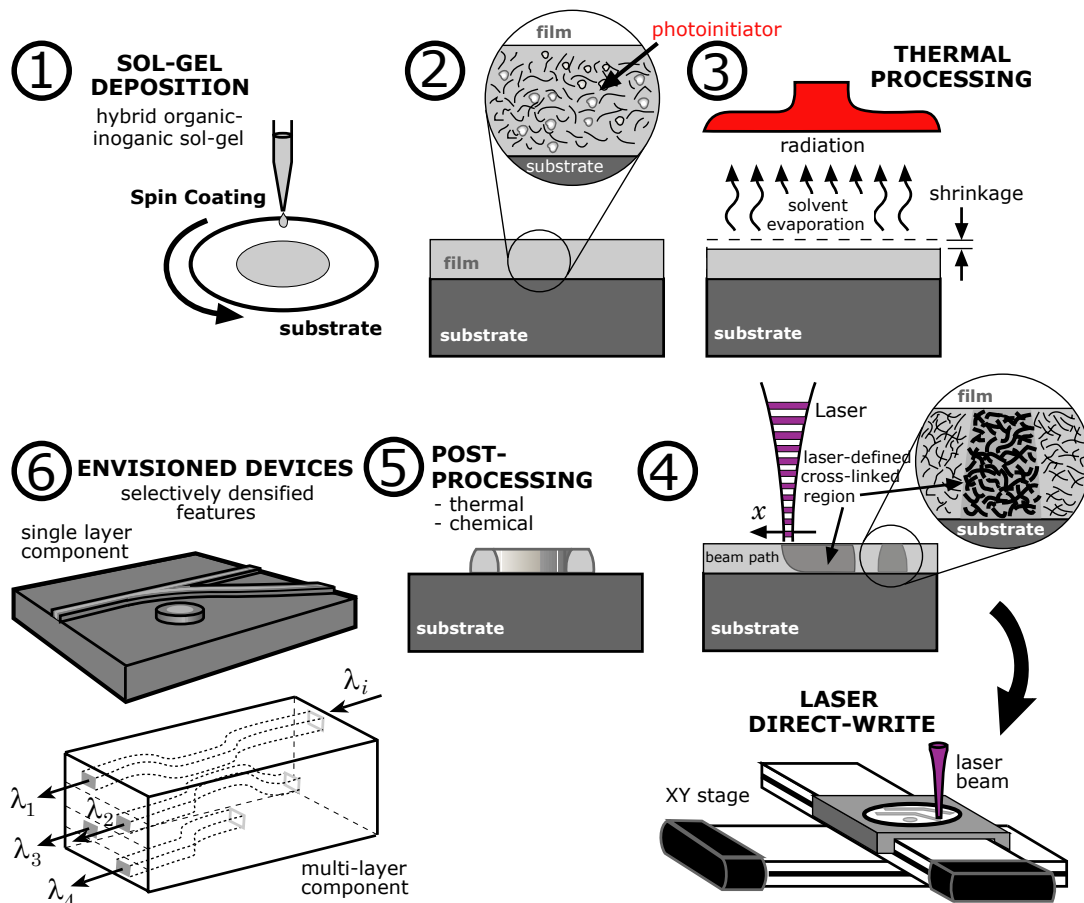
Figure 7.2. Recommended direct-write process

7.2. Future Work

Based on the work done for the development of this dissertation, the following avenues for future research are proposed. These are divided in four main areas.

7.2.1. Sol-Gel Synthesis

As seen throughout this research, the synthesis of the sol-gel plays a crucial role on the subsequent processing steps. The sol-gel process involves a great number of parameters that affect in a smaller or greater degree the physicochemical aspects of the sol-gel matrix. Therefore a detailed statistical analysis is required for the preparation of the hybrid organic-inorganic sol-gels, since these are more recent systems and much of their behavior remains to be investigated.

Particular attention should be paid to the influence that type of photoinitiator and its concentration have on the physical and chemical properties of the photopolymerized sol-gel. Chapter 5 presented a simple mathematical model that related the laser processing parameters and first order kinetic polymerization parameters to the theoretical line width. A more complete study should include aspects such as the calculation of the Dill coefficients, analogous to photolithography and photoresists (Plummer, Deal *et al.*, 2000).

With respect to the chemistry of the sol-gels, one important aspect to consider is the investigation of how to reduce undesired molecules, such as OH^- ions, that are associated to absorption losses. Hybrid sol-gels present a large content of undesired organic compounds, and recent research has focused on how to minimize them from a chemistry perspective. For example, the addition of fluorinated compounds has been investigated (Atkins and Charters, 2003).

7.2.2. Modeling of Laser-Matter Interaction

An important component of this area, involves the characterization of the refractive index profile of the laser processed area, in particular for hybrid sol-

gels. Some basic work was presented in Chapter 6, based on numerical approximation of the intensity profile of coupled light. A more complete analysis of the refractive index profile is required in order to design actual devices.

7.2.3. Multi-Photon Absorption Laser Processing

The laser-matter interaction regime used for this research is considered to be a single-photon process, mainly due to the time scale of interaction between the photon and the sol-gel. An area that has gained interest in recent years involves multi-photon processes; in particular two-photon polymerization. The process of two-photon excitation refers to the simultaneous absorption of two low-energy photons by a chromophore (Strickler and Webb, 1991), having the same effect as one photon of half the wavelength. Through two-photon absorption we can populate high energy levels that are otherwise unreachable by single photon transitions from the ground state. By using two-photon absorption, infrared radiation can polymerize certain materials over a small region of the focal spot, without loosing power as in ultraviolet polymerization, and with the ability to penetrate the material (Cumpston, Ananthavel *et al.*, 1999). With two-photon microfabrication it is possible to produce features that are smaller than the diffraction limit (shown results in the order of ~100nm), which is of particular of interest to novel photonic applications. While the direct-write process presented in this research is limited to this excitation mechanism, the two-photon approach has the advantages of a smaller feature size and better resolution.

Multi-photon absorption processing is achieved with ultra-fast pulsed lasers, such as femto-second pulsed Ti:sapphire lasers. The combination of hybrid sol-gels and multi-photon processing represents an area with great potential.

7.2.4. Novel Optical Components

The geometries fabricated throughout this research consisted in simple straight channel waveguides. A couple of attempts were made to manufacture more complex geometries. With an optimized process, a better understanding of the laser processing parameters, and with the Beta 1 station fully functional, more complex geometries can be attempted. This will expand the base of applications for the proposed direct-write process.

In addition to fabricating traditional optical networking components, there is interest among faculty of the Laboratory for Freeform Fabrication at The University of Texas at Austin for pursuing a different route. This involves investigating the possibility of fabricating components that take advantage of the graded index nature induced by a Gaussian or decaying irradiance distribution of a laser.

Bibliography

Agrawal, G. P. (1997). *Fiber-Optic Communication Systems*. 2nd, NY, John Wiley & Sons.

Almeida, R. M. (1998). "Spectroscopy and structure of sol-gel systems." *Journal of Sol-Gel Science and Technology* **13**(1-3): 51-59.

Almeida, R. M. and E. E. Christensen (1997). "Crystallization Behavior of SiO_2-TiO_2 Sol-Gel Thin Films." *Journal of Sol-Gel Science and Technology* **8**: 409-413.

Almeida, R. M., T. A. Guiton*, et al.* (1990). "Characterization of silica gels by infrared reflection spectroscopy." *Journal of Non-Crystalline Solids* **121**: 193-197.

Almeida, R. M. and C. G. Pantano (1990). "Structural investigation of silica gel films by infrared spectroscopy." *Journal of Applied Physics* **68**(8): 4225-4232.

Almeida, R. M., H. C. Vasconcelos*, et al.* (1994). "Relationship between infrared absorption and porosity in silica-based sol-gel films." *Sol-Gel Optics III*, SPIE **2288**: 678-687.

Andrews, M. P., P. L. Zhang*, et al.* (1999). "Spinnable and UV-Patternable Hybrid Sol-Gel Silica Glass for Direct Semiconductor Dielectric Layer Manufacturing." *SPIE - Advances in Resist Technology and Processing XVI*, Santa Clara, CA, SPIE **3678**: 1252-1262.

Armani, D. K., T. J. Kippenberg*, et al.* (2003). "Ultra-high-Q toroid microcavity on a chip." *Nature* **421**: 925-928.

ASTM-D445-01 (2001). *Standard Test Method for Kinematic Viscosity of Transparent and Opaque Liquids (the Calculation of Dynamic Viscosity)*, ASTM.

Atkins, G. R. and R. B. Charters (2003). "Optical Properties of Highly Fluorinated and Photosensitive Organically-Modified Silica Films for

Integrated Optics." *Journal of Sol-Gel Science and Technology* **26**: 919-923.

Atkins, G. R., R. B. Charters*, et al.* (2001). "Photosensitive ormosil system for integrated optics." *Optical Devices for Fiber Communication II*, Proceedings of SPIE **4216**: 154-163.

Atkins, G. R., R. M. Krolikowska*, et al.* (2000). "Optical properties of an ormosil system comprising methyl- and phenyl-substituted silica." *Journal of Non-Crystalline Solids* **265**: 210-220.

Bae, B.-S. and O.-H. Park (2001). "Direct laser writing of self-developed waveguides in benzyldimethyketal-doped sol-gel hybrid glass." *Journal of Materials Research* **16**(11): 3184-3187.

Bäuerle, D. (2000). *Laser Processing and Chemistry*. 3rd, Berlin, Germany, Springer-Verlag.

Bäuerle, D. (2002). "Laser processing and chemistry: recent developments." *Applied Surface Science* **186**: 1-6.

Beaman, J. J., J. W. Barlow*, et al.* (1997). *Solid Freeform Fabrication*. Norwell, MA, Kluwer Academic Pub.

Beaman, J. J., K. L. Wood*, et al.* (2001). *Cooperative Research in Optical Networking Technologies*. Internal report. Austin, TX, University of Texas at Austin, Laboratory for Freeform Fabrication.

Birnie, D. P. (1997). "Combined Flow and Evaporation During Spin Coating of Complex Solutions." *Journal of Non-Crystalline Solids* **218**: 174-178.

Blanc, D., S. Pelissier*, et al.* (2003). "Photo-induced swelling of hybrid sol-gel thin films: Application to surface micro-patterning." *Journal of Sol-Gel Science and Technology* **27**(2): 215-220.

Blanc, D., S. Pelissier*, et al.* (1999). "Self-Processing of Surface-Relief Gratings in Photosensitive Hybrid Sol-Gel Glasses." *Advanced Materials* **11**(18): 1508-1511.

Born, M. and E. Wolf (1999). *Principles of Optics*. 7th, Cambridge, UK, Cambridge University Press.

Box, G. E. P., W. G. Hunter*, et al.* (1978). *Statistics for Experimenters*. New York, NY, John Wiley & Sons.

Bräutigam, U., H. Bürger, *et al.* (1989). "Some aspects of property tailoring of sol-gel derived thin SiO_2 films." *Journal of Non-Crystalline Solids* **110**: 163-169.

Brinker, C. J., A. J. Hurd, *et al.* (1990). "Sol-gel thin film formation." *Journal of Non-Crystalline Solids* **121**: 294-302.

Brinker, C. J., A. J. Hurd, *et al.* (1992). "Review of sol-gel thin film formation." *Journal of Non-Crystalline Solids* **147&148**: 424-436.

Brinker, C. J. and G. W. Scherer (1985). "Sol-Gel Glass I: Gelation and Gel-Structure." *Journal of Non-Crystalline Solids* **70**: 301-322.

Brinker, C. J. and G. W. Scherer (1990). *Sol-Gel Science.* 1st, San Diego, CA, Academic Press, Inc.

Brinker, C. J., G. W. Scherer, *et al.* (1985). "Sol-Gel Glass II: Physical and Structural Evolution During Constant Heating Rate and Experiments." *Journal of Non-Crystalline Solids* **72**: 345-368.

Brusatin, G., M. Guglielmi, *et al.* (1997). "Microstructural and optical properties of sol-gel silica-titania waveguides." *Journal of Non-Crystalline Solids* **220**: 202-209.

Buestrich, R., F. Kahlenberg, *et al.* (2001). "ORMOCERs for Optical Interconnection Technology." *Journal of Sol-Gel Science and Technology* **20**: 181-186.

Campbell, S. A. (2001). *The Science and Engineering of Microelectronic Fabrication.* New York, NY, Oxford University Press.

Carslaw, H. S. and J. C. Jaeger (1986). *Conduction of Heat in Solids.* 2nd Ed., Oxford, U.K., Oxford University Press.

Charters, R. B., B. Luther-Davies, *et al.* (1999). "Improved Performance of Laser Written Channel Waveguides Using a TEM*01 Beam." *IEEE Photonics Technology Letters* **11**(12): 1617-1619.

Chia, T. (1992). *Laser Densification of Gel-Silica Glasses and Optical Application.* PhD Dissertation. University of Florida,

Chia, T., L. L. Hench, *et al.* (1994). "Thermal Modeling of Laser-Densified Microlenses." *Applied Optics* **33**(16): 3486-3492.

Christensen, C. M. (1997). *The Innovator's Dilemma.* Boston, MA, Harvard Business School Press.

Church, K. H., C. Fore, *et al.* (2000). "Commercial applications and review for direct write technologies." *Materials Development for Direct Write Technologies*, San Francisco, CA, USA, Materials Research Society **624**: 3-8.

Clark, K. B. and S. C. Wheelright (1994). *The Product Development Challenge.* Boston, MA, Harvard Business Review.

Coudray, P., J. Chisham, *et al.* (1997). "Ultraviolet light imprinted sol-gel silica glass low-loss waveguides for use at 1.55 μm." *Optical Engineering* **36**(4): 1234-1240.

Coudray, P., J. Chisham, *et al.* (1996). "Ultraviolet light imprinted sol-gel silica glass waveguide devices on silicon." *Optics Communications* **128**: 19-22.

Cumpston, B. H., S. Ananthavel, *et al.* (1999). "Two-photon polymerization initiators for three-dimensional optical data storage and microfabrication." *Nature* **398**(6722): 51-54.

Das, S. (1998). *Direct Selective Laser Sintering of High Performance Metals - Machine Design, Process Development and Process Control.* Ph.D. Dissertation. University of Texas at Austin, Austin, Texas.

Deckard, C. R. (1988). *Selective laser sintering.* Ph.D. Dissertation. University of Texas at Austin, Austin, Texas.

Decker, C. (2002). "Light-induced crosslinking polymerization." *Polymer International* **51**: 1141-1150.

Du, X. M. and R. M. Almeida (1997). "Effects of Thermal Treatment on the Structure and Properties of SiO_2-TiO_2 Gel Films and Silicon Substrates." *Journal of Sol-Gel Science and Technology* **8**: 377-380.

Emslie, A. G., F. T. Bonner, *et al.* (1958). "Flow of a Viscous Liquid on a Rotating Disk." *Journal of Applied Physics* **29**(5): 858.

Fabes, B. D., et al (1992). "Laser Densification of Optical Films." *Sol-Gel Optics II*, SPIE **1758**: 227-234.

Fabes, B. D., D. J. Taylor, *et al.* (1990). "Laser Processing of Channel Waveguide Structures in Sol-Gel Coatings." *Sol-Gel Optics*, SPIE **1328**: 319-328.

Fallahi, M., R. Bedford, *et al.* (2002). "Photopatternable sol-gel for compound semiconductor processing." *Journal of Vacuum Science Technology B.* **20**(6): 2942-2945.

Fardad, M. A., M. P. Andrews, *et al.* (1998). "Fabrication of ridge waveguides: a new sol-gel route." *Applied Optics* **37**(12): 2429-2434.

Fardad, M. A., M. P. Andrews, *et al.* (1997). "Novel Sol-Gel Fabrication of Integrated Optical Waveguides." *SPIE - Integrated Optics Devices*, SPIE **2997**: 72-78.

Fardad, M. A. and M. Fallahi (1998). "Organic-inorganic materials for integrated optoelectronics." *Electronics Letters* **34**(20): 1940-1941.

Fardad, M. A. and M. Fallahi (1999). "Sol-Gel Multimode Interference Power Splitters." *IEEE Photonics Technology Letters* **11**(6): 697-699.

Fardad, M. A., O. V. Mishechkin, *et al.* (2001). "Hybrid Sol-Gel Materials for Integration of Optoelectronic Components." *Journal of Lightwave Technology* **19**(1): 84-91.

Fardad, M. A., T. Touam, *et al.* (1997). "UV-light imprinted Bragg grating in sol-gel ridge waveguide with almost 100% reflectivity." *Electronics Letters* **33**(12): 1069-1070.

Fardad, M. A., E. M. Yeatman, *et al.* (1995). "Effects of H_2O on structure of acid-catalysed SiO_2 sol-gel films." *Journal of Non-Crystalline Solids* **183**: 260-267.

Fielding, J. P. (1999). *Introduction to Aircraft Design*. Cambridge University Press, UK.

Fouassier, J.-P. (1995). *Photoinitiation, Photopolymerization, and Photocuring: Fundamentals and Applications*. Munich, Hanser Gardner Publications.

Fowles, G. R. (1989). *Introduction to Modern Optics*. Toronto, Ontario, Dover Publications.

Gallardo, J., A. Duran, *et al.* (2002). "Structure of inorganic and hybrid SiO_2 sol-gel coatings by variable incidence infrared spectroscopy." *Journal of Non-Crystalline Solids* **298**: 219-225.

Ganz, D., et al (1997). "Fast CO_2 Laser Firing of Sol-Gel SnO_2:Sb Coatings." *Journal of Materials Science Letters* **16**: 1233-1235.

Ganz, D., G. Gasparro, *et al.* (1998). "Laser Sintering of SnO_2 : Sb Sol-Gel Coatings." *Journal of Sol-Gel Science and Technology* **13**: 961-967.

Ganz, D., A. Reich, *et al.* (1997). "Laser Firing of Transparent Conducting SnO_2 Sol-Gel Coatings." *Journal of Non-Crystalline Solids* **218**: 242-246.

Gilbert, J. C. and S. F. Martin (2002). *Experimental Organic Chemistry*. 3rd, Orlando, FL, Harcourt, Inc.

Grandi, S., P. Mustarelli, *et al.* (2002). "Synthesis of GeO_2-doped SiO_2 aerogels and xerogels." *Journal of Non-Crystalline Solids* **303**: 208-217.

Guglielmi, M., P. Colombo, *et al.* (1992). "Characterization of laser-densified sol-gel films for the fabrication of planar and strip optical waveguides." *Journal of Non-Crystalline Solids* **147&148**: 641-645.

Guglielmi, M., A. Martucci, *et al.* (1998). "Spinning Deposition of Silica and Silica-Titania Optical Coatings: A Round Robin Test." *Journal of Materials Research* **13**(3): 731-738.

Gvishi, R., U. Narang, *et al.* (1997). "Novel, Organically Doped, Sol-Gel Derived Materials for Photonics." *Applied Organometallic Chemistry* **11**(2): 107-127.

Hall, D. G. (1993). "The role of silicon in optoelectronics." *Proceedings of the Symposium on Silicon-Based Optoelectronic Materials*, San Francisco, CA, Materials Research Society **298**: 367-378.

Hecht, J. (1999). *Understanding Fiber Optics*. 3rd, NJ, Prentice Hall.

Hench, L. L. (1998). *Sol-Gel Silica*. Westwood, NJ, Noyes Publications.

Hibino, Y. (2003). "Silica-based planar lightwave circuits and their applications." *MRS Bulletin* **28**(5)**:** 365-371.

Holmes, A. S., R. R. A. Syms, *et al.* (1993). "Fabrication of Buried Channel Waveguides on Silicon Substrates Using Spin-On Glass." *Applied Optics* **32**(25): 4916-21.

Hunsperger, R. G. (2002). *Integrated Optics: Theory and Technology*. 5th, Berlin, Springer-Verlag.

II_VI (2004). *Tutorial: Determining Spot Size*. http://www.iiviinfrared.com/ttr_detspotsize.html

Jacobs, P. F. (1992). *Rapid prototyping & manufacturing: fundamentals of stereolithography*. Dearborn, MI, Society of Manufacturing Engineers.

Jain, V. K., J. Franz, *et al.* (2001). "Emerging Trends in Fiber Optic Networks." *Fiber and Integrated Optics* **20**(2): 95-124.

Kashyap, R. (1999). *Fiber Bragg gratings*. San Diego, CA, Academic Press.

Keddie, J. L., P. V. Braun, *et al.* (1994). "Interrelationship between Densification, Crystallization, and Chemical Evolution in Sol-Gel Titania Thin Films." *Journal of the American Ceramic Society* **77**(6): 1592-96.

Keddie, J. L. and E. P. Giannelis (1990). "Ion-Beam Analysis of Silica Sol-Gel Films: Structural and Compositional Evolution." *Journal of the American Ceramic Society* **73**(10): 3106-3109.

Keddie, J. L. and E. P. Giannelis (1991). "Effect of Heating Rate on the Sintering of Titanium Dioxide Thin Films: Competition between Densification and Crystallization." *Journal of the American Ceramic Society* **74**(10): 2669-2671.

Klein, L. C., Ed. (1988). *Sol-gel technology for thin films, fibers, preforms, electronics, and specialty shapes*. Park Ridge, N.J., Noyes Publications.

Klein, L. C. (1991). "Sol-Gel Coatings." *Thin Film Processes II*. Ed.: J. L. Vossen and W. Kern. San Diego, CA, Academic Press**:** 501-522.

Kogelnik, H. (1975). "Theory of dielectric waveguides." *Integrated Optics*. Ed.: T. Tamir. Berlin, Germany, Springer-Verlag. **7:** 13-81.

Kuebler, S. M., S. Ananthavel, *et al.* (1999). "Two-photon polymerization initiators for efficient three-dimensional optical data storage and microfabrication." *Proceedings of the 1999 Quantum Electronics and Laser Science Conference (QELS '99), May 23-May 28 1999*

IQEC, International Quantum Electronics Conference Proceedings: 52.

Lee, H. J., R. K. Prud'homme, *et al.* (2001). "Cure depth in polymerization: Experiments and theory." *Journal of Materials Research* **16**(12): 3536-3544.

Lewis, J. A. (2000). "Colloidal Processing of Ceramics." *Journal of the American Ceramic Society* **83**(10): 2341-2359.

Liu, B., A. Shakouri, *et al.* (2000). "A wavelength multiplexer using cascaded three-dimensional vertical couplers." *Applied Physics Letters* **76**(3): 282-284.

Maruo, S. and K. Ikuta (1998). "New microstreolithography (Super-IH process) to create 3D freely movable micromechanism without sacrificial layer technique." *1998 International Symposium on Micromechatronics and Human Science*, IEEE: 115-120.

Maruo, S. and K. Ikuta (1999). "Movable microstructures made by two-photon three-dimensional microfabrication." *1999 International Symposium on Micromechatronics and Human Science*, IEEE: 173-178.

McCormick, A. (1994). "Recent progress in the study of the kinetics of sol-gel SiO$_2$ synthesis reactions." *Sol-Gel Processing and Applications.* Ed.: Y. A. Attia. NY, Plenum Press.

McGill, R. A., D. B. Chrisey, *et al.* (1998). "Matrix assisted pulsed laser evaporation (MAPLE) of functionalized polymers: Applications with chemical sensors." *Laser Applications in Microelectronic and Optoelectronic Manufacturing V, Jan 26-28 1998*, San Jose, CA, United States, The International Society for Optical Engineering **3274**: 255-266.

Meyerhofer, D. (1978). "Characteristics of Resist Films Produced by Spinning." *Journal of Applied Physics* **49**(7): 3993-3997.

Miura, K., J. Qiu, *et al.* (1997). "Photowritten optical waveguides in various glasses with ultrashort pulse laser." *Applied Physics Letters* **71**(23): 3329-3331.

Moore, J. H., C. C. Davis, *et al.* (1991). *Building scientific apparatus.* Cambridge, MA, Perseus Books Pub.

Morishita, K. (1986). "Index profiling of three-dimensional optical waveguides by the propagation-mode near-field method." *Journal of Lightwave Technology* **4**(8): 1120-1124.

Najafi, S. I., C.-Y. Li, *et al.* (1995). "Integrated Optics Devices by Ultraviolet Light Imprinting in Sol-Gel Silica Glass." *SPIE - Functional Photonic Integrated Circuits*, San Jose, CA, SPIE **2401**: 110-115.

Najafi, S. I., T. Touam, *et al.* (1998). "Sol-Gel Glass Waveguide and Grating on Silicon." *Journal of Lightwave Technology* **16**(9): 1640-1646.

Nelson, J. C. (1993). *Selective laser sintering: a definition of the process and an empirical sintering model.* Ph.D. Dissertation. The University of Texas at Austin, Austin, Texas.

ORMOCER (2003). http://www.isc.fraunhofer.de/alteseiten/ormocere_e/index_o0.html

Othonos, A. (1999). *Fiber Bragg gratings.* Boston, MA, Artech House.

Otto, K. and K. L. Wood (1998). "Product evolution: A reverse engineering and redesign methodology." *Research in Engineering Design* **10**(4): 226-243.

Otto, K. and K. L. Wood (2001). *Product Design*. NJ, Prentice Hall.

Pahl, G. and W. Beitz (1996). *Engineering design : a systematic approach*. London, Springer-Verlag.

Park, O.-H., J.-I. Jung*, et al.* (2001). "Photoinduced condensation of sol-gel hybrid glass films doped with benzildimethylketal." *Journal of Materials Research* **16**(17): 2143-2148.

Parrill, T. M. (1994). "Heat treatment of spun-on acid-catalyzed sol-gel silica films." *Journal of Materials Research* **9**(3): 723-730.

Patela, S. (2002). *Fabrication methods of planar waveguides and related structures*. http://www.patela.prv.pl

Pelli, S., G. C. Righini*, et al.* (1996). "Direct Laser Writing of Ridge Optical Waveguides in Silica-Titania Glass Sol-Gel Films." *Optical Materials* **5**: 119-126.

Pierre, A. C. (1998). *Introduction to Sol-Gel Processing*. Kluwer Academic Pub.

Piqué, A. and D. B. Chrisey (2002). *Direct-Write Technologies for Rapid Prototyping Applications*. San Diego, CA, Academic Press.

Plummer, J. D., M. D. Deal*, et al.* (2000). *Silicon VLSI Technology*. New York, NY, Prentice Hall.

Primeau, N., C. Vautey*, et al.* (1997). "Effect of thermal annealing on aerosol-gel deposited SiO_2 films: A FTIR deconvolution study." *Thin Solid Films* **310**(1-2): 47-56.

Pugh, S. (1991). *Total design : integrated methods for successful product engineering*. Reading, MA., Addison-Wesley Pub. Co.

Que, W., Z. Sun*, et al.* (2001). "Effects of titanium content on properties of sol-gel silica-titania films via organically modified silane precursors." *Journal of Physics D: Applied Physics* **34**: 471-476.

Que, W., Y. Zhou*, et al.* (2001). "Preparation and Characterization of $SiO_2/TiO_2/\gamma$-glycidoxypropyltrimethoxysilane composite materials for optical waveguides." *Applied Physics A* **73**: 171-176.

Ramkumar, K., S. K. Ghosh*, et al.* (1993). "Stress variations in TEOS-based SiO_2 films during ex-suit thermal cycling." *Journal of the Electrochemical Society* **140**(9): 2669-2673.

Ramkumar, K. and A. N. Saxena (1992). "Stress in SiO_2 films deposited by plasma and ozone tetraethylorthosilicate chemical vapor deposition processes." *Journal of the Electrochemical Society* **139**(5): 1437-1442.

Righini, G. C. and S. Pelli (1997). "Sol-Gel Glass Waveguides." *Journal of Sol-Gel Science and Technology* **8**: 991-997.

Roco, M. C., S. Williams*, et al.* (1999). *Vision for Nanotechnology Research and Development in the Next Decade*. Maryland, Loyola College.

Rubahn, H.-G. (1999). *Laser Applications in Surface Science and Technology*. Surrey, Great Britain, John Wiley & Sons.

Ruizpalacios, R., J. J. Beaman*, et al.* (2001). "Investigative Study of Selective Laser Sintering of Silicon Dioxide-Based Powders." *Proceedings of the XXIII Solid Freeform Fabrication Symposium*, Austin, TX, University of Texas at Austin

Sakka, S. and K. Kamiya (1982). "The Sol-Gel Transition in the Hydrolysis of Metal Alkoxides in Relation to the Formation of Glass Fibers and Films." *Journal of Non-Crystalline Solids* **48**: 31-46.

Sakka, S., K. Kamiya*, et al.* (1984). "Formation of Sheets and Coating Films from Alkoxide Solutions." *Journal of Non-Crystalline Solids* **63**: 223-235.

Saravanamuttu, K., X. M. Du*, et al.* (1998). "Photoinduced structural relaxation and densification in sol-gel-derived nanocomposite thin films: implications for integrated optics device fabrication." *Canadian Journal of Chemistry* **76**: 1717-1729.

Scherer, G. W. (1988). "Aging and drying of gels." *Journal of Non-Crystalline Solids* **100**: 77-92.

Scriven, L. E. (1988). "Physics and Applications of Dip Coating and Spin Coating." *Better Ceramics Through Chemistry III*, Materials Research Society **121**: 717-729.

Seco, A. M., M. C. Goncalves*, et al.* (2000). "Densification of Hybrid Silica-Titania Sol-Gel Films Studied by Ellipsometry and FTIR." *Materials Science and Engineering B* **76**: 193-199.

Shaw, D. J. and T. A. King (1990). "Densification of Sol-Gel Silica Glass by Laser Irradiation." *Sol-Gel Optics*, SPIE **1328**: 474-479.

Shriver, D. F. and M. A. Drezdzon (1986). *The Manipulation of Air-Sensitive Compounds*. NY, John Wiley & Sons.

Siegel, R. and J. R. Howell (1992). *Thermal Radiation Heat Transfer*. 3rd., Washington, D.C., Hemisphere Pub. Corp.

Siegman, A. E. (1986). *Lasers*. Mill Valley, CA, University Science Books.

Soppera, O. and C. Croutxe-Barghorn (2003). "Real-time Fourier transform infrared study of free-radical UV-induced polymerization of hybrid sol-gel. I. Effect of silicate backbone on photopolymerization kinetics." *Journal of Polymer Science, Part A: Polymer Chemistry* **41**(5): 716-724.

Soppera, O. and C. Croutxe-Barghorn (2003). "Real-time Fourier transform infrared study of the free-radical ultraviolet-induced polymerization of a hybrid sol-gel. II. The effect of physicochemical parameters on the photopolymerization kinetics." *Journal of Polymer Science, Part A: Polymer Chemistry* **41**(6): 831-840.

Steen, W. (1998). *Laser Material Processing*. London, UK, Springer-Verlag.

Strickler, J. H. and W. W. Webb (1991). "Three-dimensional optical data storage in refractive media by two-photon point excitation." *Optics Letters* **16**(22): 1780-1782.

Syms, R. R. A. (1994). "Silica-On Silicon Integrated Optics." *Advances in Integrated Optics*. Ed.: S. Martellucci, A. N. Chester and M. Bertolotti. NY, Plenum Press**:** 121-150.

Syms, R. R. A. (1994). "Stress in Thick-Sol Phosphosilicate Glass Films Formed on Si Substrates." *Journal of Non-Crystalline Solids* **167**: 16-20.

Syms, R. R. A. and A. S. Holmes (1994). "Deposition of thick silica-titania sol-gel films on Si substrates." *Journal of Non-Crystalline Solids* **170**: 223-233.

Taylor, D. J., D. P. Birnie*, et al.* (1995). "Temperature Calculation for Laser Irradiation of Sol-Gel Films on Oxide Substrates." *Journal of Materials Research* **10**(6): 1429-1434.

Taylor, D. J. and B. D. Fabes (1992). "Laser processing of sol-gel coatings." *Journal of Non-Crystalline Solids* **147&148**: 457-462.

Taylor, D. J., B. D. Fabes*, et al.* (1990). "Laser Densification of Sol-Gel Coatings." *Materials Research Society Symposium*, Materials Research Society **180**: 1047-1052.

Tervonen, A. (1999). "Challenges and Opportunities for Integrated Optics in Optical Networks." *Integrated Optics Devices III, SPIE*, SPIE **3620**: 2-11.

Ullman, D. G. (2002). *The Mechanical Design Process*. 3rd, New York, NY, McGraw-Hill.

Ulrich, K. T. and S. D. Eppinger (2000). *Product Design and Development*. 2nd, Boston, MA, McGraw Hill.

van Blaaderen, A., R. Ruel*, et al.* (1997). "Template-directed colloidal crystallization." *Nature* **385**: 321-324.

Vlasov, Y. A., X.-Z. Bo*, et al.* (2001). "On-chip natural assembly of silicon photonic bandgap crystals." *Nature* **414**(6861): 289-293.

von Allmen, M. and A. Blatter (1995). *Laser-Beam Interactions with Materials*. Berlin, Germany, Springer-Verlag.

Wang, H. (1999). *Advanced Processing Methods for Microelectronics Industry Silicon Wafer Handling Components*. Ph.D. Dissertation. The University of Texas at Austin, Austin, TX.

Weisenbach, L., B. J. J. Zelinski*, et al.* (1991). "The influence of processing variables on the optical properties of SiO_2-TiO_2 planar waveguides." *Submolecular Glass Chemistry and Physics*, SPIE **1590**: 50-58.

Welch, A. J., M. J. C. van Germet*, et al.* (1995). "Definitions and overview of tissue optics." *Optical-thermal reponse of laser-irradiated tissue*. Ed.: A. J. Welch and M. J. C. van Germet. New York, Plenum Press**:** 15-26.

Woollam, J. A., B. Johns*, et al.* (1999). "Overview of Variable Angle Spectroscopic Ellipsometry (VASE), Part I: Basic Theory and Typical Applications." *Critical Reviews of Optical Science and Technology*, Denver, Colorado, SPIE **CT72**: 3-28.

Wright, J. D. and A. J. M. Sommerdijk (2001). *Sol-Gel Materials: Chemistry and Applications*. Amsterdam, Gordon and Breach.

Xia, Y. and G. M. Whitesides (1998). "Soft lithography. Annual Reviews Inc, Palo Alto, CA, USA**:** 153-184.

Young, M. (2000). *Optics and Lasers*. Berlin, Germany, Springer-Verlag.

Young, R. J. and P. Lovell (1991). *Introduction to Polymers*. 2nd edition, New York, NY, Chapman and Hall.

Zhang, X., X. N. Jiang*, et al.* (1999). "Micro-stereolithography of polymeric and ceramic microstructures." *Sensors and Actuators A: Physical* **77**(2): 149-156.

Vita

Rodrigo Ruizpalacios was born in Mexico City, Mexico on August 16, 1972, the son of Dr. Guillermo Ruiz-Palacios and Dr. Beatriz Remus Ruizpalacios. He attended the Instituto Tecnologico y de Estudios Superiores de Monterrey (ITESM) in Monterrey, Nuevo Leon, Mexico where he received Bachelor of Science and Master of Science degrees in Mechanical Engineering in May 1995 and December 1997, respectively. He worked at the Center for Integrated Manufacturing Systems (CSIM) at the ITESM in Monterrey, Nuevo Leon, Mexico from January 1998 to July 1999. In August 1999 he was awarded a Fulbright-Garcia Robles scholarship and admitted to The University of Texas at Austin to pursue a Ph.D. in Mechanical Engineering. Rodrigo is married to Laura Elena Cruz Ruizpalacios.

Permanent address: Camino al Cedral #20

San Buenaventura, Tlalpan

Mexico, D.F. Mexico 14430

This dissertation was typed by the author.